MULTIVARIATE IMAGE ANALYSIS AND REGRESSION FOR INDUSTRIAL PROCESS MONITORING AND PRODUCT QUALITY CONTROL

By

MANISH H. BHARATI, B. Eng., M. Eng.

A Thesis

Submitted to the School of Graduate Studies

in Partial Fulfillment of the Requirements

for the Degree

Doctor of Philosophy

McMaster University

MIA/MIR FOR INDUSTRIAL PROCESS MONITORING AND PRODUCT QUALITY CONTROL

...to my parents, Harish and Devika Bharati

DOCTOR OF PHILOSOPHY (2002) McMASTER UNIVERSITY

(Chemical Engineering) Hamilton, Ontario

TITLE: Multivariate Image Analysis and Regression for Industrial Process Monitoring and Product Quality Control

AUTHOR: Manish H. Bharati,

B. Eng. (Ryerson Polytechnic University)

M. Eng. (McMaster University)

SUPERVISOR: Professor John F. MacGregor

NUMBER OF PAGES: xviii, 216

Abstract

On-line Multivariate Image Analysis (MIA) and Multivariate Image Regression (MIR) methods are developed for purposes of on-line monitoring and feedback control of industrial processes that are equipped with vision systems. The thesis progresses via three main investigative studies through applications of the proposed methods in the steel manufacturing and forest products industries. These studies are concerned with (i) vision based automatic grading of softwood lumber; (ii) empirical modeling of pulp and paper characteristics using multi-spectral imaging sensors; and (iii) texture based classification of steel surface samples with image texture analysis.

The first industrial application study addresses the problem of automatic quality grading (classification) of sawn softwood lumber based on visually identifying the severity and distribution of common defects. An extended MIA approach for on-line monitoring of true color (RGB) image representations of lumber boards is proposed, which provides both qualitative and quantitative measures of lumber defects. The proposed approach involves developing a robust MIA model on typical defects commonly found in lumber. These defects are then monitored using the MIA model on lumber boards being imaged by an on-line RGB imaging sensor. The Near-Infrared (NIR) wavelength region (900 nm – 1700 nm) of the electromagnetic spectrum is also investigated for lumber defect analysis using MIA of multi-spectral NIR images. Advantages and shortcomings of using NIR imaging spectroscopy versus RGB cameras for lumber grading are highlighted.

The second industrial application involves empirical model based prediction of the properties of finished dry pulp sheets and the classification of paper samples having different compositions. In the pulp study a novel MIR technique extracts relevant feature information from multi-spectral images of the samples acquired through NIR imaging

spectroscopy, and uses Partial Least Squares (PLS) regression to relate the extracted NIR feature space to the corresponding (non-image) quality data measured via laboratory analysis. The proposed MIR scheme is successfully used to monitor pulp quality variations in an at-line mode on an industrial pulp process during several grade changes. In the paper classification problem the feature space, extracted from NIR spectroscopic images, is further interrogated using Principal Component Analysis (PCA) to classify the finished samples based on their chemical ingredient information.

The third industrial application addresses the problem of classifying steel sheet samples based on their overall surface roughness characteristics. A novel MIA based image texture analysis technique has been proposed, which extracts textural features from grayscale, color, or multi-spectral images in the latent variable space of PCA. The proposed method enables interactive texture analysis of individual images using visual MIA tools. Furthermore, a MIA model can be developed to monitor textural features from various images for the purpose of image classification. The scheme is illustrated on a set of steel surface images with varying degrees of roughness characteristics. Image classification achieved by the proposed technique is compared with that obtained by other classical multivariate statistical methods and conventional texture analysis approaches.

Acknowledgements

This doctorate degree has certainly been one of the most challenging yet rewarding experiences of my life. There are many people to thank whose help, encouragement and contributions made this work possible.

Most importantly, I would like to express my deepest gratitude to my supervisor, Dr. John F. MacGregor, for his continuous guidance and unconditional support throughout the course of my master's and doctorate degrees that I undertook with him. I would also like to thank him for his genuine kindness and true faith in my abilities throughout the ups and downs of my past seven years with him. I have learnt a lot from him and for this I will be forever indebted. I am also very thankful to the Department of Chemical Engineering at McMaster University for providing me with financial support during these years.

Due to the industrial application oriented nature of this work obtaining representative data was a critical factor, which was made possible by Mr. Bill Tropper and Mr. Marc Champagne from Tembec Inc., and Mr. Barry Brusey and Mr. Victor Tychowsky from Dofasco. Their immense help and expertise are greatly appreciated.

In 1988 my parents, Harish and Devika Bharati, left a comfortable life in India and migrated to Canada in order to make their only child's future brighter, and enable him to achieve his potential to the fullest. Besides providing him emotional and financial support they taught him the true value of love, respect and knowledge. From the deepest core of my heart I would like to thank you very much mom and dad. This work is dedicated to you for your many sacrifices and unconditional love, which has molded me into the man that I am today.

I would also like to express my sincere thanks to my aunt, Dr. Renuka G. Swami, who has loved me like a mother, and given me inspiration and strength in all stages of my life. I love you more than you know.

Over the past seven years as a graduate student at McMaster University I have had the good fortune to meet and interact with many people from all over the world. Many friendships were formed, which have touched me in unique ways. I would like to thank all my old and new friends from the process control graduate student group for the lively discussions, social and sporting activities we shared during my stay. To my friends from the Department: Ivan, Jason, Bhupinder, Tracy, Carl, Ali, Niki, San, Ruijie, Seongkyu, Tong, Thanassis, François, Jean-François, Barb, Kevin, Koji, Jose, Honglu, June, Jesus, Steve, Song, Ken, Ed, Laura, and Christiane, I feel fortunate to have found friends like you. I will miss you dearly.

To my closest friends, Tracy, Carl, San, Niki and Sanjay, each and every one of you have touched my heart in various stages of my life. To have friends like you is an honor, and I will cherish all the fond memories we shared for the rest of my life.

Finally, I would like to say a special thanks to my loving wife Pooja, whose love, patience and immense support gave me the strength to finish the final two years of my doctorate degree.

Contents

List of Tables

List of Figures

Chapter 1

Introduction

Maintaining product quality to meet varying customer demands is of the utmost importance for the manufacturing industry. A lot of research is being conducted to develop novel process monitoring schemes for quality control. On-line sensors provide the foundation for all such schemes. Sometimes even the simplest on-line sensors (e.g. thermocouples) are quite expensive to install. New inexpensive on-line sensor technology is of great demand in such industries. With the recent advents in imaging technology over the past decade it is becoming clear that digital cameras may possess the ability to meet these demands in a very economical way. Digital cameras have great potential as on-line imaging sensors in many industries with spatially distributed systems that traditionally require visual information processing for quality inspection of solid or heterogeneous products on moving process lines. The major difficulty lies in the efficient extraction of relevant information from the digital images in real-time and relating them to product quality and process performance.

This thesis focuses on developing methods that incorporate digital imaging sensors and digital imagery into monitoring and feedback control of such industrial processes. In particular, the thesis develops multivariate statistics based [e.g. Principal Component Analysis (PCA)] image analysis methods that allow extraction of relevant data from digital imagery in various industrial applications.

Image data carries large amounts of information in the form of light intensities at various pixel locations. Traditionally, digital image analysis techniques have focused on visually enhancing feature information via manipulation of pixel intensities in the spatial domain of the image. The enhanced image is then either thrseholded to count feature pixels, or put through some simple statistical analyses to gather a quantitative description of feature information. Unlike traditional image analysis techniques the multivariate statistics based image analysis methods developed in this thesis extract product quality relevant information from digital images without necessarily working in the spatial domain of the image.

The extracted image feature information is typically most correlated with product quality characteristics, its local and overall properties, its spatial variations in surface texture, etc. This new image feature space proves to be useful in many industrial process monitoring and control situations. It can be used to infer product quality in an on-line monitoring scheme; to classify products into various quality grades; or to potentially perform feedback control as part of an inferential control scheme using visual imaging sensors.

In the past multivariate statistics based image analysis methods have successfully been used for feature extraction in various off-line applications ranging from remote sensing to microscopy [Geladi et. al., 1996]. Through these initial applications the image analysis methods have come to be commonly known as Multivariate Image Analysis (MIA) and Multivariate Image Regression (MIR).

The main objectives of the thesis are to explore the potentials of applying MIA and MIR techniques in on-line industrial process monitoring and control schemes for purposes of fault detection, soft-sensor modeling of product properties, and product classification for quality assurance. For successful on-line application several extensions and modifications to (previously off-line) MIA and MIR techniques have been developed throughout the thesis. In conjunction with these objectives this thesis progresses through a number of investigative and preliminary studies of the applications of the proposed methodologies in the steel manufacturing and forest products industries (specifically softwood lumber, pulp and paper manufacturing). Presented below is a brief description of each application along with a discussion of its objectives and contributions of the study.

1.1 Multivariate Image Analysis for Softwood Lumber Grading

A typical sawmill produces lumber boards with varying degrees of quality, depending upon the severity and distribution of defects. Correct grading of softwood lumber based on overall quality is of paramount importance in the forest products industry because there is a substantial pricing differential between lumber grades. Traditionally, the task of lumber grading has been entrusted with skilled human graders who are responsible for making several grading (classification) judgments every minute. Although lumber graders are trained individuals with set grading rules, they are sometimes inconsistent in their grading judgments due to various factors ranging from fatigue to wood variations. Consequently efforts have been made in the past decade to replace man with imaging sensors and image analysis algorithms for automatic lumber grading.

Various grayscale and color imaging sensors have been used to meet this goal. In the majority of lumber grading applications the images have been analyzed using traditional image processing techniques to extract lumber features for classification. However, it has been difficult to develop one robust classification method due to the inherent variation in lumber (even within the same species). Lately, researchers [Hagman, 1997] have recognized that lumber grading is a multivariate problem. They have proposed MIA and MIR techniques for extracting features from off-line multispectral images of lumber in the ultraviolet (UV) and visible (VIS) wavelengths.

The primary objectives of this work are to extend MIA techniques for on-line monitoring of specific defects in RGB color images of lumber boards, and to explore the potential of the NIR wavelength spectrum for lumber feature extraction. The proposed on-line monitoring approach consists of developing a robust MIA model, which incorporates inherent lumber variations. The model is used on-line to detect and isolate defective pixels from a set of lumber boards passing under a RGB digital camera.

The main contribution of this work is a novel application of MIA to developing an on-line industrial lumber-grading scheme. The work provides a successful feasibility study for on-line monitoring of several common lumber defects. Another contribution of this work is an exploratory study of the NIR spectrum for extracting subtle lumber features. The study contributes by highlighting the advantages and shortcomings of using NIR imaging spectroscopy versus RGB cameras for automatic lumber grading. This is the first time that the 900nm – 1700 nm NIR wavelength range has been investigated for lumber imaging.

1.2 Multivariate Image Analysis and Regression Modeling of Pulp and Paper Characteristics

The forest products industry produces pulp and paper in varying grades to be used as raw materials in the manufacture of many specialty end products like rayon, pharmaceuticals, photographic film etc. Customers demand adherence to strict specifications on each grade. To gain customer satisfaction the forest products industry routinely performs extensive quality control tests to monitor product quality. Some of these tests require complicated wet chemistry laboratory procedures, which are quite time-consuming and taxing on the testers. Furthermore, most of these tests are naturally destructive, thus requiring multiple samples for a complete quality analysis. There is a need to develop rapid testing procedures, which would ideally be able to provide multiple product quality tests from a single sample in a non-destructive manner.

Recently the forest products industry has discovered the potential of Near-Infrared (NIR) spectroscopy as a means to achieve these goals. During the last decade several applications of characterizing pulp and paper using NIR spectroscopy have emerged in the literature. These studies use single point NIR probes to gather spectral readings of the sample, which are then analyzed using multivariate statistical methods like Principal Component Analysis (PCA) and Partial Least Squares (PLS) regression. A shortcoming of using NIR probes on solid pulp and paper samples is their inability to provide multiple-point readings across the samples to determine spatial variation in their chemical characteristics. This issue has been addressed with the recent advent of NIR imaging spectroscopes, which acquire simultaneous readings across a solid sample as a multi-spectral digital image.

This work introduces a novel MIR technique, which extracts relevant feature information from multi-spectral NIR images of finished pulp and paper samples. The extracted NIR feature space is then used in one of the following two manners. It is either decomposed using PCA to characterize paper samples based on their chemical ingredients, or it is used to develop empirical models of pulp properties through PLS regression modeling between NIR image feature vectors of a pulp sample and its laboratory analyzed quality data. The methodology is illustrated on a set of industrial pulp samples, which were imaged at the pulp mill immediately after production, and prior to laboratory quality testing in an 'at-line' fashion.

The contribution of this work is mainly in providing a framework for a novel MIR modeling technique, which can be used to relate feature information from process images (obtained by on-line imaging sensors) with corresponding quality information from regular (non-image) data obtained from other sources. This work also introduces NIR imaging spectroscopy for the first time in the pulp- and paper-manufacturing sector of the forest products industry. Some work from this chapter has been presented at the Control Systems 2002 conference [Bharati et. al., 2002].

1.3 Texture Based Classification of Steel Surface Images

In the steel manufacturing industry product quality is often monitored by performing random checks on steel rolls, through various tests on cutout sections, prior to shipping. An indicator of overall steel quality is its surface roughness properties. As the quality of the rolled steel declines its surface becomes rougher. An automatic steel texture analysis scheme is desirable, which could be used to classify the product based on surface roughness.

Extracting texture/roughness information from grayscale, color, or multi-spectral images for off-line quality control or on-line feedback control is a difficult problem. Various statistical, structural, and spectral texture analysis approaches have been proposed in the literature over the past three decades. This work introduces a novel MIA based image texture analysis technique, which extracts image texture features into the latent variables of PCA. The new feature space is used to classify steel sample images based on surface texture information. The classification achieved by the proposed texture analysis scheme is compared with that achieved through other classical multivariate statistical methods and conventional texture analysis methods.

The contribution of this work is threefold. First, it presents a novel multivariate statistical image texture analysis technique that is flexible enough to be used on grayscale, color, or multi-spectral digital images. Second, it presents an overview and comparison of several conventional and multivariate statistical methods, along with their relative effectiveness for steel classification using surface roughness indicators. Third, in the course of this work, insight has been provided into the fundamental issue of the role spatial information plays when extracting image texture information using other multivariate statistical classification methods like PLS-Discriminant Analysis (PLS-DA). This point proves to be the main shortcoming of such multivariate statistical methods compared to conventional texture analysis techniques that work in the spatial domain of the image.

1.4 Thesis Outline

Including the current introduction, this thesis consists of 6 chapters. Some background of common imaging sensors and literature reviews of both traditional and multivariate statistics based image analysis techniques have been covered in chapter 2.

Chapters 3-5, which cover the three main industrial application studies, form the core of the thesis. Applications of the developed image analysis methods in the forest products industry are covered in chapter 3 (softwood lumber grading) and chapter 4 (pulp and paper modeling). Chapter 5 presents applications of various image texture analysis methods to classify steel surface images. Finally, chapter 6 summarizes the results obtained in the thesis, draws some conclusions and highlights some areas for future work.

Chapter 2

Imaging Sensors and Analysis of Image Data

This chapter provides background information and technical details on two digital imaging sensors (RGB color camera and NIR multi-spectral camera) that are used in the forest products industrial applications described in the thesis. A brief introduction to Multivariate Image Analysis (MIA) and Multivariate Image Regression (MIR) techniques is also provided in this chapter. These techniques form the backbone of the methods developed in the subsequent chapters of the thesis.

2.1 Industrial Vision Based Sensors

There are many types and variations of vision sensors used in a vast array of applications ranging from microscopy to outer space exploration. Most of such applications come in varying degrees of complexity and sophistication, ranging from a simple monitoring of the presence (or absence) of a product on a moving web, to something as complex as diagnosing whether a brain tumor is cancerous or benign. As far as the manufacturing industry is concerned imaging sensors form the heart of many vision based monitoring systems.

Perhaps the most commonly used industrial vision sensor is the monochrome (grayscale) camera, which acquires visible light intensities from black to white in various shades of gray. Monochrome cameras are useful in such industrial applications not requiring color information to perform the required tasks. Examples include acquiring shape information of finished parts on a production line, verifying correct position of labels on containers and reading their barcodes etc. If color information is critical for proper monitoring one can use a color-imaging sensor like a Red Green Blue (RGB) 3-channel camera. One such digital RGB camera has been used to monitor defects for automatic lumber grading in the following chapter of this thesis. Further details of the camera have been provided in section 2.1.1. Both monochrome and RGB cameras have been vastly researched and developed over the past three decades. They are commercially available in various configurations, sizes, and resolutions to meet the demands of most industrial applications.

The above-mentioned monochrome and color cameras acquire images based on light intensities in the human visible wavelength spectrum of 400 nm to 700 nm. Over the past decade several imaging sensors have also been developed that are sensitive to light beyond the visible spectral wavelength range. These 'spectral' cameras can acquire images in light wavelengths on either side of the human visible spectrum. Ultraviolet (UV) cameras are sensitive to light in the wavelength range of 100 nm to 400 nm. Such cameras have been used in various space exploration and environmental applications. On the other side of the visible spectrum several Near-Infrared (NIR) and thermal Infrared (IR) imaging cameras have also been realized, which are sensitive to light in the 900 nm - 2500 nm and 2500 nm - 14000 nm wavelength ranges, respectively. Thermal IR cameras find use in several heat sensing applications like night vision, "hot spot" detection in electrical equipment etc. NIR cameras have been used in many industrial applications including semiconductor wafer inspection, forensics, on-line inspection and sorting of food products for contaminants etc. Chapter 4 of this thesis employs the use of a modified NIR camera in the pulp and paper manufacturing industry. Further details of the NIR camera have been provided in section 2.1.2.

A new dimension has recently been added to vision based sensors with the incorporation of light scattering spectrographs attached to cameras. These instruments are called imaging spectroscopes, which simultaneously acquire an image of a scene at multiple wavelengths. Imaging spectroscopes have been developed for both the visible and NIR spectra. Section 2.1.2.3 discusses further details of the NIR imaging spectroscope used in this thesis.

One can generally categorize most industrial vision sensors into two groups based on their ability to resolve light intensity. First, those cameras where each pixel produces one averaged light intensity reading over a certain band of wavelengths (e.g. monochrome, UV, NIR, IR cameras). Second, those cameras where each pixel records multiple light intensities at different wavelength bands (e.g. RGB cameras, and imaging spectroscopes).

Besides the cameras described above there are several imaging sensors that have also been specially developed for the fields of medical diagnosis and microscopy. Typical medical imaging sensors include Ultrasound, Magnetic Resonance Imagers (MRI), Computed Tomography (CT) scanners, X-Ray imagers, etc. Further details on such imaging sensors can be acquired from various sources [Mackay, 1984; Grainger et. al., 2001].

The following sections give a detailed description of the two types of imaging sensors used to acquire the digital images in chapters 3 and 4 of this thesis.

2.1.1 True Color RGB Cameras

A digital camera is a device that converts an optical image of an object into its electronic rendition using arrays of photon-sensitive charge-coupled devices (CCD). Humans prefer to see images of objects in color rather than grayscale because they use a combination of spectral content (color) and reflected light intensity from the object to form and interpret its image. The color vision of the human eye is explained by the tri-stimulus theory, which proclaims that any color can be simulated by mixing three basic colors in different proportions. The most commonly used combination of three basic colors is red, green, and blue (RGB). Typical electronic devices like the television, computer monitors, and digital RGB cameras approximate color by combining three intensity gray-value images (channels) that are given the respective values of red, green, and blue [Geladi et. al., 1996].

The CCD sensor is the heart of all digital cameras. It captures light photons and converts them into electrical charges proportional to the amount of illumination received. RGB digital cameras contain silicon CCD sensors which are sensitive to light photons in the human visible wavelength spectrum. RGB cameras use two basic methods to capture color using CCD arrays. One method uses a single CCD array upon which a grid of color filters is placed in a mosaic pattern so that only one of red, green or blue light reaches any given pixel. The most common color filter pattern used in single CCD array RGB cameras is the Bayer pattern [Bayer, 1976]. Using a combination of pixel quadrants to produce color at each pixel the resulting image is formed. The second method of capturing color in RGB cameras is through use of three separate CCD arrays, one for each of red, green, and blue light. An optical prism assembly is used to separate an image into 3 color components (RGB), with each spectral component image being captured with a different CCD array. Such RGB cameras are commonly called 3-CCD cameras. Image resolution is tripled in a 3-CCD camera due to three times as many pixels as compared with a single CCD array RGB camera.

RGB digital camera technology has evolved very rapidly in the past decade to produce both high-resolution and high-speed cameras at reasonable prices. CCD arrays with resolutions of over 3 million pixels are common in many RGB digital cameras available in the market today. These cameras either use mechanical or electronic shutters that operate as fast as 10 μs, which is fast enough to provide blur-free images of many high-speed events.

There are mainly two types of CCD array configurations commonly used in digital cameras. The first type is a CCD area array camera, which uses a rectangular grid of pixels to capture a 2-dimensional image of an object. Such cameras are well suited for imaging applications where the objects are smaller than the field of view of the camera. With the quick acquisition speeds attained by today's RGB cameras one can adequately capture color images of moving objects using an area array CCD sensor. The second type of CCD array configuration is the line scan camera, which uses a CCD array lined-up as a single row of pixels. Line scan cameras capture 1-dimensional images per scan. If one is interested in imaging a long continuous moving object such as sheets of pulp, lumber boards, textile etc. line scan cameras can rapidly capture multiple line images aligned perpendicular to the direction of motion to produce a 2-dimensional image.

The lumber board color image data analyzed in chapter 3 of this thesis has been acquired at Centre de Recherche Industrielle du Quebec (CRIQ), Quebec using an industrial high-speed line scan RGB digital camera. The camera, which is manufactured by TVI Vision Oy (Finland), acquires successive line images of moving lumber at a scan rate of 1525 Hz. It acquires a RGB line image using a 3-CCD linear array architecture behind a prismatic beam splitter to acquire separate red, green, and blue scans. Further technical details and specifications of the camera can be obtained through following the links to the "Pricolor series" industrial line scan RGB cameras on the website of TVI Vision at http://www.tvi.fi (as of April 29, 2002). At CRIQ the camera has been integrated with other signal processing hardware and data processing software to form an on-line lumber board vision system. Figure 2.1 illustrates a superficial description of the vision system used at CRIQ to acquire the lumber images.

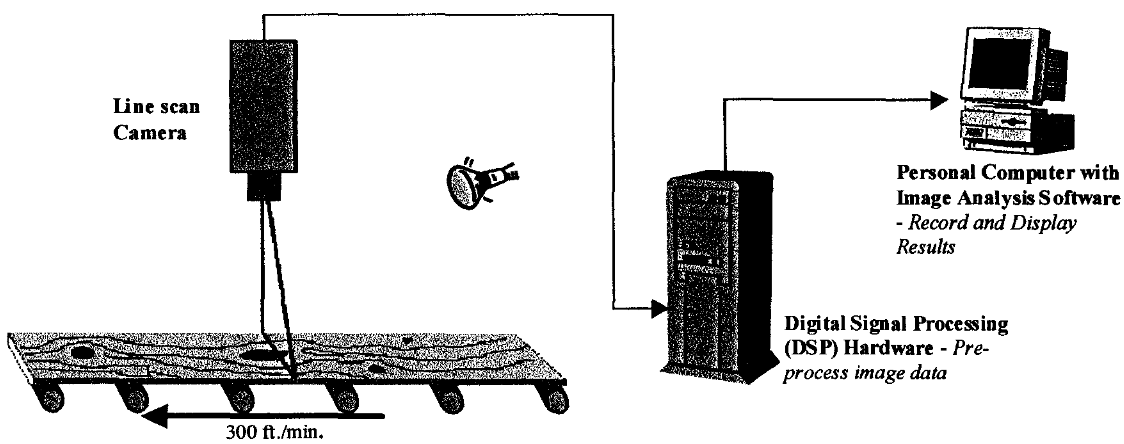

Figure 2.1 Schematic of a lumber vision system used to image moving lumber boards

2.1.2 Near-Infrared (NIR) Cameras

The Near-Infrared (NIR) spectrum has been defined as the region of light having wavelengths between 700 nm and 2500 nm, which is beyond the human visible light spectrum (400 nm to 700 nm). NIR digital cameras are different than the above discussed monochrome and color cameras as they have CCD sensors that respond to light (energy) in the NIR wavelength region. Some features of the NIR spectrum have been briefly discussed in section 2.1.2.1.

Some of the first NIR cameras used exotic sensors that required external cooling in order to remove noise from the images and prevent the CCD element from damaging, as it was very sensitive to temperature fluctuations. Lately, un-cooled room temperature NIR cameras have been realized with the inception of Indium Gallium Arsenide (InGaAs) CCD detectors. InGaAs detectors are highly sensitive to light in the NIR wavelengths from 900 nm to 1700 nm, which is well beyond the range of silicon CCD detectors used in RGB cameras. Besides the visible spectrum, silicon CCD detectors are also sensitive to light in the low NIR wavelength region of 700 nm to 1100 nm. In standard color RGB digital cameras light beyond the visible spectrum is blocked from the CCD detectors as it interferes with the quality of the visible image. Some specialized VIS-NIR cameras have been produced using silicon CCD detectors that are sensitive to both the visible and low NIR wavelength spectra. However, InGaAs CCD detectors are exclusively used in cameras designed to capture light in the wavelength region of the NIR spectrum.

Like RGB cameras one can obtain NIR digital cameras with CCD detectors arranged in configurations like area array or line scan. Furthermore, one can also obtain NIR cameras attached with an array of multiple probes that provide simultaneous local NIR readings at specific points across a sample. As expected, images acquired by NIR cameras are grayscale in nature since pixel intensities usually represent the total amount of NIR reflectance (or absorbance) of light being projected on the imaged object.

Some work presented in chapter 3 and all of chapter 4 of this thesis employs a modified InGaAs CCD area array NIR digital camera to acquire multispectral images of lumber, pulp and paper samples. Further details of this camera and its modification into an imaging spectrograph are provided in sections 2.1.2.2 and 2.1.2.3, respectively.

2.1.2.1 The NIR Spectrum

The NIR spectrum (700 nm to 2500 nm) is characterized by overtones and combinations of molecular vibrations, which occur in the mid-Infrared wavelength region (2500 nm to 50,000 nm) of the electromagnetic spectrum. Vibrations in molecular bonds occur when absorbing radiation, which results in a transition of one vibrational energy level. This is observed through sharp absorbance peaks at selected mid-IR wavelengths for certain organic compounds. According to quantum mechanical selection rules transitions of more than one energy level are not allowed if the vibrations are harmonic. However, molecules exhibit anharmonic vibrations at higher vibrational states [Antti, 1999], which lead to the allowance of energy transitions of more than one energy level. Such transitions are called overtones, which provide the basis for the NIR spectrum. If two or three separate anharmonic vibrations absorb one part each of the incident radiation this type of absorption gives rise to combination bands in the NIR spectrum [Svensson, 1999].

There are a number of bands of overtones and combinations for many functional groups in the NIR spectrum of an organic compound. These bands overlap to give rise to a smooth spectrum with broad peaks, which makes the NIR spectrum of the organic compound more difficult to interpret as compared to its mid-IR spectrum. However, NIR spectroscopy does have many advantages. First, there is hardly any need for sample preparation thus allowing the technique to be applicable to a sample in any physical or chemical state. Second, NIR measurements are gathered very rapidly in a non-invasive manner, thus allowing the sample to be re-used after being measured, or sent on for further analysis [Antti, 1999].

Due to the smooth and overlapping nature of the absorbance peaks in the NIR spectrum, collecting NIR absorption or reflectance readings of multiple samples produces very similar looking spectral signatures. Chemical differences between such samples are described by subtle differences in these signatures. With the advent of digital technology NIR spectral readings are generally digitized into many hundreds of narrow wavelength bands. Since the NIR spectrum is smooth these wavelength bands are highly correlated with each other. Multivariate statistics based chemometric techniques like PCA and PLS have excelled in efficiently extracting subtle differences in NIR spectra of multiple samples, and using this information to empirically model many sample properties. The field of *multivariate calibration* [Martens et. al.; 1989] develops the theory and application of such chemometric techniques in spectral data. There have been many successful industrial applications of chemometrics with NIR spectroscopy, some of which include food products [Hildrum et. al., 1992], forest products [Antti, 1999], plastics [van den Broek et. al., 1996], chemicals [Beebe et. al., 1998]; pharmaceuticals and biomaterials [Stark et. al., 1986].

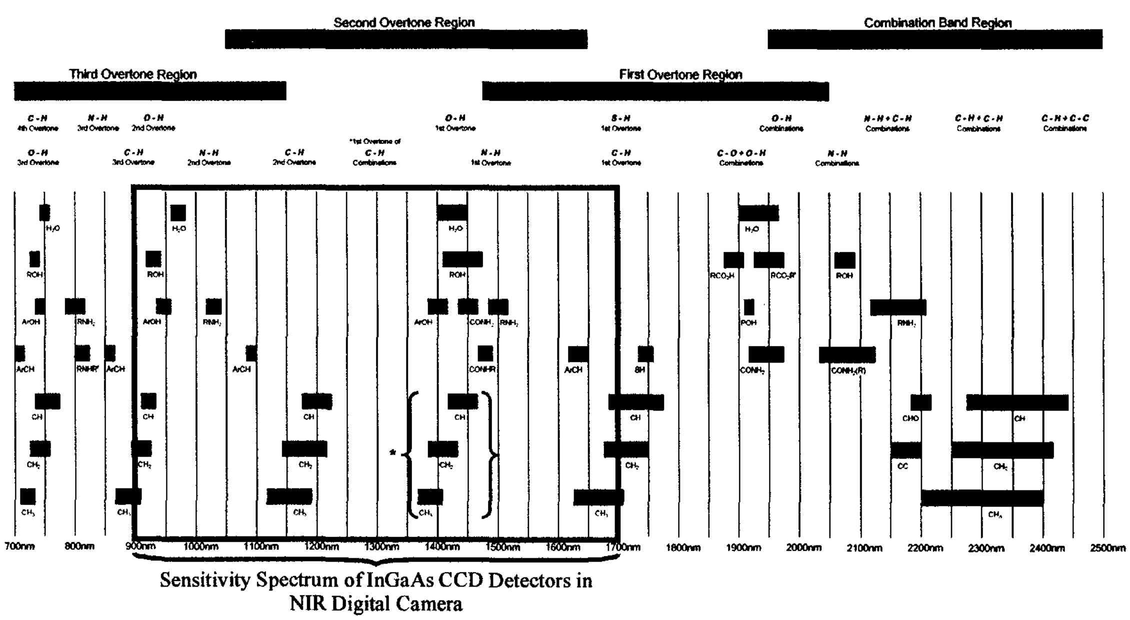

Figure 2.2 Near-Infrared absorptions chart indicating major analytical bands and their peak positions, courtesy FOSS NIRSystems

Important bands in the NIR spectrum arise from overtones and combinations of molecular vibrations of many functional groups in organic compounds. Common functional groups exhibiting NIR absorbance are: O-H, C-H, N-H, and S-H because X-H bonds are the most anhormonic in nature [Svensson, 1999]. Figure 2.2 illustrates a NIR absorptions chart (courtesy FOSS NIRSystems), which indicates the major analytical bands and their relative peak positions in the NIR spectrum. Furthermore, it also illustrates the NIR absorption ranges of the above-mentioned functional groups. Further details and theory of the NIR spectrum can be gained from [Whetsel, 1968; Stark et. al., 1986; McClure, 1994].

As mentioned before the instrument used to acquire NIR reflectance measurements in this thesis is an InGaAs CCD area array camera, which is sensitive in the wavelength range of 900 nm to 1700 nm (highlighted in figure 2.2). This range is primarily dominated by parts of the third overtone region (700 nm to 1150 nm), the full second overtone region (1050 nm to 1650 nm), and parts of the first overtone region (1450 nm to 2000 nm). As seen from figure 2.2 the main functional groups that absorb radiation in the wavelength range of the NIR camera are: C-H, O-H, and N-H. Finally it should be noted here that the O-H functional group exhibits its first overtone band near the 1400 nm to 1500 nm wavelength region, which is captured by the NIR camera. It has been established in the literature that NIR spectroscopy is a very good indicator of water (moisture) due to its sensitivity to the O-H functional group [Whetsel, 1968]. However, moisture fluctuations between samples can also produce unwanted variations in their NIR spectra, which need to be addressed. This issue is further discussed in section 4.4.4.1 of the thesis.

2.1.2.2 Details of NIR Camera Used in Thesis

The NIR digital camera used to acquire images of lumber (chapter 3), pulp and paper (chapter 4) is a room temperature InGaAs CCD area array camera equipped with a CCD temperature stabilizer at 18°C. Most of the general information about the NIR camera has been discussed in section 2.1.2. What follows are some technical details of the camera and its modification into an imaging spectrometer.

In its native form the NIR camera (as purchased from the supplier) captures an average NIR reflectance image, with every pixel element of the InGaAs focal plane array producing a single reflectance intensity averaged over the 900 nm to 1700 nm wavelength range. The focal plane array has 128 × 128 pixels, with each physical pixel being 60 μm × 60 μm. Although the optical sensitivity of the CCD detector is wider, its quantum efficiency is greater than 75% only in the 1000 nm to 1600 nm wavelength range. The camera has a frame rate of 60 Hz and produces non-interlaced progressive scan readouts of the image.

The NIR camera has been purchased from Sensors Unlimited Inc., (USA). The model number is SU128-1.7RTD. For further details regarding this camera please consult http://www.sensorsinc.com (as of April 29, 2002) and follow the links to their 'NIR Imaging Cameras' section.

Upon comparing the scan rates of the RGB line scan camera described in section 2.1.1 with that of the above-mentioned NIR camera (i.e. RGB ⇒ 1525 Hz; NIR ⇒ 60 Hz) it can be inferred that the response times of the silicon CCD detectors present in the RGB camera are much smaller than those of the NIR camera's InGaAs CCD detectors. Due to this bottleneck NIR cameras cannot reach the speeds achieved by some of the high-speed RGB cameras. Currently RGB cameras are much better suited for on-line monitoring of high-speed industrial processes with small time constants (e.g. on-line lumber grading at a process moving at 300 ft./min.). However, NIR camera technology is evolving very rapidly and the response time lag between the CCD detectors in NIR and RGB cameras is getting smaller. The methods developed in this thesis are ideal for both RGB as well as NIR cameras used for on-line monitoring of industrial processes. As a result, the framework has already been provided for on-line process monitoring using NIR imaging sensors once the technology becomes advanced enough to handle the speed requirements of some typical high-speed industrial processes like pulp and paper manufacturing. In the context of this thesis the NIR camera has been used for mainly off-line imaging of moving objects at much slower speeds (up to ~20 ft./min.) as compared to the RGB camera used to image moving lumber boards.

The above-mentioned NIR digital camera has not been used in its original form in this thesis. It has been modified into a multi-spectral imaging spectrometer, which is capable of acquiring NIR reflectance images of a moving object in multiple wavelength bands. The following sub-section discusses the modifications made to the area array camera.

2.1.2.3 Modification of NIR Camera into Imaging Spectrometer

A direct-sight imaging spectroscope [Hyvarinen et. al., 1998] has been attached between the front optics lens and the camera back to modify the NIR digital camera into an imaging spectrometer. The spectroscope consists of an entrance slit, focusing lenses, and a Prism-Grating-Prism (PGP) element encased in a hollow tube. Light enters the spectroscope in a horizontal line through the entrance slit and gets vertically dispersed into its continuous spectral distribution as it goes through the lenses and PGP element. This results in an array of wavelength-specific horizontal lines of light that are captured by the CCD area array detectors in the camera back as a 2-dimensional intensity image. The horizontal axis (i.e. columns) of the captured image represents the spatial dimension, whereas the spectral dimension is represented by the vertical axis (i.e. rows). Figure 2.3 illustrates the basic operating principle of the direct-sight imaging spectroscope [Herrala et. al., 1996].

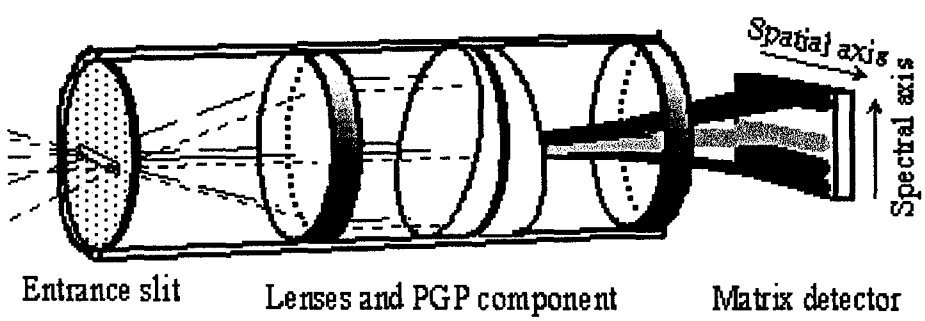

Figure 2.3 Schematic of direct-sight imaging spectroscope used to convert an area array camera into an imaging spectrometer, courtesy Spectral Imaging Ltd.

The imaging spectroscope used in this thesis has been purchased from Spectral Imaging Ltd. Its model number is 'ImSpector N17'. The spectroscope has been specifically designed to vertically disperse a horizontal line of light into its NIR spectrum spanning the 900 nm to 1700 nm wavelength range. The spectrally dispersed lines are imaged using the InGaAs CCD area array of the NIR camera described in section 2.1.2.2. Further technical details and specifications of the imaging spectroscope can be obtained from http://www.specim.fi (as of April 29, 2002).

As mentioned before the pixel resolution of the CCD array in the NIR camera is 128×128 pixels. Thus, the spectrally dispersed image captured by the InGaAs CCD array has dimensions of 128 rows and 128 columns. As a result, the continuous NIR reflectance spectrum (900 nm to 1700 nm) of 128 spatial pixels is vertically digitized into 128 discrete wavelength bands increasing from bottom to top. Each band of the digitized spectrum (represented by a row of the 2-dimensional image) has a spectral resolution of approximately 6.25nm.

With its design the imaging spectroscope converts the NIR camera with a CCD area array into a line scan NIR spectral imaging system. For each imaged line of a moving object the system records a spatial-spectral (i.e. x vs. λ) intensity image. Figure 2.4 illustrates a spatial-spectral intensity image of a line scanned from a moving pulp sample recorded by the NIR imaging spectroscope. For visual enhancement the intensity image has been color-coded using the coloring scheme described in the color bar towards the right of the image.

Line scan cameras inherently capture 1-dimensional images of objects in the spatial domain. As shown in section 2.1.1 the second spatial dimension is captured upon recording multiple lines across a moving object at constant velocity in a perpendicular direction to the scan. Similarly the line scan NIR imaging spectrometer captures the 2nd spatial dimension (y) of an object upon moving it in front of the imaging system. Upon capturing multiple line scans the corresponding x-λ images recorded by the imaging spectrometer per line scan are joined into a 3-dimensional multi-spectral image dataset; the 3rd dimension of which represents the other spatial dimension (y). Figure 2.5

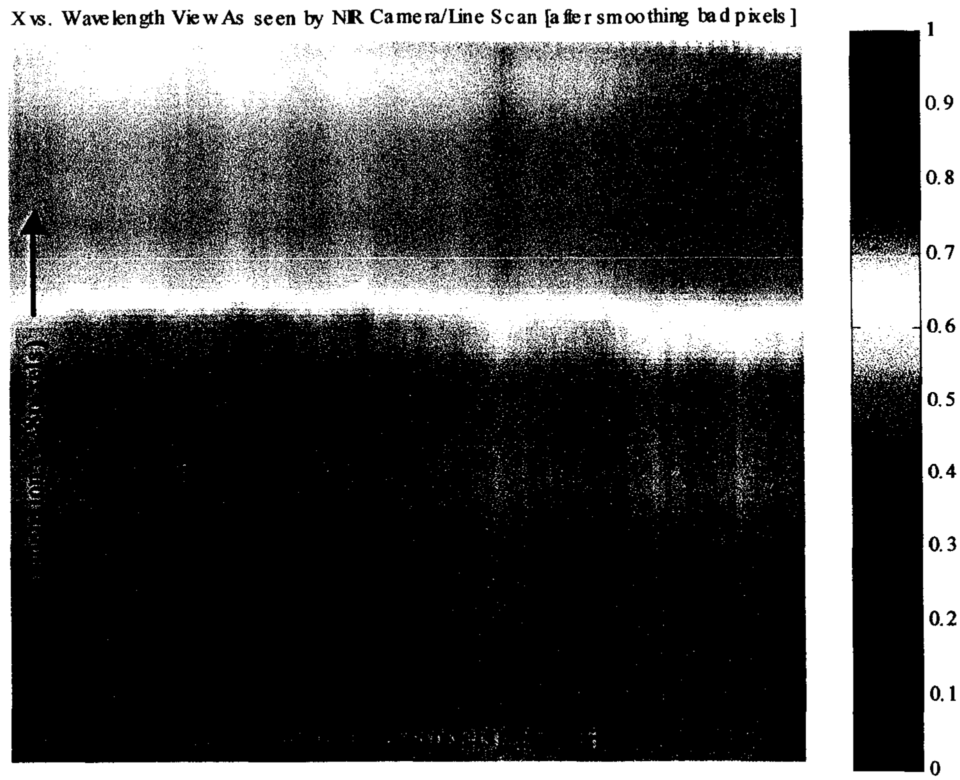

Figure 2.4 Digitized NIR reflectance spectra of a line scan of pulp recorded by the imaging spectrometer as a 128 pixels × 128 pixels spatial-spectral intensity image

illustrates the working principle of the imaging spectrometer to capture the *x*-*y* spatial dimensions of a sample on a moving web.

The resulting 3-dimensional dataset is a multi-spectral NIR reflectance image with 2 spatial dimensions and 1 spectral dimension ($x \times y \times \lambda$). Due to the size of the CCD area array in the NIR camera the maximum pixel resolution in the x and λ dimensions is 128 pixels each. However, the number of lines scanned across the moving object can control the pixel resolution of the y dimension. Furthermore, the physical length of the scanned section of an object can be controlled through the number of lines scanned, whereas the distance between the object and the imaging spectrometer can control the width of the scanned section.

All images captured by the line scan spectral imaging system in this thesis have been acquired using a scanner assembly to move the object. The speed of the scanner bed is controlled in 20 increments through a desktop computer. The imaging

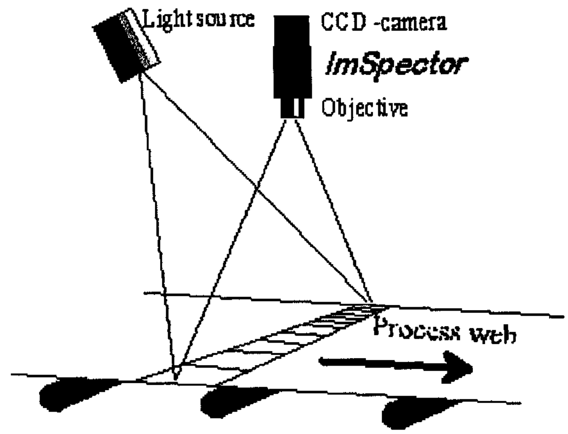

Figure 2.5 Capturing spatial dimensions of a moving sample on a process web using the line scan spectral imaging system, courtesy Spectral Imaging Ltd.

spectrometer is also connected to the computer through a frame grabber board. A halogen lighting source attached with fiber-optic cables arranged in a horizontal line has been used to illuminate the object at a 45° angle with respect to the scanner bed. Typically image acquisition requires a well-illuminated object with even lighting from at least two sources at opposite 45° angles to remove any shadows cast by the object. However, in this thesis the objects being imaged are flat in nature (lumber, pulp and paper), thus only a single source of lighting was deemed adequate. Figure 2.6 illustrates the imaging spectroscope and scanner assembly used to acquire the multi-spectral NIR reflectance images in this thesis.

The manufacturing industry produces many products on a moving line or a web. On-line monitoring of such industrial processes is performed in real-time. The above-mentioned imaging spectroscope is an ideal candidate for simultaneous on-line visual monitoring in the spatial and spectral dimensions in such industrial processes producing spatially distributed solid and heterogeneous products. This is due to the nature in which the imaging spectrometer acquires the multi-spectral image. Imaging spectrometers that build multi-spectral images of an object by capturing individual 2-dimensional spatial images one wavelength at a time, and changing wavelengths through a moving grating system are not ideal for on-line process monitoring. This is because they require a stationary object as the grating scans through the wavelength spectrum to acquire the 3rd (λ) dimension of the multi-spectral image.

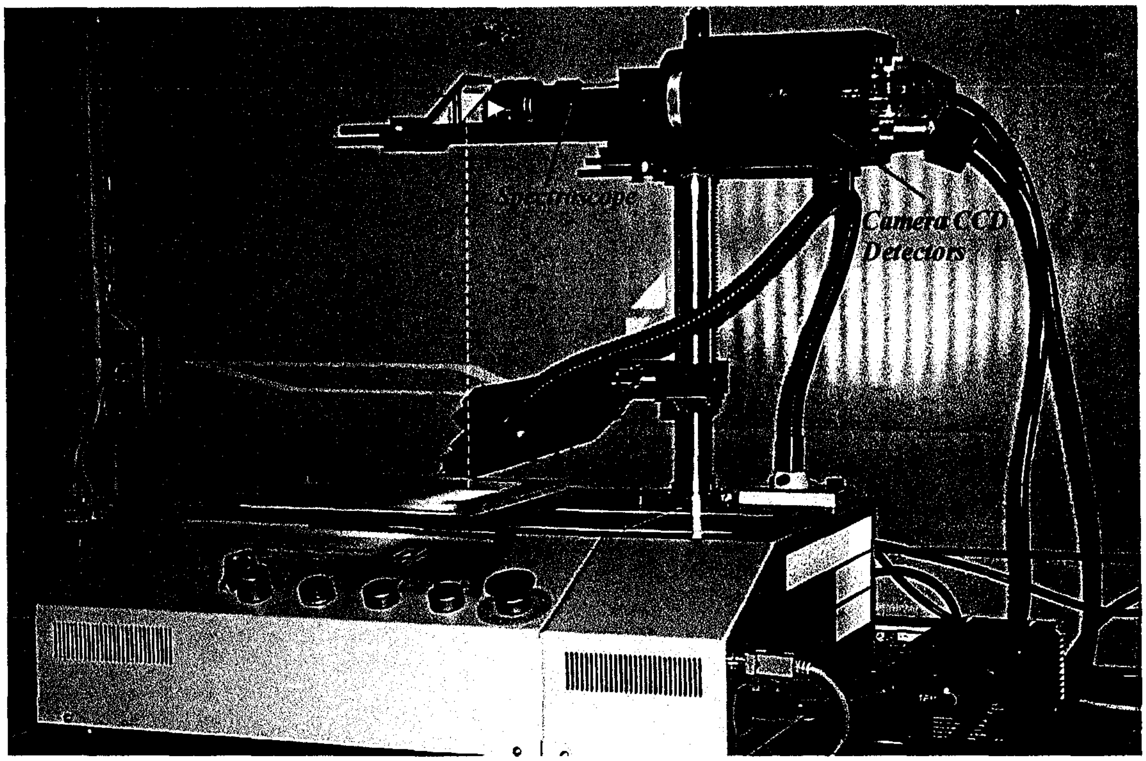

Figure 2.6 Imaging spectroscope and scanner assembly being used to acquire a multi-spectral NIR reflectance image of a pulp sample

Finally, before ending the discussion on visual sensors used to acquire the color and multi-spectral NIR images in this thesis it is worth mentioning that any image analysis technique is only as good as the quality of the acquired image. If the signal-to-noise ratio is too low, or the image quality has been compromised in any way, its analysis will produce sub-optimal results. Camera anomalies like bad pixels in a CCD array produce abnormal pixel responses to light in certain regions of the captured image. In a line scan camera an anomaly would produce a pixel-to-pixel intensity variation across the scanned image, which results in streaks in the final image along the direction of motion of the object. Such pixel anomalies were evident in the NIR camera (# bad pixels were less than 2% of total pixels on CCD array), which resulted in vertical streaks in the *x-y* dimension of the 3-dimensional multi-spectral NIR reflectance image. Section 4.7 illustrates this through an example of trying to capture spatial homogeneity in a pulp property via 2-dimensional sub-windowing of the *x-y* plane of a pulp NIR multi-spectral image. Lighting variations across the line of light also cause contrast variations across the imaged line, which result in contrast difference (e.g. shadowy trends) across the *x-y* plane of the resulting image. These shadowy trends are also evident to a lesser degree in the multi-spectral NIR images acquired by the imaging spectrometer and scanner assembly described above. Section 4.3.1 illustrates the shadows in the *x-y* plane of the multi-spectral NIR image of a paper sample, which are caused by mild light intensity variations across the halogen line lighting used to illuminate the samples on the scanner bed under the imaging spectrometer.

Figure 2.6 illustrates the NIR imaging spectrometer and scanner assembly with a Fostec "Lightline" http://www.us.schott.com/fostec (as of May 4, 2002) attached to a 150W halogen light source via fiber-optic cables to illuminate a line across the sample being imaged. The "Lightline" is mounted on an aluminum holder, which allows manual light angle adjustment to provide adequate illumination across the sample in order for the NIR multi-spectral camera to record a high contrast image.

As far as light calibration of the NIR imaging spectrometer is concerned, there is an inherent correction for light aging when the spectrometer is calibrated at the start of an imaging run. Spectrometer calibration is performed with a two-step process. First, a *dark image* is recorded with the lens cap in place to block light from entering the spectrometer. Second, a *white image* is recorded, which is captured by imaging a white reference object [DV srl, 2000]. The sample NIR reflectance R captured by the multi-spectral camera is separated from the system response by taking, pixel by pixel, the ratio of each sample image to the white image using the following equation [Hyvarinen et. al., 1998]:

$$R_{(i,j)} = \frac{\text{sample}_{(i,j)} - \text{dark}_{(i,j)}}{\text{white}_{(i,j)} - \text{dark}_{(i,j)}} \tag{2.1}$$

where, "sample$_{(i,j)}$" is the *sample image* recorded by the imaging spectrometer, "dark$_{(i,j)}$" is the *dark image* acquired by the NIR camera, and "white$_{(i,j)}$" is the image of a *white reference target* recorded by the imaging spectrometer. For absolute reflectance an OP.DI.MA 15/10 white diffuse plastic from Gigahertz-Optik (Germany) http://www.gigahertz-optik.de/pdf/m_op_di_ma.PDF (as of May 5, 2002) with a known NIR spectral reflectance was used as the white reference target. Equation 2.1 inherently compensates for both lighting spatial non-uniformity across the scene line, and light source color temperature drift with aging.

Besides equation 2.1 several signal correction methods have been proposed in the literature to compensate for scattering effects of lighting in spectroscopy. These methods are algorithm based, using post-correction of multi-spectral data to filter out the effects of such unwanted variations. Multiplicative Signal Correction (MSC) is one such popular technique for correcting light scattering variations [Martens et. al., 1989; Hagman, 1996; Eriksson et. al., 1999].

2.2 Traditional Image Analysis Techniques

Prior to discussing the use of multivariate statistics in the area of digital image analysis it is appropriate to re-visit some of the traditional digital image analysis literature. In general terms traditional image analysis refers to the extraction of numerical or graphical information of objects from digital images. By definition traditional image analysis techniques form one of several classes of the overall *Image Processing* field.

Image processing consists of several fundamental classes of operations that act to improve, correct, analyze, or in some way alter an image [Baxes, 1994]. Depending upon the final objectives one or more operations may be employed to extract information from an image. Typically, most image processing operations can be classified into two fundamental classes: (1) Image Enhancement and Restoration; and (2) Image Analysis.

Image enhancement and restoration operations are generally used to improve the quality or reduce the presence of noise in an image. These operations may be used as a pre-process to improve the image for subsequent image analysis operations. The main objective of image enhancement is to process the image to make it more visually appealing to the observer, whereas image restoration aims to correct the image from known degradations into its mathematically correct form. Common image processing operations used to enhance the visual quality of the image are contrast adjustment (e.g. input/output cropping and gamma correction), and various image histogram manipulation techniques (e.g. histogram equalization). Filtering in the spatial and/or frequency domains of an image tries to both enhance and restore image information. Spatial filters (e.g. smoothing, low-pass, high-pass, 1st and 2nd derivative edge detection filters) accentuate or remove spatial frequency of intensity variations in a pixel neighborhood of an image through various convolution operations [Bharati, 1997]. Frequency domain filters apply a frequency mask to remove specific (or a band of) spatial pixel intensity frequency components from an image. However, this mask is applied on the frequency-transformed image obtained via application of a transform (e.g. 2-dimensional Fast Fourier Transform) to convert an image from the spatial domain into a frequency magnitude image describing the combination of fundamental spatial frequency components. Image filtering techniques are well suited to restore images through removing both spatial and frequency limited noise.

Image analysis operations are used to produce an automated description of an image by quantifying its elements (features) through various mathematical descriptors of shape, size, color, texture etc. These techniques are largely used in machine vision applications that require quantitative measurement and classification of a few features in the image. The initial step in almost all image analysis processes is segmentation of the various parts (i.e. objects, regions, or features) of the image to separate them from background pixels. This process is generally performed by thresholding the pixel brightness values and/or using morphological operations to re-segment the objects into sub-groups [Ekstrom, 1984]. When segmentation is complete image analysis operations measure the segmented objects through various geometric, color, or texture descriptors. Geometric descriptors measure shape, size, area and distance of objects to provide a quantitative analysis of the image. Classification can then be performed based on this information.

The common idea behind most image processing operations is to manipulate the spatial pixel intensity variations in an image based on certain pre-defined criteria. These techniques work to alter the brightness of every pixel in the image to make it more visually pleasing, and/or enable the extraction of quantitative measures of feature pixels based on spatial descriptors like size, shape, area, texture etc.

The field of digital image processing has been well researched for the past four decades. As a result, there are many excellent references available in the literatures that fully describe its operations in great detail. The reader can consult the following references to obtain an in depth understanding of traditional image processing operations [Baxes, 1994; Ekstrom, 1984; Gonzalez et. al., 1992; Pratt, 1978; Russ, 1999; Serra, 1982]. As opposed to traditional image analysis techniques this research focuses on the application and development of multivariate statistics based image analysis methods to extract feature information.

2.3 Multivariate Statistical Image Analysis Techniques

It has been shown that image analysis techniques comprise of extracting feature information from images that is contained in a few interesting pixels, and trying to separate these feature pixels from other (background) pixels. The objective of traditional image analysis techniques is to try and extract this information working in the spatial coordinates of the image.

Multivariate statistical image analysis techniques on the other hand also try to extract feature information from images. However, the principles used here are quite different. These techniques are ideally suited for extracting variable relevant information from *multivariate images*. A "multivariate image" is here defined as any digital image consisting of multiple spatially consistent (congruent) channels, where each channel could represent a unique color, wavelength, time, or a different imaging technique [Geladi et. al., 1996]. Their analysis is accomplished by extracting (and grouping) pixels belonging to features of interest and separating them from background pixels using the differences between their signatures in the *variable* dimension (e.g. capturing differences in NIR reflectance spectra of feature pixels from those of background pixels in a multi-spectral NIR reflectance image).

This section intends to provide an overview of Multivariate Image Analysis (MIA) and Multivariate Image Regression (MIR) techniques, which use multivariate statistical methods like multi-way PCA and PLS to both extract and empirically model features of interest from multivariate image data. The chapter then concludes with a discussion of some fundamental differences between the objectives of multivariate statistical image analysis techniques and traditional image processing methods.

2.3.1 Methodology and Review of Multivariate Image Analysis

Multivariate Image Analysis (MIA) techniques, first introduced by Esbensen et. al. [1989], consist of extracting feature information from multivariate images using the latent variable spaces of multivariate statistical methods like PCA, PLS, and Principal Component Regression (PCR).

As mentioned before a multivariate image consists of a stack of congruent images, where each image in the stack represents a unique variable. A multivariate image can be represented as a 3-dimensional dataset, where 2 dimensions ($x \times y$) represent pixels in the image plane and the 3rd dimension (z) represents the variable index. Figure 2.7 illustrates an example of a 512 × 512 pixel multivariate image with 4 variables, where each variable represents a different wavelength of the electromagnetic spectrum [Bharati et. al., 1998]. The data in this multi-spectral image can be viewed either as a 3-dimensional matrix of pixel intensities, or a 2-dimensional matrix of (4 × 1 pixel) vectors at each spatial location in the (x, y) image plane where the vectors represent the wavelength spectrum of every pixel.

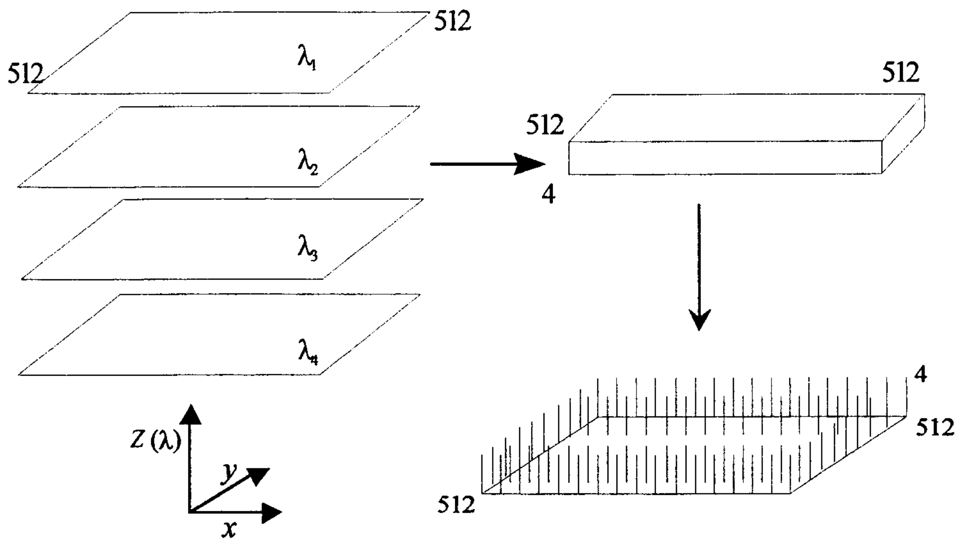

Figure 2.7 Different data representations of a 512 × 512 × 4 pixel multivariate image

The variables of a multivariate image are highly correlated with each other as they represent congruent images capturing the same pictorial information. Furthermore, multivariate images usually contain enormous amounts of data, making their analysis computationally intensive. To efficiently analyze such an enormous and highly correlated dataset MIA techniques use latent variable based multi-way PCA and multi-way PLS methods [Geladi et. al., 1989; Esbensen et. al., 1989; Grahn et. al., 1989]. These methods compress the highly correlated data by projecting it onto a reduced dimensional latent variable subspace through a few linear combinations of the variables in the multivariate data.

Multi-way PCA of a 3-dimensional $(n_x \times n_y \times n_z)$ digital image array $\underline{\mathbf{X}}$ consists of decomposing it into a series of A $(< n_z)$ principal components consisting of $(n_x \times n_y)$ score matrices $\mathbf{T}_a$ and $(n_z \times 1)$ loading vectors $\mathbf{p}_a$ plus a residual array $\underline{\mathbf{E}}$, i.e.:

$$\underline{\mathbf{X}} = \sum_{a=1}^{A} \mathbf{T}_a \otimes \mathbf{p}_a + \underline{\mathbf{E}} \tag{2.2}$$

where ⊗ denotes the Kronecker product. The principal components are ordered in the sense that the first component explains the greatest amount of variance in $\underline{\mathbf{X}}$, the second component explains the next greatest variance, and so forth. The number of components (A) necessary to extract most of the meaningful information can be determined by various procedures [Wold, 1978; Jackson, 1991].

This method of multi-way PCA is equivalent to unfolding the 3-dimensional matrix $\underline{\mathbf{X}}$ into an extended 2-dimensional matrix $\mathbf{X}$, as illustrated in Figure 2.8, and then performing ordinary PCA on it:

$$\underset{n_x \times n_y \times n_z}{\underline{\mathbf{X}}} \xrightarrow{unfold} \underset{(n_x \cdot n_y) \times n_z}{\mathbf{X}} = \sum_{a=1}^{A} \mathbf{t}_a \mathbf{p}_a^T + \mathbf{E} \tag{2.3}$$

where $\mathbf{t}_a$ is a $(n_x \cdot n_y) \times 1$ score vector, and $\mathbf{p}_a$ is a $(n_z \times 1)$ loading vector. The score vectors $\mathbf{t}_a$ (a = 1,..., A) are orthogonal, and the loading vectors $\mathbf{p}_a$ (a = 1, ..., A) are orthonormal. By unfolding the 3-dimensional multivariate image matrix $\underline{\mathbf{X}}$ into a corresponding 2-dimensional matrix $\mathbf{X}$ the multi-way PCA method treats each pixel as a separate object independent of its neighbors. This breaks the spatial dependence of neighboring pixels in the $(n_x \times n_y)$ image plane of the multivariate image. Figure 2.8 illustrates this unfolding procedure of a 512 × 512 × 4 pixel multivariate image $\underline{\mathbf{X}}$. The objects (rows) in the unfolded matrix $\mathbf{X}$ then correspond to the pixel locations in the $n_x \times n_y$ image plane of the multivariate image, whereas its columns represent unfolded variable images into long vectors.

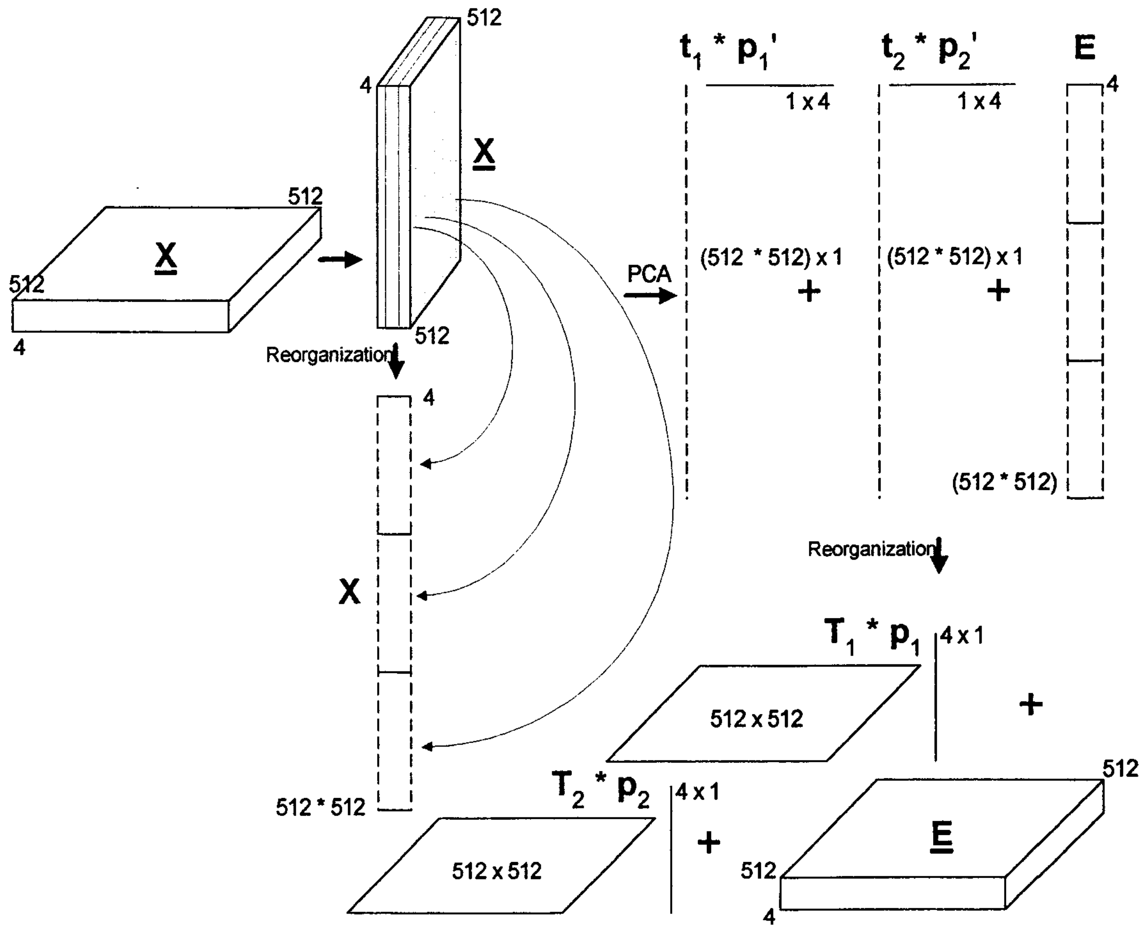

Figure 2.8 Multi-way PCA decomposition of a 512 × 512 × 4 pixel multivariate image into a linear combination of reduced dimensional latent variable subspace

The row dimension of the unfolded matrix **X** is usually very large (equal to 262,144 rows upon unfolding a 512 × 512 pixel image), whereas its column dimension is very small (4 columns representing the 4 variable images). Performing PCA on a matrix with such a high number of rows using the NIPALS algorithm [Geladi et. al., 1986] or Singular Value Decomposition (SVD) [Golub et. al., 1983] would lead to excessive computational times. Therefore, with essentially all multivariate image data having long and thin unfolded matrices, a kernel algorithm [Geladi et. al., 1989] is used. In this algorithm the kernel matrix ($\mathbf{X}^T\mathbf{X}$) is first formed, and then an SVD is performed on this very low dimensional ($n_z \times n_z$) matrix to obtain the loading vectors $\mathbf{p}_a$ (a = 1, …, A). The corresponding score vectors $\mathbf{t}_a$ are then computed via equation 2.4. The only time consuming step in this algorithm is the (one time) construction of the kernel matrix ($\mathbf{X}^T\mathbf{X}$). Further details about multi-way PCA decomposition of the above-mentioned multivariate image can be gathered from Bharati [1997].

In each dimension (a = 1, ..., A) MPCA extracts a principal component variable (score) $\mathbf{t}_a$ which is defined as a linear combination of the variables in **X**. Each element in $\mathbf{t}_a$ corresponds to a weighted average pixel over the 4 variables. The corresponding loading vector $\mathbf{p}_a$ gives the particular linear combination.

$$\mathbf{t}_a = \mathbf{X}\mathbf{p}_a \tag{2.4}$$

If $\underline{\mathbf{X}}$ were a multi-spectral image each principal component score would extract a particular spectral feature (i.e. a unique linear combination of the pixel intensities over the spectrum of n_z wavelengths). The reorganized score matrix $\mathbf{T}_a$ is a representation of the image in terms of that spectral feature.

Upon completion of PCA on **X**, the $(n_x \cdot n_y) \times 1$ score vectors $\mathbf{t}_a$ (a = 1, ..., A) can then be reorganized back into $(n_x \times n_y)$ score matrices $\mathbf{T}_a$ (a = 1, ..., A) giving a representation of the original $\underline{\mathbf{X}}$ array as expressed in equation 2.2 and illustrated in figure 2.8. In this way one can see that the scores themselves represent images in the original $(n_x \times n_y)$ scene space; $\mathbf{T}_1$ being the image with the largest variance, followed by $\mathbf{T}_2$ with the second largest variance, and so forth. MIA allows the user to visually determine if adequate information has been extracted by the reduced dimensional latent variables from the multivariate image. Furthermore, the residuals $\underline{\mathbf{E}}$ can also be reorganized into their 3-dimensional matrix representation and visually analyzed as a multivariate image to determine the remaining structure in each variable image after extracting the latent variables. A reconstructed multivariate image, which eliminates much of the unstructured noise from the original image, can be obtained by using only the dominant A principal components:

$$\hat{\underline{\mathbf{X}}} = \sum_{a=1}^{A} \mathbf{T}_a \otimes \mathbf{p}_a \tag{2.5}$$

where the residual component $\underline{\mathbf{E}}$ has been omitted. However, such Multi-Way PCA (MPCA) methods are not very useful for image enhancement, as they are not specifically designed to sharpen edges or enhance other specific features in the image. Some of the traditional image processing operations discussed in section 2.2 provide more powerful approaches to image enhancement or restoration. The strength of the MPCA based MIA technique is in its ability to extract and isolate feature pixels from background pixels in highly correlated image data.

MIA extracts feature pixels through the inherent duality between its score images $\mathbf{T}_a$ and score plots. Since MPCA scores $\mathbf{t}_a$ are orthogonal to each other it gives well-reasoned meaning to plot them against one another as scatter plots. MIA score plots give a compressed representation of the intensity information at each pixel location in terms of the score values (t_1, t_2, ...) of the dominant principal components. These score values summarize the dominant variable features of the image at each pixel location. If, at different pixel locations in an image the same combination of variable intensities were present, their score value combination (t_1, t_2) would be almost identical. Regardless of the spatial locations of the various occurrences of this feature in the image space, MPCA would represent it by the same combination of score values (t_1, t_2). Therefore, by plotting the score values of the dominant principal components (t_1, t_2) for each object (i.e. each pixel location) in a scatter plot, the score combinations for all pixel locations in the scene space having the same characteristics in their variable intensities would plot on top of one another or at least in the same neighborhood. This results in score point clusters representing features having similar characteristics of variable combinations. Score plots are actually 2-dimensional histograms where each dimension represents a principal component, and the histogram bins represent the frequency of feature pixels having similar combinations of principal component values.

MIA Example: RGB Color Image of Lumber

The above MPCA decomposition of multivariate images and subsequent analysis of the results are best presented by way of an example. The multivariate image used in this example is a RGB (3 channel) color image of the face of a 1″ × 4″ × 24″ piece of lumber. Figure 2.9 illustrates the lumber sample multivariate image of size 746 × 343 × 3 pixels. Besides sound wood with annular rings the image also depicts three types of defects typically found in lumber samples, like knots (sawn tree branches), splits (cracks in wood), and pitch (resinous material) pockets.

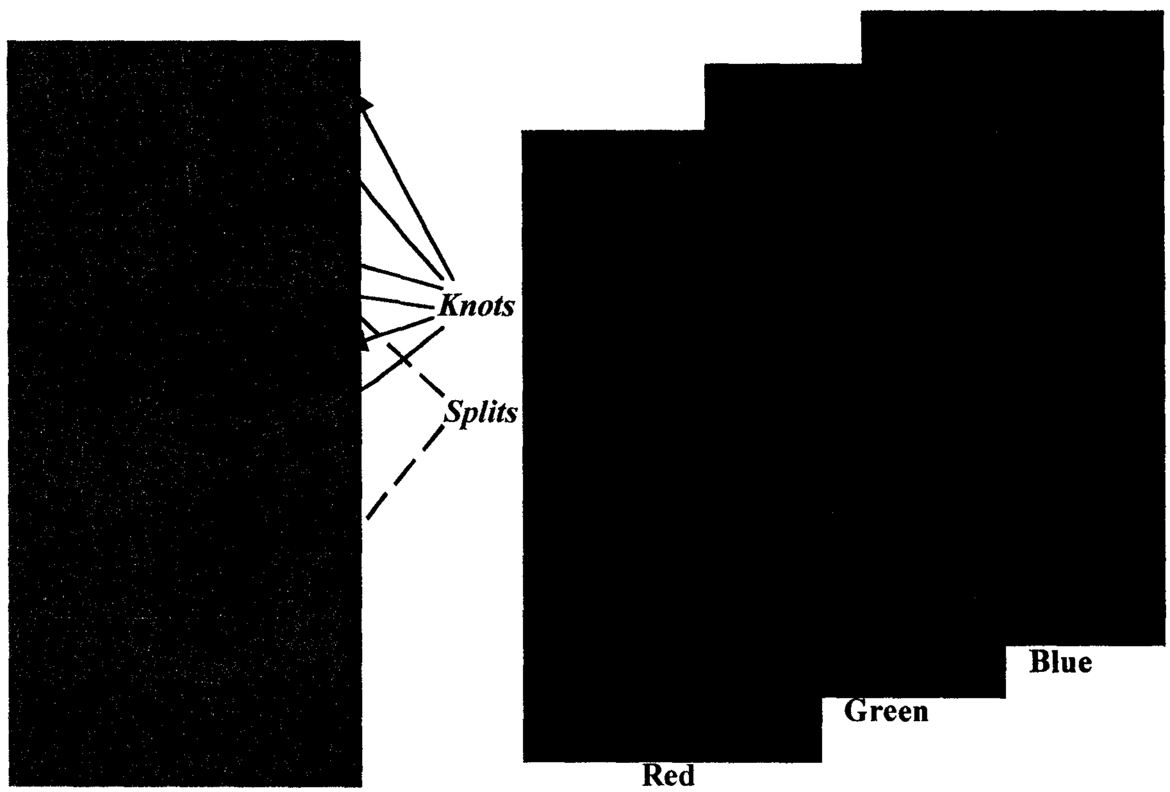

Figure 2.9 A 3 channel multivariate image representation of a 746 × 343 pixel RGB color image of a sawn lumber sample depicting typical lumber defects like knots, splits, and pitch pockets

The data contained in the three variables of the lumber multivariate image is both enormous in size (746 × 343 × 3 = 767,634 pixels) and the observations are highly correlated with each other. Table 2.1 presents a matrix of correlation coefficients between the 3 color channels of the lumber multivariate image.

Table 2.1 Correlation matrix of color channels in the RGB multivariate image of lumber

	Red	*Green*	*Blue*
Red	1	0.963	0.833
Green		1	0.905
Blue			1

MPCA has been used to decompose the 3 channel lumber image into a linear combination of two score and loading vectors, where the third principal component automatically represents the left over information attributed to noise. The feature information extracted by the first two principal components (PC), and that left over in the third PC can be visually determined by observing the re-folded score matrices $\mathbf{T}_1$ to $\mathbf{T}_3$ as individual grayscale images or a false color-composite RGB image as illustrated in figure 2.10. It can be observed from the $\mathbf{T}_1$ grayscale image that the first principal component

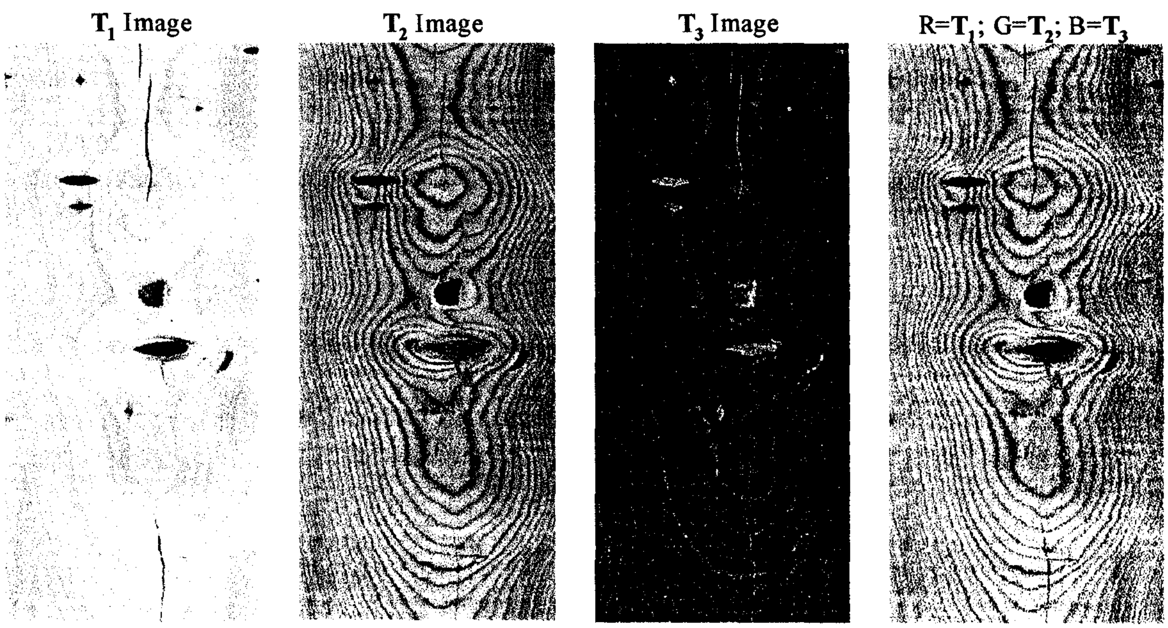

Figure 2.10 Grayscale and false color-composite image representations of MPCA scores $\mathbf{T}_1$ to $\mathbf{T}_3$ upon decomposing the multivariate image of sawn lumber

extracts mainly contrast information between sound wood (bright pixels) and darker lumber defects like knots and splits. The $\mathbf{T}_2$ grayscale image reveals a contrast difference between the pitch pockets (dark pixels) and all other features in the lumber sample.

Although the $\mathbf{T}_3$ grayscale image contains some structure, it can be concluded that the signal-to-noise ratio beyond the first two principal components is small. As a result, only $A = 2$ principal components are used in the subsequent analyses in this example.

The cumulative percent sum of squares in the multivariate image as explained by the first two principal components is 99.995% (99.959% and 0.036%, respectively). The loading vectors for these two dimensions are {Red-Green-Blue}: $\mathbf{p}_1^T = [0.722\ 0.588\ 0.365]$, $\mathbf{p}_2^T = [-0.523\ 0.117\ 0.845]$. From these loading values it can be seen that the first PC represents something similar to an average of the three colors, whereas the second PC mainly represents a contrast between Red and Blue colors.

A scatter plot of the first two score vectors ($\mathbf{t}_1$ vs. $\mathbf{t}_2$) is illustrated as a color-coded 2-dimensional histogram in figure 2.11, where $\mathbf{t}_1$ values increase from left to right and $\mathbf{t}_2$ values increase from top to bottom. Every point in this score plot represents a unique pixel in the ($n_x \times n_y$) image plane of the RGB multivariate image. Color-coding was done because this plot contains 255,878 score combinations, one for each of the 746 × 343 pixel locations in the original image. Similar feature pixels in the original image yield almost identical (t_1, t_2) score combinations, which results in many overlapping points in this scatter plot. The number of overlapping pixels represented by a single point in a

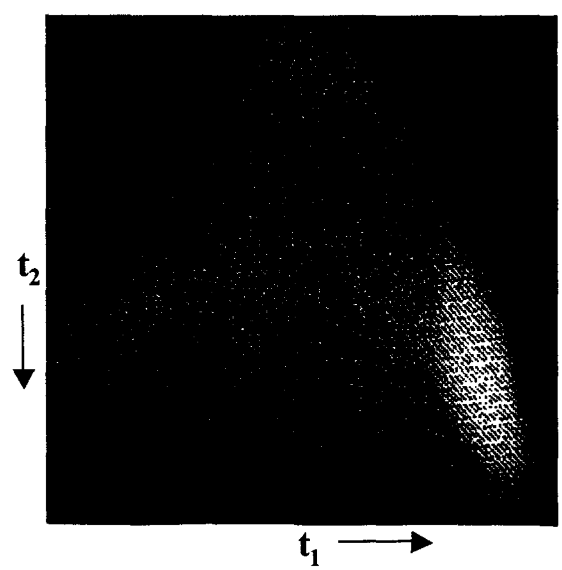

Figure 2.11 Color-coded $\mathbf{t}_1$ vs. $\mathbf{t}_2$ scatter plot of the lumber sample multivariate image

score plot is called the pixel density. Following Bharati [1997] a 2-dimensional histogram of 256×256 bins is constructed, where each bin is assigned a color depending upon the number of pixels falling in that bin. The color-coding scheme uses cold colors (e.g. black) to represent bins with a low number of overlapping pixels and hot colors (e.g. white) to represent bins having the highest pixel density. The color-coding progresses from black to white in various shades of red, orange, and yellow. Further details of the histogram construction and its color-coding scheme can be found in Bharati [1997].

It is relatively easy to detect outlier pixels, which are remote from the main pixel clusters in the score space scatter plot (figure 2.11) of the lumber image. It is also easy to detect the high-density pixel cluster towards the bottom right of the score plot and the various pixel density gradients that exist both within and between this and the other two minor clusters towards the top and bottom left of the score plot. As mentioned earlier, pixels having similar spectral features in the multivariate image will have comparable combinations of score values and result in point clusters in the score plot. This fact can be put to use in segmentation of feature pixels from the multivariate image through delineating pixel classes in the score plots. In effect, one can delineate a tentative data class corresponding to pixels having similar feature vectors in the RGB color space.

Pixel class delineation may be carried out in many ways. One approach is to select an area in the score space and highlight the corresponding pixels belonging to this area in the image space. The selected area in the score space is in fact a local model, which is chosen to delineate a tentative class of pixel data from the rest. The procedure of selecting an area in the score space is called 'masking' in the MIA literature [Bharati et. al., 1998]. Various sizes and shapes of masks can be selected via simple graphical operations on the score plots upon displaying their color-coded 2-dimensional histograms as false-color images on a computer monitor.

This procedure of masking point clusters and outlier pixels in the score space and highlighting the chosen pixels in the image space forms the backbone of the MIA feature extraction strategy. To successfully delineate a class of pixels it becomes imperative to study both the score and image spaces simultaneously. The ability to toggle between the image space and score space is quite fast and easy since both spaces can be displayed as images on a computer monitor.

It is relatively simple to interrogate the score space by masking several clusters and projecting the masked pixels back to the image space. The main point cluster towards the bottom right of the score space scatter plot represents majority of the pixels in the lumber image. As a result, this cluster must belong to a dominating feature in the image. Sound wood pixels cover majority of the area in the lumber sample, thus it can be inferred that the main score cluster belongs to sound wood feature. The purpose of this example is to illustrate the power of MIA in extracting subtle features like typical lumber defects (e.g. knots, splits, pitch pockets). Sound wood pixels are considered as background since they do not contain these features. Upon masking the other two score point clusters towards the top and bottom left of the score plot one can realize the true power of MIA techniques.

Figure 2.12(a) re-plots the $\mathbf{t}_1$ - $\mathbf{t}_2$ score plot of figure 2.11, but with blue and green polygon masks covering the two minor point clusters towards the bottom left and top, respectively. The pixel classes which have been masked in this score plot are highlighted in figure 2.12(b) where each pixel with a $\mathbf{t}_1$ - $\mathbf{t}_2$ score combination lying under the respective masks has been re-plotted as an overlaid blue or green pixel on the false color-composite RGB image of the 3 latent variables $\mathbf{T}_1$ to $\mathbf{T}_3$. From this figure it is evident that the class of pixels highlighted by the blue mask in the score space belongs to knots and splits, whereas the pitch pockets class is highlighted as the green mask. Since all the highlighted pixels have similar spectral combinations in the RGB space, they map into the two regions masked by the polygons in the score space.

By repeated use of the masking/highlighting procedure with different polygon masks a *signature* of every feature existing in the image space (regardless of its subtlety or spatial location) can be isolated in the score space. Due to the ability to switch easily between score and image spaces, MIA can also be employed as a reverse mode image analysis tool. Specific pixels belonging to known features of interest in the image space can be highlighted in the score space to determine the region which represents their

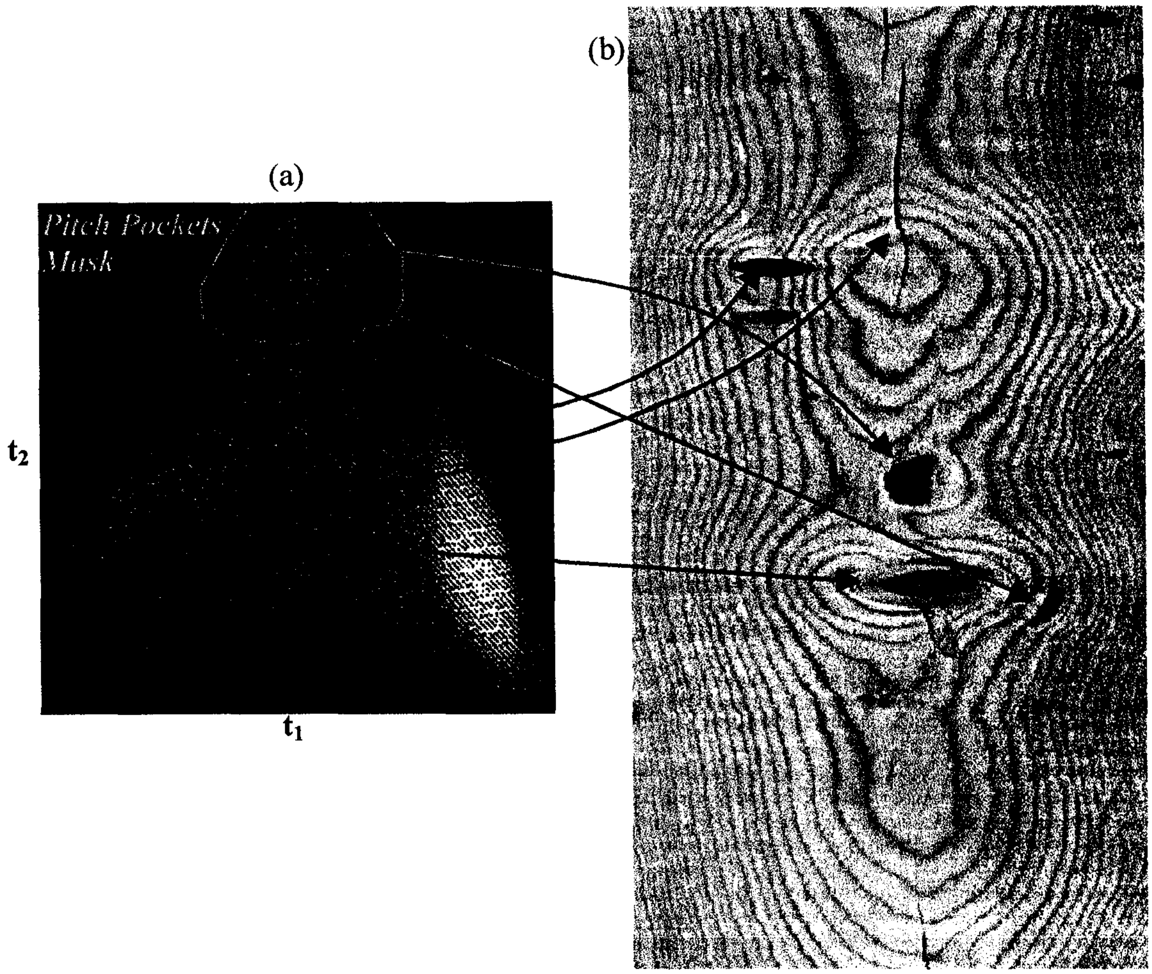

Figure 2.12 (a) $\mathbf{t}_1 - \mathbf{t}_2$ score plot of lumber image with polygon masks of the upper (green) and lower left (blue) point clusters. (b) False color-composite score image with overlay of highlighted pixels from the two classes outlined in (a).

corresponding score combinations. The area surrounding the highlighted score points can then be masked using a reasonably sized polygon. As a result, subtle features that are subjectively difficult to identify in the image space may easily be identified using the reverse mode application of MIA. Geladi et al. [1996] list several other modes of MIA that employ the use of the image space - score space relationship.

One of the first uses of multivariate statistical methods (particularly PCA) in the field of digital image analysis dates back 30 years, mainly in the field of remote sensing using multi-spectral satellite images of the earth surface [Ready et. al., 1973]. Most of the literature during that time was concerned with using PCA in remotely sensed multi-spectral images for noise reduction and data compression [Wheeler et. al., 1976; Kaneko, 1978; Byrne et. al., 1980; Singh et. al., 1985]. These publications lead to the idea that once the principal component score images ($\mathbf{T}_1$, $\mathbf{T}_2$,…) were obtained from the multi-spectral images, they could be further analyzed using traditional image analysis techniques and a priori knowledge to visually enhance features like minerals for classification. The first "ground-breaking" application that made use of the latent variables as raw data to analyze multivariate images (i.e. MIA) came from the chemometrics community [Esbensen et. al., 1989]. This article presented the idea of using not only the reconstructed PC images, but also the raw score vectors (scatter plotted against each other) to assist in analyzing the multivariate image. It was shown that the power of the PCA approach lay in its ability to extract and isolate specific image features in a common region of the score space, and then, once the feature was detected, to reveal the locations where it occurred in the scene space. In their original form the main ideas of MIA were appropriate for off-line analysis of fixed images. Bharati et. al. [1998] extended MIA methods for real-time monitoring of time-varying processes through an example of feature monitoring in a sequence of multi-spectral images of a satellite as it passed over a certain geographical region of the earth's surface. Such moving processes are common in the manufacturing industry, where digital cameras capture a sequence of digital images (or movies) to visually monitor product quality.

2.3.2 Methodology and Review of Multivariate Image Regression

Multivariate regression includes calibrating empirical models between two blocks of (typically multivariate) data. Besides the variables in the **X**-block, which is called the *independent* or *predictor* dataset, in multivariate regression there is also a *dependent* **Y**-block of *response* variable(s). The goal of the calibration is to develop a regression model relating **X** and **Y**, so that in future **Y** can be calculated or predicted from **X**. When such regression model building is applied to multivariate image data, it is called

Multivariate Image Regression (MIR) [Geladi et. al., 1996]. Different regression techniques are used in MIR to first model the relationship between the two sets of image data. This model is then used for predicting future response variables from subsequent predictor images.

The idea of MIR was first formally introduced by Geladi et. al. [1991], who tried to develop a Principal Component Regression (PCR) model [Næs et. al., 1988] between a multivariate satellite image $\underline{\mathbf{X}}$ and a congruent univariate image $\mathbf{Y}$. Besides PCR models the MIR literature has also used other types of multivariate regression modeling techniques to relate $\mathbf{X}$ and $\mathbf{Y}$ image data. It is not the purpose of this thesis to discuss the theory and development of various MIR models used in the literature. This section discusses the common goals and ideas between few of the previously published MIR modeling techniques, and provides a literature review of various MIR applications.

Geladi et. al. [1996] define a regression model relating two images with matching pixel positions using the form:

$$\mathbf{G}_2 = f(\mathbf{G}_1) \tag{2.6}$$

where $\mathbf{G}_1$ is a predictor image, $\mathbf{G}_2$ is the response image and f is an empirical relation between the images. Typically, MIR models between images are developed using some sufficient set of pixels that adequately represent the scene or features that need to be related between $\mathbf{G}_1$ and $\mathbf{G}_2$. As a result, for the model building stage ***both*** the predictor ($\mathbf{G}_1$) and response ($\mathbf{G}_2$) images are required. Although the regression coefficients in the developed MIR model could be interpreted, the main goal of MIR is image prediction. Almost always, a developed regression model needs to be tested by predicting a response image ($\hat{\mathbf{G}}_2$) using a test predictor image ($\mathbf{G}_{1\ \text{test}}$) and comparing the predicted response with the true (known *a priori*) response image ($\mathbf{G}_{2\ \text{true}}$).

Three basic procedures of developing a regression model between predictor and response images of a training set have been typically used in the MIR literature. These are Multiple Linear Regression (MLR) [Geladi et. al., 1996], Principal Component Regression (PCR) [Geladi et. al., 1991], and Partial Least Squares (PLS) Regression [Lindgren et. al., 1994; Hagman, 1996; Lied et. al., 2000]. Further details on the methodology of PLS regression modeling may be gathered from the following sources [Geladi et. al., 1986; Höskuldsson, 1988; Burnham et. al., 1996]. It should be noted here that a kernel-based PLS algorithm [Lindgren et. al., 1993] is exclusively used in MIR based on PLS regression models. This algorithm helps avoid the computational overload that might otherwise arise in handling the enormous data size of typical multivariate images. The final prediction equation to be used to calculate the response image $(\hat{\mathbf{G}}_2)$ is common between the three procedures. However, the theory associated with developing the regression coefficients between $\mathbf{G}_1$ and $\mathbf{G}_2$ images of the training set is quite different. To gain further details on the theoretical derivations of the three image regression models the reader may consult the above references. Figure 2.13 summarizes the common idea behind the model development stage of these three types of MIR models.

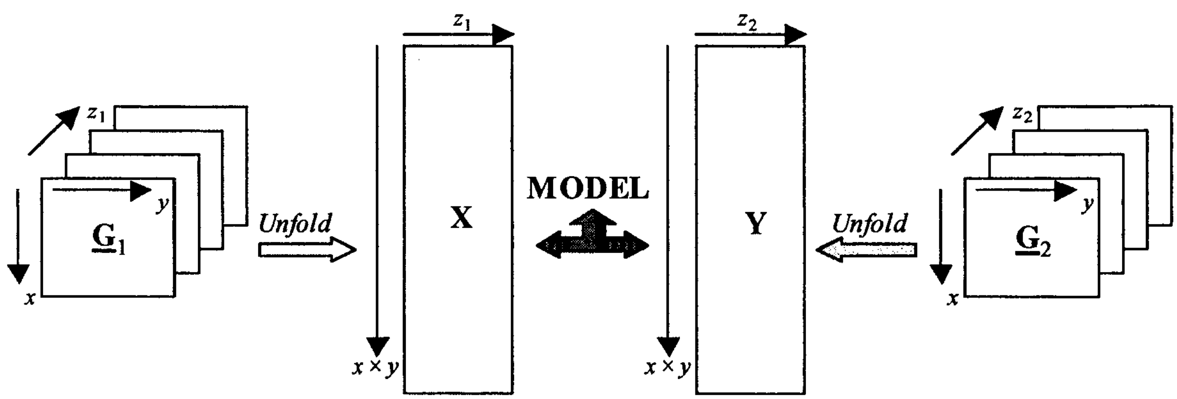

Figure 2.13 Multivariate Image Regression model relating two sets of images

As seen from figure 2.13 the basic requirement for the three MIR modeling procedures is that both the predictor and response datasets have to be (univariate or multivariate) images. Depending upon the specific application one might or might not have perfect congruence between the two sets of images [Geladi et. al., 1996]. However, the common objectives of all three MIR modeling procedures are to create some kind of pixel-to-pixel empirical map between the predictor and response images during the training stage of the models.

Once trained MIR models have been used for predicting multivariate image features in many applications like predicting ground truth data from multi-spectral satellite images in remote sensing [Shibayama et. al., 1991]; isolating wood features in multivariate images of lumber [Hagman, 1996]; modeling and classifying types of pigments in a multi-spectral microscopic image of a painted chinaware [Geladi et. al., 1994]. Grahn et. al. [1995] and Geladi et. al. [1996] give good literature reviews of various other applications of MIR techniques.

Grahn et. al. [1989b] showed one of the first applications of using a MIR model as a feature pixel classifier in multivariate images. They used a special case of MIR modeling to discriminate known tissue types in Magnetic Resonance Images (MRI), where the response variable **Y** was a binary image. Pixels belonging to the tissues of interest were coded as 1 (white), and the remaining image was coded as 0 (black). The trained model was then used on a new test MRI image, which produced predictions as a grayscale image with higher pixel intensities (near 1) for the modeled tissues. Hagman [1996] used a similar classification approach with PLS regression models to discriminate lumber features from multi-spectral images of sawn wood. An MIR application in the food industry [Lied, 2000] tried to discriminate different types of vegetables using PLS models trained with binary response images.

Training a PLS regression model for MIR with a binary image as a 'dummy' response variable provides the model with a priori knowledge of the class belongings of the pixels in the features of interest. This MIR approach is a modified version of the PLS Discriminant Analysis (PLS-DA) method [Sjöström et. al., 1986], which finds a model that separates classes of observations (pixels) on the basis of their **X**-variables. Providing a priori class belongings to PLS-DA rotates the projections of the multivariate image pixels in the latent variable scatter plots such that the focus is on class separation ("discrimination") [Eriksson et. al., 1999]. There are some inherent conditions that must be satisfied when using PLS-DA for feature pixel classification in MIR. Section 3.5 discusses some of these issues in detail with the help of a conceptual feature modeling and classification example in a lumber image.

As mentioned before the MIR methods developed in the literature to this point rely on regressing two images with each other and using the developed model to predict pixel intensities in subsequent images. In contrast to those MIR methods chapter 4 of the thesis develops a novel MIR approach using PLS regression models [Geladi et. al., 1986] to relate multivariate images of pulp with laboratory measured (non-image) pulp quality data. The developed model is successfully used to infer pulp quality from process multivariate images.

2.3.3 Comparing Traditional and Multivariate Statistics based Image Analysis Techniques

Digital image analysis techniques (both traditional and multivariate statistics based) aim to extract a few interesting feature pixels from largely uninteresting background features in digital images. However, as highlighted in this chapter, there are some fundamental differences between their methodologies and applications. What follows is a brief comparison of the strengths of the two categories of digital image analysis methods.

Traditional image analysis techniques are designed to extract quantitative measures of objects (features) working on every pixel in the 2-dimensional image space. These techniques are assisted by several image enhancement and restoration operations, which manipulate the intensities of individual or groups of pixels to help the image look visually pleasing to the observer and remove any unwanted noise. The objective is to try and make the feature pixels discernible from background pixels in order to extract the required information. These techniques achieve their objectives while working in the spatial dimensions of the digital image.

On the other hand, multivariate statistics based image analysis techniques like MIA and MIR focus on extracting feature pixels from uninteresting background pixels while working in the projected latent variable spaces of the multivariate image. The pixels in the multivariate image are projected onto reduced dimensional latent variable scatter plots based on their signatures in the variable dimension (e.g. NIR reflectance spectra of pixels in a multi-spectral NIR image). Feature pixels having similar spectral signatures group into a common region of the plots, whereas pixels with different spectra would be projected away from this group. Using these projections MIA and MIR techniques create optimal local models within the latent variable subspace to separate feature pixels from background pixels.

The strengths of multivariate statistics based image analysis techniques do not lie in trying to make the image noise free, or make it look visually pleasing. Traditional image analysis techniques are far superior at achieving these goals. However, multivariate statistics based methods are excellent at discerning feature information that is sensitive in the variable dimension of the multivariate image. In a 3-dimensional pixel matrix ($n_x \times n_y \times n_z$) these techniques essentially extract information that is *orthogonal* to the ($n_x \times n_y$) image plane. Once the feature is extracted in the latent variable subspace, it can be mapped back to the image plane to reveal the spatial locations of the pixels.

Upon unfolding the multivariate image MIA and MIR techniques loose all spatial information of the pixels in the image plane. Rather, they concentrate on explaining the spectral information in the pixels. The loss of spatial information may or may not prove to be disadvantageous depending upon the final objectives of the application. Chapters 3 and 4 illustrate examples where the loss of spatial information poses no disadvantage to multivariate statistics based image analysis techniques, as the objectives there are to extract spectral information from images. However, chapter 5 illustrates an application in which the loss of spatial information proves to be disadvantageous when using these techniques to extract image texture information.

Chapter 3

Multivariate Image Analysis for Softwood Lumber Grading

3.1 Introduction

Wood has historically been one of the most popular building materials due to its various desirable properties, adaptability in a wide variety of uses, and its relatively low cost. In Canada the forest products industry generates a large portion of its revenue from softwood lumber trading to various construction and furniture industries worldwide. Some of the commonly found softwood species in Canada are fir, spruce, and pine. The production chain of softwood starts as logs in the forests, which are sawn into lumber boards of specific dimensions by sawmills. Prior to shipping every piece of sawn lumber is examined and classified into one of several wood quality grades.

Hagman [1996] defines the quality of a lumber board as a function of the highest grade, which is then reduced by the occurrence of quality molding features (defects). The degradation in quality is amplified by the frequency, size, and location of such undesirable features. According to the Canadian Lumber Grading Manual [1998] typical defects found in softwood lumber may be divided into three broad groups, being:

- Natural Defects - which are caused by nature and develop within the living tree (e.g. various types of knots, pitch pockets, decay, wane, bark pockets etc.);
- Manufacturing Defects – those caused by equipment during the sawing and handling of lumber (e.g. raised grain, torn grain, fiber pull, machine burn etc.);

- Seasoning Defects – those caused when sawn lumber dries (e.g. splits, warped boards etc.).

The work presented in this chapter addresses selected softwood lumber defects from two of the above three groups. They are knots, splits, wane, pitch pockets, and bark pockets. A "*knot*" as it appears on a piece of lumber is a portion of a branch cut through by the saw. Knots are by far the most common defects found in sawn lumber. They come in various sizes, shapes, and quality. "*Pitch*" is defined as an accumulation of resinous material in the lumber. "*Pitch pockets*" and "*Bark Pockets*" are well-defined openings between the annular growth rings of the tree containing liquid or granulated pitch or pieces of bark, respectively. A "*wane*" is defined as bark or lack of wood at the edges of a sawn piece of lumber. "*Splits*" are cracks that occur in the lengthwise direction of sawn lumber due to rapid evaporation of moisture from the wood surface. A complete list of definitions and descriptions of most defects in Canadian softwood lumber can be gathered from the NLGA Standard Grading Rules for Canadian Lumber [1991].

To obtain a distinct wood quality the lumber board has to be introduced to a rule based system, which accounts for the number, size and position of its defects. However, due to the inherent variability in defects as well as sound wood structure itself (both between and within species) it is difficult to automate such a system. As a result, lumber classification based on assigned quality grade has traditionally been a result of human judgment after careful visual inspection of each piece.

The human lumber grader is entrusted with the classification of lumber that is of great value to the forest products industry and so is expected to be accurate and consistent in placing pieces in their proper grade. Lumber graders are highly trained individuals with many years of grading experience to make split second decisions about the quality of every lumber piece at production speeds of up to 30 boards per minute [Åstrand, 1996]. However, human errors and inconsistencies in grading lumber are also common due to variability in their judgment, especially when it comes to lumber samples that are at the borderline of two grades. For example, two graders, or even the same grader might grade a questionable lumber sample differently at different times of the day or days of the week. Furthermore, many factors like fatigue or mental state play a big role in human judgment, which sometimes results in misjudgment in assigning lumber grade. Erroneously downgraded lumber results in a significant loss to the forest products industry due to the substantial price difference between grades. At the same time upgrading low quality lumber results in long-term profit loss due to dissatisfied customers.

Facing stringent customer demands and tough competition in an unforgiving economy the forest products industry is aggressively exploring new and innovative approaches of automatic lumber grading. The main objective for such approaches is the correct and consistent classification of lumber boards based on assigned grade resulting from a quantitative analysis of lumber quality (i.e. defects). Several vision-based systems equipped with different types of imaging sensors, data processing hardware and various image processing algorithms have previously been proposed in the literature to address this need.

Åstrand [1996] provides an excellent literature review of many proposed strategies and algorithms for automatic lumber grading via detection and classification of lumber defects. Some of the early work proposed methods using grayscale images of lumber boards where the image was subdivided into a number of rectangular sub-images and the classification was carried out on each sub-image independently to determine if it belonged to clear wood or a defect [Conners et. al., 1983; Sobey et. al., 1989]. Defect segmentation based on thresholding the grayscale image has also been proposed due to the fact that most lumber defects are darker than the surrounding clear wood [Klinkhachorn et. al., 1991; Lee et. al., 1991; Kim et. al., 1994].

Color based classification of lumber defects has also been well researched in the literature. Conners et. al. [1985] established the requirements of a color-based wood inspection system in which they made some tests comparing grayscale and RGB based sub-image classification utilizing first order statistics and a Bayesian classifier. Several color vision-based systems for wood inspection using RGB cameras have since been proposed [Polizleitner et. al., 1990; Silvén et. al., 1994; Kauppinen et. al., 1995]. The common idea here being the use of shape or morphological features in conjunction with color information to improve lumber defect classification.

Over the last decade several researchers have recognized the potential of using color spectral information in RGB images to help detect and classify lumber defects [Maristany et. al., 1991; Adel et. al., 1993; Brunner et. al., 1992 & 1993]. These researchers proposed various mathematical transformations of the RGB color space to enhance color differences between clear wood and lumber defects. Brunner et. al. [1992] concluded that a two dimensional color space (within the 3-dimensional space of RGB) was sufficient for separating knots and pitch from clear wood. This conclusion has also been confirmed in the previous chapter (section 2.3.1) where MIA is performed on an RGB lumber image. It can be seen that the 2-dimensional score space of MIA could easily separate knots and splits from pitch pockets and clear wood in the 3-dimensional RGB image (figure 2.12).

Brunner et. al. [1993] later concluded that an extended-dimension color space based on a higher spectral resolution than the standard RGB could enhance the performance of a wood inspection system. Vaarala et. al. [1995] used an imaging spectrometer (similar to the one described in section 2.1.2.3) to acquire 57 channel multi-spectral lumber images in the human visible wavelengths (VIS) of the electromagnetic spectrum. A few representative pixels were selected from the multi-spectral images, and their corresponding VIS spectra were analyzed using PCR to classify the pixels based on their spectral signatures.

Hagman [1992] illustrated the first application of MIA techniques for off-line feature detection and classification in sawn lumber boards by successfully classifying blue stain and knots in the sore plots of a multi-spectral lumber image captured with multiple monochromatic filters within the VIS and NIR wavelength spectrum. In his PhD thesis Hagman [1996] investigated off-line MIA and MIR based techniques for lumber feature extraction and modeling of multi-spectral images acquired through an imaging spectrometer in the VIS spectrum. He also investigated imaging lumber with microwave, X-ray and CT-scanners.

This chapter proposes an extension of MIA techniques for on-line monitoring of specific lumber defects in RGB color images of softwood lumber boards. The technique provides both qualitative and quantitative results that can be used for automatically assigning quality grades to lumber boards at production speeds based on pre-chosen defective features. The proposed strategy is illustrated through an example of grading 38 lumber boards from three species (Balsam fir, White spruce, and Jack pine) based on pre-selected defects like knots, splits, wane, pitch and bark pockets.

The chapter also presents the first study on the use of NIR imaging spectrometers for the analysis and classification of lumber. Certain indistinguishable lumber features in the RGB color space are shown to be successfully differentiated using MIA of NIR multi-spectral lumber images. This is illustrated through an example of isolating sub-features of two types of knots in NIR multi-spectral images.

Finally, the chapter discusses a few conditions that must be met in order to use PLS-DA based MIR techniques to classify feature pixels in multivariate images. The conditions are illustrated through a conceptual example of MIR modeling of lumber features with a PLS-DA algorithm.

The chapter is structured as follows. Some imaging details of softwood lumber boards are first presented, along with a representative illustration of the lumber dataset. Off-line MIA of softwood lumber is then described with an emphasis on feature extraction from multi-spectral NIR images. This is followed by the extension of MIA techniques to the on-line monitoring of lumber defects using RGB images. A discussion of MIR techniques using PLS-DA models is then presented, followed by conclusions and contributions of the work.

3.2 Softwood Lumber Imaging

It is obvious that the results of whatever image analysis techniques are applied to grade lumber depend on the quality of the images received from the imaging sensors. In order to capture all possible lumber defects one would require multiple imaging sensors, which are either sensitive to different regions of the electromagnetic spectrum or construct images based on non-visual information. Grayscale and RGB color cameras are among the most commonly used imaging sensors in vision-based softwood lumber grading systems [Kauppinen et. al., 1995]. Besides these cameras lumber images have also been acquired from microwave sensors, which construct an image based on attenuation and phasing of microwaves through lumber [Hagman, 1996]. Several applications of medical imaging sensors to capture lumber images have also been reported. Examples include, X-Ray imaging sensors, Computed Tomography (CT) scanners [Hagman, 1996], and Magnetic Resonance Imagers (MRI) [Chang et. al., 1989].

As mentioned in the previous section imaging spectrometers in the VIS wavelength spectrum have recently been used as a part of a vision-based lumber classification scheme [Hagman, 1996; Astrand, 1996]. Besides the VIS wavelength spectrum imaging spectroscopes have also been realized in the very near-infrared (680 – 1100 nm) and intermediate (450 – 900 nm) wavelengths [Vaarala et. al., 1995]. Hagman [1996] illustrates a short test of the intermediate imaging spectrometer for lumber imaging. This thesis illustrates the first published application of lumber image acquisition using an imaging spectrometer working in the NIR wavelength range (900 – 1700 nm).

The main focus of this chapter will however revolve around information extraction from RGB images of lumber for purposes of on-line classification. A brief exploratory analysis of lumber using NIR multispectral imaging is included to determine its potential contributions, and compare its advantages and shortcomings with RGB imaging for lumber defect analysis.

3.2.1 Color (RGB) Imaging

Technical details of the specific RGB line-scan camera used to image moving lumber boards have been provided in chapter 2 (section 2.1.1). This section presents some experimental details pertaining to the lumber imaging that was performed using the RGB line-scan camera at CRIQ.

A schematic of the vision-based system used to image moving lumber boards has previously been illustrated in figure 2.1. The Digital Signal Processing (DSP) unit was programmed with edge-detection and alignment algorithms to pre-process the continuous line-scans acquired from the RGB camera into a lumber image prior to analysis in the personal computer. The pre-processing was mainly done to account for the leading and trailing ends of the lumber board, as well as correct for lateral movement of the boards on the conveyor belt as they passed under the camera. All RGB lumber images used in this thesis are the final corrected versions recorded by the personal computer.

An important part of the vision-based system is the proper and consistent illumination of the lumber samples. Wood surfaces can look drastically different depending upon the direction and angle of the illumination [Åstrand, 1996]. Spectrally stable illumination is needed when using multi-spectral cameras like RGB or imaging spectrometers. The lumber boards imaged using the color vision system at CRIQ were illuminated with multiple fluorescent lights in a semi-circle spanning all angles between 45° and 135° with respect to the lumber board surface. In the subsequent analyses of all RGB lumber images it has been assumed that the lumber boards were adequately illuminated to provide maximum contrast (i.e. signal-to-noise ratio) between clear wood and lumber defects.

Light calibration is another important issue in the long-term use of on-line vision-based systems. This is due to the aging and deterioration of the lamp, which results in improper illumination of the sample over time. Lumber itself has many color variations, which would get enhanced if the lighting intensity were to change over time. For long-term on-line color vision-based systems there is a definite need to maintain light intensity and color to ensure the adequacy of the empirical models developed in automatic lumber grading systems. Light calibration is not applied in this thesis, since the system used to image lumber boards performed the imaging within 30 minutes, which is too short a time-span to have any illumination differences due to light aging.

Figure 3.2 illustrates RGB color images of 4 pre-selected lumber samples, which contain examples of typical lumber defects to be detected and classified using the methods proposed in this chapter.

3.2.2 Near-Infrared (NIR) Multispectral Imaging

Chapter 2 (section 2.1.2) provides a detailed description of the NIR line-scan imaging spectrometer, which has been assembled using a NIR digital camera and an imaging spectroscope. Some further experimental details on using the spectrometer for imaging lumber boards are discussed below.

Using the line-scan NIR imaging spectrometer a reflectance image of a lumber board was captured with 300 lines as the sample moved on the scanner bed at a speed of (~10 ft./min.). In its uncorrected form the resulting multi-spectral image dimensions were $300(x) \times 128(y) \times 128(\lambda)$ pixels. However, due to presence of a few bad pixels in the NIR camera the raw image was pre-processed to spatially smooth the reflectance values at questionable pixel locations and remove two right columns (127 and 128) in the x-y plane of the multi-spectral image. The signal-to-noise ratio of the NIR reflectance was not consistent in the full spectral range (900 nm – 1700 nm) of the imaging spectrometer. There was considerable noise at the two extremes of the spectrum. As a result the full NIR spectrum spanned by 128 wavelength images was cut to 79 images spanning a reduce NIR spectrum (1144 nm – 1670 nm). After pre-processing the final image dimensions were $300 \times 126 \times 79$ pixels. Figure 3.1(a) illustrates a multi-spectral NIR reflectance image of the lumber sample at three wavelengths (1204 nm, 1405 nm, and 1609 nm). Besides clear wood the lumber sample contains two typical defect features (a decayed bark-ringed loose knot and splits). The three wavelength images show unique lumber defect feature information captured by different regions of the NIR spectrum. Finally, for purposes of comparison a RGB color image of the same sample has also been illustrated in figure 3.1(b).

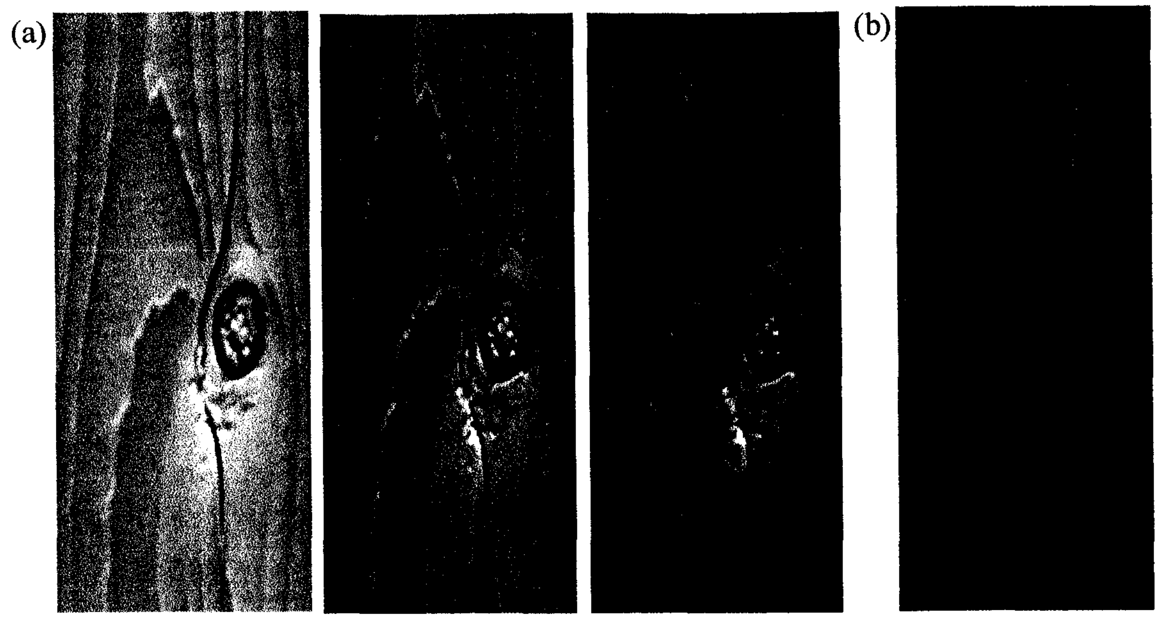

Figure 3.1 (a) Three wavelength images (1204 nm, 1405 nm, 1609 nm) from a NIR multi-spectral image of a lumber sample containing two defects (splits & knot). (b) RGB color image of the same lumber sample

It can be seen from the RGB color and the three NIR wavelength images in figure 3.1 that the information extracted by the two sensors is different. RGB captures color-based contrast in the lumber, whereas chemical information reflected by the lumber features is captured by the NIR imaging sensor. The RGB camera can differentiate the knot (darker contrast) from surrounding clear wood (lighter contrast) due to a difference in their colors. It should be noted that 'color' is defined as reflected light in the human visible wavelength spectrum (400 – 700 nm). The NIR imaging spectrometer on the other hand cannot differentiate the wood in some parts of knot from the surrounding clear wood because they contain similar chemical information. The main difference between these features is their color contrast. Since NIR is insensitive to color (i.e. it captures light reflectance *beyond* the human visible wavelength spectrum) it cannot 'see' any difference between parts of the knot and clear wood. It can be noted that the NIR spectrometer easily distinguishes the bark ring surrounding the loose knot from the wood within the knot core and clear wood. This information could be critical if one were interested in detecting bark-ringed (loose) knots for lumber quality assessment. Section

3.3.2.1 illustrates an example where this information has been used to differentiate between loose and firm knots.

3.2.3 Description of Lumber Data

The samples used for this study have been selected from the shelves of a lumber retailer. It is assumed that the samples had been screened before reaching their destination. As a result, the collected lumber sample quality is relatively good. The samples do not contain the full spectrum of typical defects encountered by lumber graders in the sawmill. However, the purpose of this study was to explore the feasibility of applying MIA methods for on-line lumber grading. Keeping this in mind, for the sake of simplicity the number and types of lumber defects in the dataset used for the study

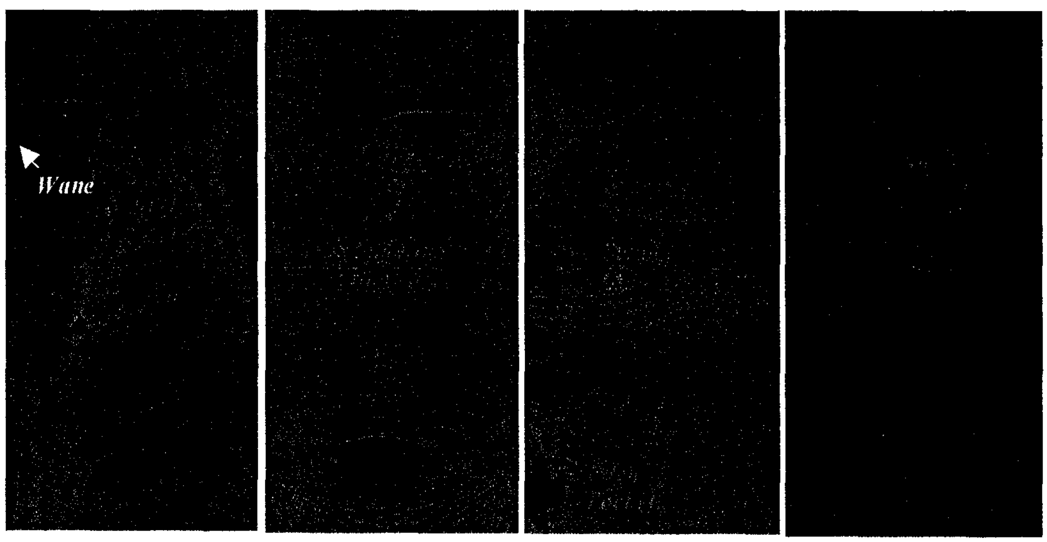

Figure 3.2 RGB color images of 4 pre-selected lumber board samples containing various types of knots, splits, wanes, pitch & bark pockets

were intentionally kept low. Typical defects found in the lumber dataset ranged from various types of knots, splits, wane, bark pockets, and pitch pockets. These are some of the most common defects (>85%) encountered by human graders in a typical sawmill.

Each lumber sample has physical dimensions of 1″ (Thickness) × 4″ (Width) × 24″ (Length), with only one of the 24″ × 4″ faces being imaged by the RGB and NIR cameras. As mentioned before the lumber dataset consists of 38 such lumber samples from three different softwood species (Balsam fir, White spruce, and Jack pine). The methods used in this study are applicable to all three lumber species. As a result, information about the lumber species has been omitted. Figure 3.2 illustrates four a priori selected lumber board samples from the dataset, which have been imaged with the RGB line-scan camera as $712(x) \times 345(y) \times 3(\lambda)$ pixel multivariate images. These lumber samples cover various examples of all the above-mentioned defects in different sizes, shapes, and color contrast.

3.3 Off-Line Multivariate Image Analysis of Softwood Lumber

Multi-spectral images of softwood lumber in the VIS spectrum have previously been analyzed for typical defects using MIA and MIR based techniques [Hagman, 1997]. Section 2.3.1 of this thesis presents an MIA example on an RGB color image of a lumber board to extract some typical lumber defects.

The main objective of this section is to provide a comprehensive study of lumber imaging in the NIR wavelength spectrum, and to explore its ability to help extract typical lumber defects using MIA of multi-spectral NIR lumber images. Furthermore, the study aims to compare the advantages and shortcomings of NIR imaging spectroscopy over RGB color imaging for off-line lumber quality assessment.

3.3.1 MIA of True Color RGB Lumber Images

The example of MIA on a RGB lumber image presented in section 2.3.1 of this thesis illustrates extraction of lumber defect features like splits, knots, and pitch pockets from clear wood. This is achieved by masking point clusters in the latent variable *score space* of the first two Principal Components ($\mathbf{t}_1 - \mathbf{t}_2$) and highlighting the masked pixels in the *image space* using a false-color composite image of the three scores. The duality between the score and image spaces allows the manual delineation of such lumber defects from clear wood.

From the results obtained in the example study some general conclusions can be drawn about lumber feature information captured by RGB imaging sensors. Upon observing the signs and magnitudes of the elements in the $\mathbf{p}_1$ loading vector [Red = 0.722; Green = 0.588; Blue = 0.365] and investigating corresponding scores as $\mathbf{T}_1$ image (figures 2.10) it is clear that the first PC explains something close to the average of the three colors in the RGB image. Thus clear wood pixels, which are brighter than pixels belonging to the lumber defects exhibit higher $\mathbf{t}_1$ values in the $\mathbf{t}_1 - \mathbf{t}_2$ score plot (figure 2.11). On the other hand, darker lumber features like splits and knots exhibit lower $\mathbf{t}_1$ values. These two lumber defects are delineated from other features via a common mask in the low $\mathbf{t}_1$ region of the $\mathbf{t}_1 - \mathbf{t}_2$ score plot (figure 2.12a). From the proximity and tightness of the score cluster representing pixels belonging to knots and splits it can be seen that RGB is not sensitive enough to be able to further differentiate between these two types of defects. Besides being insensitive to differences between lumber defects like knots and splits this section will illustrate that RGB imaging is also insensitive to differences among other dark contrast lumber defects like wane and bark pockets.

The elements of the second loading vector $\mathbf{p}_2$ [Red = -0.523; Green = 0.117; Blue = 0.845] indicate that the second PC produces a contrast between red and blue colors. Ohta et. al. [1980] also confirm this trend in the first two Principal Components of a PCA decomposition of RGB images. In the corresponding score image $\mathbf{T}_2$ of the second PC (figure 2.10) it can be seen that contrast differences between pitch pockets (dark pixels) and remaining lumber features (bright pixels) have been captured. Pitch pockets have been delineated with a mask covering the low $\mathbf{t}_2$ score point cluster in the $\mathbf{t}_1 - \mathbf{t}_2$ score plot (figure 2.12a).

Using MIA on RGB lumber images for detection of defects one can easily segment dark contrast features like knots (along with splits, wane and bark), and unique color features like pitch pockets from clear wood. Thus, if one were interested in simply detecting these lumber features without considering any further segmentation of the defects into: (i) types of knots, or (ii) differentiating between dark contrast defects like knots and splits, then MIA on RGB images can provide sufficient information. However, if further segmentation detail is required, then simple classification of defects based on color (contrast) is not enough. One might need to detect the chemical structure of the various defects and segment them into different classes based on this information. MIA on NIR multi-spectral images of lumber could provide this further detail.

3.3.2 MIA of Multi-spectral NIR Lumber Images

A study of lumber classification using NIR imaging spectroscopy is presented here with the aim of exploring critical feature information that might be captured by the NIR wavelengths of the electromagnetic spectrum. MIA is used as the analysis tool for extracting such information.

Analysis of lumber feature information captured by the NIR wavelength spectrum is best illustrated through an example of extracting lumber defect pixels from a multi-spectral NIR image of a lumber board. Details of the lumber sample used in this study have been described in section 3.2.2. Figure 3.1 illustrates three NIR wavelength images and a RGB color image of the sample. The two lumber defect features that have been highlighted in figure 3.1 are a decayed bark-ringed loose knot and vertical splits.

MPCA was performed on the 300 × 126 × 79 pixel multi-spectral NIR lumber image after unfolding it into a 2-dimensional (37,800 × 79) array. A detailed description of MIA has been described in chapter 2 (section 2.3.1) with an example study on a 3-variable RGB lumber image. As a result, MIA algorithm details have not been included here. In contrast to RGB image data, multi-spectral NIR images contain a much larger variable dimension. In this example the lumber image has 79 variables (wavelengths).

The 79-variable multivariate image was decomposed into a linear combination of 5 Principal Component scores and loadings, which cumulatively explained 99.996% of the total sum of squares in the image. This is a ~96% data reduction, indicating most meaningful lumber feature information can be condensed into ~4% of the original image data. The true power of MIA techniques can be realized in this example, as these techniques can efficiently extract meaningful feature information from this new low-dimensional feature space.

No pre-scaling of image data is generally performed in MIA [Geladi et. al., 1989]. The first PC typically explains average pixel contrast, which is >99% of the sum of squares in the multivariate image. As a result, in MIA the explained sum of squares does not provide a true indication of the adequacy of the MPCA model. A much more powerful description of model adequacy can be obtained upon visually observing the PC scores and model errors (residuals) as pixel brightness values of intensity images. Figure 3.3 illustrates the 5 MPCA score images and the remaining SSE (sum of squared errors) as pixel intensities of a grayscale image.

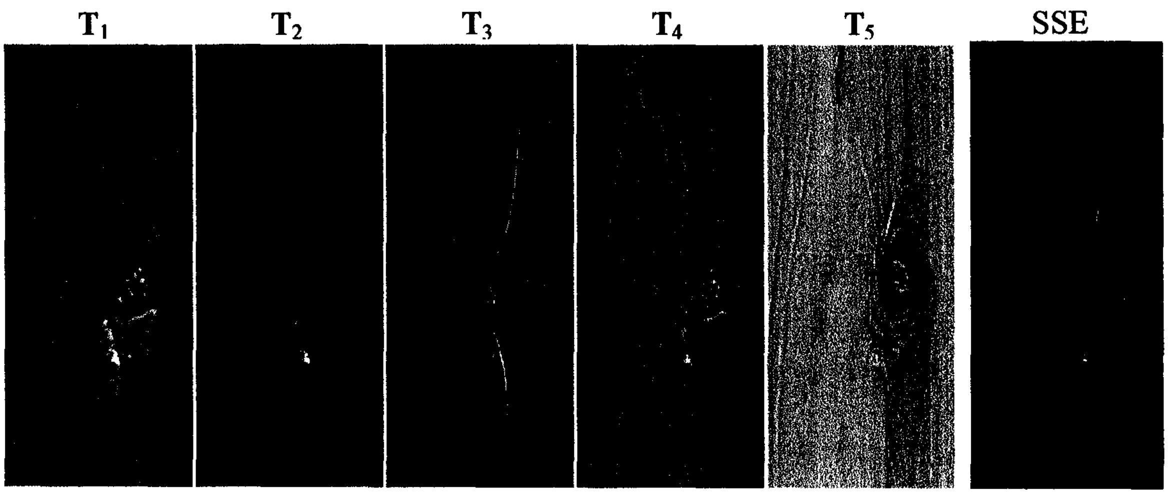

Figure 3.3 Five PC score images and SSE image of MPCA decomposition on a multi-spectral NIR lumber image

Upon observing the (mostly dark) pixel data of the SSE image in figure 3.3 it can be said that after extracting 5 Principal Components there is very little structural feature information remaining in the multivariate image. Only a few pixels from the splits and knot core can be seen in the SSE image, which indicates that these two lumber features are more complex than the remaining features.

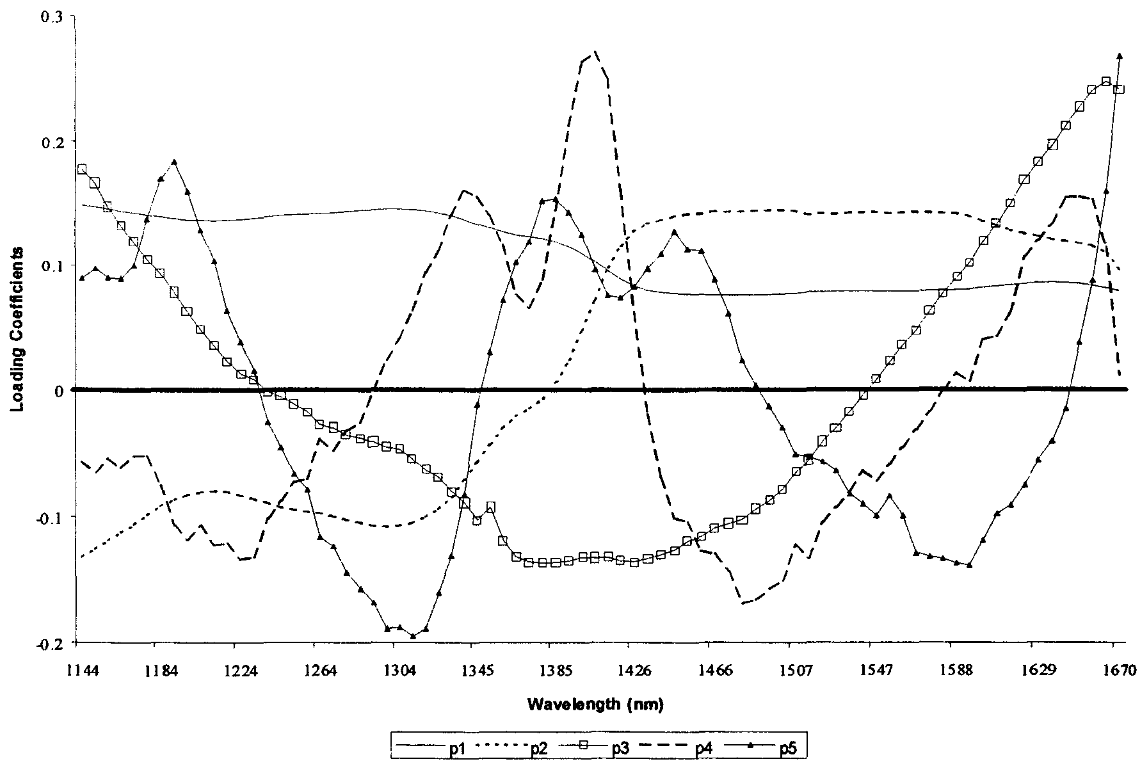

Figure 3.4 Coefficient plot of five PC loading vectors of MPCA decomposition on a multi-spectral NIR lumber image

Lumber feature information extracted by each PC of the model can be visually observed in the corresponding score images of figure 3.3. As mentioned before PC scores are weighted-averages of the variables in the multivariate image. The individual weights assigned to each variable are summarized in the corresponding PC loadings. In this case each score image is a unique weighted-average of 79 wavelength images in the NIR spectrum. Figure 3.4 illustrates a line plot of the 5 PC loading vectors used to decompose the multi-spectral NIR lumber image.

It can be seen from figure 3.4 that different parts of the NIR wavelength spectrum have been highlighted by the coefficients of the 5 PC loading vectors. This NIR spectral information is reflected in the lumber features of the corresponding PC score images. Table 3.1 summarizes the lumber feature information in the PC score images from figure 3.3.

Table 3.1 Feature information in MPCA model of multi-spectral NIR lumber image

PC	Observation (Loading Vector – Figure 3.4)	Observation (Score Image – Figure 3.3)
1	All wavelengths approximately equally weighted	• Average contrast information of all pixels in the image
2	Contrast between low (1140 – 1300 nm) and high (1430 – 1670 nm) wavelengths	• Highlights annular rings of clear wood • Cannot differentiate splits from clear wood • Cannot differentiate bark-ring of knot from annular rings in clear wood
3	Contrast between mid (1350 – 1450 nm) and ends (low & high) of NIR spectrum	• Highlights splits (bright pixels) • Cannot differentiate between knot and clear wood
4	Weighs specific wavelength bands (see figure 3.4)	• Highlights contrast between springwood (bright pixels) and summerwood (dark pixels) • Highlights edges of splits (dark pixels)
5	Weighs specific wavelength bands (see figure 3.4)	• Highlights bark ring and some knot wood (dark pixels) • Cannot differentiate between splits and clear wood • Cannot differentiate between decayed knot wood and clear wood

Besides observing individual PC scores as intensity images one can also construct false color-composites of two or three PC score images to visually pool the information captured by the MPCA scores. Figure 3.5 illustrates false color-composite images of various combinations of four PC score images ($\mathbf{T}_1$, $\mathbf{T}_2$, $\mathbf{T}_3$, and $\mathbf{T}_5$). The 4th PC has been intentionally excluded since it does not contribute (as much as the other 3 PCs) in highlighting the lumber defect features.

The ability of MIA to delineate lumber defects from clear wood has been previously illustrated (section 2.3.1) using manually created masks in the score space scatter plots and highlighting the corresponding pixels in the false color-composite score image space. The same strategy has been applied here in order to delineate the bark ringed loose knot and splits from clear wood. Since 5 PCs have been extracted in this example, one can create up to 10 unique combinations of PC pair scatter plots. However, the 4th PC has been excluded from further analyses. Thus a maximum of 6 unique PC pair combinations can be scatter plotted with each other. Point clusters can be interrogated in these scatter plots using the masking/highlighting strategy of MIA. Switching between the image and score spaces allows one to delineate the lumber defects

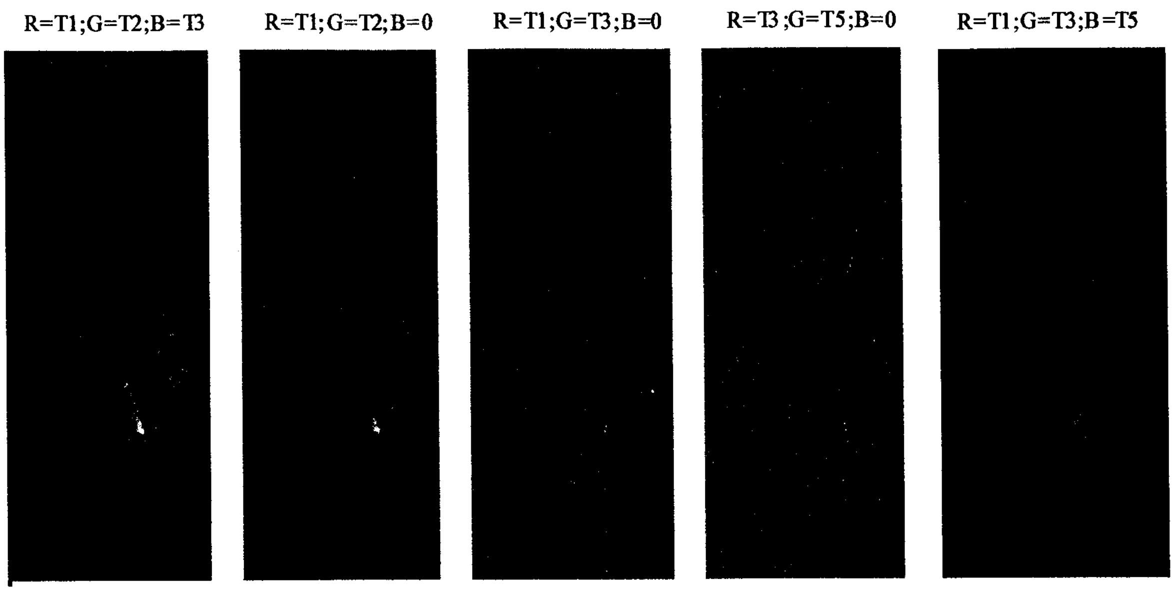

Figure 3.5 False color-composite images from various combinations of $\mathbf{T}_1$, $\mathbf{T}_2$, $\mathbf{T}_3$, and $\mathbf{T}_5$ score images

from clear wood. Figure 3.6 illustrates the masking/highlighting strategy of MIA in 3 (out of a possible 6) PC pair scatter plots to delineate the loose knot and splits from clear wood. For graphical clarity binary images have also been included, which indicate the spatial locations of classified features as black pixels.

It can be seen from figure 3.6(a) that the $\mathbf{t}_1 - \mathbf{t}_2$ score space can successfully delineate parts of the loose knot and the upper split from clear wood. However, it cannot differentiate between the two lumber defects. This is because these two features are completely confounded with each other in the first two PCs resulting in similar (t_1, t_2) combinations. The $\mathbf{t}_1 - \mathbf{t}_3$ scatter plot in figure 3.6(b) is more successful in differentiating parts of the loose knot (blue mask) from the splits (magenta mask). The 3rd PC ($\mathbf{t}_3$) direction is the main contributor for this separation. Observing the corresponding binary images of the classification achieved by the masks in the $\mathbf{t}_1 - \mathbf{t}_3$ scatter plot it can be concluded that some misclassification is present between the two lumber defects. The best separation between the two lumber defects is achieved upon masking the corresponding point clusters in the $\mathbf{t}_3 - \mathbf{t}_5$ scatter plot illustrated in figure 3.6(c). The binary images of the classified lumber defects produces the least number of misclassified

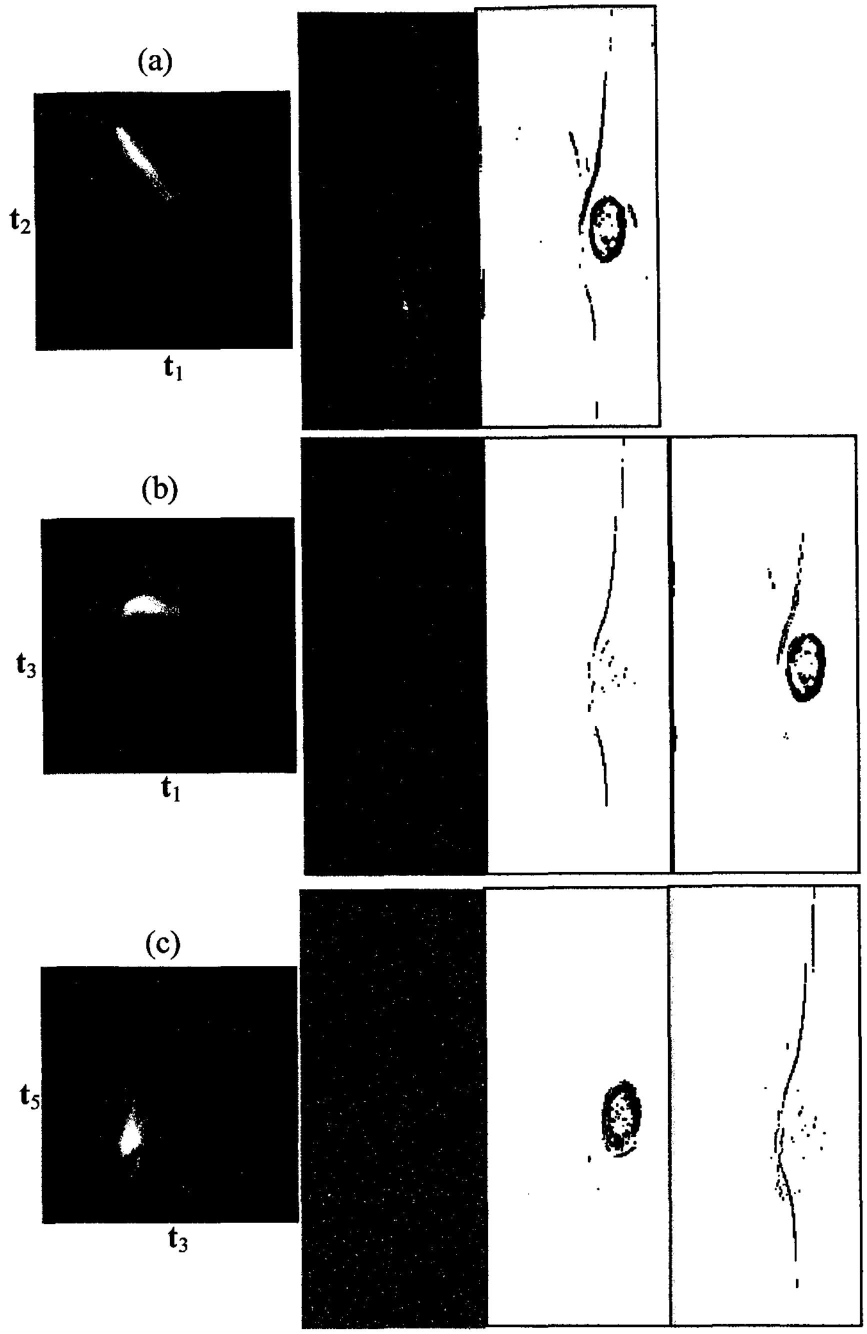

Figure 3.6 Delineating lumber defects via masking/highlighting strategy of MIA. (a) $\mathbf{t}_1 - \mathbf{t}_2$ PC score space. (b) $\mathbf{t}_1 - \mathbf{t}_3$ PC score space. (c) $\mathbf{t}_3 - \mathbf{t}_5$ PC score space

feature pixels. Observing the $\mathbf{T}_3$ and $\mathbf{T}_5$ score images in figure 3.3 it is clear that these two PCs carry the most discriminating information, which differentiates the two lumber defects from clear wood.

Some general conclusions can be drawn from the results of the MIA application illustrated in this section. NIR imaging spectroscopy seems to be a promising technology that can be used for off-line quality analysis of softwood lumber boards. Rather than color, NIR multi-spectral images produce contrast between lumber features based on their chemical information. This is the main reason why it is possible to differentiate between lumber features like knots and splits using MIA. These lumber defects could not be differentiated (section 2.3.1) through RGB lumber image analysis.

An important observation that can be made from the above example is that a knot is not considered to be a single feature when imaged using a NIR imaging spectrometer. It is imaged as a very complex feature that is made up of a mixture of several "sub-features" within itself. This is because a knot is a sawn branch of the tree, which may contain a wide variety of woods in different quantities and textures. Furthermore, depending upon the age of the knot, these woods might be in different stages of decay. Every such sub-feature of a knot emits a unique chemical signature that is captured in a different wavelength range of the NIR spectrum. Thus it can be concluded that the NIR imaging spectrometer is capable of resolving the detail of a knot at a much finer level as compared to a RGB camera. Hagman [1996] made similar observations about knot complexity using a visible wavelength multi-spectral image of a test knot.

The following section discusses various techniques that could be used to dissect sub-features of a spectrally complex feature (e.g. lumber knots) in the PC space of its multi-spectral image. One such technique is illustrated through an example of extracting a knot sub-feature to differentiate between two types of knots in a multi-spectral NIR lumber image.

3.3.2.1 Multi-Dimensional Masking in MIA Score Plots to Isolate Knot Features

As mentioned before analysis of knots in multi-spectral NIR lumber images is not a trivial problem. This is mainly due the complex chemical structure present in a typical knot, which results from the union of various lumber components. Each component of a knot might have a unique spectral signature in the NIR wavelengths of the electromagnetic spectrum. Imaging lumber using a NIR imaging spectrometer produces great contrast in those pixels representing the various components (sub-features) of a knot.

From the example presented in the previous section it can be seen that MPCA decomposition of a multi-spectral NIR knot image requires more than 2 PCs to adequately capture all the unique spectral information present in its various sub-features. However, the masking/highlighting strategy of MIA discussed so far can only delineate image features using 2-dimensional masks in the scatter plots of PC score pairs. To adequately delineate all the sub-features of a knot one needs to develop a multi-dimensional mask in the MIA score space of its multi-spectral image.

It should be noted that developing multi-dimensional masks for dissecting knots is strictly a theoretical study. If one were interested in extracting a knot (as a whole entity) from clear wood, MIA of RGB lumber images can easily delineate this feature in 2 PCs. The main objective of this theoretical study is to develop an analysis tool, which can be used to model spectrally complex features that might arise in various industrial applications being monitored by multi-spectral imaging sensors.

Many approaches can be tried to develop a multi-dimensional mask, which extracts complex knot sub-features captured by more than two PCs on a common basis. The strategy explained below takes a practical approach to pool the desired knot sub-feature pixels from various masks in multiple PC pair score plots of MPCA performed on its multi-spectral image.

The proposed approach is best illustrated through a conceptual example study. Figure 3.7 illustrates a RGB color image and a false color-composite of the first three PC score images of MPCA on a multi-spectral NIR image depicting six knots from different lumber boards. The top three knots in the composite image are loose knots, whereas the bottom three knots are firm. As illustrated in figure 3.7 one distinguishing feature that differentiates loose knots from other types of knots is the presence of bark rings and gaps around the circumference of the knot interface with clear wood. If one could isolate this sub-feature in a lumber image it would then be possible to differentiate loose knots from other lumber features. The darker bark rings around the loose knots can be visually identified in the RGB image (figure 3.7). Thus, traditional image analysis techniques on the RGB image could be used to segment the loose knots. However, if using MIA of the

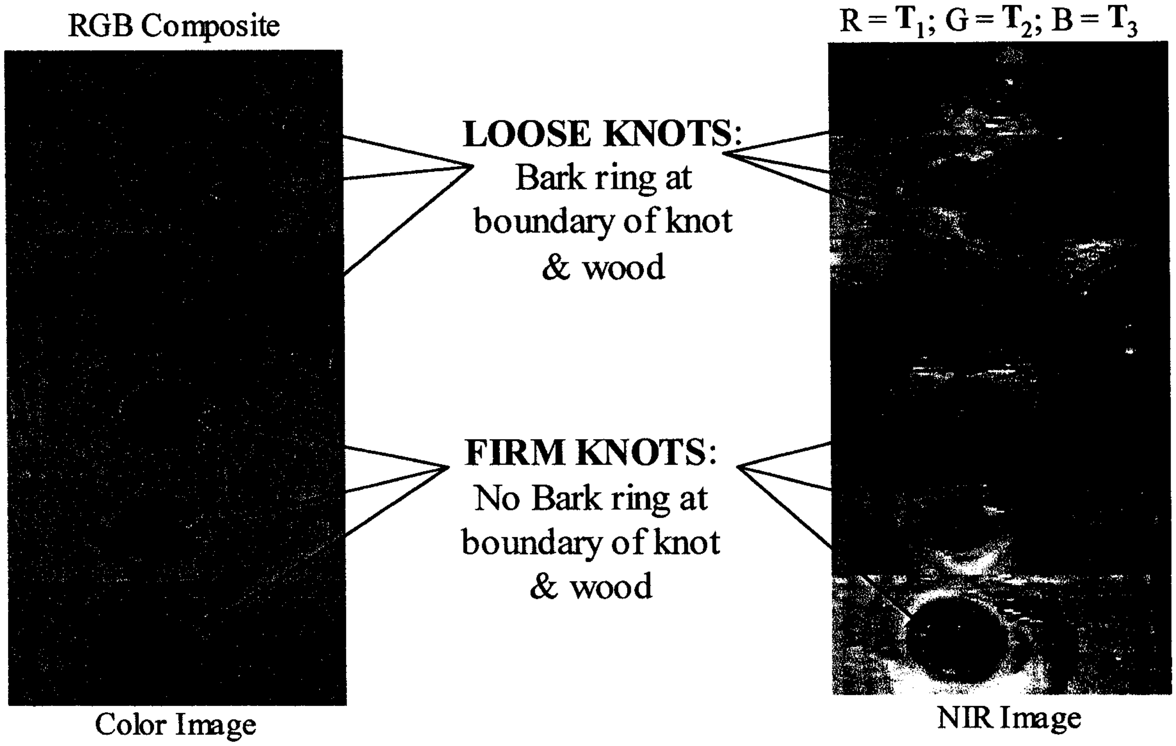

Figure 3.7 RGB color image and a false color-composite PC score image from MPCA of a multi-spectral NIR image of six knots (3 loose knots & 3 firm knots)

RGB image part of the problem is the overlap of bark ring feature pixel scores with other knots features in the MIA score space. The proposed multi-dimensional masking strategy is used in the MIA score space of the multi-spectral NIR image to differentiate between loose and firm knots by isolating bark rings and gaps at the knot-wood interface of the three loose knots.

The 245 × 126× 79 pixel multi-spectral NIR image was decomposed into a linear combination of 7 significant PCs using MPCA. The individual knot feature information captured by the 7 PCs can be observed in the corresponding PC score images. Figure 3.8 illustrates the 7 PC score images along with an intensity image of the remaining SSE after removing 7 PCs from the multi-spectral image. It can be seen from the SSE image that most of the knot structure has been removed from the multi-spectral image by the 7 PCs of the MPCA model.

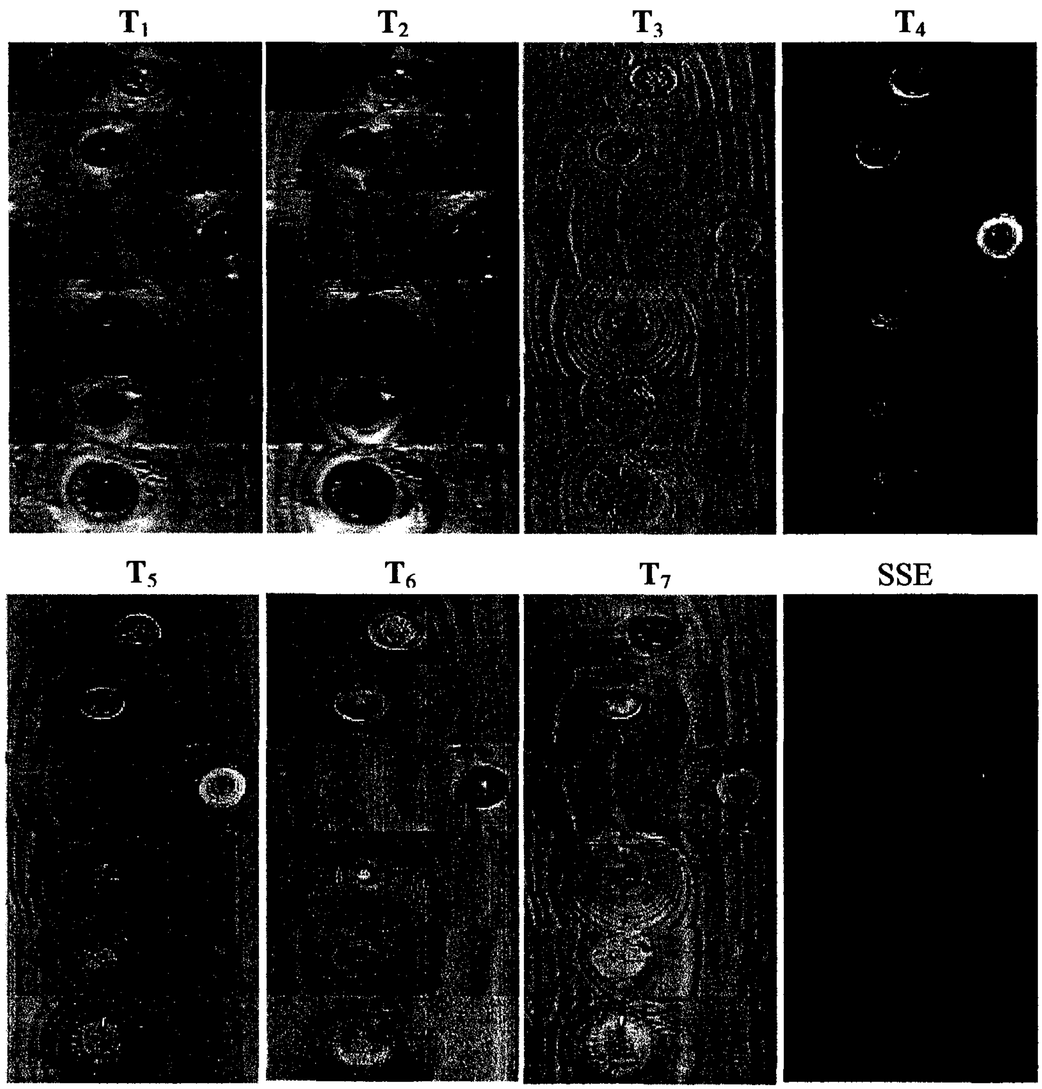

Figure 3.8 PC score images and SSE image of a 7-dimensional MPCA model of the multi-spectral NIR knots image

Using different combinations of the 7 PCs, up to 21 unique PC pair score scatter plots can be created. As seen from the PC score images in figure 3.8 the MPCA model explains different knot structures in each of the 7 significant PCs. Thus it can be inferred that all 21 PC pair scatter plots should be used to extract knot sub-features like bark rings and gaps around the loose knots. Pixels belonging to these sub-features could be delineated from other features using manually created masks in each of the 21 PC pair score plots, and highlighting the corresponding masked pixels in the false color-composite score images of the PC pairs. The duality between MIA score and image spaces greatly assists in determining adequate sizes and shapes of the 21 masks in order to capture all pixels belonging to the knot sub-features.

As mentioned before knots contain various sub-features; some of which might be confounded with each other in certain PCs of the MPCA model. When these PCs are scatter plotted against each other it becomes impossible to remove the confounding effects of some features. This is because pixels from multiple features would be part of the same point cluster. No mask, regardless of its size or shape, can fully delineate the confounded feature pixels in such two-dimensional scatter plots, which would lead to misclassified pixels. Mask sizes and shapes could be manually chosen depending upon the acceptable misclassifications of non-feature pixels as features, or vice versa. The two extreme scenarios of creating mask sizes/shapes are described below.

The *conservative approach* produces smaller feature masks, as its objective is to not have misclassifications of non-feature pixels as features. This approach disregards any misclassifications of feature pixels as non-features. This is analogous to setting the type II error to zero. On the other hand, the *aggressive approach* sets the type I error to zero. This approach produces larger masks. Its objective is to include all feature pixels regardless of misclassified non-feature pixels as features. Ideally an optimization routine could be set-up to produce an optimal mask size and shape, which minimizes pixel misclassifications of both types (i.e. minimize both type I and type II errors). However, setting-up such an optimizer is not a trivial task, as it would have to incorporate the inherent non-linearities of manually created masks in the MIA score plots. MIA models of features are extremely non-linear due to the irregularly shaped score space masks for adequately capturing their corresponding pixels in the multivariate image. Set-up and

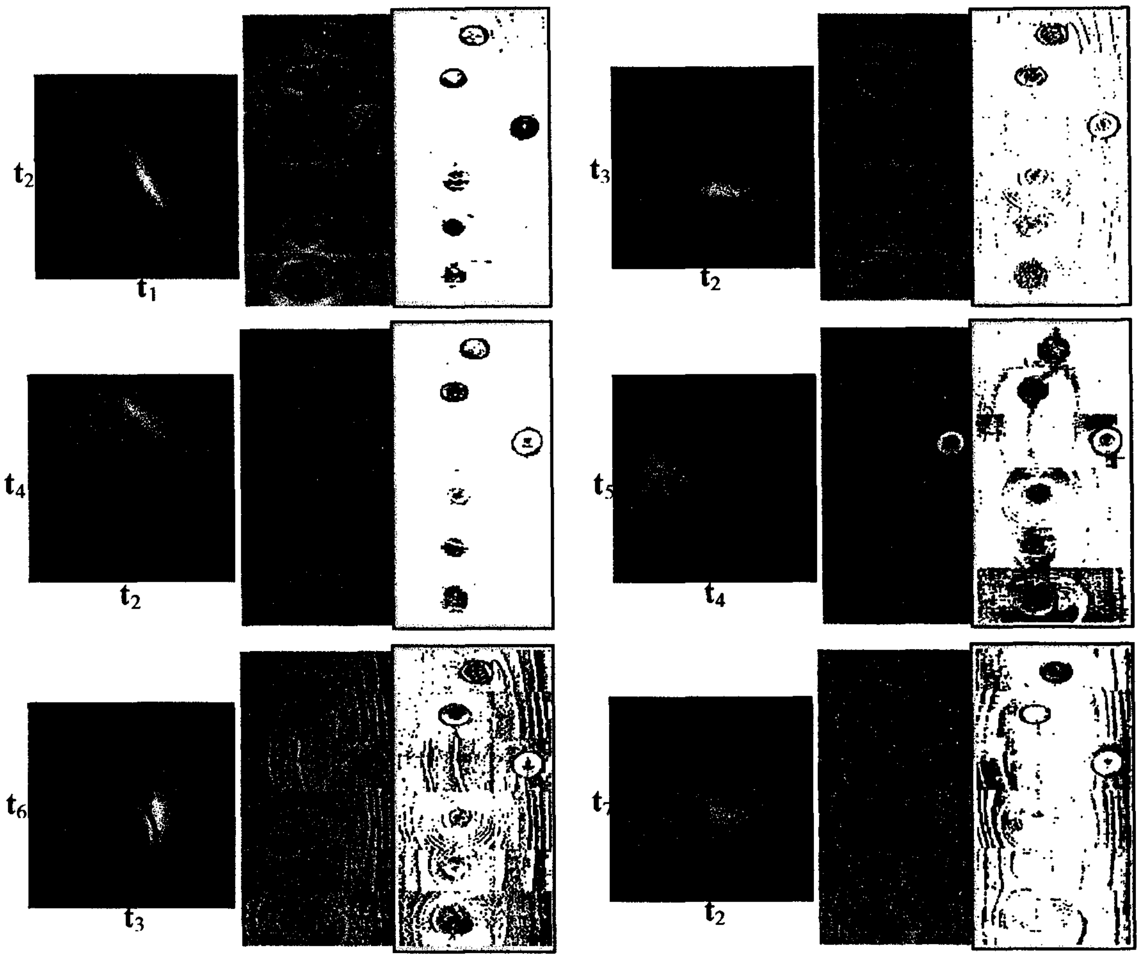

Figure 3.9 Modeling loose knot sub-features in multiple score plots via multi-dimensional masking

implementation of the above-mentioned mask size and shape optimization routine is beyond the scope of this thesis. Instead, the *aggressive approach* has been used in the 21 PC pair score plots of the knots image example to mask feature pixels belonging to bark rings and gaps around loose knots. Sizes and shapes of the 21 masks were manually chosen to include all pixels belonging to the loose knot sub-features, regardless of any misclassified pixels from other lumber features.

Figure 3.9 illustrates the masking/highlighting procedure to delineate the bark rings and gaps around the loose knots in 6 out of the 21 PC pair scatter plots. The masked pixels have been highlighted (as blue) and overlaid on the corresponding false color-composite score images of the 6 PC pairs. Binary images of the masked pixels have also been illustrated to determine the classification achieved.

It can be seen from the highlighted pixels in figure 3.9 that there is misclassification of various other lumber and knot features along with the correctly classified features of interest (i.e. bark rings and gaps surrounding the top three loose knots). Such confounding is present in all 21 PC pair scatter plots. This is expected since we have set the type I error to zero, thus ensuring that the resulting 21-dimensional mask captures all pixels belonging to the features of interest. It can be seen from the 7 PC score images in figure 3.8 that each PC captures unique spectral information of the various sub-features in the six knots. Furthermore, it can also be seen that different lumber features are confounded with various sub-features in the knots through the 7 PCs. If it can be assumed that in each of the 7 PCs different lumber features are confounded with the bark ring and gaps of the loose knots, then an intersection operation capturing common pixels in all 21 masks would result in a perfect delineation of these sub-features. However, if this assumption is violated the intersection operation would misclassify some feature pixels as non-features.

(a) (b) (c)

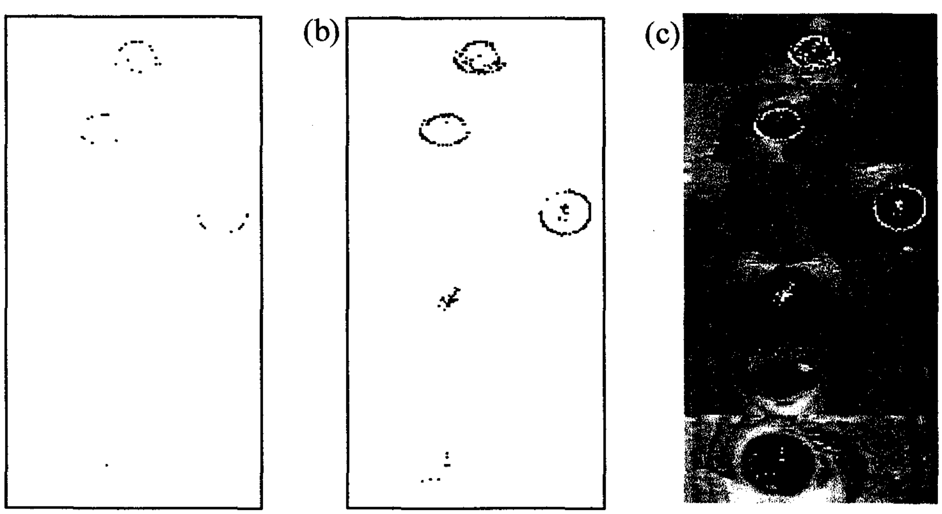

Figure 3.10 (a) Spatial locations of common pixels in 21 masks. (b) Spatial locations of common pixels in 18 out of 21 masks. (c) Overlay of common pixels from (b) on false color-composite score image of first three PCs

Figure 3.10(a) illustrates the spatial locations of the common pixels in all 21 masks in the MIA score space of the multi-spectral NIR knots image. It can be seen that the 21-dimensional mask captures some pixels from the bark rings and gaps of the three loose knots. However, due to the violation of the assumed confounding of features in the 7 PCs there is also some misclassification of feature pixels as non-features. Upon relaxing the tolerance of the intersection operation to capture common pixels in 18 out of the 21 masks it can be seen that the bark rings and gaps around the loose knots have been adequately captured. The binary image illustrating the spatial locations of the resulting feature pixels using the relaxed intersection operation is illustrated in figure 3.10(b). Finally, figure 3.10(c) overlays the highlighted knot sub-feature pixels on the false color-composite image of the first 3 PCs. It can be seen from this image that some pixels belonging to cracks in the firm knots in the bottom half of the image have also been classified as feature pixels. This classification is valid due to the fact that gaps surrounding the loose knots are in fact cracks, which have been modeled as feature pixels by the multi-dimensional mask.

The results obtained from the example study presented in this section illustrate that with MIA and a multi-dimensional masking strategy it is possible to resolve spectrally complex features from high-dimensional multi-spectral images.

3.3.3 Comparing MIA on RGB and NIR Lumber Images

Before concluding the section on off-line MIA of softwood lumber, a brief comparison of the extracted feature information from RGB and NIR multi-spectral lumber images is presented below.

Most wavelengths of the NIR imaging spectrometer could not distinguish between some lumber components within knots and surrounding clear wood as these features had common chemical information between them. On the other hand, the RGB camera could easily distinguish knots from clear wood. MIA of RGB lumber images could extract knots and splits from clear wood using only 2 PCs, whereas MIA of multi-spectral NIR lumber images revealed complex structures within knots which took up to 5 or 7 PCs to fully explain. Using MIA of RGB lumber images is adequate if one is simply interested in being able to separate out a knot as a whole entity from clear wood (without any distinction of the type of knot). As far as normal lumber grading is concerned this level of detail might be adequate. In that case RGB imaging has an advantage over multi-spectral NIR imaging. Another advantage of RGB imaging is a smaller amount of data handling (3-variables) as compared to multi-spectral NIR imaging (up to 128 variables).

However, if one were really interested in scanning wood and looking at diagnosing different types of knots and analyzing those sub-features within knots that make them different from each other (e.g. bark rings and gaps around the circumference of loose knots, or presence of certain types woods in decayed knots), then the resolution achieved by NIR multi-spectral imaging would allow such an analysis. Conversely, the level of detail extracted by RGB cameras is not enough to perform such an analysis. Furthermore, NIR multi-spectral imaging also has the advantage of being able to distinguish between lumber defects like knots and splits due to differences in their chemical signatures. This of course, could not be achieved in MIA of RGB lumber images due to similar color (contrast) between these defects. Thus, if a detailed off-line MIA of softwood lumber defects is the main goal then NIR multi-spectral imaging proves to be much more advantageous than RGB imaging.

3.4 Monitoring Defects Through MIA for On-line Softwood Lumber Grading

As mentioned before several vision-based softwood lumber grading schemes have previously been proposed in the literature. Most of these approaches aim to isolate lumber defects from clear wood using various segmentation routines based on pixel intensity, color contrast, or shape measures in grayscale or color images of lumber boards. Off-line analysis of lumber defects based on their spectral signatures in the RGB color and NIR spectrum has been illustrated in the previous section.

This section, the main thrust of the chapter, proposes a novel lumber grading approach using an on-line extension of MIA modeling techniques on RGB color images of lumber boards. Common lumber defects are modeled in the score spaces of MIA, and the developed model is then used to detect these defects from various lumber boards in real-time. The proposed monitoring scheme is directly applicable to the lumber grading industry for detecting lumber defects based on their color spectral information. The scheme is developed for on-line situations where the vision-based system could be used to assist human graders.

Although the MIA model has been developed using lumber samples from two lumber species (Balsam Fir, and White Spruce), it is robust enough to correctly capture the modeled lumber defects from all three species used in the study (i.e. also from Jack Pine). A priori knowledge of the lumber species is typically available to lumber graders in sawmills. As a result, individual MIA models for specific lumber species could also be developed, and a switch to the appropriate model could be easily made when the lumber species are changed at the sawmill.

3.4.1 Monitoring Lumber Defects in True Color RGB Images

Feature pixel monitoring from a sequence of time-varying multivariate images was proposed by Bharati et. al. [1998] using an on-line extension of MIA techniques. The main concepts of the approach are used to monitor lumber defects from RGB color images of 38 lumber samples.

The primary ideas of the proposed approach are as follows. A multi-way PCA model is built off-line on a training or calibration image, which contains all typical features that one might be interested in detecting using the on-line monitoring scheme. This training image may be a single image, which contains all such features of interest, or it may be a composite image put together from sections selected out of many different images. From the off-line MIA of the training image, masks are developed in the score space, which correspond to those features that one desires to monitor. Upon applying the training image MPCA model to the new test images ($\underline{\mathbf{X}}_{test}$ unfolded to $\mathbf{X}_{test}$), values of the scores are computed for the dominant principal components $\mathbf{t}_{a(test)}$ (equation 2.4) using the corresponding MPCA loading vectors of the training image $\mathbf{p}_{a(tr)}$. The point clusters in the score space scatter plot can then be updated using the calculated PC scores of the new image. By monitoring the changing score point cluster intensities (pixel densities) under each mask area in the score plot one can then track the appearance and disappearance of the modeled features in the new images. Upper tolerance limits can be set on the pixel densities in each mask area. These limits might be chosen simply on a subjective basis, or, as in Statistical Process Control (SPC) charts, on the underlying statistical distribution of pixel densities when the process is subject only to common cause variation. Upon discovering violation of the tolerance limits for any feature being monitored, one can investigate further by switching to the image space to reveal the spatial pixel locations of the modeled feature.

To build a good training model it is extremely important to select a training image that contains representative samples of all the features that need to be monitored in the new images. In the case of lumber grading the features of interest to be monitored from various lumber board samples are typical defects like knots, splits, wanes, pitch pockets, and bark pockets. A good representative training image must contain ample pixels from all of these features of interest. Furthermore, in order to make the MIA model robust, the training image should also contain typical lumber variations like color contrast and texture differences between samples. Figure 3.11 illustrates the training image used for the lumber-grading study. It is a 712 × 345 × 3 RGB image created from a composite of various defects in different sections of 6 lumber sample images. Besides containing all lumber defects to be monitored, the composite image also captures typical color contrast and texture variations through the lumber sample data used in the study.

MPCA decomposition of the 3-variable RGB training image was performed using the strategy illustrated in section 2.3.1. Two significant PCs were extracted, which

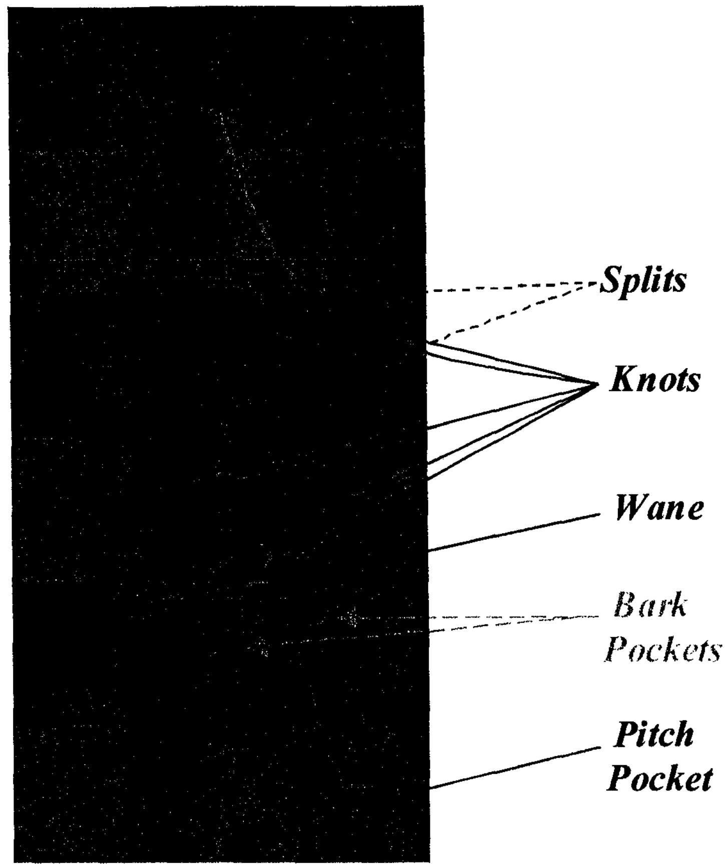

Figure 3.11 Composite lumber image used to train MIA model for on-line lumber grading

cumulatively explained 99.988% of the total sum of squares in the training image. The corresponding loading vectors for the dominant PCs were: $\mathbf{p}_{1(tr)}^T$ = [0.723 0.583 0.370]; $\mathbf{p}_{2(tr)}^T$ = [-0.573 0.207 0.793]. The off-line MIA training model was calibrated through customized local area masking of point clusters in the score plot of the two dominant PCs ($\mathbf{t}_{1(tr)}$ vs. $\mathbf{t}_{2(tr)}$), and highlighting the masked pixels in the corresponding false color-composite of the three PC score images $\mathbf{T}_{1(tr)}$ to $\mathbf{T}_{3(tr)}$. The sizes and shapes of these masks were determined by using the previously discussed (section 2.3.1) iterative procedure of feature extraction from multivariate images. Figure 3.12(a) illustrates the $\mathbf{t}_{1(tr)} - \mathbf{t}_{2(tr)}$ score plot of the training image with blue and green polygon masks covering point clusters of pixels from various lumber defects. The spatial locations of the masked pixels have been highlighted (with appropriate colors) in the false color-composite PC score image illustrated in figure 3.12(b).

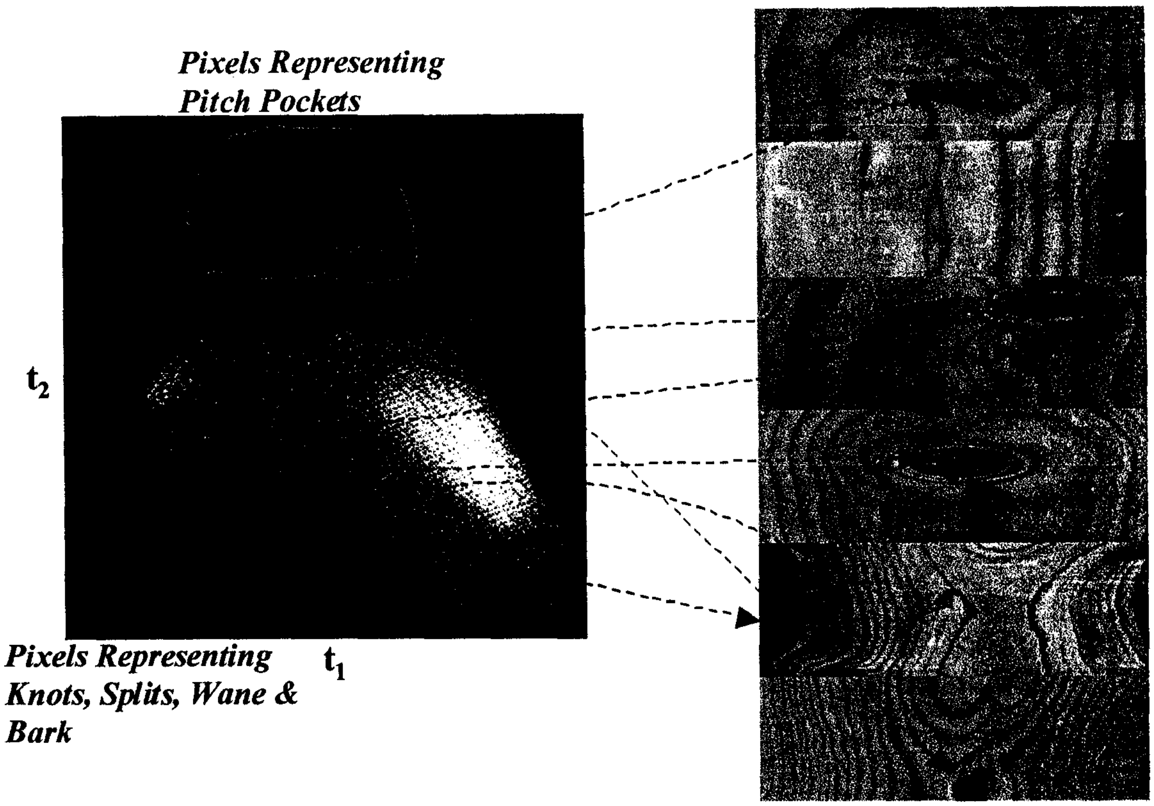

Figure 3.12 (a) $\mathbf{t}_{1(tr)} - \mathbf{t}_{2(tr)}$ score plot of the lumber training image with blue and green polygon masks capturing lumber defect pixels. (b) False color-composite of PC scores of the lumber training image with highlighted lumber defect pixels modeled in (a)

Using the two customized local area masks in figure 3.12(a), along with the two MPCA loading vectors $\mathbf{p}_{1(tr)}$ and $\mathbf{p}_{2(tr)}$ the calibration of the off-line MIA training model was complete. The training model could then be used to monitor the modeled lumber defects from RGB images of the 38 softwood lumber samples used in this study. Each of the (712 × 345 × 3 pixel) RGB images of the 38 lumber samples $\underline{\mathbf{X}}_{test}$ was decomposed into its score space with the help of the MIA training model. The lumber sample image was rearranged into a 245,640 × 3 element two-way array $\mathbf{X}_{test}$ and multiplied with the training image loading vectors $\mathbf{p}_{1(tr)}$ and $\mathbf{p}_{2(tr)}$ to produce the corresponding score vectors $\mathbf{t}_{1(test)}$ and $\mathbf{t}_{2(test)}$. These new score vectors were then scatter plotted against each other as score plots and folded back into score images. As a result of the decomposition, 38 $\mathbf{t}_{1(test)}$ - $\mathbf{t}_{2(test)}$ score plots can be plotted. Figure 3.13 illustrates $\mathbf{t}_{1(test)}$ - $\mathbf{t}_{2(test)}$ score plots of 6 (out of 38) test images.

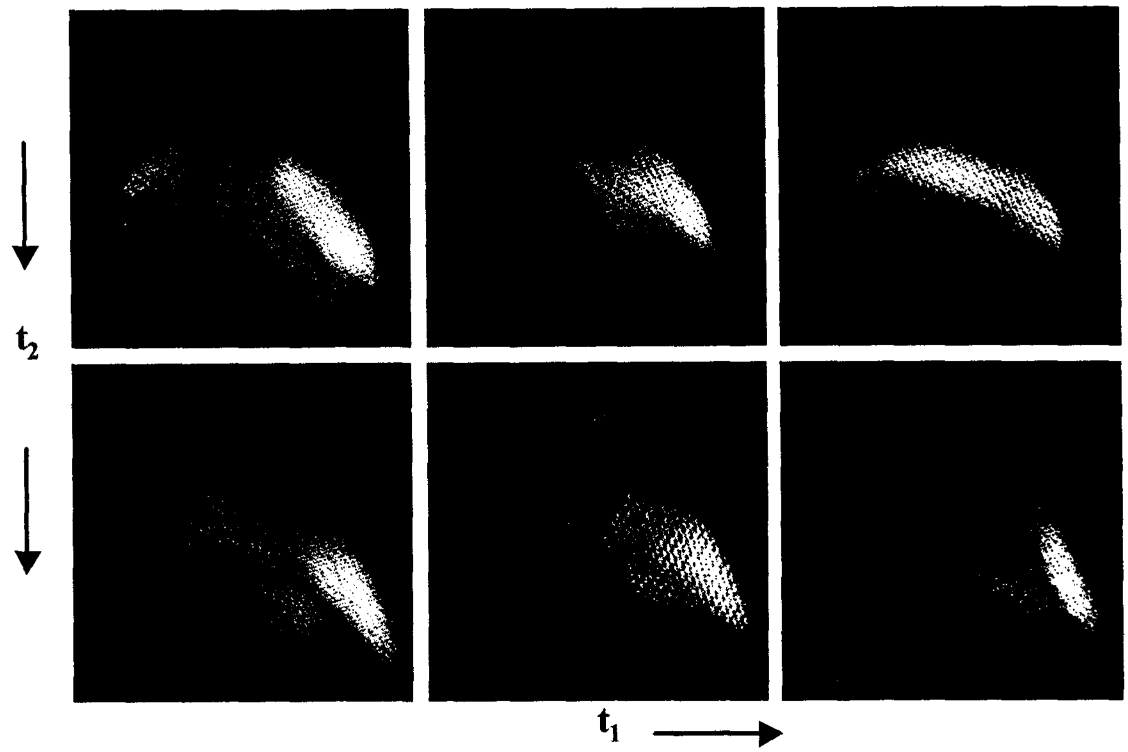

Figure 3.13 $\mathbf{t}_{1(test)}$ - $\mathbf{t}_{2(test)}$ score plots of RGB images from 6 lumber sample images out of lumber dataset

Upon observing the 6 scatter plots one can see that there is considerable shifting of the bright score point cluster at the bottom right of each plot. From the previously shown MIA example on the RGB lumber image (section 2.3.1) we know a priori that score points in this cluster correspond to clear wood pixels. As mentioned before there is considerable color and contrast variations in softwood lumber not only between different species but also within the same tree. Since the dataset used in this study spans 3 different softwood lumber species such variations in clear wood are expected. The composite training image (figure 3.11) was constructed with these variations in mind. As far as MIA for lumber grading is concerned pixels belonging to clear wood are background features, which are of no interest (or consequence) to the analysis. Minor color contrast variations in clear wood do not matter to MIA as long as the color contrasts of the lumber feature pixels (i.e. defects) are consistent. However, if the variations are severe this could lead to faulty results as score points from background features would overlap into the masks of the lumber defects, thus causing false alarms.

Although this issue did not severely affect the results in the current lumber grading study, it is worth addressing this problem due to its universal nature. Such problems could potentially occur in other applications of MIA for on-line monitoring where uninteresting variability in background pixels may interfere with feature pixel delineation in the score space scatter plots. Appendix A discusses the various approaches one could use to align the PC score plots of test images with that of the training image.

As mentioned before (section 2.3.1) PC score plots are color-coded representations of 2-dimensional histograms of the score vectors. The score plot alignment strategy used in this lumber-grading study is to match the means of the 38 lumber image 2-D histograms with that of the training image. Performing the histogram mean matching in the PC score plots of the lumber images results in a change in their average color contrasts to match that of the training image. Since the score point cluster belonging to clear wood represents the majority of the pixels in each lumber image it is evident that a shift of the PC scatter plots would mostly affect the pixel contrast of clear wood features. As a result, aligning the PC score plots of the test lumber images results in standardizing the average color contrasts of the different types of lumber samples used in the dataset. Results of the achieved alignment of the PC score plots in the lumber dataset have been further explained and illustrated in Appendix A.

Using the MIA training model masks on the aligned PC score plots of the 38 lumber images it was possible to objectively monitor the pixels belonging to typical lumber defects like knots, splits, wane, pitch and bark pockets. The proposed monitoring scheme uses the power of MIA to break the spatial dependence of the modeled pixels from lumber sample images and transforms them into specific regions of the updating score plots based on their color spectra. Pixel densities of the score point clusters under

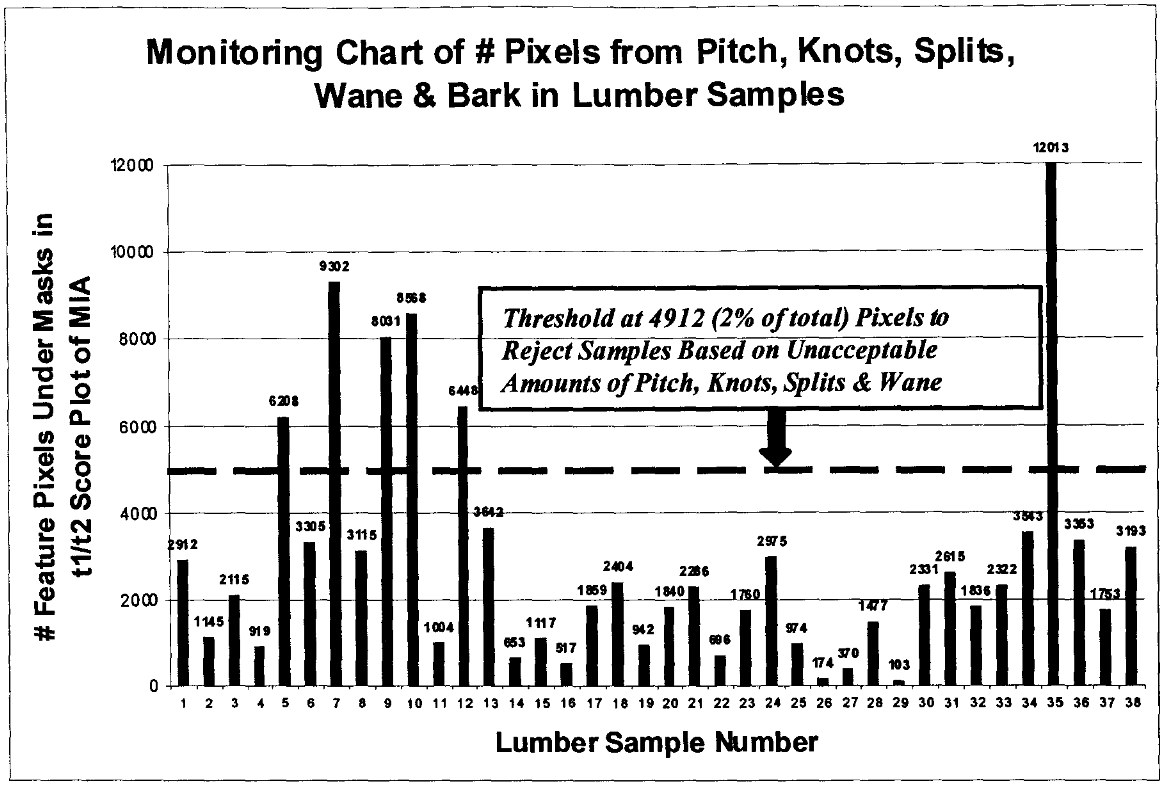

Figure 3.14 Control chart of total number of pixels belonging to modeled lumber defects in 38 lumber sample images. An arbitrary tolerance limit has been set to determine model rejection

the two masks were monitored by enumerating the exact number of pixels falling in the regions of the masks for each of the 38 lumber samples.

As far as automatic lumber grading is concerned a simple control chart could be used to record and illustrate the total number of pixels belonging to the masked feature pixels from typical lumber defects in each lumber sample. Based on process understanding and previous experience tolerance limits could be set in the control chart to accept or reject a sample for a particular grade. Figure 3.14 illustrates a control chart with the total number of pixels captured by both masks in the PC score plots of the 38 lumber samples in the dataset. Control charts with a count of lumber defects captured by each individual mask can also be plotted to determine whether the lumber defects were pitch pockets or the darker contrast defects (knots, splits, wanes, bark pockets). In this case a common control chart measuring all modeled defects has been used since the grading decision is not concerned with the types of defects. The height of each bar in the chart represents a total count of pixels from all modeled lumber defects in a lumber sample image. As an example, a tolerance limit has been set at 4912 pixels (2% of total pixels in each lumber image) to reject a lumber sample based on an unacceptable amount of defects.

Using the above-mentioned monitoring scheme the need to look at each lumber sample for grading is minimized to only the model rejects. All monitoring can be performed by counting the total pixels in the masked regions of the updating PC score plots as each lumber sample passes under the RGB line scan camera. If one is interested in determining the exact spatial locations of the modeled defect pixels, the masked PC score points can be highlighted in the corresponding PC score images. Using these highlighted lumber images one can then determine the types and spatial distributions of the various lumber defects on the sample. Furthermore, the adequacy of the MIA model can also be intermittently checked using such highlighted images to visually determine misclassification of the modeled defects. Figure 3.15 illustrates the PC score plots and corresponding false color-composite PC score images of 4 lumber samples from the dataset used in this study.

It can be seen from the control chart and highlighted PC score images of the lumber samples that the proposed MIA monitoring scheme can efficiently capture typical defects from RGB color images of lumber boards. Such a monitoring scheme can be used in a sawmill for pre-grading lumber samples upstream of human graders in order to screen the obvious rejects, which could be further analyzed to determine the amount of downgrading required. The monitoring scheme provides the grader with a simple interface, where the need to look at images is greatly reduced. All monitoring is performed in the updating score plots and the corresponding control chart. Prior to visual grading of the model rejects, the highlighted defect pixels in the corresponding lumber image could further assists the graders in their eventual grading decision.

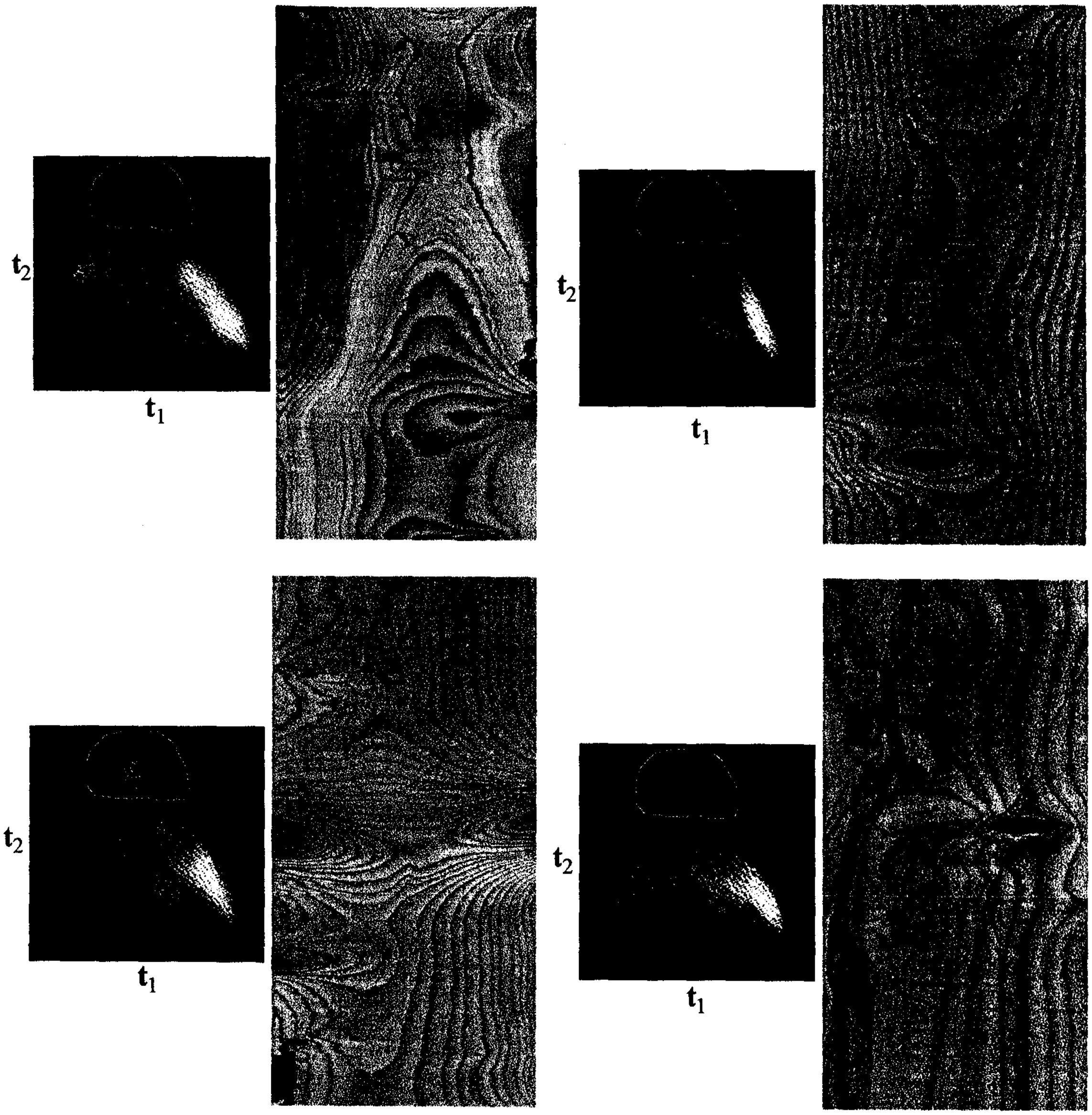

Figure 3.15 Highlighting lumber defects in $\mathbf{t}_1 - \mathbf{t}_2$ score plots and false color-composite PC score images of 4 lumber samples

3.4.2 Monitoring Lumber Defects in NIR Multi-spectral Images

Typical sawmills produce lumber boards at very high speeds, which puts a demanding requirement on the lumber graders for fast decisions in assessing the quality of every piece. The same demand would be placed on a vision-based lumber scanning system, which would be used to grade every piece of lumber at production speeds. As mentioned in chapter 2 (section 2.1) several industrial vision-based systems have been realized with high-speed imaging sensors that can handle the speed requirements of a typical sawmill. The RGB line-scan camera used to image the lumber boards in this thesis is a perfect example of such an imaging sensor. Unfortunately, the technology behind NIR imaging spectroscopy is still in its infant stages. Most of today's NIR digital cameras do not possess the ability to match the image acquisition speeds of high-speed RGB and grayscale cameras. This shortcoming makes lumber defect monitoring infeasible using current NIR imaging technology.

The existent image acquisition speed gap between current NIR imaging sensors and RGB and grayscale cameras may be eliminated in the future with the advent of newer and faster NIR imaging technology. Upon fulfillment of the speed requirements NIR imaging spectroscopy could be a very effective way of lumber grading. The framework and methodology of the monitoring scheme would be exactly the same as that illustrated with RGB color lumber images in section 3.4.1. Similar monitoring and control charts could be used for various lumber feature pixels based on their chemical information. It has already been illustrated in section 3.3.2 that multi-spectral NIR images are capable of resolving lumber features at a much finer resolution as compared to RGB images (e.g. details on knots, differentiating between different types of knots, resolving differences between knots and splits etc.). Thus, one could ideally monitor lumber features at a much finer resolution using NIR imaging spectroscopy in the sawmill. The only difference in such a monitoring scheme would be in the spectral dimension of the multivariate images (e.g. the NIR imaging spectrometer used in this thesis can capture images in up to128 wavelengths, as opposed to 3 color channels captured by RGB cameras).

3.5 Modeling Lumber Defects Through Multivariate Image Regression

This section is intended to be a discussion of some issues that are concerned with feature modeling through MIR techniques. As previously stated (section 2.3.2) the basic idea of MIR is to build an empirical model between two sets of (typically multivariate) image data. The image regression modeling technique of concern in this section is the application of a pixel-wise classification approach using Discriminant PLS (PLS-DA) modeling to isolate features (pixels) of interest from background information in a multivariate image.

Traditionally PLS-DA models have been used as one of the many techniques to classify multivariate data in the pattern recognition literature [Wold et. al., 1984; Sjöström et. al., 1986; Eriksson et. al., 1999]. In MIR these models are used for pixel-wise classification of features from a new multivariate image into pre-defined classes. The general concept of using PLS-DA to classify multivariate image data has been discussed in section 2.3.1, and is illustrated in figure 3.16. A 'dummy' response variable Y binary image is used to provide a priori knowledge of the class belonging of every feature pixel in the multivariate image $\underline{\mathbf{X}}$. The PLS-DA model is *trained* to develop an empirical relation between the two images, such that it can later be used to calculate predictions of $\hat{\mathbf{Y}}$ from new $\underline{\mathbf{X}}$ multivariate images. Based on the provided class-memberships in the training stage the PLS-DA model tries to maximally separate the intensities of member and non-member pixels in a new multivariate image $\underline{\mathbf{X}}_{new}$. The adequacy of the PLS-DA model can be visually determined upon observing the predicted response variable $\hat{\mathbf{Y}}$ as a grayscale image, where typically brighter pixels (intensity near 1) represent modeled features.

Hagman [1996] illustrated one of the first applications of a PLS-DA based MIR modeling approach in the field of softwood lumber grading. The proposed approach,

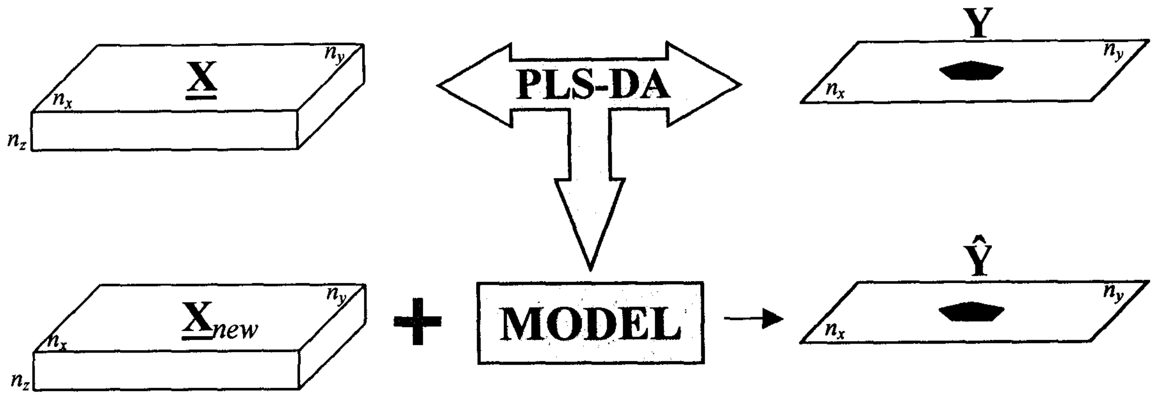

Figure 3.16 PLS-DA based MIR between a multivariate image $\underline{\mathbf{X}}$ and a binary class-membership image **Y**. The class-membership in **Y** is given for each pixel as 1 (member) or 0 (non-member)

termed Multivariate Image Projections to Latent Structures (MIPLS), was used to *individually* model typical lumber features like knots, pitch, clear wood, compression wood, different types of rot etc. The basic methodology of the proposed MIPLS approach is as follows. First, MPCA decomposition of a multivariate lumber image $\underline{\mathbf{X}}$ is carried out to produce PC score plots and images, which are interrogated via MIA masking/highlighting to delineate the lumber feature of interest. The highlighted feature pixels are thresholded to give a binary dummy image (**Y**). Second, a PLS-DA model (using the kernel-PLS algorithm [Lindgren et. al., 1993]) is built to relate the feature pixels in $\underline{\mathbf{X}}$ with **Y**. The model is built using a representative training dataset, which is extracted via sub-sampling pixels from various regions of $\underline{\mathbf{X}}$ and corresponding pixel locations in **Y**. Finally, the PLS-DA model coefficients are used on the entire lumber sample image to create a predicted response $\hat{\mathbf{Y}}$, which is scaled to a grayscale image representation for visualization, and thresholded to segment the modeled feature pixels. An error image ($\mathbf{E} = \mathbf{Y} - \hat{\mathbf{Y}}_{Threshold}$) is calculated to (visually and objectively) determine the feature information not modeled.

Separate MIPLS models were built by Hagman [1996] to classify each individual lumber feature on images of single lumber boards and composite images of multiple pieces. Once trained the classification models performed reasonably well to predict spatial locations of several lumber features (e.g. knots, clear wood etc.) without much misclassification. However, there were certain lumber features (e.g. compression wood) that did not classify satisfactorily in many of the MIPLS models.

It has been well documented in the literature [Geladi et. al., 1986; Höskuldsson, 1988; Martens et. al., 1989; Burnham et. al., 1996; Eriksson, 1999] that PLS methods decompose multivariate data into a reduced dimensional subspace based on a different objective than PCA. PLS aims to explain the variation in both the **X** and **Y** multivariate data blocks, and at the same time improve the relation between the two. This results in PLS components of the **X**-block being projected in a different plane as compared to projections of its PCA components. The amount of rotation, tilting, or shifting of the PLS components (as compared to PCA) is dependent on the information in the **Y** data block. Similar trends have also recently been reported by Lied et. al. [2000] in an application of PLS methods in MIR. Upon providing class-membership information of each pixel as binary **Y** images PLS-DA models of a multivariate image $\underline{\mathbf{X}}$ project its PCs in a plane, which maximally separates the pixels into one of two classes. This in turn results in a new PC score plot to find the direction of greatest discrimination between the score cluster of the feature pixels from background scores. However, one must meet some basic requirements in order to achieve good classification using PLS-DA models.

A fundamental condition that must be satisfied when using PLS-DA models for classification is that the classes must be "tight" and occupy a small and separate volume in the space defined by the variables of **X**. Several researchers [Sjöström et. al., 1986; Eriksson et. al., 1999] have pointed out this requirement of PLS-DA models in pattern recognition. The same condition must be satisfied in order to classify feature pixels using PLS-DA models in MIR. This indicates that the selection of the feature pixel class in the binary **Y** image should be such that the resulting score points of the feature are tightly clustered and separated in the PLS score plots. In doing so, one ensures that the selected class is "homogeneous" within itself. One cannot select pixels from parts of a homogeneous class and try to discriminate them from rest of the pixels in a multivariate image. Another issue concerned with MIR of feature pixels using PLS-DA model based classification is that even if the classes are "tightly" clustered and well separated in the PLS score plots a PLS-DA model with a *single* **Y** binary image (i.e. a PLS1-DA model) might not be adequate. In such cases better classification would be achieved using a PLS-DA model with *multiple* **Y** binary images (i.e. a PLS2-DA model). Each **Y** image in such a model would highlight pixel locations of a unique feature to be classified.

The MIPLS models developed by Hagman [1996] provided good classification of those lumber features where the above conditions were satisfied. However, those lumber features exhibiting loose score clusters due to a lack of homogeneity and similarity with other features did not classify well. It was noticed that the MIPLS models misclassified compression wood with knots and clear wood. It was later illustrated that compression wood is an integral part of both features [Hagman, 1997]. Thus it was not possible to separately model compression wood pixels present only in knots or in clear wood since it resulted in an inhomogeneous class definition in the **Y** binary image used to train the MIPLS model.

Similar misclassification issues have also been reported in other literature where separate PLS1-DA models were used to individually classify three different types of vegetables (maize, peas, and carrots) in a multivariate image [Lied, 2000]. Two of the three models produced good classification results due to tight clustering and separation of the modeled feature pixels in the PLS score plots. However, the third PLS1-DA model resulted in misclassifications due to inseparable score clusters of the three vegetables in its PLS score plot.

Appendix B presents an example study, which illustrates the importance of meeting the above-mentioned requirements when using PLS-DA models in MIR. Separate PLS1-DA models are used to classify two types of features from RGB images of lumber boards. Furthermore, a conceptual example is shown where a PLS1-DA model would be inadequate even if the feature classes are tightly clustered in the PLS score plot. Classification achieved using a PLS2-DA model is better in such situations. The examples show that good feature classification is achieved only when the above-mentioned conditions have been satisfied.

The discussion of PLS-DA models in this section has been concerned with their use as classifiers of individual pixels in an image. In section 5.4.3 of this thesis another application of PLS-DA has been shown where such models have been used to classify whole images of steel based on certain pre-define criteria.

3.6 Conclusions and Contributions

This chapter has developed an extension of (previously off-line) MIA techniques to monitor time changing images from on-line cameras, and illustrated their application in a real industrial process-monitoring situation for lumber defect detection in the softwood lumber industry. The technique provides both qualitative and quantitative results that can be used for automatically assigning quality grades to lumber boards at production speeds.

The proposed technique captures more than 85% of the common defects that a typical human lumber grader encounters in the sawmill. It can potentially be used on-line to pre-screen lumber from various species based on defects that are dependent on color and contrast (e.g. knots, splits, wane, bark, pitch etc.) through vision-based systems using high speed RGB imaging sensors. A lesser burden would thus be placed on the human graders who could then concentrate on detecting more difficult defects in the pre-screened lumber boards. In ensuring a robust on-line MIA model that can adequately capture lumber defects from multiple lumber species exhibiting high variability in their background feature colors and contrasts, a score space alignment strategy has been proposed. The proposed strategy is one of many possible alignment techniques, which can be further refined based the requirements of the application under study.

The chapter also presents an exploratory study of analyzing complex lumber features like knots using NIR imaging spectroscopy with off-line MIA techniques. The study illustrates the power of NIR imaging spectroscopy to resolve such complex lumber features into a combination of sub-features at a finer level based on differences in their chemical structures. A multi-dimensional MIA masking strategy has been developed to fully capture such complex features, which are typically explained by multiple PCs spanning a higher number of components than the standard two dimensional masks used in typical PC pair score scatter plots. A working example has been presented to isolate bark rings of a loose knot upon pooling the information from 2-dimensional score masks in multiple PC pairs.

Advantages and shortcomings of NIR multi-spectral imaging as compared to RGB imaging have been discussed for purposes of lumber grading. Previously, no studies had been conducted on lumber in the wavelength spectrum of the NIR digital camera used in this chapter. The study highlights those lumber defects that can and cannot be detected with RGB and NIR imaging sensors. Such information could be of great value to the softwood lumber industry when deciding to purchase imaging scanners for automatic lumber grading in the sawmill. A framework has been laid out for monitoring lumber defects based on chemical information if one used the proposed on-line MIA scheme with NIR imaging spectrometers.

Finally, the chapter highlights some basic requirements that must be satisfied in order to adequately isolate features of interest from background features in multivariate images when using PLS-DA models in MIR. Although these conditions have been widely recognized in the pattern recognition literature no study has so far been conducted to highlight the impact of these issues with pixel-wise classification of features in multivariate images using PLS-DA models in a Multivariate Image Regression scheme.

Chapter 4

Multivariate Image Analysis and Regression Modeling of Pulp and Paper Characteristics

Multivariate Image Regression techniques have been previously discussed in chapters 2 and 3, where both the predictor and response variables were images. This chapter introduces a novel MIR modeling technique that is ideal for industrial process monitoring situations, where feature information from multivariate process images of a product can be modeled with its *non-image* quality data. Such models can then be used on-line with new process images to infer product quality.

The work is entirely concerned with image based modeling of finished product samples, and using the developed models to predict certain properties that are deemed to be critical indicators of product quality. This chapter is intended to be a feasibility study of the proposed methods in the pulp and paper manufacturing sectors of the forest products industry.

4.1 Introduction

Pulp and paper are forest products made from wood fibers, which go through a series of chemical and mechanical treatments in order to reach their final state. The forest products industry largely manufactures pulp and paper as intermediate products, are supplied to other manufacturing industries for further refinement into various end use products. Some typical end use products that require pulp and paper as raw materials are various types of plastics, rayon, pharmaceuticals, food additives, finished papers ranging from newsprint to high quality colonial bond paper upon which this thesis has been printed. To serve such a broad range of applications a typical mill usually produces pulp and paper in a variety of grades, with each grade having its own end use properties.

Adhering to the unique specifications laid-out by the end use product manufacturers is of the utmost importance to the forest products industry. As a result, pulp and paper manufacturers perform various tests at every stage of the process to ensure exact specifications are met. Furthermore, to gain customer satisfaction a large number of complicated quality control tests are also performed on the finished products to ensure that the expected pulp and paper quality is being maintained for every manufactured grade.

The majority of the quality control tests on finished pulp and paper are preformed in analytical laboratories, where complicated wet-chemistry procedures are employed to determine the product's chemical properties. Some of these tests are time-consuming and require constant attention from technicians. Such stringent demands some times induce undesirable experimental errors, which reflect on the perceived quality of the finished product. Most wet-chemistry tests are naturally destructive to the solid pulp and paper samples since they require dissolving the sample into alkaline or acidic solutions prior to analysis. As a result, multiple samples are required to obtain a complete chemical property analysis of the finished pulp and paper products.

To overcome the above-mentioned issues with wet-chemistry analytical procedures the forest products industry is aggressively exploring new technologies for quality control of finished pulp and paper samples. Ideally such technology should enable rapid testing of the samples, and simultaneously provide multiple chemical properties from a single sample in a non-destructive manner.

After observing the success of Near-Infrared (NIR) spectroscopy used with chemometric methods like PCA and PLS to characterize samples in the pharmaceutical, food and chemical industries many pulp and paper manufacturing companies are starting to invest a large amount of money in this technology for quality analysis of their products. What makes NIR spectroscopy attractive is its ability to characterize solid, semi-solid, liquid and vapor samples without the need for any special sample preparation [Wold et. al., 1998]. This technology provides both flexibility and speed to help achieve the goals of rapidly analyzing finished pulp and paper samples in a non-destructive manner. Over the past decade these techniques have become quite popular in the pulp and paper manufacturing sectors of the forest products industry.

Several applications of NIR spectroscopy in the pulp and paper industry have recently emerged in the literature. Birkett et. al. [1988] and Antti et. al. [2000] illustrated the ability of NIR spectroscopy, along with chemometric methods, to predict kappa number in pulp. Several other applications that attempt to predict pulp yield and cellulose content using these techniques have also been published [Shultz et. al., 1990; Wright et. al., 1990; Woitkovich et. al., 1994]. Easty et. al. [1990] illustrated the power of NIR spectroscopy to measure hardwood content in a bleached hardwood-softwood pulp blend, and measured lignin content of unbleached pulp. The ability to characterize pulp and paper properties using NIR spectroscopy with chemometrics methods has been illustrated through several application examples, some of which are provided in the following references [Wallbäcks et. al., 1991 and 1995; Antti et. al., 1996; Champagne et. al., 2001].

The work presented in this chapter contributes to the field of NIR spectroscopic analysis of pulp and paper through an investigative study of using NIR imaging spectroscopy with MIA techniques to extract chemical information from multi-spectral images of finished pulp and paper samples. It is first illustrated through a paper classification example that such information can be used to characterize pulp and paper upon imaging the finished samples using a NIR imaging spectrometer.

A novel PLS based MIR technique is then developed, which regresses the extracted feature information from multi-spectral NIR images of finished pulp samples with their chemical property variables. The pulp property data has been obtained via measurements in the quality control laboratory of a pulp mill using wet-chemistry analytical techniques. Development of the MIR models forms the main contribution of this chapter. These models are then used with new process NIR multi-spectral pulp images to monitor pulp quality without the need for tedious wet-chemistry analysis. These models are also used to investigate spatial variations of pulp properties across the imaged section of the sample through a proposed sub-windowing technique.

The chapter is organized as follows. First, a description of NIR spectroscopy in pulp and paper industries is provided, which focuses on comparing traditional (single point probe-based) and recently emerging (image-based) NIR spectrometers for pulp and paper analysis. Second, a brief paper classification study illustrates the potentials of NIR multi-spectral imaging and MIA to extract relevant feature information from finished paper samples. The same strategy has then been used to extract feature information from multi-spectral NIR images of finished pulp samples. The extracted information MIR models are then used for predicting and monitoring pulp quality from an industrial process through various grades. Finally, a framework is presented for investigating pulp heterogeneity through inferring the spatial distribution of its properties across the imaged section of a pulp sample.

4.2 Near-Infrared Spectroscopy in Pulp and Paper Industry

The basic principle of a NIR spectrometer is to shine incident light on a sample and measure the reflected (or transmitted) light at different NIR wavelengths. Traditionally, NIR spectrometers have consisted of a fiber-optic probe detector made from special crystals like Indium-Gallium-Arsenide (InGaAs), Germanium (Ge), Indium-Arsenide (InAs) etc. [Buchanan et. al., 2000]. This detector is highly sensitive and provides precise NIR measurements after averaging many scans over a local region of the sample being tested. The measurement is performed at a particular point on a solid (or semi-solid) sample, or in an encased chamber (e.g. test tube) for a liquid (or gaseous) sample. Traditional (probe-based) NIR spectroscopy has been applied in many industries for over four decades. This technology has been well researched and documented in the literature [Whetsel, 1968; Stark et. al., 1986; Burns et. al., 1992]. Some of today's advanced and sophisticated (probe-based) spectrometers (e.g. FOSS NIRSystems <http://www.foss-nirsystems.com> as of May 19, 2002) can acquire light reflectance readings in the full NIR wavelength spectrum (700 nm to 2500 nm) with very little reduction in quantum efficiency (i.e. signal-to-noise ratio) throughout the spectral range.

NIR spectrometers have to be properly calibrated against samples of known chemical composition, since spectra from these instruments are essentially non-specific with broad overlapping peaks of different constituents. As mentioned before chemometric methods like PCA and PLS have been widely used to extract relevant chemical information from highly correlated digitized spectra of today's NIR spectrometers connected to high-speed computers [Martens et. al., 1989; Hildrum et. al., 1992; Beebe et. al., 1998]. All previously mentioned NIR spectroscopy applications in the pulp and paper industry (section 4.1) have used traditional probe-based instruments.

One of the shortcomings of probe-based NIR spectrometers is their inability to provide simultaneous multiple point readings across solid samples. Such information could be vital to determine the homogeneity of the sample based on the spatial distribution of its chemical information across a certain area. If required, one can perform some pre-processing to bring the solid sample in liquid or gaseous form prior to performing NIR measurement to produce an overall spectral reading. However, if this were not possible the NIR probe would have to be manually placed at multiple locations across the solid sample to gather such spatial homogeneity information.

Lately, this issue has been addressed with the introduction of NIR imaging spectrometers. These instruments work on the same principle as their traditional counterparts except for their detector, which in this case is a NIR digital camera. The basic functionality of NIR imaging spectroscopy has been previously described in chapters 2 and 3 (sections 2.1.2.3 & 3.2.2) of this thesis. NIR imaging spectrometers acquire multi-spectral digital images of solid (or heterogeneous) samples, thus producing a 2-dimensional grid of digitized NIR reflectance spectra at multiple spatial locations across the scanned sections of the samples. This is equivalent to multiple NIR probe-detectors spread across the surface of a solid sample. This technology also enables acquiring measurements without destruction of the sample, thus allowing further analysis of the sample after imaging.

Because this technology is still developing, the spectral range covered by most NIR imaging spectrometers is limited as compared to that of traditional probe-based instruments. As a result, if one were to consider each pixel of the acquired multi-spectral NIR image as a single point sensor its NIR reflectance reading would be less sensitive in resolution than that obtained through a probe-based instrument at the same point of the sample. However, the tradeoff for instantly having simultaneous multiple point measurements in a non-invasive manner makes NIR imaging spectroscopy a viable alternative to traditional probe-based instruments.

The probe-based detectors produce a NIR reading upon taking multiple scans at a particular spatial point and averaging them. On the other hand, the imaging spectrometer used in this thesis functions as a line-scan multi-spectral camera, which instantly captures the digitized NIR reflectance spectrum of each spatial point along a line perpendicular to the moving sample. The resulting 3-dimensional multi-spectral NIR image is obtained upon joining multiple scanned lines. As a result, the NIR spectra at any spatial location across the imaged section are not averaged.

It has been previously pointed out (section 3.4.2) that today's NIR cameras do not possess the acquisition speeds required for on-line imaging of fast moving samples like pulp and paper sheets on a process web in an industrial scale machine. However, one could conceptually use NIR multi-spectral cameras on-line to sub-image the pulp or paper sheets upon acquiring intermittent lines across the moving web. Similarly it can be argued that traditional probe-based NIR spectrometers could also conceptually be used for on-line monitoring of pulp and paper processes. A NIR probe can be fixed at a specific location across the process web, thus producing a reading along a line in the web direction as the pulp or paper sheet moves. Since probe-based spectrometers normally acquire multiple scans and average them to produce a reading, the resulting NIR spectrum would be an average of many scans over the linear section of the pulp or paper sheet along the web direction.

Using an on-line NIR probe detector for monitoring pulp and paper processes might be adequate if the cross directional product variations are not critical. However, NIR imaging spectrometers would provide a much clearer picture if such variations are important as the process moves.

All pulp and paper samples used in this chapter have been measured with the NIR imaging spectrometer and scanner bed assembly described in section 2.1.2 of this thesis. The imaging was performed in off-line experiments conducted in a laboratory setting. The sample images were not averaged, thus no modifications were made to the raw NIR spectra of the pixels in the acquired multi-spectral images.

4.3 Classification of Characterized Paper Using NIR Imaging Spectroscopy

This section presents a paper classification study using multi-spectral NIR images of specially designed paper samples, which contain controlled chemical additives. Since the paper samples are white in color, analyzing RGB color images of the samples would not provide any useful information. The main objectives of this study are to investigate the ability of NIR imaging spectroscopy to extract the pre-defined composition information from paper samples, and use it to classify the samples based on differences in their chemical make-up. This study is intended to be a pre-cursor to the pulp-modeling application of NIR imaging spectroscopy, which is addressed in section 4.4 of this chapter.

A set of specially created paper samples was obtained from ASTM (The American Society for Testing Materials) in summer, 2000 by the Department of

Chemical Engineering at McMaster University. These samples were originally created for ASTM's research program to study the aging of printing and writing papers [Arnold, 2001]. The composition (ingredients) of each sample was varied in a designed experiment fashion. Table 4.1 shows the manipulated ingredient variables. It can be seen that 9 different combinations of 6 ingredients have been used to create the paper dataset in this study. Each combination was used to produce several reams of 8.5″ × 11″ paper sheets, with thickness comparable to ordinary photocopy paper.

Table 4.1 Paper composition manipulation chart of 6 ingredient variables

Paper Sample Composition

Sample Number	Pulp Type Number 1	Pulp Type Number 2	Nominal pH	pH Control Chemical	Calcium Carbonate	Internal Size	Number of Reams
1	100% Bleached Softwood Kraft	None	5	Alum	None	2#/T Rosin	**8**
2	100% Bleached Softwood Kraft	None	8.1	Sodium carbonate	5%	None	**7**
5	100% COTTON	None	5	Alum	None	2#/T Rosin	**19**
10	20% Bleached Softwood Kraft	80% Hardwood BCTMP	8.1	Sodium carbonate	5%	None	**6**
11	50% Bleached Softwood Kraft	50% Bleached Hardwood Kraft	8.1	Sodium carbonate	None	None	**6**
12	50% Bleached Softwood Kraft	50% Bleached Hardwood Kraft	8.1	Sodium carbonate	5%	None	**14**
13	50% Bleached Softwood Kraft	50% Hardwood BCTMP	8.1	Sodium carbonate	5%	None	**8**
14	50% Bleached Softwood Kraft	50% Hardwood BCTMP	5	Alum	None	2#/T Rosin	**11**
15	50% Bleached Softwood Kraft	50% Bleached Hardwood Kraft	8.1	Sodium carbonate	5%	4#/T AKD	**2**
							81

This study uses NIR imaging spectroscopy with chemometric methods to classify paper samples based on their unique ingredient combinations. The 9 unique combinations of paper samples were imaged using the NIR imaging spectrometer and scanned bed assembly (figure 2.6). Each sample was labeled according to the number assigned in table 4.1. Since the thickness of a single paper sheet was not enough to trap all incident light it was decided to use a stack of sheets from the same sample while imaging. Enough sheets were used to ensure no light penetrated through the stack. The thickness of each stack was kept constant. Three repeats of each paper sample were imaged with different stacks randomly chosen from the reams. The complete dataset consisted of 27 multi-spectral NIR images. Each stack was imaged with the scanner bed moving at a speed of 10 mm/s. Details of the resulting multi-spectral NIR image are as follows:

- The NIR spectrum used for the study was 933 nm to 1663 nm, which was discretized into 110 individual wavelength images.
- The approximate paper surface area imaged was 155 mm (L) × 110 mm (W), which was represented by 500 pixels (L) × 126 pixels (W). This resulted in dimensions of 500 × 126 × 110 pixels for each of the 27 multi-spectral NIR images.

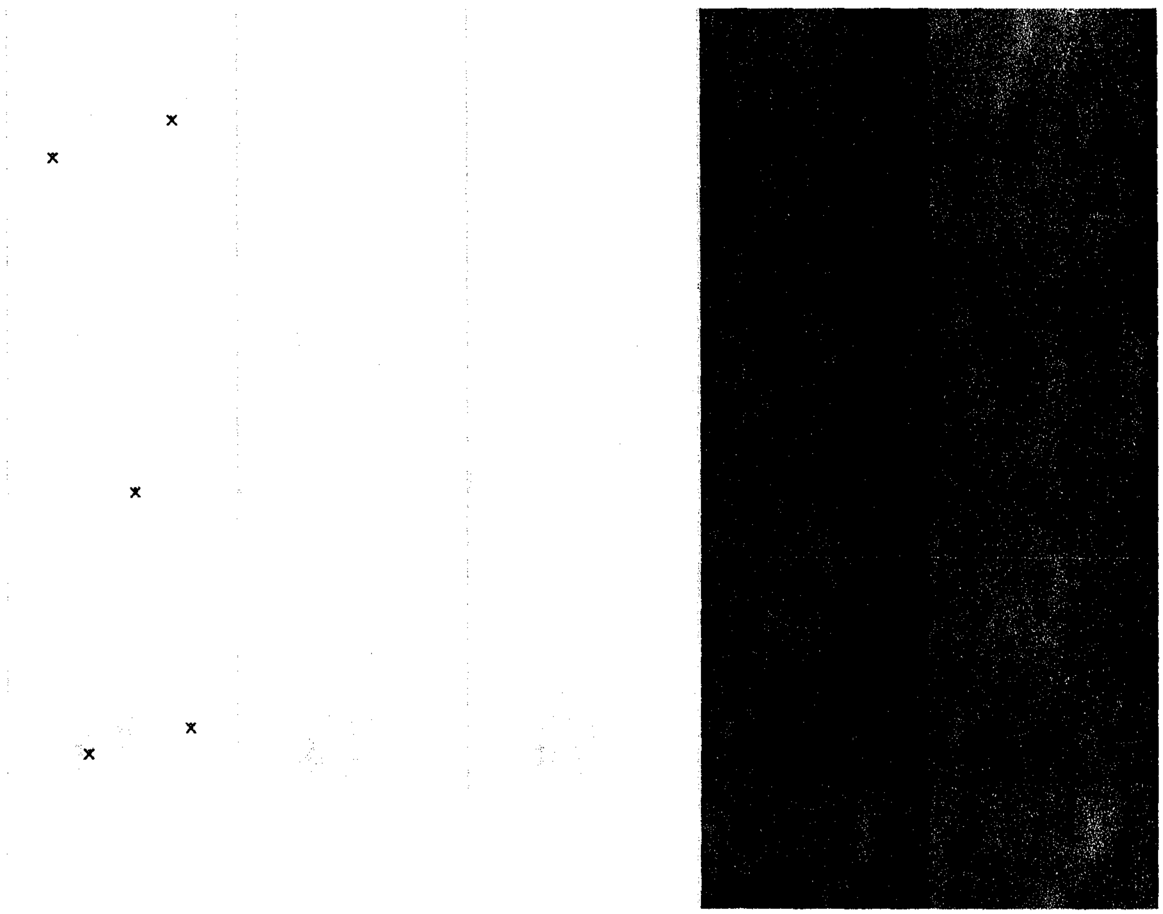

(a) 933nm **(b)** 1105nm **(c)** 1311nm **(d)** 1459nm **(e)** 1657nm

Figure 4.1 Multi-spectral NIR reflectance image of paper sample 1 acquired at 5 wavelengths

Figure 4.1 illustrates an example of a multi-spectral NIR reflectance image of paper sample 1 (table 4.1) at 5 out of the 110 NIR wavelengths. The darker pixels represent high NIR absorbance (low reflectance) regions in the paper sample. The NIR spectra of 5 selected pixels (highlighted as × on figure 4.1(a)) are illustrated in figure 4.2.

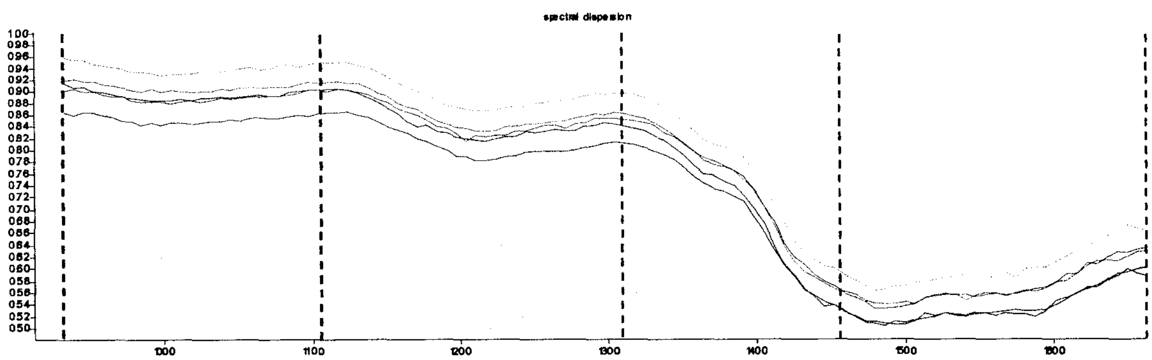

Figure 4.2 NIR reflectance spectra of 5 selected pixels from paper sample 1 (spatial locations of pixels marked as × in Figure 4.1(a)). Vertical red lines represent the wavelengths at which the images in Figure 4.1 are sampled

It can be seen from figure 4.2 that reflectance is generally high in the lower end of the NIR spectrum with a lowering trend that starts around 1400 nm (signifying a higher NIR absorbance region). As mentioned in section 2.1.2 (and illustrated in figure 2.2) the 1400 – 1650 nm region generally covers the 1st overtone of the C-H combinations, and O-H, N-H functional groups. The 1400 – 1500 nm wavelength range is particularly sensitive to moisture (H_2O). As a result, it can be inferred that the "dip" in the NIR spectra of the 5 pixels around this range is largely due to moisture (in atmosphere and paper), C-H, O-H and N-H bonds. Similarly, it can also be inferred that the small "dip" in the NIR reflectance spectra around 1200 nm is due to the absorbance of the C-H functional group in its 2nd overtone region (figure 2.2).

In order to meet the objectives of the study an appropriate methodology was developed to extract relevant feature information from the multi-spectral NIR images. A new feature space was chosen in a way such that it was representative of the paper samples, and at the same time enhanced differences between the samples based on their chemical make-up. MIA was used to extract such a feature space from the 27 sample images.

4.3.1 MIA of Multi-spectral NIR Paper Images

MIA techniques using MPCA decomposition have been previously discussed in chapter 2 (section 2.3.1). Using the same methodology all 27 multi-spectral NIR images

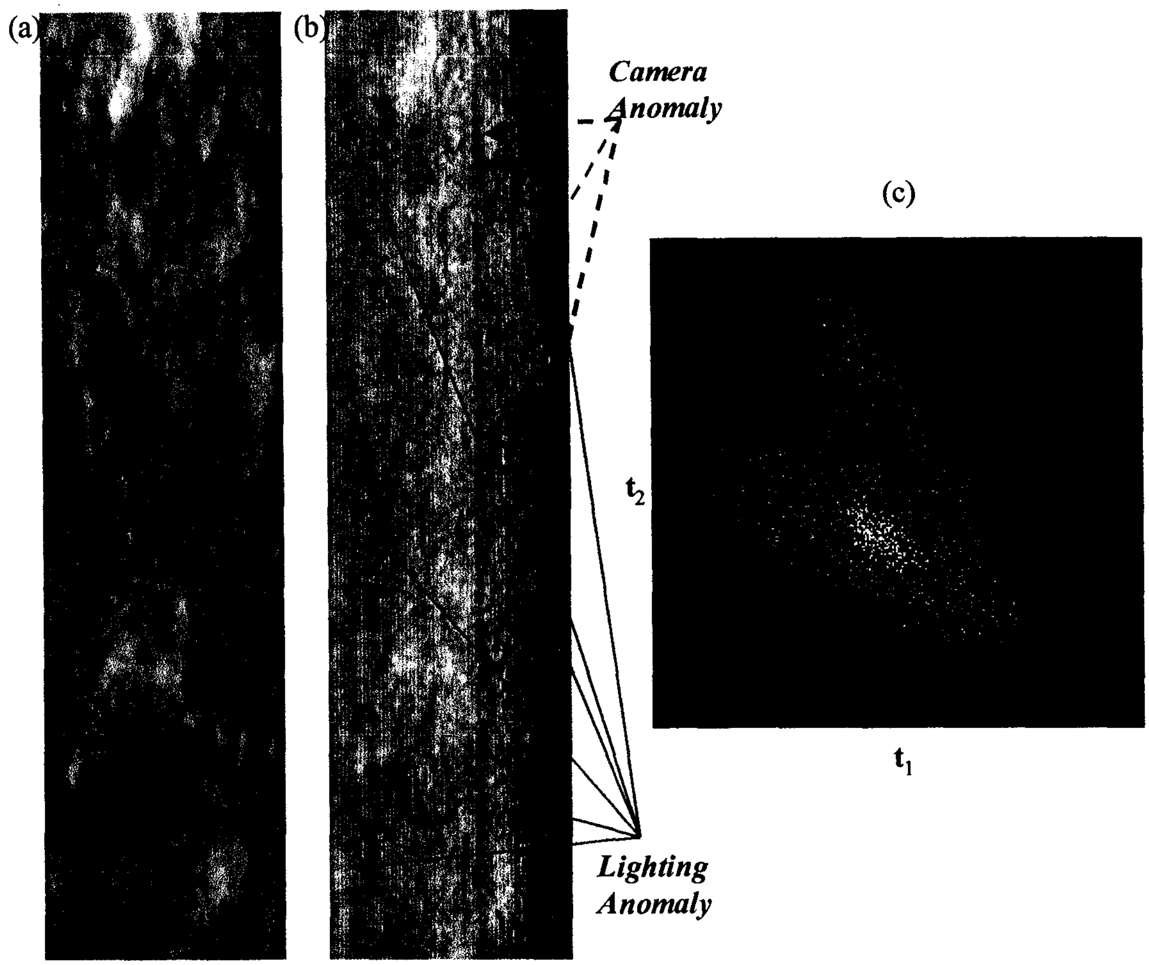

Figure 4.3 MIA score space of multi-spectral NIR image of paper sample 1. (a) $\mathbf{T}_1$ image; (b) $\mathbf{T}_2$ image; and (c) $\mathbf{t}_1 - \mathbf{t}_2$ scatter plot

of paper were decomposed into linear combinations of scores and loading vectors. Using the score ($\mathbf{T}_1$ and $\mathbf{T}_2$) and sum of squared error (SSE) images as indicators to visually determine the amount of structural information explained by the principal components it was determined that 2 PCs captured most of the feature information from the NIR images. As a result, MPCA was used to decompose each sample image into a linear combination of 2 score and loading vectors. Figure 4.3 illustrates the resulting 2 PC score space images and scatter plot upon decomposing the NIR multi-spectral image of paper sample 1. Since there was very little remaining structural information in the multi-spectral NIR image after extracting 2 PCs, the SSE image consisted of only dark pixels and thus has not been shown here.

As mentioned before (section 2.3.1) MPCA scores are weighted averages of the variables in a multivariate image. Thus the two MPCA score images (figures 4.3(a) and 4.3(b)) are weighted averages of the 110 individual wavelength images in the multi-spectral NIR image of paper sample 1. The loading vector $\mathbf{p}_1$ defines the individual weights related to each wavelength used in producing $\mathbf{T}_1$, whereas loading vector $\mathbf{p}_2$ contains weights forming $\mathbf{T}_2$. Figure 4.4 illustrates the MIA loading space defined by the 2 PCs of the NIR multi-spectral image of paper sample 1. The loading vectors $\mathbf{p}_1$ and $\mathbf{p}_2$ are illustrated as NIR spectra with individual weights on the 110 wavelengths.

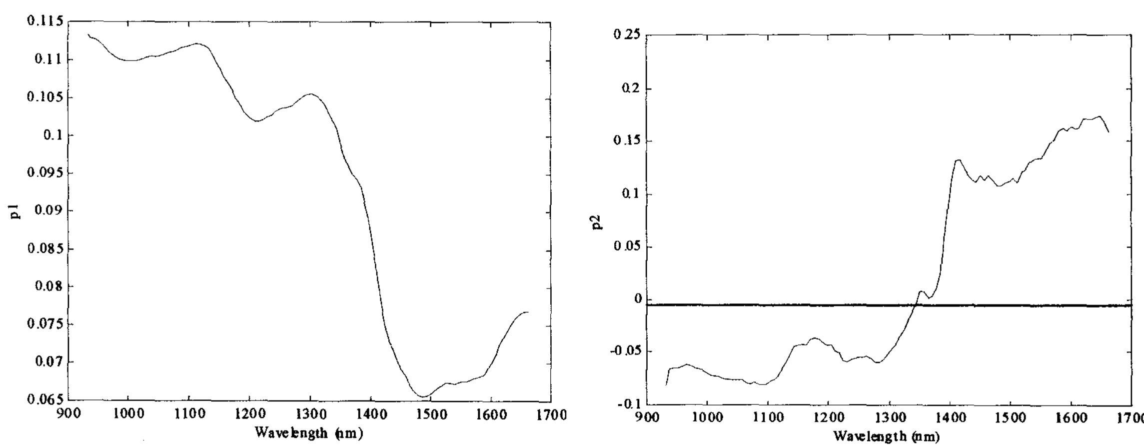

(a) (b)

Figure 4.4 MIA loading space of multi-spectral NIR image of paper sample 1. (a) $\mathbf{p}_1$ loading vector coefficients; and (b) $\mathbf{p}_2$ loading vector coefficients

Upon comparing the individual NIR spectra of the 5 selected pixels from paper sample 1 (figure 4.2) with the NIR spectrum of $\mathbf{p}_1$ (figure 4.4(a)) it can be seen that the 1st PC loading coefficients follow the same trends. From the theory of MIA [Geladi et. al., 1996] it can be shown that $\mathbf{p}_1$ represents a normalized mean spectrum of all pixel spectra throughout the *un-scaled* multivariate image. As a result, $\mathbf{p}_1$ represents an *average NIR spectrum* across the spatial pixels in the multi-spectral NIR paper image.

It could be argued that in obtaining such an average NIR spectrum over the pixels of the paper image, the resulting PC loading is in some remote way similar to the averaging of the scans performed by a probe-based NIR spectrometer. The difference being that an imaging spectrometer performs the averaging over multiple single scan spectra from a section of the sample, whereas a probe detector would average spectra over multiple scans at the same point on the sample.

Since no mean-centering of the image is usually performed in MIA the 1^{st} PC explains mean variability throughout the data. Thus, $\mathbf{T}_1$ (being a weighted average image) represents an *average NIR reflectance image* over the 110 wavelength images (based on the mean NIR spectrum). Those pixels having dark intensities in the $\mathbf{T}_1$ image (figure 4.3(a)) represent spatial locations with lower NIR reflectance (higher absorbance) through the 110 wavelengths, and vice versa.

It can be observed from figure 4.3(b) that the 2^{nd} PC mainly captures lighting and camera anomalies. The $\mathbf{T}_2$ score image illustrates the lighting anomalies along the right of the sample (darker pixels), as well as a camera anomaly as a vertical dark streak towards the right of the center of the image. It can be seen from the pixels in the $\mathbf{T}_2$ image (figure 4.3b) and the non-smooth nature of the spectrum defining the coefficients of $\mathbf{p}_2$ loading vector (figure 4.4(b)) that the signal-to-noise ratio (SNR) has dropped considerably after extracting the 1^{st} PC. Furthermore, the sum of squares of the multi-spectral NIR image of the paper sample explained by the 1^{st} PC is 99.988%, whereas that explained by the 2^{nd} PC is only 0.010%. Thus it can be concluded that only the 1^{st} significant PC extracted from the 110 wavelength multi-spectral image contains valuable feature information.

4.3.2 Transforming Multi-spectral NIR Paper Images to Feature Space

The transformation of raw image data into a new feature space is the most critical step in the success or failure of the proposed classification technique. Prior knowledge should be used as much as possible in extracting relevant information from image data that is most indicative of (and correlated with) the feature information sought. The objective in the paper classification study was to capture overall paper characteristics that were 'global' in nature (i.e. independent of surface variations). The paper samples for this study were produced as part of a designed experiment under controlled conditions with unique pre-determined recipes for each sample. As a result, spatial information (present in the score space of MIA) carried little value in predicting these overall paper characteristics (i.e. ingredients).

It was decided to use the MIA loading space as *feature* vectors for classification of the paper samples. This is because the MPCA loading vectors represented overall chemical information through average NIR spectra of all pixels across the imaged section of the paper. Since the 2nd PC contained little structural information this study exclusively relied on the 1st PC loading vector $\mathbf{p}_1$ as the feature vector of each paper sample. It was assumed that the $\mathbf{p}_1$ loading vector captured the NIR characteristics of the paper at a set combination of the 6 ingredient variables. If any differences existed in the paper characteristics they would be reflected in their feature vectors.

Individual MPCA decompositions were performed on all 27 multi-spectral NIR images, and the corresponding $\mathbf{p}_1$ loading vectors were extracted. These feature vectors were organized as rows of a new *feature matrix* $\mathbf{X}_{\mathbf{feature}}$. Figure 4.5 illustrates the feature extraction step. $\mathbf{X}_{\mathbf{feature}}$ has dimension of 27 (rows) × 110 (columns). For graphical clarity and better interpretability 9 (out of 27) unique feature vectors of $\mathbf{X}_{\mathbf{feature}}$ (only one repeat per sample number) have been illustrated in figure 4.6 with corresponding sample numbers identified in the legend. As expected the feature vectors of the paper samples were very similar, with slight differences in their average NIR spectra.

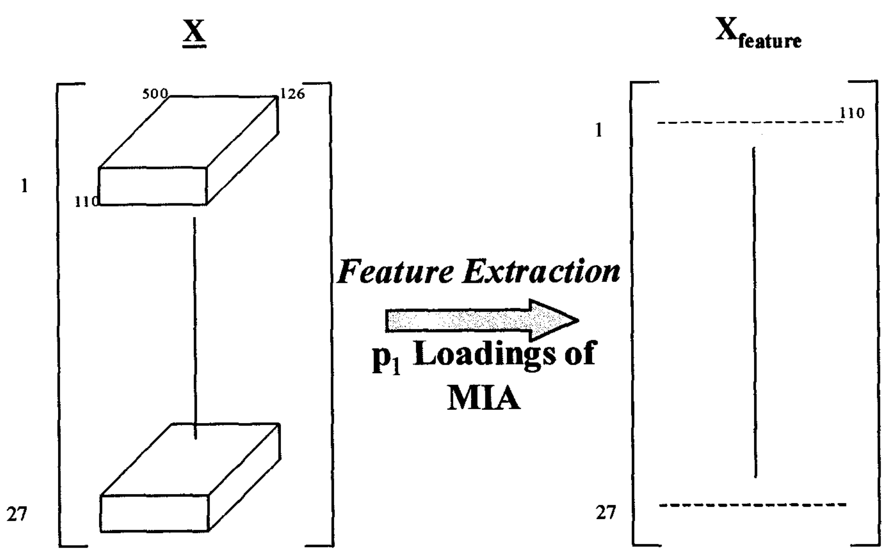

Figure 4.5 Feature extraction from 27 multi-spectral NIR images ($\underline{\mathbf{X}}$) to produce feature matrix $\mathbf{X}_{\mathbf{feature}}$ containing MPCA $\mathbf{p}_1$ loadings as rows

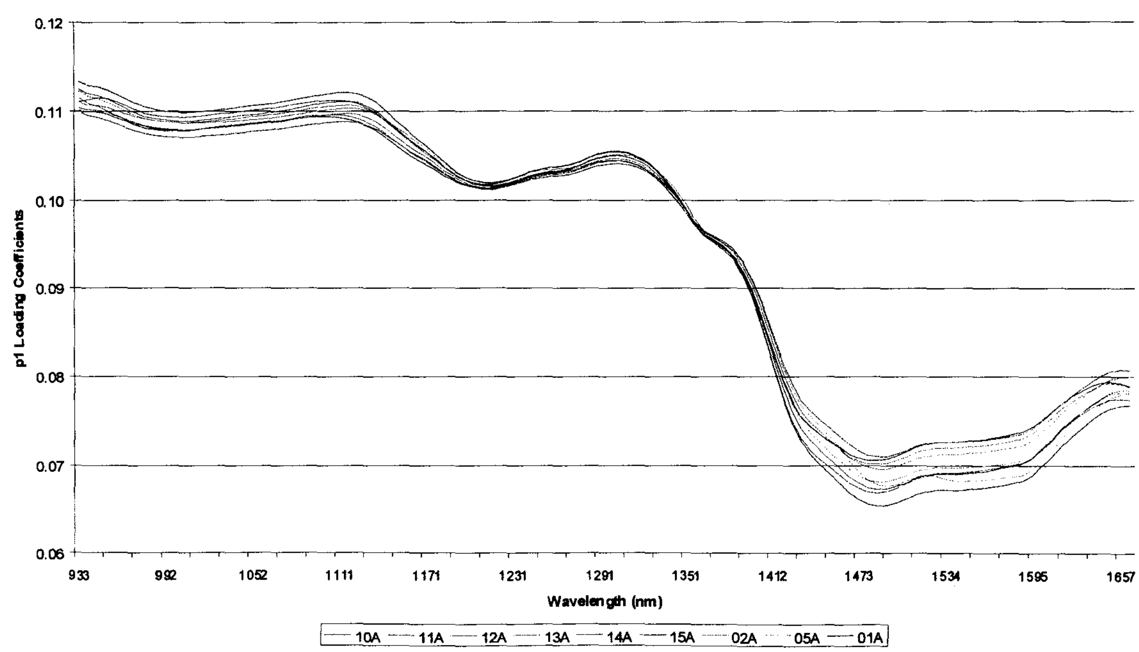

Figure 4.6 Representative NIR feature space ($\mathbf{p}_1$ loadings vectors) of 9 multi-spectral NIR paper images

4.3.3 PCA of Feature Space for Paper Classification

After mean-centering the variables ($\mathbf{p}_1$ loading values at different wavelengths) in $\mathbf{X}_{\text{feature}}$ PCA was used to decompose the $\mathbf{p}_1$ loading coefficients at the 110 wavelengths into a linear combination of 2 significant PC scores and loading vectors. The variation in $\mathbf{X}_{\text{feature}}$ explained by the 2 PCs was 98.6% (cumulative). It should be noted that the scores and loadings resulting from this PCA of $\mathbf{X}_{\text{feature}}$ are different than those obtained in the initial MPCA decomposition of the multi-spectral NIR paper images to obtain $\mathbf{X}_{\text{feature}}$. Classification of the 27 feature vectors was performed in the 2 PC score scatter plot $\mathbf{t}_1^* - \mathbf{t}_2^*$, where each feature vector was represented as a single point. Figure 4.7 illustrates the $\mathbf{t}_1^* - \mathbf{t}_2^*$ scatter plot of PCA on $\mathbf{X}_{\text{feature}}$. The score points representing the 9 paper samples have been uniquely color-coded for easier interpretation. The 3 repeats for each of the 9 paper samples have been identified with letter-number combinations (e.g. 01A, 01B, and 01C representing repeats from sample 1).

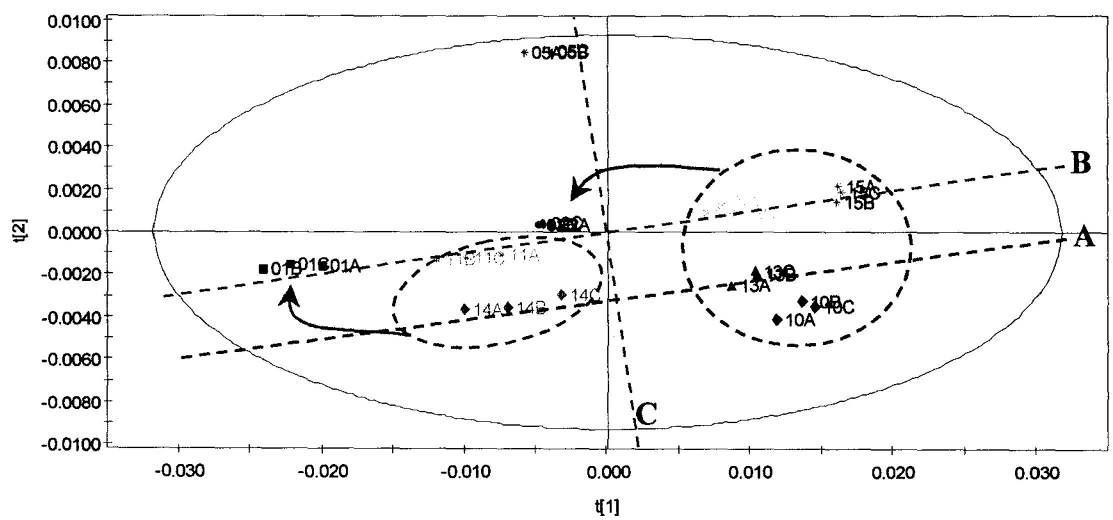

Figure 4.7 $\mathbf{t}_1^* - \mathbf{t}_2^*$ score space scatter plot of PCA on $\mathbf{X}_{\text{feature}}$ to classify feature vectors of 27 paper samples

It can be seen from figure 4.7 that the 9 types of paper sample groups representing unique ingredient compositions have been well separated into their respective point clusters. Some observations made upon comparing the classification achieved in figure 4.7 with the paper composition information in table 4.1 are summarized below.

Paper sample 5 is separated from all the other papers by its large t_2 value. Therefore, it seems as if its composition is unlike that of any of the other types of paper. Looking at the paper compositions (table 4.1) this is confirmed as sample 5 is the only sample that is composed of 100% Cotton.

Paper samples 10 and 13 seem to be very similar to each other. From table 4.1 it can be seen that both samples are composed of the same types of pulp (i.e. Bleached Softwood Kraft Pulp and Hardwood BCTMP Pulp), the only difference being the ratio of Softwood to Hardwood pulp (20% Softwood Pulp in Sample 10; 50% Softwood Pulp in Sample 13). Therefore, it can be inferred that the shift in the score scatter points from sample 10 to 13 is due to an increase in Hardwood BCTMP Pulp composition.

Paper samples 12 and 15 also seem to be very similar to each other. It can be confirmed from table 4.1 that these two samples have the same pulp types in an equal ratio (50% Bleached Softwood Kraft and 50% Bleached Hardwood Kraft). The only difference in the composition of sample 12 and 15 is 4#/T AKD internal sizing (present in sample 15). Thus, the effect of internal sizing can be identified in the score point shift from sample 12 to 15.

All the samples can be seen to follow the orientation defined by lines A, B, and C in figure 4.7. Except for sample 5 all samples are oriented along one of lines A or B. The direction from line A to B (i.e. along line C) explains increasing paper brightness as samples along line A contain Hardwood BCTMP pulp, whereas paper samples along line B contain Bleached Hardwood Kraft pulp.

Line C defines the division between samples based on Calcium Carbonate ($CaCO_3$) and Bleached Softwood Kraft pulp. Most samples (except sample 2) to the left of line C contain no $CaCO_3$, whereas samples to the right of line C contain 5% $CaCO_3$. The two groups of samples highlighted in figure 4.7 (green and blue circles) contain samples with (blue) and without (green) $CaCO_3$. The arrows indicate direction of two paper samples (1 and 2) being separated from their respective groups. This separation is because the two samples (1 and 2) contain 100% Bleached Softwood Kraft pulp (i.e. no

Hardwood pulp). Therefore, it can be said that the direction defined by lines A and B also explains Bleached Softwood Kraft pulp.

From the results obtained in the paper classification study it can be concluded that NIR imaging spectroscopy can extract relevant chemical and pulp ingredient information from finished paper samples. The crucial step is the extraction of appropriate feature information from multi-spectral NIR images. A similar feature extraction strategy (using the 1st PC loadings of MPCA) has been employed in the following section, where the extracted feature vectors are used to model chemical information in multi-spectral NIR images of finished pulp samples obtained from a pulp mill. However, the pulp data is more complicated as compared to the well-characterized paper samples used in the above study. This is because there are very little differences in the composition of the pulp samples (even though they are from different grades) since they are collected from an industrial pulping process running under routine conditions.

4.4 Modeling Pulp Properties Through Multivariate Image Regression

This section presents the main contributions of the chapter through development of a Multivariate Image Regression technique to model selected pulp properties from multi-spectral NIR images of finished chemical pulp samples. Methodology developed in the previous section is used here to extract relevant features from multi-spectral NIR pulp images. The extracted feature space is then regressed with pulp quality data (obtained from laboratory analysis) to build empirical models that predict certain pulp end properties from future process multi-spectral NIR images of dry pulp sheets.

Pulp data used in this study has been obtained from the Temiscaming (Quebec) dissolving sulphite pulp mill of Tembec Inc. The company produces over 20 different grades of specialty cellulose chemical pulp for use in the manufacture of many end products like rayon, cellophane, pharmaceuticals, plastics, food additives etc. The pulping process contains several chemical and mechanical treatments of different types of wood chips in order to extract and clean the pulp fibers, which are further bleached and treated through a variety of other chemicals (prior to drying) depending on the pulp grade desired. Every pulp grade has its unique target end properties, which are dependent on the specifications provided by the end product manufacturers who use the dissolving pulp as a raw material in their processes.

Adhering to the specifications on the end properties of every pulp grade is of the utmost importance to the pulp mill in order to maintain customer satisfaction. Therefore to monitor pulp quality a large number of quality control tests are conducted on the finished pulp samples prior to shipping the product. Most of these tests are carried out in the pulp mill's analytical laboratory where the finished pulp sample is subject to various physical and chemical analyses to determine its overall characteristics and end properties. Some of the pulp testing procedures in the analytical laboratory involve complicated and time consuming wet chemistry techniques, which are manpower intensive. Furthermore, due to the destructive nature of some tests multiple samples are required for a complete pulp property analysis. It is desirable to develop a rapid pulp quality testing technique, which would ideally be able to provide multiple pulp properties from a single sample in a non-destructive manner, and at a low cost.

In this section NIR spectroscopy is successfully used with chemometric techniques to predict pulp end properties from single point spectral readings of finished pulp samples. The work presented in this study includes an image based NIR spectroscopic modeling technique to predict multiple pulp end properties from a single multi-spectral NIR image of a finished pulp sheet.

4.4.1 Selected Pulp Properties for MIR Modeling

Since the proposed MIR modeling technique is intended to be a feasibility study, only 4 end properties of finished pulp have been selected for prediction. Each of the four properties is separately measured in the pulp mill's quality control laboratory using preset analytical wet chemistry techniques. Work instruction sheets provide detailed procedures that must be followed in order to measure the respective properties. The four pulp properties chosen for this study are: S10, S18, DCM Resin, and Intrinsic Viscosity. Each property is briefly described below.

S10 and S18 measure the alkaline solubility of finished pulp. These two properties are indicators of degraded cellulose and hemi-cellulose (low molecular weight carbohydrates) remaining in the pulp sample after pulping and bleaching of the wood chips. The analytical laboratory testing procedure to measure S10 and S18 requires dissolving the dry pulp into alkaline solutions and performing various measurements on the solutions to determine the amount of degraded cellulose and hemi-cellulose. Obtaining the final S10 and S18 measurements for each pulp sample requires approximately 1.5 hours of experimental procedures. Although no formal study has been performed, the pulp mill reported an approximate 2σ (95% CI) experimental error of ± 0.6 measurement units on laboratory measurements of the S10 pulp property, and ± 0.3 units on measurements of the S18 pulp property.

DCM Resin is a measure of the amount of remaining resinous materials in finished pulp, which are extractable with organic solvents like Dichloromethane. The analytical laboratory testing procedure for measuring DCM Resin involves dissolving the solid pulp sample into the organic solvent and extracting the solution via siphoning at regular intervals. Obtaining the final DCM Resin measurement for each pulp sample requires approximately 4 hours of experimental procedures. The experimental error for DCM Resin has not been thoroughly evaluated by the pulp mill. However the reported value is based on the CPPA (Canadian Pulp and Paper Association) standard, which gives a coefficient of variation of 6.3%.

Intrinsic Viscosity measures the average molecular chain length of the polymers making up the pulp fibers. The solid pulp sample is torn and dissolved in various reagents prior to measurement of intrinsic viscosity. Typically the experimental procedure to obtain a measurement requires approximately 20 minutes. The reported 2σ

experimental errors for the intrinsic viscosity test are approximately ±0.2 measurement units.

It is evident from the analytical laboratory procedures of the four pulp properties that the measurements are made upon destroying and/or dissolving the solid pulp samples into solutions. As a result, all four properties are *global* in nature with a single value representing the entire pulp sample. Therefore the feature extraction strategy employed in the paper classification study (section 4.3) can also be used here to extract relevant average chemical information from multi-spectral NIR images of dry pulp sheets.

The experimental errors associated with S10, S18, and Intrinsic Viscosity are absolute, whereas those related with DCM Resin are relative. In section 4.4.4 performing a logarithmic transformation prior to developing the MIR model stabilizes the experimental errors for DCM Resin.

4.4.2 Description of Pulp Dataset and Imaging Procedure

The MIR pulp modeling study was carried out in two stages. The first stage consisted of an off-line study, which involved imaging some finished pulp samples and developing the MIR models at McMaster University. The pulp samples, along with corresponding laboratory measurements of the four properties, were shipped from the pulp mill to McMaster over a period of several months. The second stage of the study involved an at-line imaging experiment, which consisted of taking the NIR imaging spectrometer to the pulp mill to image the pulp samples in the mill's analytical laboratory prior to wet chemistry analysis to measure pulp properties.

For the off-line MIR modeling study pulp samples from different grades were shipped to McMaster from the pulp mill over a period of 6 months. Prior to shipping each sample was divided into two halves with one half being shipped whereas the other half sent to the pulp mill's analytical laboratory for measurement of the four end properties. The corresponding laboratory analyzed pulp property measurements were later shipped to McMaster as the results became available. Each pulp sample was imaged at the university as it was received over the 6 month time period. Finally, individual MIR models were developed between the multi-spectral NIR pulp images and the received laboratory analysis values. To improve the model predictions a variable transformation (using ln(DCM Resin) values) and a spectral filtering technique (Orthogonal Signal Correction) were used on the data. Although the MIR models produced reasonable pulp property predictions it was sensed that the results could be further improved upon removing certain sources of variation that were inherently present in the off-line study.

Since the pulp samples were produced over a relatively long time period there were some inherent variations induced by differences in aging of the samples before they were imaged at the university. Furthermore, various technicians performed the laboratory testing of the pulp samples over 6 months, which added human variability to the results. Although the pulp samples were shipped in sealed Ziploc plastic bags there were possible moisture variations due to the time lag between production and imaging of some samples. Such unwanted moisture variations affect the NIR imaging spectrometer readings, which add variability in the MIR model predictions of the pulp properties. Due to the destructive nature of the wet chemistry laboratory procedures the pulp samples were divided into two halves. As a result, the imaged part of the pulp sample did not correspond to the laboratory tested half. This source of variability could be removed if the imaging were performed prior to the laboratory analysis on the same section of the pulp sample.

In light of the above-mentioned variability in the off-line MIR models it was decided that the results of the off-line study were not as representative of the true pulp properties as the at-line results. Therefore, these former results have thus been omitted from the thesis, and only the results from the at-line stage of the pulp modeling study are presented.

To remove the sources of variability inherent in the off-line stage of the study an at-line imaging run was performed in the analytical laboratory of the pulp mill. Another reason for the at-line study was to validate the methodology and the MIR models (developed beforehand at McMaster using off-line data) in an actual industrial setting where imaging would ideally be performed (at first) in the analytical laboratory prior to testing of the pulp properties. Eventually, the aim of the project is to install a high-speed NIR imaging spectrometer on-line as the pulp is being manufactured, and use the multi-spectral NIR pulp images with the developed models to monitor pulp quality. Thus, the at-line study provides the logical link between the off-line and on-line projects.

The procedure followed during the at-line experiment is described below. The NIR imaging spectrometer and scanner assembly (figure 2.2) was setup in the analytical laboratory of the pulp mill in order to image freshly manufactured pulp samples over a period of 3 days of regular production. Imaging was performed immediately after production of every roll thus ensuring that the pulp samples were fresh and the moisture content was constant through all the samples that were imaged. The scanned section of each pulp sample was marked using a frame. Analytical laboratory testing of the four pulp properties was carried out using pulp from within the marked boundaries of the scanned section. Thus variability induced by imaging and analyzing different parts of the pulp sample was avoided. Once imaged the pulp samples were then analyzed for the four pulp properties by the same laboratory technicians, thus ensuring minimal human variability in the analysis.

A total of 60 pulp samples were imaged over the 3 days of production during the at-line experimental run. The samples belonged to one of two main pulp grades: (1) Rayon Grade, (2) Pharmaceutical Grade. Additionally, the rayon grade was further divided into two sub-grades having different pulp end property specifications. The grade change between the two main grades was also captured during the at-line experimental run. Due to confidentiality agreements between Tembec Inc. and McMaster University the true grade names have not been presented in the thesis. Furthermore, the pulp property values have also been scaled to a relative index although the trends of the properties have been conserved in the presented results (section 4.4.4).

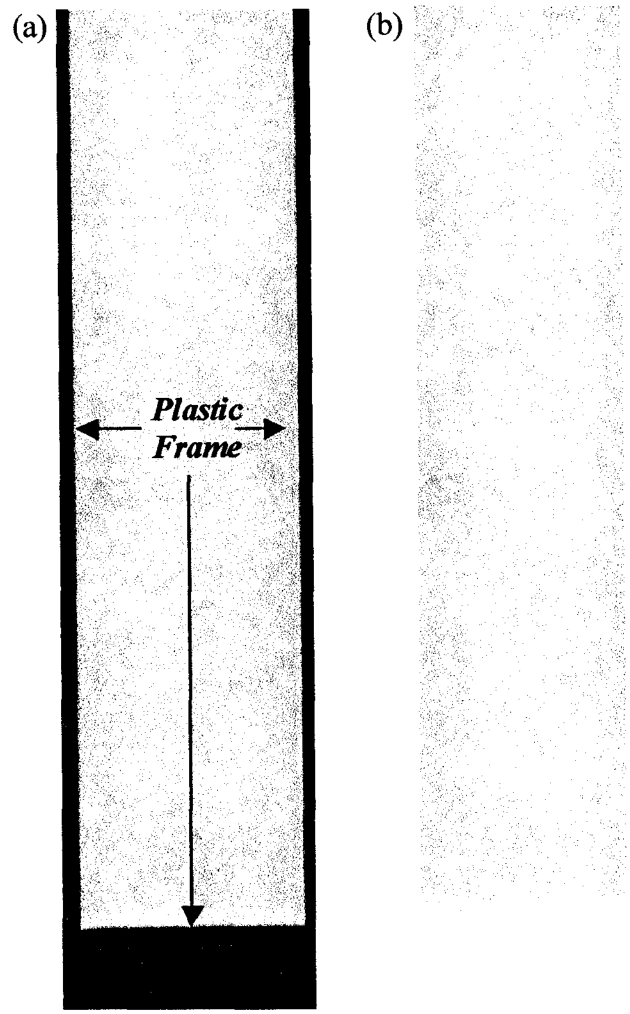

Figure 4.8 Single wavelength (1351 nm) image of pulp sample 16 from at-line experiment. (a) Raw image with plastic frame in place, (b) Cropped image after removing frame

The at-line imaging experiment was performed with each pulp sample placed on the scanner bed encased between an aluminum plate at the bottom side and a plastic frame on top. This ensured that the pulp sample lay flat under the imaging spectrometer. Furthermore, imaging the sample with the plastic frame defined the boundaries of the imaged section on the pulp sample, which was marked and forwarded to the laboratory technicians for property measurement. Figure 4.8(a) illustrates a 500 pixels (L) $\times$ 126 pixels (W) single wavelength image of a pulp sample with the plastic frame in place.

Each of the 60 multi-spectral NIR pulp images from the at-line study was manually cropped to remove the plastic frame prior to further analysis. Figure 4.8(b) illustrates the same pulp image after cropping the plastic frame.

Each pulp sample was imaged under the NIR imaging spectrometer with the scanner bed moving at a speed of 10 mm/s. Upon cropping the plastic frame from each pulp sample image a surface area of 140 mm (L) × 93 mm (W) was captured as 448 pixels (L) × 102 pixels (W) NIR reflectance images in 108 unique wavelengths spanning the 933 – 1650 nm range. For purposes of feature extraction using MIA the dimensions of each of the 60 multivariate images were 448 pixels (L) × 102 pixels (W) × 108 pixels (λ).

4.4.3 MIA of Multi-Spectral NIR Pulp Images

Extracting relevant feature information from multi-spectral NIR pulp images is a crucial step of the overall MIR modeling scheme. The extracted features should be representative of overall pulp sample characteristics as well as good predictors of chemical information affecting the pulp end properties. It was shown in the paper classification study (section 4.3.2) that MIA extracts the feature information from the multi-spectral NIR images into score and loading spaces.

MIA scores can be used if one is interested in investigating the spatial variations of feature pixels throughout the imaged area of the pulp sample. However, the main aim of this study is to infer *overall* quality data from NIR multi-spectral pulp images. As mentioned before the pulp properties have been determined through destructive wet chemistry laboratory testing of the samples. Hence spatial variations of NIR reflectance spectra are not as important here as compared to an overall indicator of pulp features throughout the imaged area of the pulp sample.

MIA loadings are indicators of pixel NIR spectral variations throughout the scanned area of the pulp sample. Thus, the loading vectors provide overall chemical feature information (related to absorbance signatures of various functional groups) in the imaged pulp sample. This is of course based on the assumptions that: (1) a weighted average NIR reflectance spectrum over the scanned area of the sample is an adequate feature vector representing overall chemical information, and (2) the chemical information captured by the feature vector is indicative of the overall pulp quality. Similar to the paper classification problem (section 4.3.2) this study also uses the first MIA loading vector $\mathbf{p}_1$ of each multi-spectral pulp image as its feature vector.

Upon performing MPCA on the multi-spectral pulp images the $\mathbf{p}_1$ loading vectors can be plotted against their respective variables (wavelengths). Figure 4.9 illustrates the $\mathbf{p}_1$ feature vector coefficients of the 60 multi-spectral NIR pulp images used in this study.

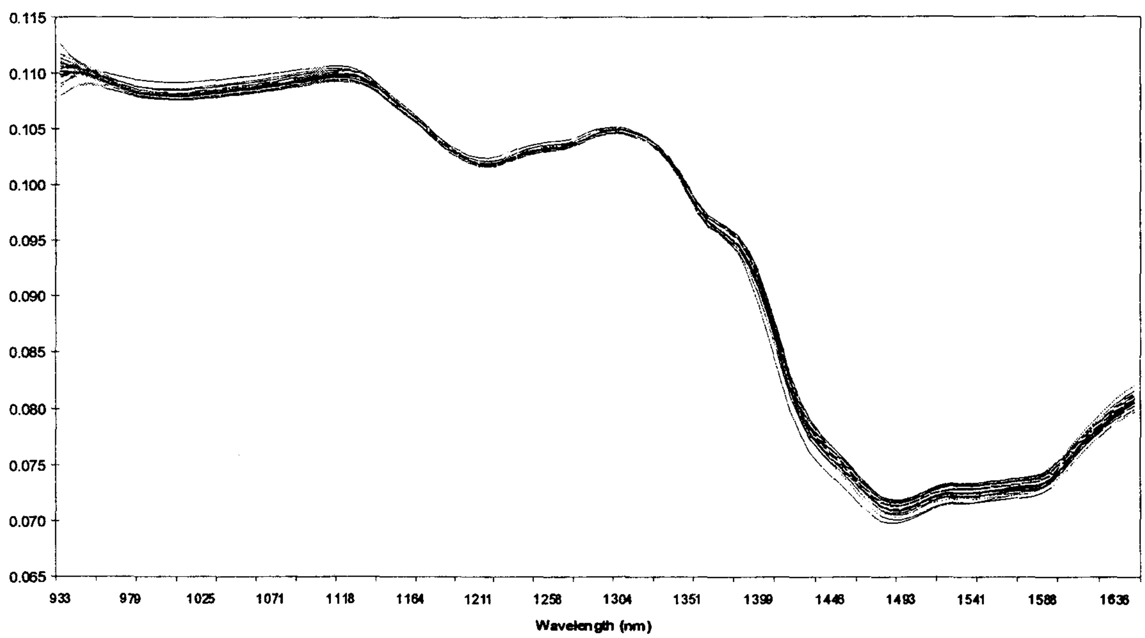

Figure 4.9 Feature ($\mathbf{p}_1$ loading) vectors of multi-spectral NIR pulp images from at-line experiment

This new feature vector set represents a feature space $\mathbf{X}_{\mathbf{feature}}$, which can be further interrogated for chemical information indicative of overall pulp quality.

Comparing trends of the $\mathbf{p}_1$ loading feature vectors in the paper classification study (figure 4.6) and the pulp modeling study (figure 4.9) it can be said that the mean NIR reflectance information from the pulp and paper samples is similar. This is expected since pulp and paper both contain treated wood fibers. Since the general trends of the $\mathbf{p}_1$ loading feature vectors for both the pulp and paper studies are similar it can be inferred that the raw NIR pixel spectra in the pulp images are also similar to those in the paper samples (figure 4.2). Thus observations made in section 4.3 regarding the absorbance signatures of various functional groups and moisture for the paper sample pixel spectra are also valid for pixel spectra of the pulp samples.

4.4.4 PLS Regression Modeling of Pulp Properties Using Feature Space of Process NIR Pulp Images

As opposed to classification of the extracted feature vectors from multi-spectral NIR pulp images the main objective of this study is to use the feature space to infer pulp properties. This is achieved via building multivariate statistical regression models between the feature space and corresponding analytical laboratory measurements of pulp properties. The multivariate regression model used to develop the empirical relation in this study is Partial Least Squares (PLS). This regression model was chosen mainly because of its ability to perform well with large amounts of highly correlated data that is usually present in NIR spectra. PLS modeling has successfully been used for multivariate calibration of pulp quality using NIR spectra as **X** (predictor), and using the chemical constituents (e.g. cellulose, hemi-cellulose, lignin) as **Y** (response) variables [Wallbäcks et. al., 1991; Antti et. al., 1996; Wold et. al., 1998]. Once trained, the PLS models can predict pulp chemical constituents from NIR spectra of new samples. Besides the above references there are some other excellent sources that provide details of PLS regression modeling with NIR spectra [Martens et. al., 1989; Beebe et. al., 1998; Eriksson et. al., 1999]. The interested reader is encouraged to consult these references for further details about PLS regression modeling as used in multivariate calibration. As far as this thesis is concerned it is assumed that the reader has some basic background knowledge of PLS. Figure 4.10 illustrates the proposed MIR scheme for this study, which is used to relate multi-spectral NIR images with pulp property data.

In figure 4.10 the feature space $\mathbf{X}_{\mathbf{feature}}$ is individually regressed with four (laboratory measured) pulp property variables using separate PLS models ($\mathbf{Y}$ = S10, S18, DCM Resin, Intrinsic Viscosity). Feature vectors from $\mathbf{X}_{\mathbf{feature}}$ were divided into two

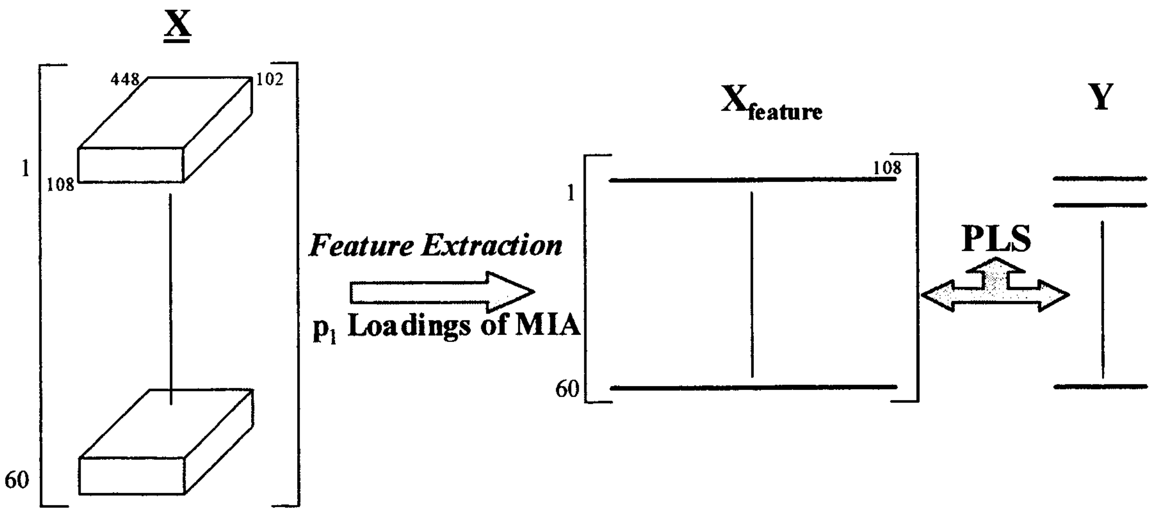

Figure 4.10 Schematic of proposed MIR strategy for predicting laboratory tested pulp properties (Y) from multi-spectral NIR pulp images ($\underline{\mathbf{X}}$)

equal parts (30 samples each) for: (1) Training the PLS models to fit the $\mathbf{Y}$ data (observations 1, 3,..., 49 of $\mathbf{X}_{\mathbf{feature}}$); and (2) Using the developed models on a validation dataset (observations 2, 4,..., 50 of $\mathbf{X}_{\mathbf{feature}}$) for predicting the pulp properties and calculating prediction errors. Alternate samples were divided into training and validation sets mainly due to the analytical laboratory measurements conducted on the pulp data. Since the analytical laboratory procedure for measuring Intrinsic Viscosity required 20 minutes this was the only pulp property that was measured for all 60 samples from the at-line study. The other three pulp properties (S10, S18, DCM Resin) were measured for only half of the dataset (i.e. every alternate sample was measured) since their analysis times were considerably longer which required more tedious wet chemistry procedures. Due to manpower shortages the pulp mill did not perform laboratory testing of the remaining pulp samples. As a result, the dataset was divided in such a way that the PLS model training set consisted of pulp samples that had been measured for all four properties. Due to the non-availability of three property measurements in the validation set PLS model prediction errors are not available for S10, S18, and DCM Resin. Nevertheless, the MIR modeling results have been presented with a comparison between Root Mean Squared Errors of Fit (RMSEE) and the reported experimental errors for S10, S18, and DCM Resin pulp properties.

Prior to application of PLS regression models the NIR spectral data in $\mathbf{X}_{\text{feature}}$ was scaled (mean-centered) with respect to the 108 wavelengths (columns). Each of the four pulp property variables in $\mathbf{Y}$ was auto-scaled to unit variance. Furthermore, it was noticed that the variance of the laboratory measured DCM Resin pulp property was proportional to the magnitude of the DCM Resin values. As a result DCM Resin values were transformed by taking the natural logarithm [ln(DCM Resin)]. Beebe et. al. [1998] and Eriksson et. al. [1999] provide several insights to different types of variable scaling and transformations that can be performed in order to remove non-linearity and improve PLS model fit and predictions. Upon transforming the DCM Resin pulp property into ln(DCM Resin) the corresponding relative experimental errors (coefficient of variation = ±6.3%) were also stabilized to absolute errors (2σ experimental error = ±0.13 measurement units).

The NIR image feature space $\mathbf{X}_{\text{feature}}$ and pulp property data $\mathbf{Y}$ were exported to SIMCA-P 9.0 [Umetrics, 2001] for PLS analysis. Four separate PLS1 models were set-up to predict each pulp property separately (i.e. $\mathbf{Y}$ was a column vector representing one property at a time). PLS1 models were built on the training set and the regression coefficients were used to predict the corresponding pulp properties for the validation set. Table 4.3 compares the results obtained via the four PLS1 models using the raw $\mathbf{X}_{\text{feature}}$ data with those obtained via spectrally filtering the $\mathbf{X}_{\text{feature}}$ variables using Orthogonal Signal Correction (OSC). It can be seen that all four PLS1 models on un-filtered data performed very poorly compared to those on spectrally filtered data in terms of model fit (RMSEE) and predictions (RMSEP). Furthermore, the $Q^2_{\text{cumulative}}$ values of the four models are quite low, which indicates that the PLS1 models cannot explain much variation in the pulp properties $\mathbf{Y}$. Finally, it can be seen that (except for ln(DCM Resin)) all four PLS1 models required a high number of latent variables to capture the variability in the data, which leads to over-fitting (indicated by $R^2_{cumulative} = 1$). Generally, if PLS regression models require such high number of latent variables to explain the variation in **Y** this indicates that there is a lot of variation in **X** that is unrelated with **Y**, which is overwhelming the model. It was also noticed that the 95% CI of most PLS1 regression coefficients for all four models included 0, which is another indication of the poor performance of the PLS1 models. Section 4.4.4.2 provides definitions of the above-mentioned model diagnostics.

A possible reason for the poor performance of the four PLS1 models is unwanted variation in the at-line experiment, which is not related to the variation of the pulp properties. As discussed in section 4.4.2 NIR spectroscopy is highly sensitive to moisture in the atmosphere and in the pulp sample. Thus, any moisture variations over the duration of the at-line experiment would reflect on the feature vectors of the pulp samples. Imaging is also sensitive to spatial characteristics of the pulp sample (e.g. surface smoothness), which induces variation in feature vectors of those pulp samples with different surface characteristics. Finally, any lighting variations over the duration of the at-line experiment would also reflect on the pulp image feature vectors. These sources of variation are not desirable as they are totally unrelated with the pulp property variations from sample to sample. As a result, one needs to remove such unwanted variation from the feature vectors in order to conserve only that variation which is most correlated with that of the pulp properties.

In order to remove unwanted variations from the pulp image feature vectors various signal correction (spectral filtering) techniques could be used. Some common approaches to filter spectral data that have been proposed in the literature include Multiplicative Signal Correction (MSC) [Geladi et. al., 1985], Standard Normal Variate (SNV) Correction [Barnes et. al., 1989], Savitsky-Golay smoothing [Savitsky et. al., 1964], Orthogonal Signal Correction (OSC) [Wold et. al., 1998], and Orthogonal Projections to Latent Structures (O-PLS) [Trygg et. al., 2001]. The basic idea in all of the above signal correction techniques is to filter the spectral data in order to enhance the predictive power of the regression model. The filtering technique used in this study for signal correction of the pulp image feature vectors to improve the PLS model predictions of pulp properties is the OSC algorithm proposed by Wold et. al. [1998]. This algorithm is pre-programmed in SIMCA-P 9.0 [Umetrics, 2001].

4.4.4.1 Orthogonal Signal Correction to Filter NIR Pulp Image Feature Space

Wold et. al. [1998] proposed a spectral filtering technique called Orthogonal Signal Correction (OSC) to remove from the **X** data systematic variation that is unrelated to **Y**. It is well known that PLS regression models are constructed to *maximize* the covariance between **X** and **Y** [Hoskuldsson, 1988; Burnham et. al., 1996]. OSC uses **Y** to construct a filter of **X** such that its components *minimize* the covariance between **X** and **Y**. In doing so OSC components are calculated such that they are *orthogonal* to **Y**. The OSC components contain unwanted systematic variations in **X**, which are not related with the variations in **Y**. Upon subtracting the OSC components from **X** a filtered predictor matrix is obtained, which contains the variations of interest that are related to the variations in **Y**. Further details about spectral signal correction through OSC have been provided in many references, some of which are [Wold et. al., 1998; Antti, 1999; Eriksson et. al., 1999; Svensson et. al., 2002].

In the pulp modeling study OSC was used to remove the previously mentioned sources of unwanted variation from $\mathbf{X}_{\mathbf{feature}}$ in order to enhance the hidden chemical information in the feature vectors, which is related to pulp property measurements. A maximum of two OSC components were removed from $\mathbf{X}_{\mathbf{feature}}$ due to the dangers of removing too much systematic variation upon removing more OSC components. It can be proven [Svensson et. al., 2002] that it is possible to continually improve correlation between **X** and **Y** if one keeps on removing OSC components from **X**. However this is due to the remaining noise in **X** being most correlated with **Y** upon removing all structural variation. Wold et. al. [1998] suggest removing a maximum of two OSC components from **X** containing NIR reflectance spectra. The amount of information removed by individual OSC components can be determined by observing the remaining % sum of squares (%SS) in **X**. Table 4.2 illustrates the variation removed from $\mathbf{X}_{\mathbf{feature}}$ by two OSC components with respect to the four pulp property variables (**Y**).

Table 4.2 OSC filtering to remove unwanted variations from $\mathbf{X}_{\mathbf{feature}}$

# OSC PC	% Sum of Squares (SS) Remaining in $\mathbf{X}_{\mathbf{feature}}$ after OSC filtering			
	Y = S10	Y = S18	Y = ln(DCM Resin)	Y = Intrinsic Viscosity
1	27.07	22.67	24.29	28.11
2	19.33	14.13	17.00	17.71
Total %SS Removed by OSC (2 PCs)	**80.67**	**85.87**	**83.00**	**82.29**

It can be seen from table 4.2 that two OSC components remove an average of approximately 82% of the original variation in $\mathbf{X}_{\mathbf{feature}}$. The removed variation is mathematically orthogonal to the variation of the pulp properties. The remaining 18% average variation in $\mathbf{X}_{\mathbf{feature}}$ is most related with the pulp properties. A better appreciation of the amount of information removed by OSC can be obtained upon observing the raw and filtered feature vectors of the pulp NIR images. Figure 4.11(a) illustrates feature vectors of two pulp samples from the at-line study. Figure 4.11(b) illustrates the signal corrected feature vectors after filtering with 2 OSC components using **Y** = Intrinsic Viscosity. The same feature vectors have been corrected using 2 OSC components with **Y** = S10 in figure 4.11(c).

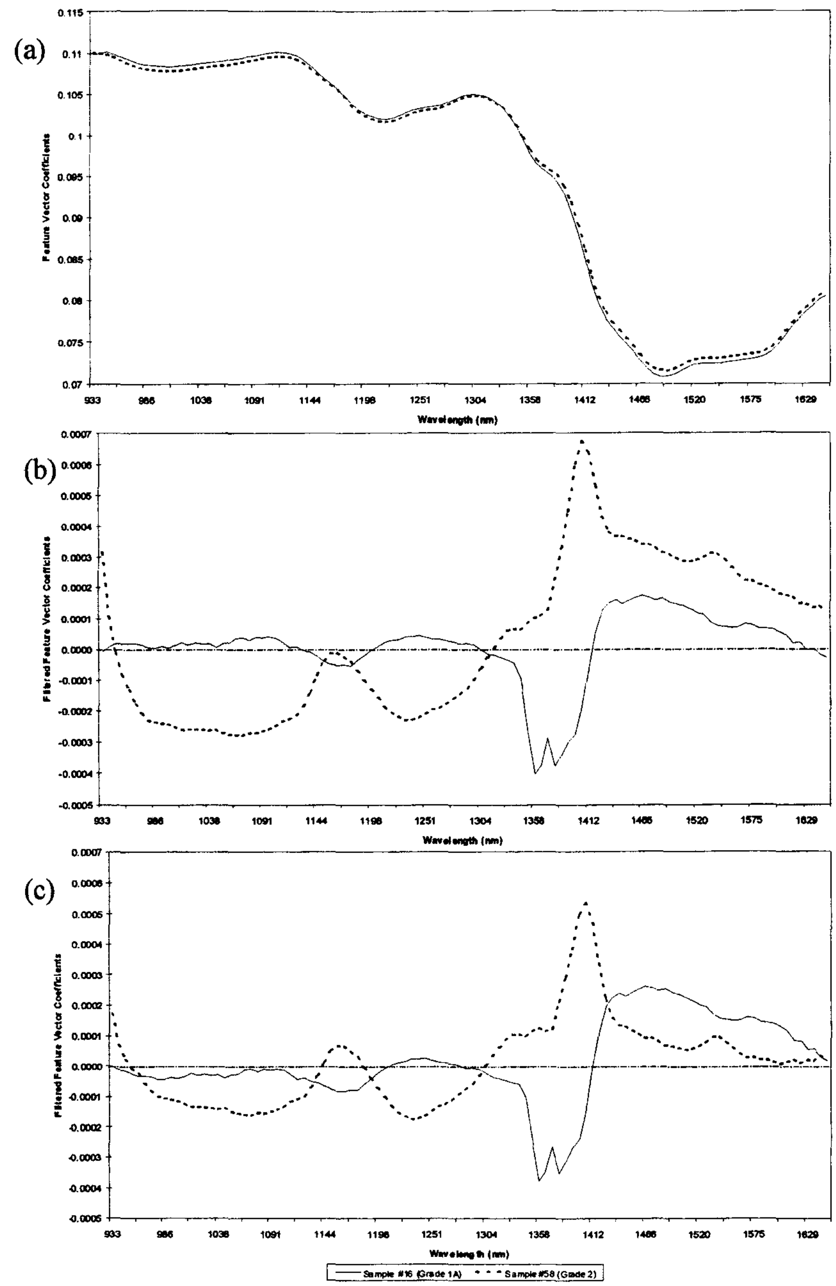

Figure 4.11 Effect of OSC filtering on pulp image feature vectors. (a) Raw feature vectors of two sample images; (b) 2 OSC PC filtered feature vectors (**Y** = Intrinsic Viscosity); (c) 2 OSC PC filtered feature vectors (**Y** = S10)

Upon comparing the magnitudes of the coefficients in the two feature vectors before and after filtering it can be concluded that OSC removes the majority of the variation in $\mathbf{X}_{\mathbf{feature}}$. Furthermore, it can also be observed that OSC removes the trends in the feature vector coefficients with respect to the NIR wavelength spectrum. Subtle differences between the feature vectors are enhanced in certain wavelengths indicating higher information content in specific regions of the NIR spectrum. Such information is most related to pulp property variations in the dataset. The OSC filtered feature space with respect to four different pulp properties was then individually PLS regressed with respective laboratory measured pulp properties to develop the empirical models.

4.4.4.2 PLS Model Results

A separate PLS1 model was developed after each OSC component between individual pulp properties and the signal corrected feature space. Model diagnostics like $R^2_{cumulative}$, $Q^2_{cumulative}$, RMSEE, and RMSEP were used to determine the adequacy of the models with respect to prediction of the four pulp properties. R^2_a is defined as the % of variance of the training data in $\mathbf{X}_{\mathbf{feature}}$ explained by the fitted PLS model with a latent variables. Model predictive ability can be determined by Q^2_a, which is defined as the % of variance of prediction errors obtained by cross-validating [Wold, 1978] the fitted PLS model with a latent variables; $Q^2_a = 1 - PRESS_a/SS_{r(a-1)}$. $PRESS_a$ is the total prediction error sum of squares obtained by cross-validating the model with a latent variables, whereas $SS_{r(a-1)}$ is the residual sum of squares of the model with $a - 1$ latent variables. As $R^2_{cumulative}$ and $Q^2_{cumulative}$ reach values close to one, a very good fit and predictive ability of the model are achieved. RMSEE is defined as the root mean squared error of estimation (fit) of the predicted variables for the fitted data using the PLS model; RMSEE $= \sqrt{\sum(\hat{y}-y)^2/N}$. Here, $\hat{y}$ and y are the predicted and observed values of the response variable, respectively. N is the number of fitted data points. RMSEP is calculated in the same manner as RMSEE, except it is defined as the root mean squared error of prediction for the data *not* used in the model building stage (i.e. on the validation dataset). Further details of the above model diagnostics are provided in the SIMCA-P 9.0 user's guide [Umetrics, 2001].

Table 4.3 shows the PLS results for the four pulp properties (S10, S18, ln(DCM Resin), and Intrinsic Viscosity) each modeled with three separate PLS models (PLS1, 1OSC+PLS1, 2OSC+PLS1). The overall "best" model, highlighted for each pulp property, has been determined by comparing the RMSEE (and RMSEP values where available) with experimental errors from laboratory measurements. The model with the closest values to the experimental errors was chosen. If the RMSEE (and RMSEP) are similar to the experimental errors it can be said that the regression models can fit (and predict) the pulp property at least as good as that obtained from laboratory testing. It can be observed from table 4.3 that signal correction of the feature space using OSC has improved the PLS model performance in terms of fitting (and predicting) the pulp properties.

Table 4.3 PLS Model Results for 4 Pulp Property Variables

S10 (*2σ Experimental Error* = ±0.600)

Method	# Orth PC	# PLS PC	R^2_{cum}	Q^2_{cum}	RMSEE
PLS1		11	1.000	0.445	0.622
OSC+PLS1	1	1	0.543	0.429	1.184
OSC+PLS1	**2**	**1**	**0.407**	**0.813**	**0.545**

S18 (*2σ Experimental Error* = ±0.300)

Method	# Orth PC	# PLS PC	R^2_{cum}	Q^2_{cum}	RMSEE
PLS1		11	1.000	0.265	0.155
OSC+PLS1	1	4	0.961	0.439	0.252
OSC+PLS1	**2**	**2**	**0.890**	**0.964**	**0.068**

ln(DCM Resin) (*Reported 2σ Experimental Error* = ±0.126)

Method	# Orth PC	# PLS PC	R^2_{cum}	Q^2_{cum}	RMSEE
PLS1		2	0.894	0.224	0.919
OSC+PLS1	1	3	0.939	0.588	0.699
OSC+PLS1	**2**	**2**	**0.885**	**0.715**	**0.596**

Intrinsic Viscosity (*2σ Experimental Error* = ±0.223)

Method	# Orth PC	# PLS PC	R^2_{cum}	Q^2_{cum}	RMSEE	RMSEP
PLS1		11	1.000	0.513	0.307	0.504
OSC+PLS1	1	2	0.705	0.521	0.683	0.584
OSC+PLS1	**2**	**3**	**0.911**	**0.894**	**0.289**	**0.451**

Model predictions $\hat{Y}$ are generally compared with observed Y values as $\hat{Y}$ vs. Y scatter plots to assess the quality of prediction. Figure 4.12 illustrates an Intrinsic Viscosity $\hat{Y}$ vs. Y plot for the validation data set. Here the 2OSC+PLS1 (with 3 PC)

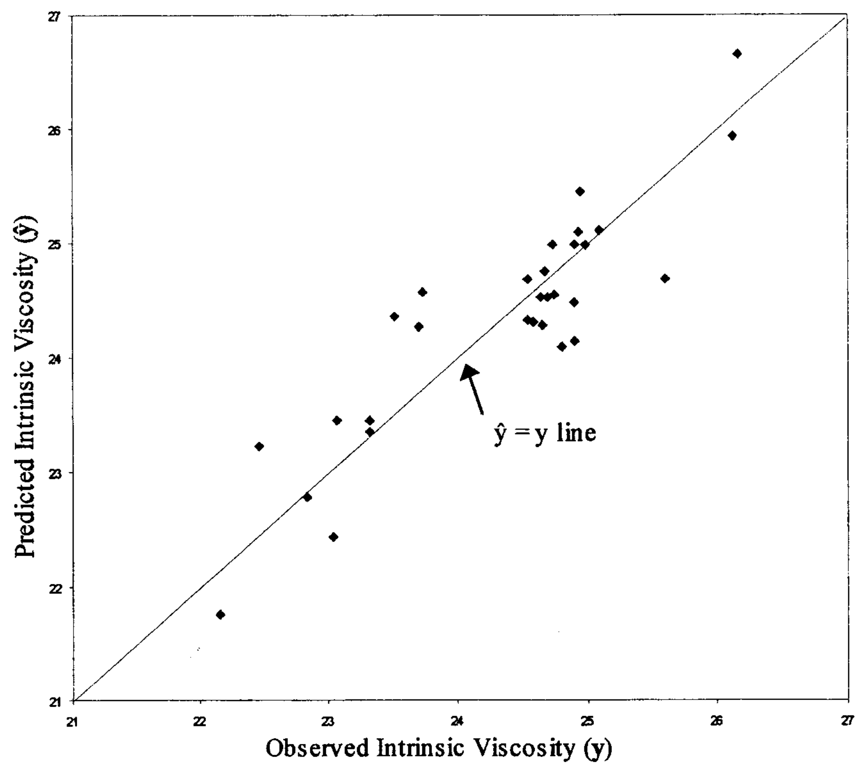

Figure 4.12 Observed versus Predicted ($\hat{Y}$ vs. Y) plot of Intrinsic Viscosity pulp property for the validation dataset

regression model was chosen for predicting Intrinsic Viscosity. Such plots give a good representation of the variability (spread) of the model predictions. An ideal PLS model should predict Intrinsic Viscosity around the $\hat{y} = y$ line (figure 4.12).

Comparing RMSEE and RMSEP with experimental errors also give good *overall* measures of model fit and predictability. However, such analyses do not provide good insight into the ability of the models to follow data trends. Since the at-line study consisted of data collected in a time sequence, it is also important for a good model to capture any time dependent trends in the pulp properties both within and between grades. Such insight is gathered by overlaying experimental results and model predictions on time series plots. The “best” PLS model predictions for each pulp property should be the one that follows the expected trends in the property from grade to grade, and is ideally within the experimental errors of the laboratory measurements. If the PLS model can predict pulp properties within the error bars for most of the samples in the validation set, then one can conclude that the model statistically performs just as good as the laboratory measurements of the true pulp properties.

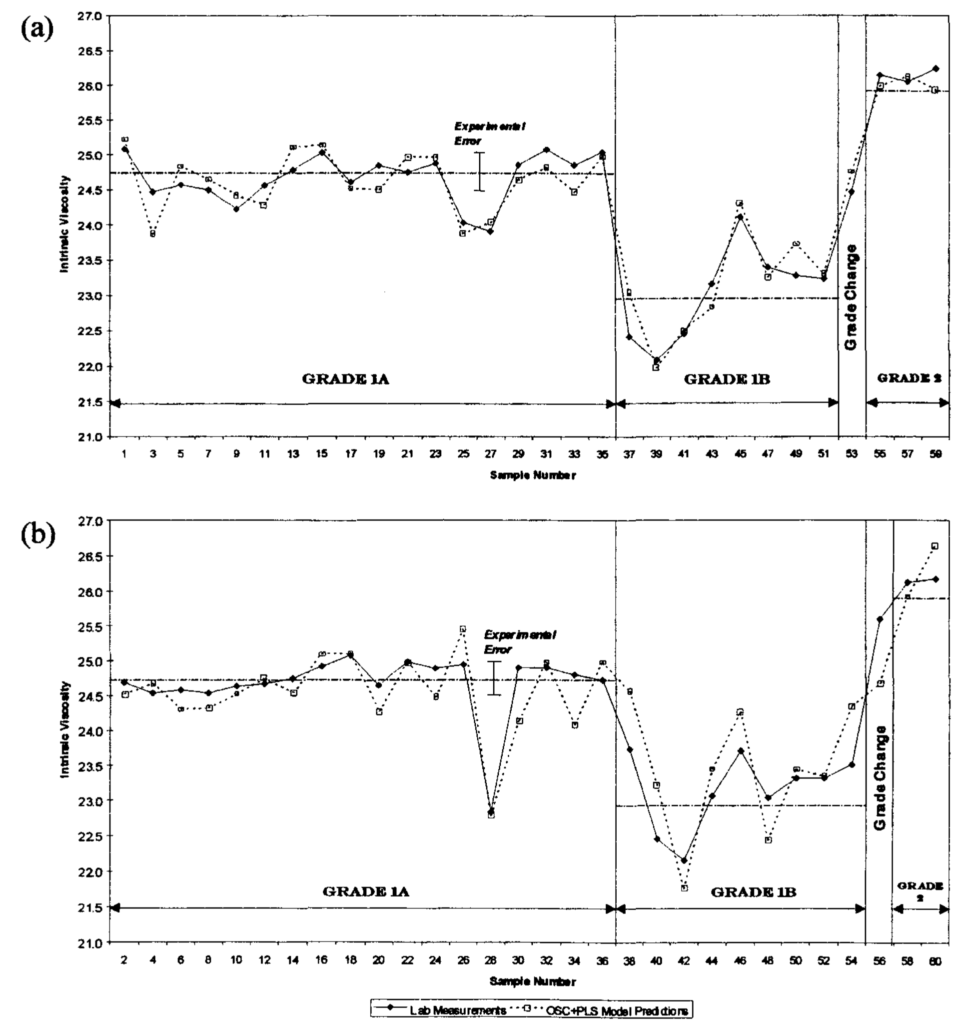

Figure 4.13 Time series plots of Intrinsic Viscosity pulp property laboratory measured data and 2OSC+PLS1(3PC) regression model. (a) Model fitted to training dataset; (b) Model predictions of validation dataset

Figures 4.13(a) and 4.13(b) illustrate the time series plots of the training and validation datasets of the Intrinsic Viscosity pulp property, respectively. One can see

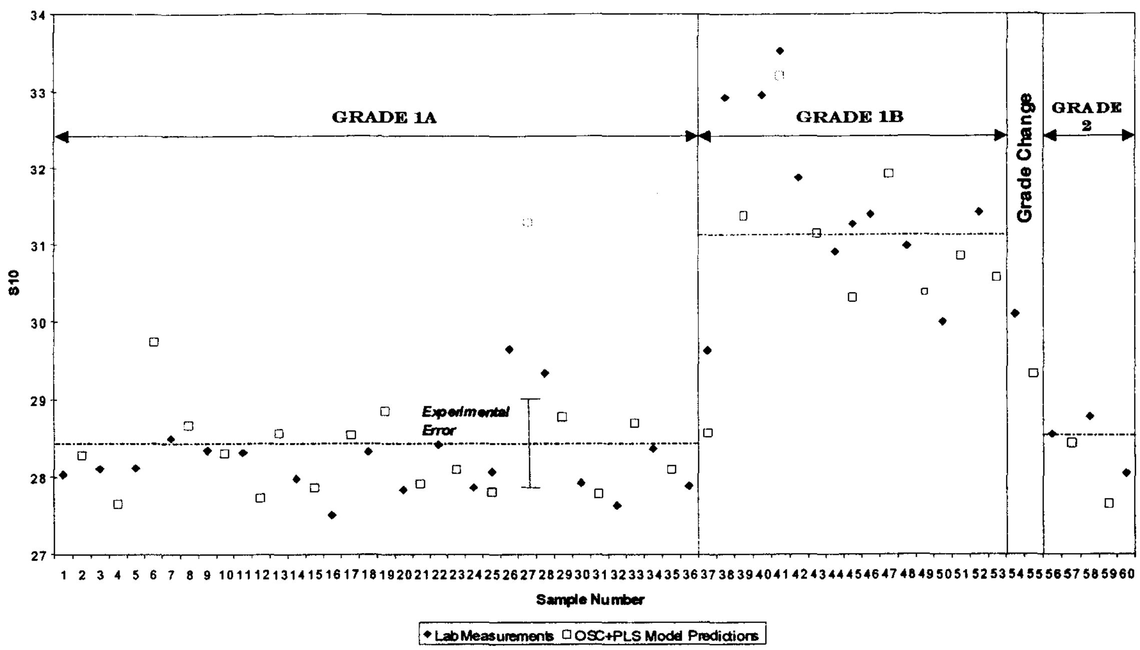

Figure 4.14 Time series plot of S10 pulp property laboratory measured data and 2OSC+PLS1(1PC) regression model

from these plots that the "best" PLS regression model (table 4.3) chosen for Intrinsic Viscosity (2OSC+PLS1 with 3 PC) closely follows the trends of the laboratory measured data from Grade 1A to Grade 1B to Grade 2 for both the training and validation sets. The error bar around the "target value" (dash-dot line) gives an idea of the 2 standard deviations of experimental errors while measuring Intrinsic Viscosity in the laboratory. The model fit and predictions seem generally within the limits defined by the laboratory measurement error bar. Figure 4.13(b) indicates that the OSC+PLS model predictions not only follow the general trends of Intrinsic Viscosity between grades, but the model is also able to detect any process upsets within a grade (e.g. temporary decrease in Intrinsic Viscosity around sample 28 in Grade 1A).

Figure 4.14 illustrates a time series plot of the S10 pulp property. PLS model predictions for the validation set have been overlaid with the training set laboratory measurements as part of a *common* time series plot. This is due to the unavailability of the validation set laboratory measurements for the S10 pulp property. It can be seen in figure 4.14 that the "best" PLS model chosen in table 4.3 (2OSC+PLS1 with 1 PC) performs reasonably well in following the S10 pulp property trends from Grade 1A to Grade 1B to Grade2. Furthermore, this model can also detect the sudden increase in the S10 value for Grade 1A around samples 27 and 28. Thus the model performs well both within and between the grades studied. The experimental error bar (±0.6) has also been illustrated here to visually assess the model's ability to predict the validation set pulp property values (even though the laboratory measured values are unavailable). Similar time series plots are illustrated in Figures 4.15 and 4.16, which represent PLS regression

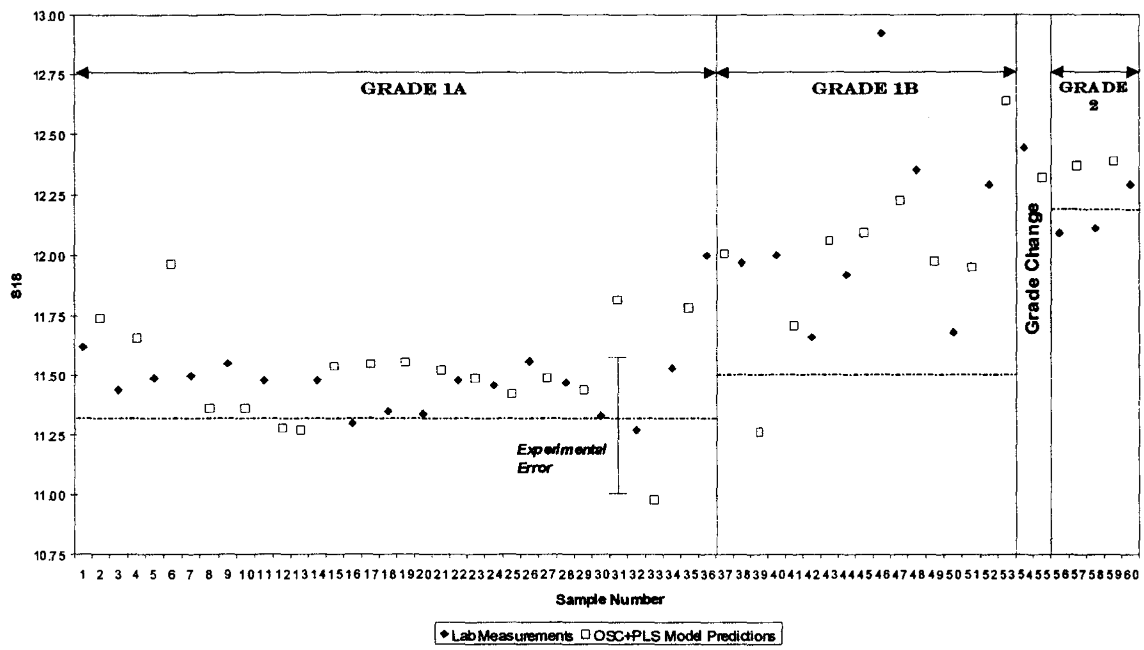

Figure 4.15 Time series plot of S18 pulp property laboratory measured data and 2OSC+PLS1(2PC) regression model

model results for S18 and ln(DCM Resin) pulp properties, respectively. The chosen PLS regression model for S18 (2OSC+PLS1 with 2 PC) also seems to perform reasonably well in following the pulp property trends from Grade 1A to Grade 1B to Grade 2.

It can be seen from figure 4.16 that the PLS model predictions for ln(DCM Resin) are not as good as the other three pulp properties. This could be attributed to the noisy laboratory measurements of the DCM Resin pulp property for Grade 1B and Grade 2. As illustrated in figure 4.16 the laboratory measurements (solid diamonds) for these grades exhibit a bouncing pattern between –15 and –18 for pulp samples 37 to 60. This may

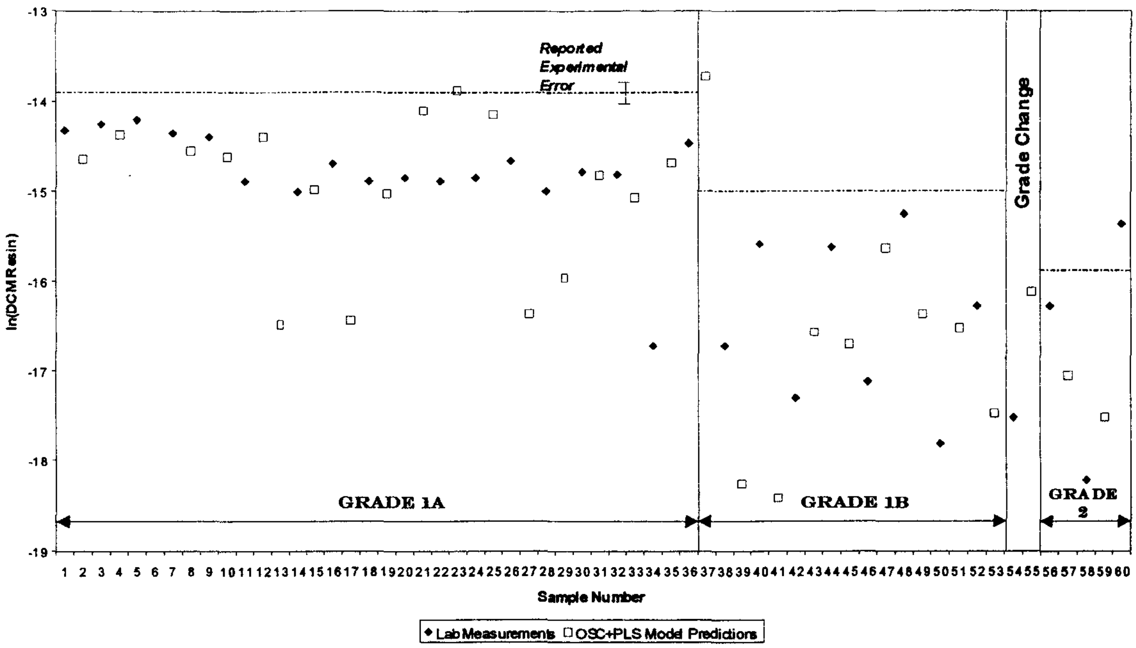

Figure 4.16 Time series plot of ln(DCM Resin) pulp property laboratory measured data and 2OSC+PLS1(2PC) regression model

contribute to a bad training set for the PLS models, which is reflected in the poor predictions of ln(DCM Resin) for the validation set.

In conclusion it can be seen that the proposed MIR scheme can adequately model 3 out of the 4 pulp properties examined in the at-line imaging experimental stage of the preliminary feasibility study. The results also meet the objective of illustrating the potential of NIR imaging spectroscopy and chemometric methods to model finished pulp end properties, which are currently being measured using lengthy (and tedious) wet chemistry techniques in the mill's analytical laboratory. The next logical step of the study would be a detailed analysis including more at-line imaging runs with a larger dataset spanning the full range of pulp grades produced by the mill. Eventually the final aim would be implementing the NIR imaging spectrometer as an integral part of an on-line monitoring scheme for pulp end properties. The tedious laboratory analyses could then be performed by exception (i.e. when a poor prediction is provided by the model), and to keep updating the MIR models after a certain time period.

4.5 Extracting Local Pulp Characteristics Using Global Regression Models

The main objective of the MIR pulp property modeling study presented in the previous section was to relate multi-spectral NIR images of finished pulp samples with their average (global) properties. In doing so the MIR calibration models lost all spatial information of the pulp samples since they used the MPCA loading vectors as the feature space to create the relationship. The work presented in this section tries to extract spatial information of a pulp sample through application of the global MIR model on sub-sections of its multi-spectral NIR image. Doing so would enable prediction of local pulp properties in addition to the previously obtained global property measures.

The reasoning for interrogating local property variations in the pulp sample is to be able to detect any significant spatial trends in the pulp property across its imaged section (e.g. consistently lower predictions of Intrinsic Viscosity on the left half of the image might indicate distributional problems in the process). The proposed strategy thus allows one to interrogate the pulp sample for its heterogeneity with respect to the property being modeled. Measuring pulp heterogeneity with respect to its end properties takes advantage of the 2-dimensional NIR spectra across the pulp sample, which is provided by the imaging spectrometer.

Upon segmenting the multi-spectral NIR image into various sub-sections and applying the global MIR model to predict local pulp properties for each sub-section one can gather a spatial distribution of predicted pulp properties throughout a pulp sample. Such a distribution can be plotted as 1-dimensional or 2-dimensional property prediction histograms. The 1-dimensional histogram gives an idea of the mean and variance of a pulp property as it is distributed through a particular sample image. The mean property prediction gives an overall measure (similar to the global MIR model predictions of the previous section), whereas the variance provides a measure of pulp heterogeneity with respect to the property being predicted.

In a typical monitoring scheme one could track both means and variances of 1-dimensional property prediction histograms for various pulp samples. If a sample with high variance is encountered it can then be visually interrogated through a color-coded 2-dimensional histogram of the predicted pulp property across the sub-sections of the pulp image.

The ideas of the proposed scheme are illustrated through an example of calculating the Intrinsic Viscosity distribution across pulp sample 16 from the at-line imaging experiment. As seen from figure 4.13(b) the chosen pulp sample belongs to the validation dataset. The laboratory measured Intrinsic Viscosity value (along with 2σ experimental errors) for the pulp sample was 25.03 ± 0.22, whereas MIR prediction using the OSC+PLS regression model was 25.14. The 448 pixel (L) $\times$ 102 pixel (W) $\times$ 108 pixel (λ) multi-spectral NIR image of the entire pulp sample was segmented into 48 sub-sections, each with dimensions 56 pixels (L) $\times$ 17 pixels (W) $\times$ 108 pixels (λ). Using the overall OSC+PLS MIR model coefficients with every sub-section image 48 individual Intrinsic Viscosity predictions were obtained across the scanned surface of the pulp sample. Figure 4.17 illustrates a 1-dimensional histogram of the 48 Intrinsic Viscosity predictions with a mean value of 24.90. The mean of the 48 predictions is a good indicator of the overall pulp Intrinsic Viscosity as it is within the 2σ experimental error of the laboratory-measured value (25.03 ± 0.22).

Although the mean Intrinsic Viscosity prediction across the 48 sub-sections is good the variance of the distribution is quite high at 41.21, with predictions ranging between 12.24 and 35.57. This can also be confirmed from figure 4.17 as the 1-dimensional histogram is in fact divided into 3 sub-distributions. Since the global MIR model has been applied on small image sub-sections one would expect the variance of predictions to be high as the individual predicted Intrinsic Viscosity of each sub-section would be influenced by local effects.

A better understanding of how the Intrinsic Viscosity predictions are distributed across the pulp image can be obtained through a 2-dimensional histogram of the 48 sub-sections. Figure 4.18 illustrates a color-coded 2-dimensional histogram of Intrinsic

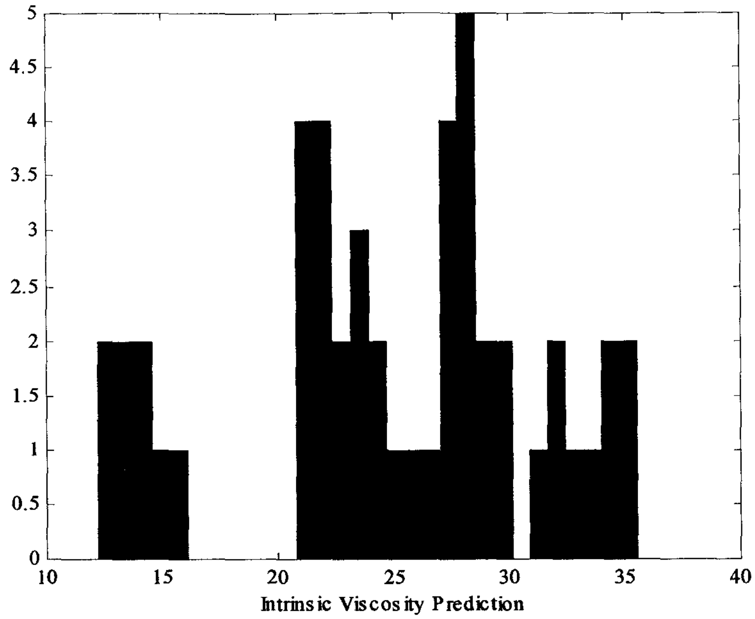

Figure 4.17 A 1-dimensional histogram of 48 Intrinsic Viscosity predictions across sub-sections of pulp sample 16 from at-line imaging experiment

Viscosity predictions across the 48 sub-sections of the pulp sample image. For comparison the segmented score image T_1 (upon performing MPCA decomposition of the multi-spectral NIR pulp image) has also been illustrated. It can be seen from the streaky patterns of the predicted pulp property in figure 4.18(b) that local effects are greatly influencing the overall variance of predicted Intrinsic Viscosity.

Upon closely observing the spatial trends of Intrinsic Viscosity predictions in figure 4.18(b) it appears that the vertical patterns are a result of influences by lighting and camera anomalies. A clearer visual representation of such anomalies is highlighted in figure 4.3(b) for the paper characterization study.

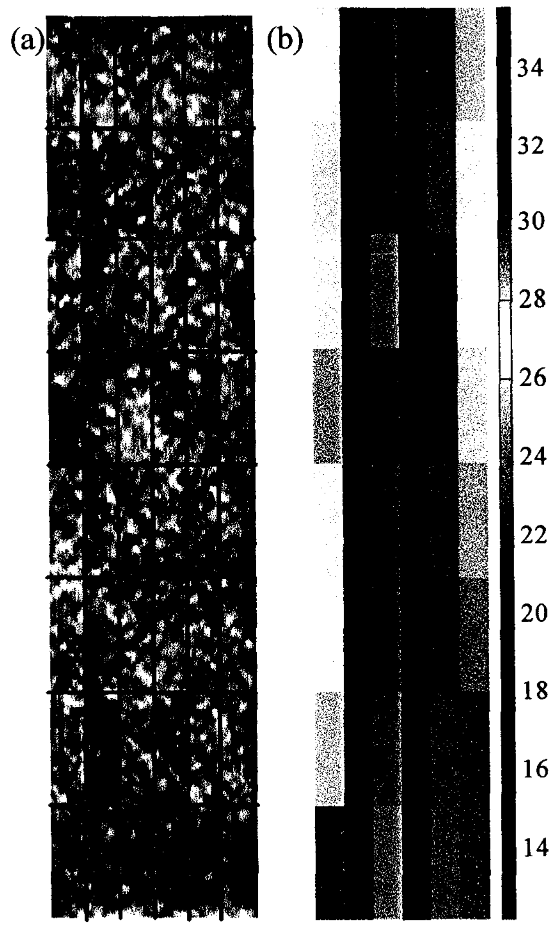

Figure 4.18 Intrinsic Viscosity distribution across 48 sub-sections of multi-spectral NIR pulp image of sample 16 from at-line experiment. (a) Segmented $\mathbf{T}_1$ score image of MPCA; (b) Color-coded 2-dimensional distribution of pulp property predictions

Since the NIR imaging spectrometer scans the pulp sample as a line-scan camera, if one were to segment the scanned line into sub-sections any lighting variations and camera anomalies across the imaged line would be enhanced in local areas. In order to average the effects of these anomalies the segmentation of the multi-spectral NIR image should preserve the full width of the scanned line. As a result, a new image segmentation scheme was used to divide the pulp image into 8 vertically aligned sub-sections that covered the full width of the original pulp sample image. The dimension of each sub-section was 56 pixels (L) × 102 pixels (W) × 108 pixels (λ). This segmentation preserved a constant effect of the lighting and camera anomalies over the 8 sub-sections. The new segmentation technique would also be more appropriate if one wanted to use the overall

MIR (OSC+PLS) model as part of an on-line Intrinsic Viscosity monitoring scheme. The overall model could be applied on sub-sections of the pulp web defined by a set number of scanned lines imaged by the spectrometer as the pulp passes under it.

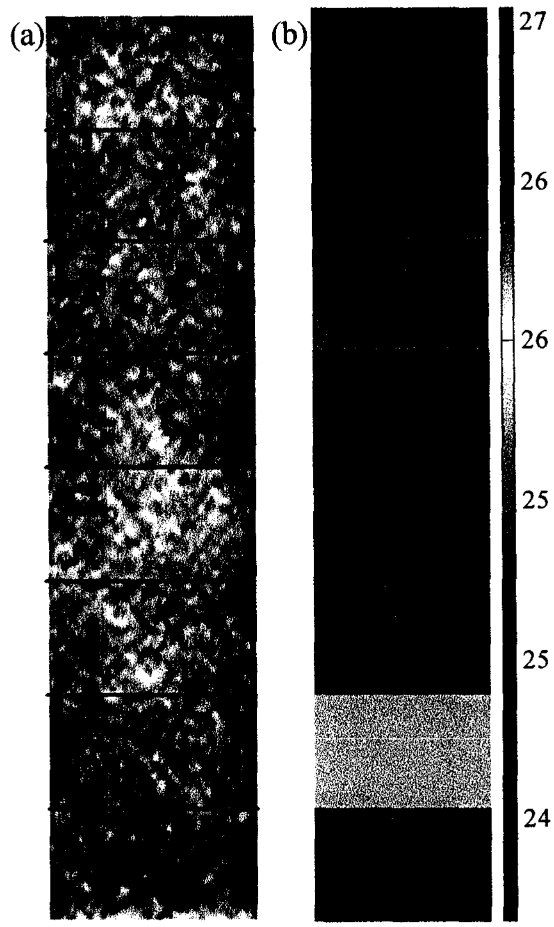

Figure 4.19 Intrinsic Viscosity distribution across 8 sub-sections of multi-spectral NIR pulp image of sample 16 from at-line experiment. (a) Segmented $\mathbf{T}_1$ score image of MPCA; (b) Color-coded distribution of pulp property predictions

Figure 4.19 illustrates the distribution of Intrinsic Viscosity predictions across 8 sub-sections of the pulp sample image upon using them with the overall OSC+PLS regression model coefficients. The corresponding segmented $\mathbf{T}_1$ score image has also been illustrated. The mean Intrinsic Viscosity prediction over the 8 sub-sections was 25.14, which was within the 2σ experimental errors of the overall laboratory measured values (25.03±0.22). The true improvement of segmenting the image using the new scheme was in the variance of the predicted properties across the 8 sub-sections, which was considerably lower at 0.849 (compared to a variance of 41.21 in the previous segmentation scheme).

The physical dimensions of the pulp sample area scanned by the imaging spectrometer were 140 mm (L) × 93 mm (W). Compared to the approximate 4.25 m width of the web upon which finished pulp is produced in the mill the imaging spectrometer covers <1% of its true horizontal dimension. As a result, it would be reasonable to assume very little variability in the spatial distribution of predicted Intrinsic Viscosity across the sub-sections of the multi-spectral NIR pulp image. This is also evident from the small variance of the predicted property distribution through the 8 sub-sections of the pulp sample image. In spite of the small variations the study develops a framework to interrogate sub-sections of finished pulp in order to investigate their predicted end properties. In future these concepts can be directly up-scaled if one had a camera focused to capture the full width of the industrial pulp roll. Although the spatial resolution of such an image might be reduced, this could be a worthwhile compensation if the heterogeneity measure were of more importance for the application.

It can be seen in figure 4.19(b) that predicted Intrinsic Viscosity of the bottom two sub-sections is higher than the predictions of the top 6 sub-sections, and in figure 4.18(b) that the predictions of the left and right vertical edges are higher than the middle sections. This trend is attributable to reflectance from the edges of the plastic frame, which was placed on top of the pulp samples while performing the at-line imaging experiment. Figure 4.8(a) illustrates the position of the plastic frame while imaging was performed. As mentioned in section 4.4.2 all pulp sample images were manually cropped at the edges of the frame to remove it from the image. Plastic contains several organic compounds thus it exhibits a unique NIR reflectance signature. This reflectance appears to have interfered with that of the pulp sample at the left, right and bottom edges of the image. However, this interference was not strong enough to interfere with the overall pulp property predictions, which were averaged across the width of the image. As a result, the Intrinsic Viscosity predictions in the top 6 sub-sections in figure 4.19(b) were close to the mean value. The interference from the bottom edge was much stronger as it was along the direction of the line-scan, which reflected brighter upon shining the line light on it at an angle of 45° (figure 2.6). These interferences cause the NIR spectrum of the pixels near the bottom edge of image to be altered, which results in higher Intrinsic Viscosity predictions as the bottom edge is approached.

Though the segmentation schemes presented above highlighted several anomalies with respect to the equipment and experimental set-up the pulp end property predictions obtained via the overall MIR modeling scheme (in section 4.4) are still valid. This is due to the averaging achieved by the feature vectors ($\mathbf{p}_1$ loadings of MPCA) over all pixels (good and bad) in the scanned image. The overall regression models calculated in the previous section would give consistent results as long as the experimental conditions remain constant in terms of equipment and set-up. However, the segmentation scheme has revealed several potential areas for improvement, which should be implemented in future experiments (e.g. fixing lighting anomalies, and using a frame that does not have a reflectance signature in the NIR spectrum).

The proposed image segmentation technique in the above study highlights several problems in the at-line experiment ranging from lighting effects to experimental set-up. Despite these problems the concept of the proposed scheme is promising as it can be used to detect spatial trends or variations in the pulp property across the imaged section. Such trends give vital heterogeneity information of the pulp sample, which cannot be obtained by averaged property measures in the laboratory or single point probe-based spectrometer readings. The technique illustrates potential advantages of using image-based spectrometers to simultaneously extract spatial and spectral feature information from multi-spectral images.

4.6 Conclusions and Contributions

A framework for a novel Multivariate Image Regression modeling technique has been developed in this work. The proposed technique can be used to relate feature information from multivariate images of finished products with corresponding quality (non-image) data obtained from other sources. Once trained, the MIR model can then potentially be used to infer quality data from product images in on-line industrial processes equipped with multivariate imaging sensors. The proposed technique has been illustrated through a feasibility study on a pulp manufacturing industrial application with promising results.

The chapter also introduces Near-Infrared imaging spectroscopy to the pulp and paper sectors of the forest products industry. Two main applications have been presented to illustrate the power of this technique in extracting relevant feature information from pulp and paper samples. A Multivariate Image Analysis based strategy has been proposed to extract overall features from multi-spectral images of pulp and paper scanned by a NIR imaging spectrometer.

The first application involves paper classification using NIR imaging spectroscopy to extract relevant chemical and ingredient information from well-characterized paper samples. The extracted feature vectors are classified using standard chemometric methods (PCA) in order to gain further insight of the extracted information. This study illustrates that the extracted feature space from multi-spectral NIR images contains vital information, which can be further used.

Besides classification the potentials of using the feature space for predicting quality data has been illustrated in the second application, which is a feasibility study in the pulp manufacturing industry. MIR models are developed using Orthogonal Signal Corrected feature vectors and PLS regression techniques to predict pulp end properties from multi-spectral NIR images of finished pulp samples. The pulp end property data has been acquired through lengthy wet chemistry analyses in the quality control laboratory of the pulp mill. Preliminary results of the proposed scheme show promise in successfully predicting and monitoring three out of the four pre-selected end properties through multiple pulp grades in an industrial mill. The eventual aim of the study is to incorporate the proposed MIR modeling technique with NIR imaging spectroscopy in an on-line pulp quality monitoring scheme.

Finally, the chapter develops concepts for studying the spatial variability of quality variables across the imaged surface of a product through application of the proposed MIR models on sub-sections of the product image. The technique is presented with an example study to extract variations in spatial characteristics of pulp, which are related to its overall end properties. The technique may be used to monitor pulp heterogeneity with respect to its end properties in future applications of the proposed MIR scheme.

Chapter 5
Texture Based Classification of Steel Surface Images

This chapter proposes a novel MIA based textural feature extraction technique. Performance of the proposed technique is compared with other texture analysis methods on a set of steel sample images for the purpose of image classification based on surface roughness characteristics.

As opposed to color and multi-spectral images used in the previous chapters of the thesis, methods presented here exclusively use grayscale image data for texture analysis.

5.1 Introduction

Although image texture is not very well defined in the literature, one can intuitively describe several image properties such as smoothness, coarseness, depth, regularity etc. with texture [Gonzalez et. al., 2000]. Many researchers have described texture using various definitions. Russ [1999] loosely defined image texture as a descriptor of local brightness variation from pixel to pixel in a small neighborhood through an image. If the image can be represented as a two-dimensional surface upon which each pixel is a square column, then the pixel intensity could be described by the elevation of each column in a three-dimensional histogram. As the adjacent pixel brightness variation increases, the surface of the three-dimensional histogram becomes less smooth. Texture can thus give a quantitative measure of the degree of surface roughness in an image.

In traditional image processing literature there are primarily three different approaches used to describe the texture of a region in an image. The three approaches are *statistical*, *structural*, and *transform-based* texture analysis methods. Statistical texture analysis techniques primarily describe texture of regions in an image through moments of its grayscale histogram. According to the number of pixels defining the local region (i.e. feature) first, second, or higher order statistics of the grayscale histogram can be used to extract textural features from images [Tomita et. al., 1990]. On the other hand, structural texture analysis techniques decompose a pattern in an image into texture elements (e.g. description of interlocked bricks in an image using regularly spaced parallel lines). In structural analysis the properties and placement rules of the texture elements define the image texture. Finally, transform-based texture analysis techniques convert the image into a new form using the space-frequency properties of the pixel intensity variations. The success of these latter techniques lies in the type of transform used to extract textural characteristics from the image. An example of one such transform is the 2-dimensional Fast Fourier Transform (2-D FFT) power spectrum, where spatial frequency information becomes easily accessible. Surveys on many of these texture analysis methods can be found in the literature [Zucker, 1976; Haralick, 1979; Matsuyama et. al., 1980].

Texture analysis has been an area of intensive research over the past 30 years. A comprehensive literature review of all proposed textural feature extraction techniques is beyond the scope of this thesis. However, a brief review of some popularly used texture analysis methods in the literature is provided below. Probably the most frequently cited method for texture analysis is based on extracting various textural features from a gray level co-occurrence matrix (GLCM) introduced by Haralick et. al. [1973]. He suggested 14 such features describing various textural aspects of the image. The GLCM method of texture analysis is further described in section 5.3 with respect to feature extraction and classification of steel surface grayscale images.

While the GLCM is a result of second order statistics on the grayscale image histogram, the run length matrix (RLM) encompasses higher order statistics of the gray level histogram. The RLM texture analysis approach characterizes coarse textures as having many pixels in a constant gray level run and fine textures as having few pixels in such a run [Galloway, 1975]. The texture spectrum (TS) matrix is a result of decomposing the texture image into a distribution of texture units, which are sets of coded comparison elements that are based on the pixel intensity variations within a neighborhood [He et. al., 1991]. Features extracted from TS have been combined with the GLCM to propose a cross-directional texture matrix (CDTM) for purposes of image classification [Al-Janobi, 2001]. Besides traditional statistical texture analysis, multivariate statistical methods have also been proposed for textural feature extraction. Singular Value Decomposition (SVD) spectrum is a summary vector of image texture represented by its singular values. The SVD spectrum has been used as a textural feature vector for image classification [Ashjari, 1982; Kvaal et. al., 1996].

Several model-based statistical texture analysis techniques have been proposed in the literature. These techniques generate an empirical model of each pixel in the image based on a weighted average of the pixel intensities in its neighborhood. The estimated parameters of the image models are used as textural feature descriptors. Coarse textures exhibit similar parameters, whereas the parameters for fine textures show a wide variation. Examples of such model-based texture descriptors are autoregressive (AR) models [Sarkar et. al., 1997], Markov random fields (MRF) [Cross et. al., 1983], and fractal models [Keller et. al., 1989].

Structural texture analysis techniques use the basic theory of image morphology [Serra, 1982] to match the spatial regularity of shapes called structural elements to define texture. Pure structural models of texture presume that image texture is a quasi-periodic arrangement of structural elements, whose description and placement rules can be used to describe texture [Roesnfeld et. al., 1970]. Several structural texture analysis approaches have been proposed in the literature, ranging from various shapes of structuring elements

[Carlucci, 1972] to conceiving real textures as distorted versions of ideal textures [Zucker, 1976].

Haralick [1982] described the autocorrelation function and the power spectrum of an image as measures of its spatial frequency characteristics. Yaglom [1962] proved that the relation between the power spectrum and autocorrelation function is through the Fourier transform. The 2-D FFT magnitude image is a visual representation of the power spectrum, which can be used to determine the spatial frequency of pixel intensities in an image. Fine textures are rich in high spatial frequencies, while coarse textures are rich in low spatial frequencies. Indhal et. al. [1998] illustrated the use of spectra from 2-D FFT magnitude images and the autocorrelation function for textural feature extraction from microscopic images. Image classification using MPCA on 2-D FFT magnitude images as feature extractors from various images has been proposed by Geladi [1992]. This approach is also used in section 5.4.1 to classify steel surface images based on texture differences.

Besides 2-D FFT the Gabor and Wavelet transforms are two of the more recently used transform-based texture analysis techniques. Both of these techniques have been preferred in image texture analysis due to their time-frequency decomposition ability. Features derived from a set of Gabor filters have been widely used in texture analysis for image segmentation [Bovik et. al., 1990]. Wavelet transform method of feature extraction has been used to characterize texture and to treat the problems of texture segmentation and classification [Chang et. al., 1993; Loum et. al., 1995; Unser, 1995]. A novel application of an Angle Measure Technique (AMT), originally developed by Andrle [1994], has been reported to extract textural feature vectors from unfolded image pixel values of several texture images for purpose of characterization and prediction of externally measured reference texture using multivariate statistical techniques like PCA and PLS [Kvaal et. al., 1998; Huang et. al., 2000].

Work presented in this chapter contributes to the field of textural feature extraction for image classification via introducing a novel MIA based image texture analysis technique. As seen in the previous chapters of the thesis MIA decomposes feature pixels into PC score scatter plots based on correlations in the variables of a multivariate image. The spatial location of pixels is completely ignored when performing the decomposition. Since image texture is a spatial property spatial correlations need to be conserved in order to capture adequate textural features. The proposed technique incorporates spatial information in the MIA framework, thus enabling MIA tools to be used for capturing textural features from images. These features can then be used for texture based image classification.

The proposed MIA technique is applied for textural feature extraction and classification of a dataset comprising of 35 steel surface images with varying degrees of surface roughness. Results are then compared with the classification achieved by other textural feature extraction methods (i.e. features from GLCM) and multivariate statistics based image classification methods on the same dataset.

The chapter progresses as follows. First, a brief description of the steel image dataset is provided, and the image classification objectives based on surface texture characteristics are presented. Second, classification of the steel dataset is performed in the feature space extracted via pre-selected textural features from GLCMs of the steel surface images. Third, PCA based unsupervised classification of the steel surface images is presented, which uses textural features extracted by 2-D FFT magnitude images of the dataset. Fourth, application of a supervised image classification scheme is illustrated through PLS-DA of the raw steel surface images. Fifth, methodology of the novel MIA based texture analysis scheme is presented, and it is then used to classify the steel surface images. Finally, some conclusions are drawn upon comparing classification results achieved by the proposed MIA technique with those obtained by the multivariate statistics based and GLCM based techniques.

5.2 Description of Steel Surface Image Data and Classification Objectives

The steel manufacturing industry maintains product quality using various process monitoring and feedback control techniques. Human intervention is still required to determine if product quality is maintained over long periods of time. Prior to shipping, steel quality is often monitored by performing random quality control checks on finished steel rolls. This is usually accomplished by cutting sections of a particular roll and performing various tests on the sections to determine if the characteristics of the product meet consumer specifications.

One of the indicators of overall product quality is smoothness of the steel surface. As the steel quality declines, it affects the surface properties of the product. This results in a coarser surface. The amount and distribution of surface pits on steel are good indicators whether or not steel surface quality has been compromised. Deteriorated steel quality is reflected in the number and severity of pits that form on its surface. Good quality steel surfaces have very few pits that are quite shallow and are randomly distributed. These surface pits become deeper and more pronounced as steel quality becomes poorer. The point when pits start to join and result in deep craters throughout the steel indicates a coarser surface, which results in bad product. Skilled operators visually determine the degree of steel surface pitting. These operators grade the steel based on various criteria that they have set for themselves from previous experiences. Unfortunately, these criteria are quite vague and operator dependent.

To eliminate the uncertainly caused by qualitative human grading, a vision based automated steel surface texture analysis system is desirable. Such a system should ideally be able to provide a more quantitative analysis of the steel surface roughness. Furthermore, based on these results the system should also be able to automatically classify steel samples into different roughness grades.

In order to develop such an automated system the steel manufacturing company carried out an off-line feasibility study using digital images of steel slabs with different surface roughness properties. Several steel slabs with varying degrees of surface pits were cut from finished steel rolls and digitally imaged in the laboratory. However, in order to highlight the surface pits, prior to imaging, each slab was pre-treated by pouring black ink upon the surface. After the ink had filled into the pits, the steel slabs were lightly cleaned with a cloth. This resulted in the steel surface pits being represented by black spots. The stained steel slabs were then digitally imaged as grayscale images.

Figure 5.1(a) illustrates an example grayscale image of a steel slab that has good surface qualities due to the nature and distribution of surface pits. An example of a bad steel surface quality grayscale image is shown in Figure 5.1(c), which contains various '*snake*' like patterns representing deep pits that have joined to form craters. Figure 5.1(b) illustrates an example of a medium quality steel surface, which contains more pronounced pits as compared to the good quality sample. However, it does not contain the serpentine patterns exhibited by the bad quality steel. It can be noted in all 3 types of steel surface images that due to the manual cleaning of excessive ink with a cloth several ink smudge marks are also evident on the steel surfaces. Similar smudge marks are prevalent throughout the dataset used in this study.

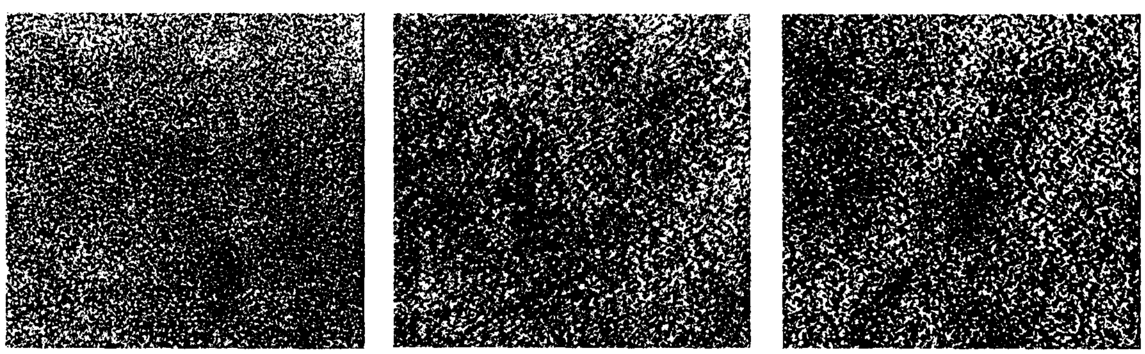

(a) (b) (c)

Figure 5.1 Examples of three types of steel surface grayscale images. (a) Good surface quality; (b) Medium surface quality; and (c) Bad surface quality

A total of 35 control steel slabs of varying surface smoothness were imaged after they underwent the ink pre-treatment process. These samples were also pre-analyzed by a trained operator for grading the steel (based on surface roughness) and each sample was labeled as good, medium, or bad surface quality (classes). Images of these control steel samples have been used for all textural feature extraction and classification methods throughout this chapter. The final objective is to determine classification efficiency of the presented techniques using the pre-labeled classes as a benchmark for comparison. It should be noted that the pre-labeled classes do contain error as a single person subjectively performed the classification. As pointed out later in this chapter there is some inconsistency between the good and medium surface quality classes. Some of the pre-labeled medium surface quality sample images are visually very close to those from the good surface quality class. Therefore, all steel image classification methods described in this chapter should be judged in context with this inconsistency in the original pre-labeling.

Table 5.1 Pre-labeled classes of the complete steel surface grayscale image dataset

Good Surface			***Medium Surface***			***Bad Surface***		
Image Label			Image Label			Image Label		
Original (Figure C.1(a))	Sample ID	Image Mean	Original (Figure C.1(b))	Sample ID	Image Mean	Original (Figure C.1(c))	Sample ID	Image Mean
001_aj	G01	0.5846	031_aj	M01	0.6105	091_aj	B01	0.4681
003_bj	G02	0.5405	032_bj	M02	0.5792	091_bj	B02	0.4708
004_aj	G03	0.5864	036_bj	M03	0.5324	092_aj	B03	0.4849
004_bj	G04	0.5773	039_aj	M04	0.5191	092_bj	B04	0.4749
007_aj	G05	0.5170	041_aj	M05	0.5382	093_aj	B05	0.4882
007_bj	G06	0.4894	047_bj	M06	0.6127	093_bj	B06	0.4896
008_aj	G07	0.4824	049_aj	M07	0.6220	094_aj	B07	0.4424
008_bj	G08	0.4789	052_aj	M08	0.6290	099_aj	B08	0.5031
015_aj	G09	0.5721	057_aj	M09	0.6165	099_bj	B09	0.5130
017_aj	G10	0.5988	061_aj	M10	0.6251	100_aj	B10	0.4832
-	-	-	063_aj	M11	0.6199	100_bj	B11	0.4876
-	-	-	065_bj	M12	0.5468	108_aj	B12	0.5192
-	-	-	073_bj	M13	0.5557	-	-	-
Overall "Good Class" Mean		**0.5427**	Overall "Medium Class" Mean		**0.5852**	Overall "Bad Class" Mean		**0.4854**
Std. Dev. Of Sample Means		0.0472	Std. Dev. Of Sample Means		0.0410	Std. Dev. Of Sample Means		0.0207

Appendix C contains the complete steel surface image dataset from the three pre-labeled surface quality classes. Each image is 8-bit grayscale (256 shades) with pixel dimensions of 479 × 508 (rows × columns). All images have been pre-processed to enhance their contrast via intensity stretching [Thompson et. al., 1995] their grayscale histograms to occupy the full intensity range (i.e. 256 shades of gray between black and white). Table 5.1 shows the division of 35 sample images into their respective pre-labeled classes. Individual image labels and some basic 1st order image statistics (sample means and standard deviations of class means) have also been provided, which would be used for interpreting the classification results achieved by various techniques presented in this chapter.

5.3 Image Texture Analysis and Classification Using Co-occurrence Matrix Features

Texture features calculated using first order statistics of the grayscale histogram of an image are susceptible to the limitation that they provide no information regarding the relative position of the pixels. Haralick et. al. [1973] proposed second order statistics based on the gray level co-occurrence matrix (GLCM), which is a 2-dimensional histogram, to overcome these limitations.

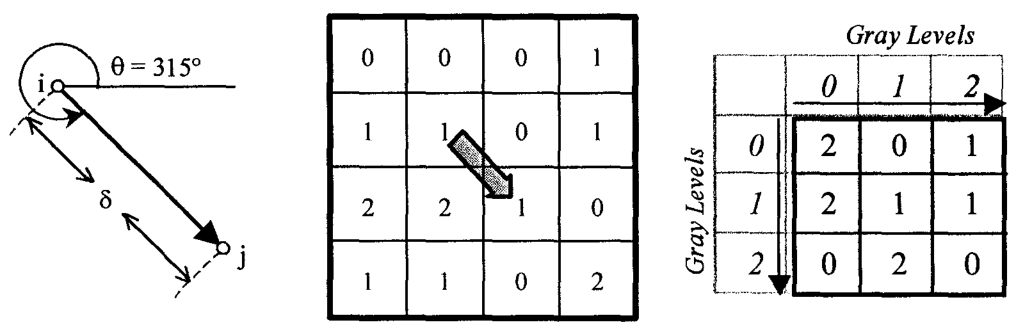

(a) (b) (c)

Figure 5.2 (a) Displacement vector with δ = 1, and θ = 315°; (b) A 4 × 4 pixel intensity image array with 3 gray levels; (c) GLCM of image in (b) using displacement vector in (a).

The GLCM of an image is an estimate of the second order joint probability $P_\delta(i,j)$, of the intensity values of two pixels (i and j) a distance δ apart along a given direction θ (i.e. the probability that i and j have the same intensity). This joint probability takes the form of a square array $\mathbf{P}_\delta$, with row and column dimensions equal to the number of discrete gray levels (intensities) in the image being examined. Figure 5.2 illustrates an example of a 4 × 4 pixel intensity image with 3 discrete gray levels (0,1,2), and the corresponding GLCM with $\delta = 1$, and $\theta = 315°$ [i.e. a displacement vector $(x_{lag}, y_{lag}) = (1,1)$]. The GLCM illustrated in figure 5.2(c) contains the number of times a given pixel pair, separated by the displacement vector, has a unique gray level combination. For example, the element in the 2nd row and 1st column (i.e. the number 2) in the GLCM corresponds to the number of times the displacement vector encounters a pixel with gray level 1, when starting at a pixel with gray level 0. If an intensity image were entirely flat (i.e. contained no texture) the resulting GLCM would be completely diagonal. As the image texture increases (i.e. as the texture becomes coarser) the off-diagonal values in the GLCM become significant.

Pixel intensity resolution of the steel surface grayscale images used in this chapter is 8-bit, which would result in GLCMs with dimensions of 256 rows × 256 columns for a given displacement vector. Finding GLCMs for all δ and θ would require a prohibitive amount of computation. Haralick et. al. [1973] suggested using GLCMs calculated from four displacement vectors with $\delta = 1$, or 2 pixels, and $\theta = 0°$, 45°, 90°, and 315°. Another reduction in computation speeds can be achieved by quantizing the image into a fewer gray levels.

In the steel surface texture analysis study GLCMs were calculated for all 35 grayscale images without re-quantizing the gray level resolution. Due to the computational overload 1 or 2 GLCMs are commonly calculated on a texture image with a set combination of δ and θ. Changing θ controls the direction of the examined textural features in an image. Since texture in the steel images is independent of rotation, there would be little effect of changing θ on their analysis. Changing δ can control the scale of the examined textural features in an image. In the steel classification study only one GLCM was calculated for each grayscale image using a single displacement vector with $\delta = 1$, and $\theta = 315°$ [$(x_{lag}, y_{lag}) = (1,1)$]. The scale of the displacement vector was intentionally chosen to be 1 for sake of consistency with the MIA based texture analysis method (described in section 5.4.3), which concentrates on examining steel surface texture displaced by one pixel. Each of the 35 resulting GLCMs for the steel surface dataset could be visually represented as a 256 × 256 element 2-dimenional color-coded histogram with the same coloring scheme previously used to describe the PC score scatter plots of MIA (section 2.3.1). Such a representation could be used for a qualitative analysis through visually determining the probability distribution of gray levels separated by the displacement vector. Figure 5.3 illustrates the resulting GLCMs of the previously illustrated (figure 5.1) example steel surface grayscale images from each of the three surface quality classes.

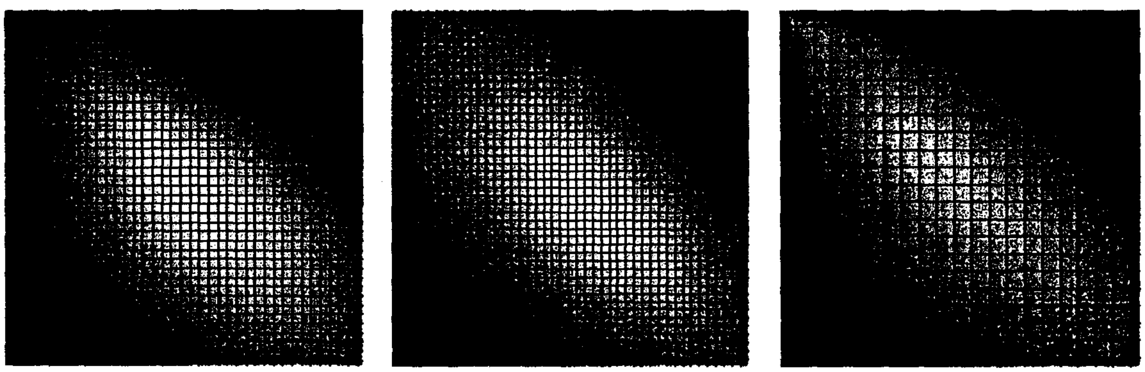

(a) (b) (c)

Figure 5.3 Visually representing GLCMs of example steel surface images using color-coded 2-dimensional histograms. (a) Good surface quality (figure 5.1(a)); (b) Medium surface quality (figure 5.1(b)); (c) Bad surface quality (figure 5.1(c)).

It can be seen from the three GLCMs in figure 5.3 that the majority of the co-occurrence between two pixels separated by the given displacement vector occurs for similar grayscales (represented by brighter pixels along the main diagonal of $\mathbf{P}_\delta$). As the difference between gray levels of the two pixels gets larger the probability distribution declines. According to Haralick [1982] coarse textures are generally represented by a slowly decaying probability distribution with distance, whereas a more rapid decline in the distribution represents fine textures. This trend can also be confirmed upon comparing the distribution patterns of the GLCM of good quality steel surface (having fine texture) in figure 5.3(a) with that of bad quality steel surface (having coarse texture) in figure 5.3(c).

Haralick et. al. [1973] proposed a quantitative analysis of the GLCM through 14 textural descriptors calculated from $\mathbf{P}_\delta$. Among the 14 statistics the following two have been used to extract textural features from all 35 GLCMs of the steel surface grayscale image dataset.

$$\text{Contrast} = \sum_{k=0}^{n-1} k^2 \sum_{i=1}^{n} \sum_{\substack{j=1 \\ |i-j|=k}}^{n} P_\delta(i,j) \tag{5.1}$$

$$\text{Correlation} = \frac{\sum_{i=1}^{n}\sum_{j=1}^{n} i \cdot j P_\delta(i,j) - \mu_x \mu_y}{\sigma_x \sigma_y} \tag{5.2}$$

where;

$$\mu_x = \sum_{i=1}^{n} i \sum_{j=1}^{n} P_\delta(i,j) \tag{5.3}$$

$$\mu_y = \sum_{j=1}^{n} j \sum_{i=1}^{n} P_\delta(i,j) \tag{5.4}$$

$$\sigma_x = \sum_{i=1}^{n} (i-\mu_x)^2 \sum_{j=1}^{n} P_\delta(i,j) \tag{5.5}$$

$$\sigma_y = \sum_{j=1}^{n} (j-\mu_y)^2 \sum_{i=1}^{n} P_\delta(i,j) \tag{5.6}$$

Contrast is a measure of the amount of local variations present in the image, whereas correlation is a measure of linearity in the image. A large correlation value in the direction θ implies considerable linear structure in that direction [Tomita et. al., 1990]. The two statistics were used as a feature space to classify the steel samples based on image texture captured by the GLCM. Figure 5.4 illustrates the achieved classification upon scatter plotting the contrast and correlation statistics for the 35 steel surface images. The samples have been pre-labeled according to the surface quality classes defined in table 5.1. It can be seen that most of the samples have correctly clustered into their three pre-defined classes. However, it can also be seen that there is some misclassification between the good and bad classes. The medium and good classes are also misclassified to a great extent.

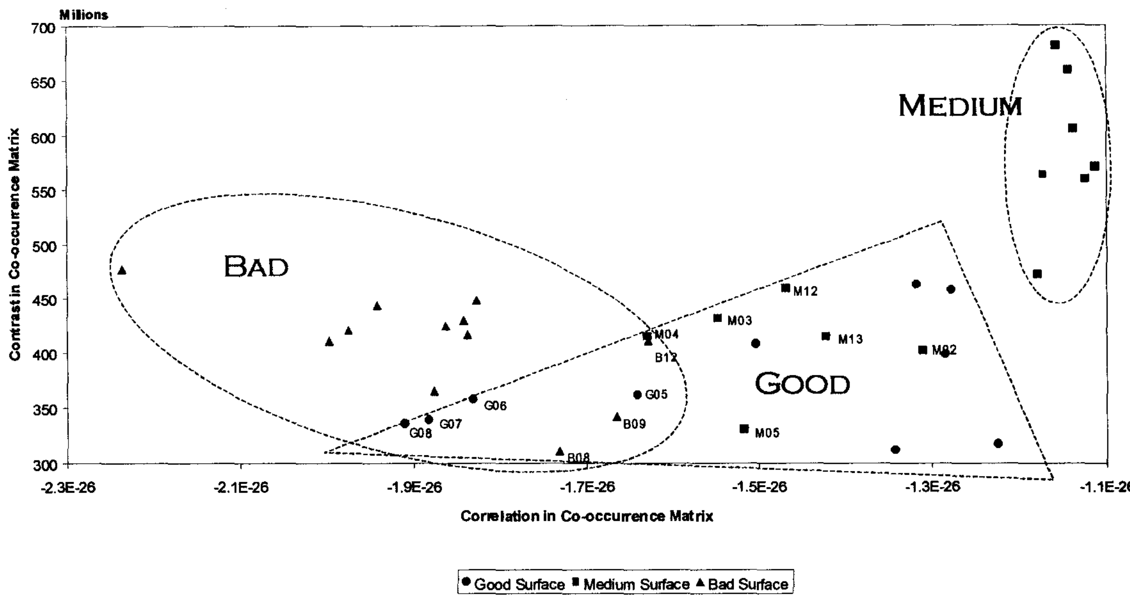

Figure 5.4 Steel surface image classification in textural feature space of GLCM

Upon observing the manually highlighted groupings in figure 5.4 (done for visual purposes only) it can be said that due to misclassifications between good and bad classes the classification achieved by the GLCM approach is poor. This limited conclusion is of course based on the contrast and correlation texture descriptors with the given displacement vector and angle. Misclassification between the good and medium classes is expected due to the progressive nature of surface pitting as steel quality is compromised. Upon taking a closer look at some of the medium surface quality images (e.g. M01 = 031_aj, M02 = 032_bj, M03 = 036_bj, M05 = 041_aj) in figure C.1(b) (Appendix C) and comparing them with images from good surface quality (figure C.1(a)) it can be seen that they are almost similar. Furthermore, the manually highlighted group of medium surface quality samples M06 to M12 (047_bj to 065_bj in figure C.1(b)) is in fact a result of higher contrast, which has been adequately captured by the contrast texture descriptor in figure 5.4.

Finally, it should be noted that texture-based classification using descriptors of the GLCM is one of many image-processing techniques that could be used to achieve the classification goals of the steel surface dataset described previously. The GLCM approach was used here mainly due to its popularity in the image processing and pattern recognition communities. The classification results obtained via this technique are used as a benchmark to compare subsequent texture-based classification methods presented in the remainder of this chapter.

5.4 Multivariate Statistical Approaches to Image Texture Analysis and Classification

As seen in the previous section texture-based feature extraction from images using traditional image analysis techniques focuses on spatial information extracted from the neighborhood of each pixel. Such information could be used to either segment different textures within an image or globally characterize the image based on overall texture. Methods presented below focus on the latter problem of image characterization based on overall textural properties.

This section presents the main thrust of the chapter through various applications of multivariate statistical methods (PCA and PLS) for purpose of texture-based image classification. The actual classification is performed in appropriate feature spaces derived from textural features of the images. These features are either extracted using 2-D FFT power spectra, or through provision of a priori knowledge of the class belongings of each image (based on texture properties) to train multivariate statistical models for discriminating the images. A novel *multivariate* approach for image texture analysis is also presented in this section, which is based on theoretical concepts of MIA methods.

Classification efficiencies of the presented techniques are determined by characterization of the steel surface images into their pre-labeled surface quality classes.

5.4.1 Unsupervised Classification Using MPCA on 2-D FFT Magnitude Images

Transform-based texture analysis methods concentrate on extracting frequency related texture information from images. As opposed to extracting pixel intensity variations in the spatial domain the 2-dimensional Fast Fourier Transform (2-D FFT) explains spectral content of such variations through transformation of the spatial image into a frequency spectrum of many sine waves of different frequencies, amplitudes and directions. Each frequency component has a magnitude and phase value. The 2-D FFT may be thought of as a 2-dimensional representation of the image power spectrum. Theoretical and mathematical details regarding the 2-D FFT can be gathered from various image-processing texts [Pratt, 1978; Gonzalez et. al., 1992].

Upon transforming an image using 2D-FFT the magnitude part of the resulting frequency array can itself be viewed as an intensity image of the same dimension, which shows frequency components of pixel intensity variations in the original image. The magnitude of each frequency component is indicated by the pixel brightness at the frequency location in the magnitude image. Higher magnitudes, which are generally near the low frequency regions, are represented by brighter pixels. All frequencies begin at the center of the image (i.e. at 0 or "DC") and progress outward (both horizontally and vertically) until the Nyquist frequency (1/2 the sampling rate of the image). As a result, magnitude images of the 2-D FFT are generally logarithm transformed thus preventing the higher magnitude frequencies from overwhelming other information in the image. Furthermore, the negative frequencies (i.e. the left half) in the magnitude image are symmetric mirrors of the positive (right half) frequencies, thus they convey redundant information. Hence, only the right halves of the resulting logarithm transformed magnitude images may be used to convey all of the spectral information.

Since the 2-D FFT allows one to visually determine the spatial frequency content of an image, any repetitive patterns would be captured as high intensity pixels at appropriate frequency locations in the corresponding magnitude image. As a result, 2-D FFT has been used to filter images in order to remove frequency-limited noise (or other repetitive patterns) [Baxes, 1994; Bharati, 1997]. Various researchers have also proposed the use of FFT spectra as texture feature descriptors [Tomita et. al., 1990], which could be used for characterizing images based on overall texture [Geladi, 1992], or multivariate prediction of externally measured textural data [Indhal et. al., 1998].

An approach suggested by Geladi [1992] is used in this section to classify the steel surface images based on their surface texture characteristics. In the proposed strategy, called "ASUNIM" (analysis of a set of univariate images), Geladi suggested unsupervised classification of a set of grayscale images of various types of wood chips through a multivariate feature space. The loading vectors of a constructed multivariate image defined the feature space. As mentioned previously (section 2.3.1) a multivariate image consists of several *congruent* variable images. In order to transform the incongruent grayscale images into a common base Geladi suggested converting them into their respective 2-D FFT magnitude images and stacking them as variables of a multivariate image. In doing so the resulting multivariate image conserves textural frequency information in its variables. Upon decomposing the multivariate image (using MPCA) into a linear combination of scores and loading vectors, the resulting latent variable space may be used for texture-based classification of the grayscale images. Classification can be performed in the scatter plots of the MPCA loading vectors.

It has been shown in section 4.3 that the MPCA loading space can provide valuable feature information regarding multivariate images. In MIA the loading vector coefficients are weighted averages of pixel intensities across an image [Geladi et. al., 1996]. Thus it can be assumed that the MPCA loading plot can be used as an appropriate descriptor of image texture extracted by the 2-D FFT spectra. Figure 5.5 illustrates a schematic of the approach used to convert the 35 steel surface grayscale image dataset into variable images of a multivariate image.

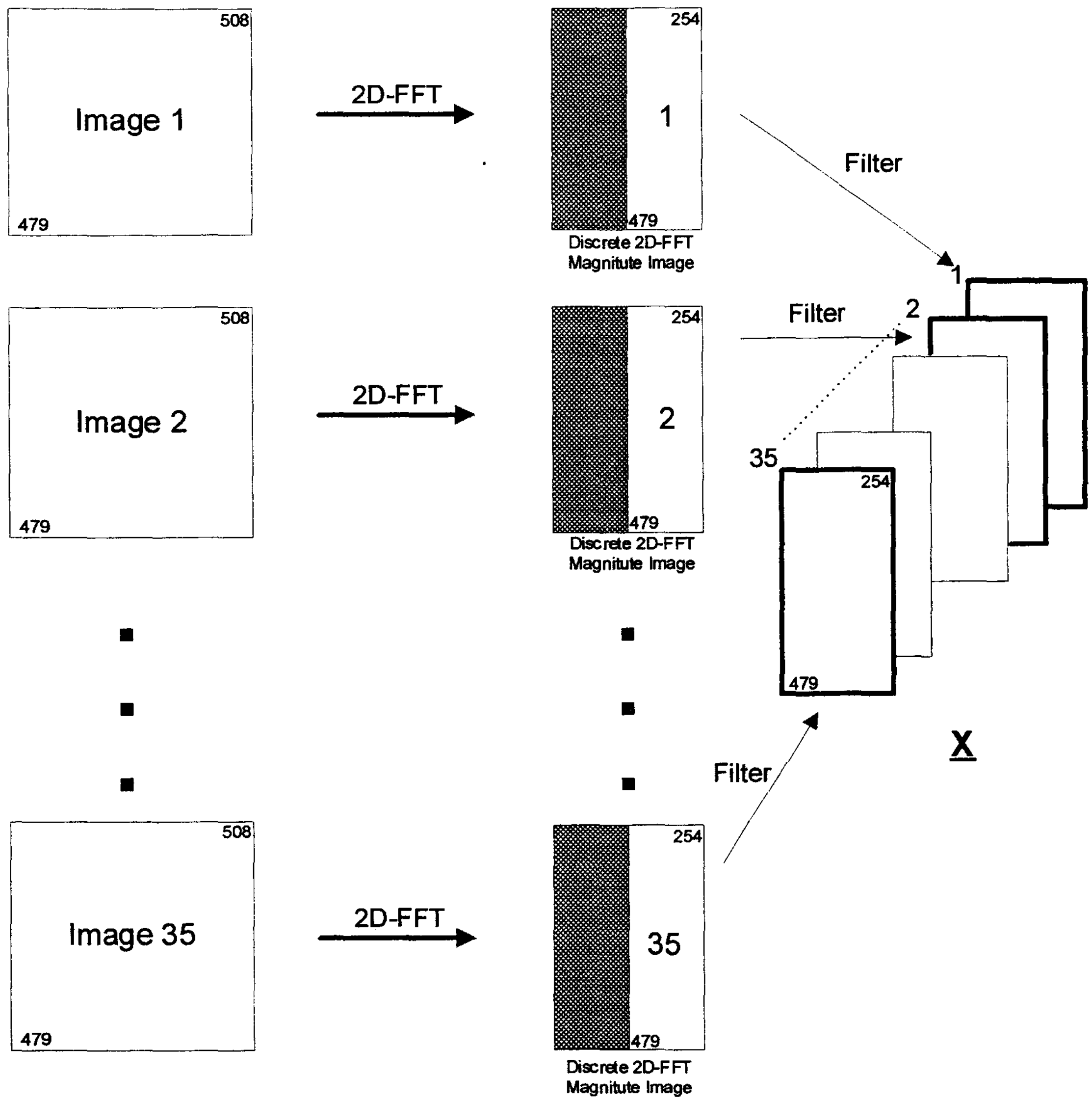

Figure 5.5 Schematic of various preprocessing steps used to construct a 35 variable multivariate image from the dataset of steel surface grayscale images

As seen in figure 5.5 the 35 2-D FFT magnitude images of the steel surface dataset were cropped and stacked into a (35 variable) multivariate image of size 479 × 254 × 35 pixels. However, prior to stacking each 2-D FFT magnitude image was passed through a "Gaussian" filter (9 × 9 pixel convolution kernel, with $\sigma = 0.5$) [Baxes, 1994]. This filter serves as a low-pass smoothing function, which is mainly used to remove traces of high-frequency noise from the texture images. Such smoothing improves the signal-to-noise ratio, which results in a better feature space for classification. Further details on the Gaussian filter and other similar windowing functions may be found in Jenkins et. al. [1969]. Figure 5.6 illustrates examples of 2-D FFT magnitude images of the three steel surface images previously shown in figure 5.1. The 2-D FFT magnitude images have been appropriately filtered and cropped (i.e. only the right halves are shown).

(a) (b) (c)

Figure 5.6 Corresponding 2-D FFT magnitude images (after necessary pre-processing) of three example steel surface images illustrated in figure 5.1. (a) Good surface quality; (b) Medium surface quality, and (c) Bad surface quality

As mentioned before, fine textures generally exhibit higher frequencies whereas coarse textures exhibit lower frequencies. Similar trends can be observed in figure 5.6(c) where the 2-D FFT image of bad steel surface (coarse texture) exhibits brighter pixel intensities towards the lower frequency regions (towards left-centre of image) as compared to the good and medium surface images (figures 5.6(a) and (b), respectively).

Upon decomposing the constructed multivariate image $\underline{\mathbf{X}}$ it was noticed that 99.78% of the total variation in $\underline{\mathbf{X}}$ was cumulatively explained in the first 3 PCs (PC1 =

99.76%; PC2 = 0.014%; PC3 = 0.011%). As expected, the first PC explained most of the variation in $\underline{\mathbf{X}}$ (since no data pre-scaling was performed prior to MPCA decomposition). From results of the MIA example illustrated in chapter 2 (section 2.3.1) it can be inferred that PC1 would explain average contrast information in the variable images of $\underline{\mathbf{X}}$, whereas contrast differences between the variables would be emphasized by subsequent PCs. Keeping this in mind, the loading space of PC2 and PC3 was used to discriminate the 35 variable images of $\underline{\mathbf{X}}$. Upon scatter plotting the $\mathbf{p}_2$ loading coefficients of the 35 variable images against those of the $\mathbf{p}_3$ loadings each image is represented as a single point. The resulting point clusters in the $\mathbf{p}_2 - \mathbf{p}_3$ scatter plot may then be used to test the achieved classification of the steel surface images according their pre-labeled surface quality. Figure 5.7 illustrates the unsupervised classification of the steel surface images in the $\mathbf{p}_2 - \mathbf{p}_3$ scatter plot of MPCA on $\underline{\mathbf{X}}$. Clustering of the variable images is based on texture information extracted by 2-D FFT in the spectral domain. Images exhibiting similar spectral patterns of steel surface roughness are grouped together to form a class. The sample points have been pre-labeled according to the surface quality classification shown in table 5.1.

According to the manually highlighted classes in figure 5.7 (done for visual purposes) it can be seen that the achieved classification using the above strategy is quite good. PC2 tries to mainly discriminate samples of bad steel surface quality (higher $\mathbf{p}_2$ values) from others. On the other hand, PC3 tries to discriminate between steel samples of good (higher $\mathbf{p}_3$ values) and medium (lower $\mathbf{p}_3$ values) surface qualities. Upon comparing the above results with those obtained using GLCM textural features (figure 5.4) it can be seen that the 2-D FFT based texture extraction gives a much better classification of the steel surface dataset. As opposed to the classification obtained using GLCM features there is no misclassification between the good and bad surface steel samples in figure 5.7. Furthermore, the misclassification between good and medium quality steel samples has also reduced. Only 1 good surface quality pre-labeled sample (G09 = 015_aj) is misclassified with the point cluster representing medium surface quality samples. Whereas 2 pre-labeled medium surface quality samples (M09 = 057_aj,

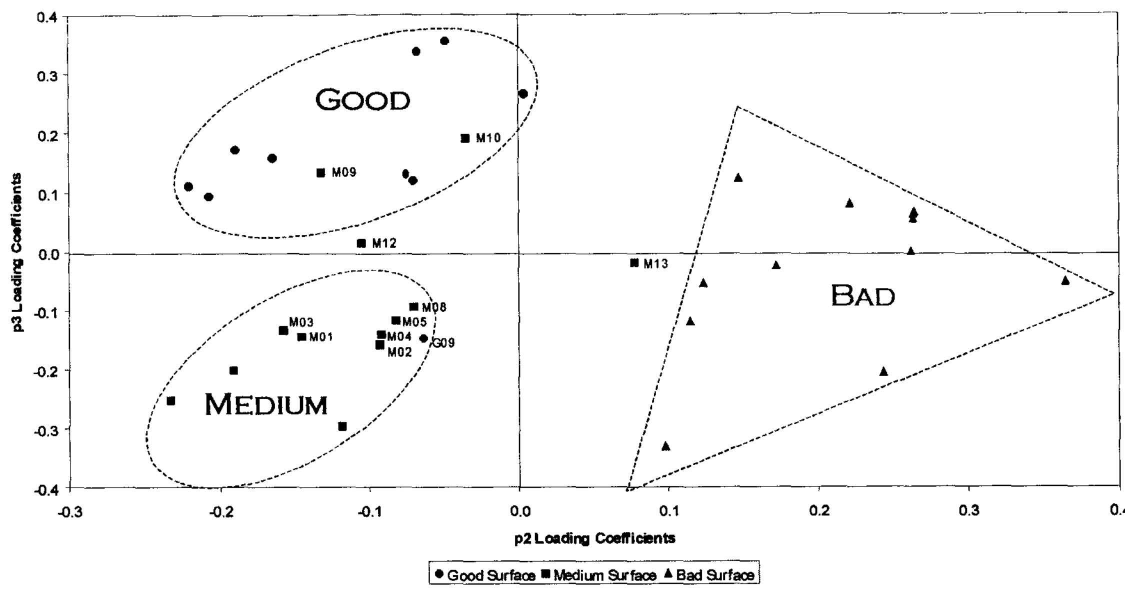

Figure 5.7 Steel surface image classification in multivariate feature space of 2-D FFT

and M10 = 061_aj) have been misclassified with the good surface class. Medium quality sample M12 (065_bj) is between good and medium classes, whereas sample M13 (073_bj) is near the bad quality class. It should be noted that the misclassified samples in figures 5.4 and 5.7 are not common. Different feature extraction steps used in the two techniques can explain this discrepancy. The GLCM feature extraction approach exclusively depends on spatial co-occurrence of pixel intensities, whereas the 2-D FFT approach solely uses frequencies of pixel intensity variations to extract features. As a result, different information is captured in either approach, which highlights different steel surface texture characteristics in the dataset.

As opposed to extracting spatial or spectral textural features to perform classification, the following section presents a supervised image classification approach, which relies on a priori knowledge of the class belongings of the images in order to discriminate them.

5.4.2 Supervised Classification of Steel Surface Images Using PLS-DA Regression Modeling

In the previous section a single MPCA model was used on a set of 2-D FFT magnitude images representing steel samples from one of three possible classes. However, prior knowledge of their class belonging was not used when classification was performed. The MPCA model was just used to approximate the data in $\underline{\mathbf{X}}$ as closely as possible. This section presents a *supervised* classification approach using a Partial Least Squares Discriminant Analysis (PLS-DA) multivariate regression model to discriminate the steel surface grayscale images based on their pre-assigned class belongings.

Basic principles of multivariate regression modeling have been previously discussed in chapter 2 of this thesis (section 2.3.2). Furthermore, chapter 3 (section 3.5) discusses the PLS-DA regression modeling approach with respect to pixel-wise classification of a multivariate image. As opposed to pixel-wise classification the approach presented here uses PLS-DA regression modeling to classify entire images into various pre-defined classes.

The PLS-DA scheme presented in this section is used in its conventional pattern recognition sense to classify the steel surface images as data points in the PLS discriminant plots [Sjöström et. al., 1986]. A multivariate characterization data matrix **X** is constructed, which contains unfolded pixel data from a set of steel surface images as observations (row vectors). Since the class belonging of each image is known a priori this information is provided through a **Y** matrix of dummy (0,1) variables in order to train the PLS-DA regression model. The model is built between **X** and **Y** for a training set of images comprising of representative samples from each class. Once trained, the PLS-DA model parameters can be used on a validation set of new images in order to predict their class belongings.

A training set of 25 steel surface images representing the three surface qualities was chosen to develop the PLS-DA regression model. Class memberships of the 25 samples were provided as three dummy variables of the **Y** array (with dimensions: 25 rows × 3 columns). The developed model was then tested on a validation set of the remaining 10 steel sample images. Division of the steel surface image dataset into the training and validation sets is illustrated in table 5.2.

Table 5.2 Division of steel surface image data into training and validation sets

Good Surface		***Medium Surface***		***Bad Surface***	
Training Set Sample ID	Test Set Sample ID	Training Set Sample ID	Test Set Sample ID	Training Set Sample ID	Test Set Sample ID
G01 (*001_aj*)	G04 (*004_bj*)	M01 (*031_aj*)	M03 (*036_bj*)	B01 (*091_aj*)	B02 (*091_bj*)
G02 (*003_bj*)	G06 (*007_bj*)	M02 (*032_bj*)	M06 (*047_bj*)	B03 (*091_bj*)	B04 (*092_bj*)
G03 (*004_aj*)	G08 (*008_bj*)	M04 (*039_aj*)	M10 (*061_aj*)	B05 (*093_aj*)	B10 (*100_aj*)
G05 (*007_aj*)	-	M05 (*041_aj*)	M11 (*063_aj*)	B06 (*093_bj*)	-
G07 (*008_aj*)	-	M07 (*049_aj*)	-	B07 (*094_aj*)	-
G09 (*015_aj*)	-	M08 (*052_aj*)	-	B09 (*099_bj*)	-
G10 (*017_aj*)	-	M09 (*057_aj*)	-	B11 (*100_bj*)	-
-	-	M12 (*065_bj*)	-	B12 (*108_aj*)	-
-	-	M13 (*073_bj*)	-	-	-

Figure 5.8 illustrates a schematic of the PLS-DA model building stage of the proposed approach. Pixels from 25 steel surface grayscale images of the training set (originally each image had dimensions: 479 × 508 pixels) were unfolded into observations of the predictor array **X** (with dimension: 25 rows × 243,332 columns). As seen in figure 5.8 the resulting **X** data array is wide and short, with the number of variables (columns) far exceeding the observations (rows). Variables of **X** represent unique pixel locations through the steel surface images. A kernel-based PLS algorithm proposed by Rännar et. al. [1994] (to handle such wide data arrays) was used to develop the PLS-DA regression model between **X** and **Y**. The purpose of this study is to use the PLS algorithm in order to achieve the classification goals. Hence, this section concentrates on the obtained results without presenting any PLS algorithm details. A basic understanding of PLS regression modeling is presumed in order to interpret the following discussion. Besides the above reference further details of PLS regression modeling may be found in [Geladi et. al., 1986; Höskuldsson, 1988; Geladi, 1988; Eriksson et. al., 1999].

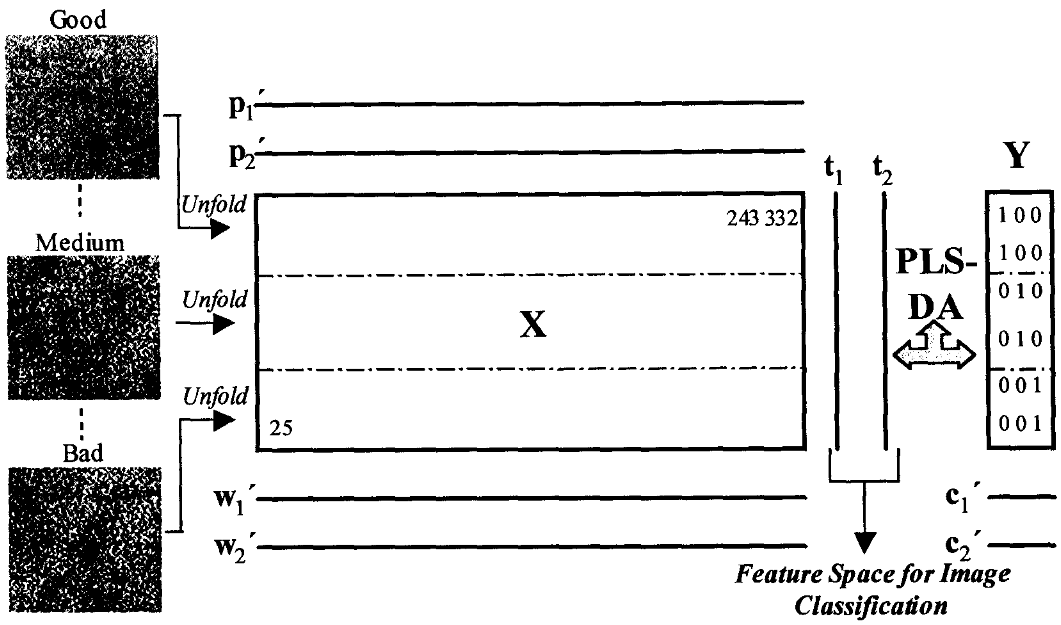

Figure 5.8 Schematic of training a PLS-DA model to discriminate steel surface images

After mean-centering the data (both **X** and **Y**) a PLS regression model of the form

$$\mathbf{X} = \mathbf{T}\mathbf{P}^{\mathrm{T}} + \mathbf{E} \qquad (5.7a)$$

$$\mathbf{Y} = \mathbf{T}\mathbf{C}^{\mathrm{T}} + \mathbf{F} \qquad (5.7b)$$

was develop with 3 PCs, which cumulatively explained 97.83% of the variation in **Y** (PC1 = 45.34%; PC2 = 44.39%; PC3 = 8.10%). In equation (5.7) **T** is a (25 rows × 3 columns) matrix of score vectors (as columns); **P** & **C** are loading matrices, and **E** & **F** are residual matrices for the **X** and **Y** spaces, respectively. The latent variables ($\mathbf{t}_1$, $\mathbf{t}_2$, $\mathbf{t}_3$) of the resulting PLS-DA model try to provide a multivariate description of the observations in **X**, which simultaneously accounts for their class memberships provided in **Y**. As a result, the projections of the data in the corresponding latent variable score plots of the PLS-DA model are rotated in order to maximally separate (discriminate) the observations based on class memberships. It is left up to the PLS-DA loading coefficients ($\mathbf{p}_1$, $\mathbf{p}_2$, $\mathbf{p}_3$) to determine appropriate weights for each pixel location (variables of **X**) in order to satisfy the class belongings provided in the dummy **Y** matrix.

Figure 5.9 illustrates a scatter plot of the first two PC score vectors ($\mathbf{t}_1 - \mathbf{t}_2$) of the trained PLS-DA model using the steel surface training set data from table 5.2. The third PC has been excluded from analyses, as it did not contribute to the discrimination of the data (PC3 only explained 8.10% of the variation in **Y**). In figure 5.9 each steel surface image has been pre-labeled according to the a priori class memberships defined in table 5.1. Solid points represent the training set samples from three surface quality classes. According to the manually highlighted point clusters in figure 5.9 (done for visual purposes) it can be seen that the discrimination of the training set steel sample images is very good in the 2 PC score vectors of the PLS-DA regression model.

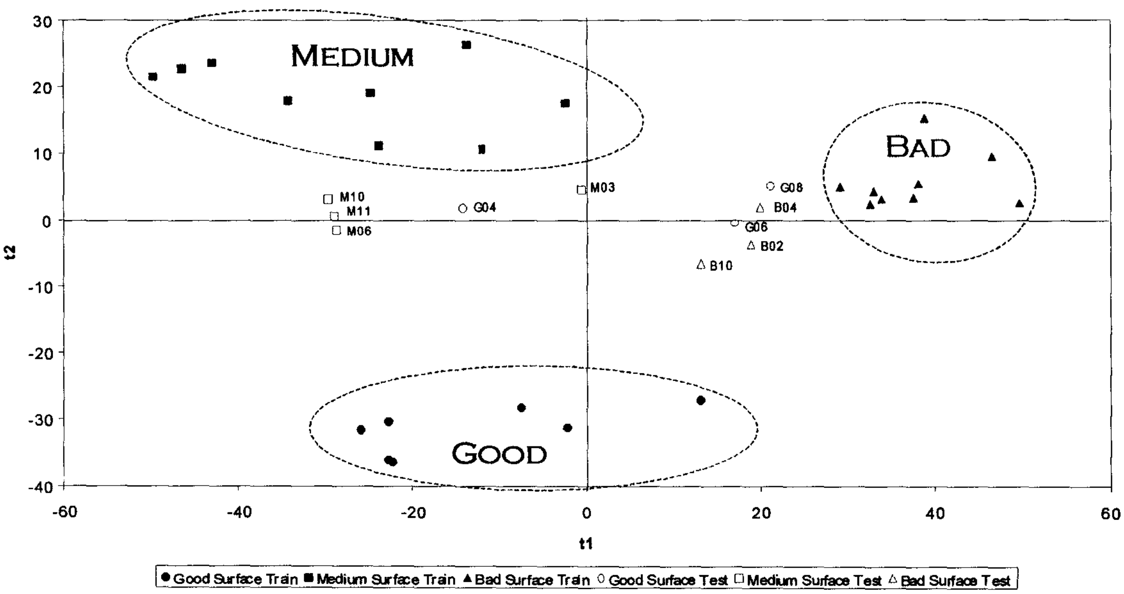

Figure 5.9 Steel surface image classification in the PC score space of PLS-DA regression model

A regression model developed from a training set is of little use if it cannot adequately predict unknown **Y**-values from a validation set of new **X** observations. Hence, the developed PLS-DA model was used on 10 steel surface images from the validation set (table 5.2). The results obtained from the model validation can be analyzed in two possible ways. First, one could analyze the PC scores (t_1, t_2) of a candidate image as a score point in the ($\mathbf{t}_1 - \mathbf{t}_2$) score plot, and compare its location with respect to the score clusters of the three training set steel surface classes. Second, upon comparing the

$\hat{\mathbf{Y}}$ predictions of candidate images to the expected dummy response of the three variables (i.e. to see if they are approaching 0 or 1 to determine class belonging). The $\hat{\mathbf{Y}}$ predictions can be obtained from the PLS-DA regression model using the following equation.

$$\hat{\mathbf{Y}}_{new} = \mathbf{T}_{new}\mathbf{C}^{T} \tag{5.8}$$

Validation results obtained from the PLS-DA model for the steel surface image dataset have been overlaid as hollow score points in the $(\mathbf{t}_1 - \mathbf{t}_2)$ score plot of figure 5.9. The $\hat{\mathbf{Y}}$ predictions of the validation samples are shown in table 5.3. It can be seen from these results that the PLS-DA model fails to adequately classify new steel surface images based on surface quality characteristics. Although the PLS-DA classification in the training stage produced tight and well separated score clusters (figure 5.9), none of the 10 validation set samples fell into their respective pre-labeled classes. All score points of the validation set samples were near one (or both) of the zero axes of the $(\mathbf{t}_1 - \mathbf{t}_2)$ score vectors, which indicated that the PLS-DA model did not have enough information to properly discriminate them into their respective classes. Similar trends can also be observed in the $\hat{\mathbf{Y}}$ predictions of the validation set samples (table 5.3). None of the $\hat{\mathbf{Y}}$'s are close to their expected value of 1 for the appropriate class and zero for the other class.

The steel surface grayscale image dataset used in this chapter has also been used for PLS-DA based classification with a 2-dimensional extension of the wavelet transform (WT) PLS algorithm proposed by Trygg et. al. [1998]. This work has been included as an example study in the SIMCA-P 9.0 user's guide [Umetrics, 2001]. A single thresholding was applied to the wavelet transformed steel surface images prior to unfolding the thresholded wavelet coefficients into a short and wide predictor array $\mathbf{X}_{WT}$, which is a reduced version of the multivariate characterization data matrix $\mathbf{X}$ used in this study. The achieved reduction was in the number of variables (columns) of $\mathbf{X}$. In performing such a reduction the idea was to concentrate the discriminant information by removing noisy variables (columns) prior to application of PLS-DA for classification of the steel surface images. The PLS-DA regression model was developed using $\mathbf{X}_{WT}$ and a dummy $\mathbf{Y}$ array in a similar manner as described above.

Table 5.3 $\hat{\mathbf{Y}}$ predictions of the validation set steel surface images using PLS-DA regression model

		EXPECTED $\hat{\mathbf{Y}}$			OBSERVED $\hat{\mathbf{Y}}$		
Candidate Image ID	Pre-Labeled Class of Candidate	$\hat{y}_1$	$\hat{y}_2$	$\hat{y}_3$	$\hat{y}_1$	$\hat{y}_2$	$\hat{y}_3$
G04	Good Surface	1	0	0	0.297	0.522	0.181
G06	Good Surface	1	0	0	0.248	0.228	0.523
G08	Good Surface	1	0	0	0.115	0.278	0.607
M03	Medium Surface	0	1	0	0.196	0.457	0.347
M06	Medium Surface	0	1	0	0.394	0.622	-0.016
M10	Medium Surface	0	1	0	0.330	0.669	0.001
M11	Medium Surface	0	1	0	0.368	0.627	0.005
B02	Bad Surface	0	0	1	0.286	0.173	0.541
B04	Bad Surface	0	0	1	0.178	0.253	0.569
B10	Bad Surface	0	0	1	0.363	0.175	0.461

Although a different training and validation set was used, results obtained via the WT technique were comparable to figure 5.9. Again the wavelet based PLS-DA model performed quite well in discriminating the three classes in the training stage, however the classification of the validation samples was poor.

The reason for the poor performance of the PLS-DA classification approaches presented in this section is due to the loss of spatial information upon unfolding the grayscale steel surface images into row vectors of **X**. In the training stage a priori class memberships were provided, which guided the PLS-DA decomposition to generate a model that was specific to the 25 steel surface images of the training set. However, as shown in figure 5.9 and table 5.3, that model was not robust enough to classify *new* images. Texture is a function of spatial variations in neighboring pixel intensities throughout an image. Upon unfolding the pixel arrays from the steel surface images one removes this information. The PLS-DA model is independent of permutations of the columns of the **X** matrix, i.e. it is independent of the location of the pixels relative to one another. As the main objective of the study was to classify steel images based on surface texture, the loss of spatial information is a huge disadvantage of the traditional multivariate statistical classification methods.

Spatial information is also lost upon unfolding 3-dimensional pixel intensity data from multivariate images into long 2-dimensional data arrays for MPCA based MIA (section 2.3.3). However, as far as MIA is concerned the loss of spatial information is not disadvantageous as these methods try to extract *spectral* (i.e. variable specific) information in order to group similar pixels in the score space. Furthermore, image data in MIA is multivariate with multiple *congruent* variable images forming the dataset. On the other hand, when using PLS-DA to classify texture images from different steel samples there is no congruency between any two images. Thus, a variable (column) of **X** only contains pixel intensities of multiple images at a particular spatial location. For all intensive purposes it does not matter to the regression model if the variables were permuted with each other (e.g. exchanging columns 1 and 125 in **X**). Similar models would result (in terms of data fit and predictive ability) for many permutations.

Finally, the supervised classification approach presented in this section illustrates the limitations of multivariate statistics based image analysis techniques for extracting spatially dependent texture information. This is due to the complete ignorance of spatial pixel intensity variations when decomposing unfolded image data.

The lost spatial information could be regained to a certain extent if each individual texture image were complimented with its spatially shifted counterpart as a new *variable* of a multivariate image. The resulting dataset may then be analyzed using MPCA and MIA. In that case the model would be forced to explain local variations of pixel intensities over a pre-defined neighborhood (depending upon number of pixel shifts). This approach of texture analysis using MIA is discussed in the next section.

5.4.3 Classification Using MIA of Spatially Shifted and Stacked Steel Surface Images

Multivariate Image Analysis methods (as described in section 2.3.1) are extremely efficient at extracting feature information based on pixel spectra from multivariate images. However, these techniques completely loose spatial information upon decomposing the multivariate image data into PC score space scatter plots. On the other hand, traditional texture analysis methods (as shown in section 5.3) exclusively work in the spatial coordinates of an image to extract feature information from pixel intensity variations in a specific pixel neighborhood. As shown in the previous section (5.4.2) these local variations are extremely important descriptors of image texture. As a result, one needs to incorporate the spatial information within the multivariate statistical framework in order to perform texture analysis using MIA.

A novel image texture analysis technique is presented in this section. It uses the advantageous features of MPCA based MIA methods in order to extract necessary roughness information from images. The proposed scheme is used for interpretive texture analysis of individual steel sample grayscale images as well as for surface roughness based classification of the steel surface image dataset.

Upon observing the steel surface images in figure 5.1 it can be seen that the main distinguishing feature between the surface pits and the background pixels is a sharp change in pixel intensities at the edge of each pit. In order to create a meaningful feature-space for maximum distinction between the three steel surface qualities it becomes important to enhance the spatial distribution of pit edge pixel intensities in each sample image.

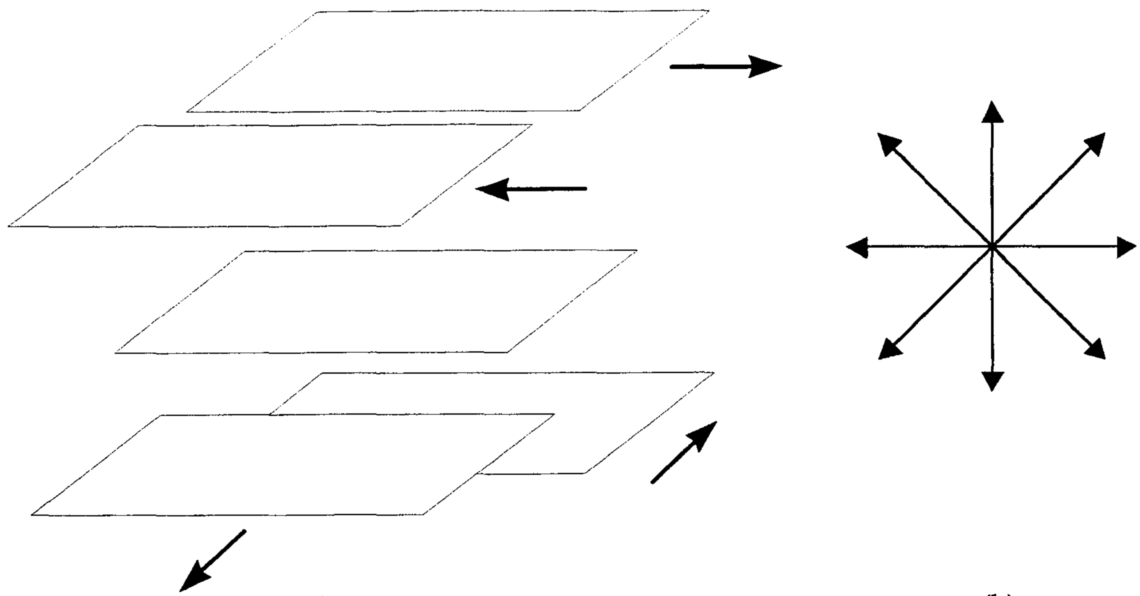

(a) (b)

Figure 5.10 (a) A multivariate image created via spatial shifting in 4 adjacent directions and stacking the shifted images. (b) Eight possible directions in which an image could be shifted

One possible technique of capturing this spatial distribution is through spatially shifting the steel surface grayscale image in adjacent directions, and then stacking the shifted images on top of each other to form a three-way pixel array. The resulting three-dimensional image data is a multivariate image where the third (i.e. variable) dimension is the spatial shifting index. Each image in such a stack would illustrate the same feature information. However, sharp pixel intensity changes in a local pixel neighborhood would be further enhanced in such a representation. This is because adjacent pixel intensity variations get supplemented to every pixel in the two-dimensional image plane of the three-way array. Schematically, this information can be viewed as a vector in the variable (i.e. shifting index) dimension of the multivariate image. Figure 5.10(a) illustrates such a multivariate image that is created by spatially shifting an image in four adjacent directions, and stacking the shifted images on top of each other. Each variable vector (figure 2.7) in such a multivariate image representation contains pixel information from a chosen neighborhood of pixels depending upon the amount and direction of shifting applied to the image.

As far as the steel surface images are concerned the optimal amount and direction of spatial shifting is dependent on the shapes and sizes of the major surface pits. Generally, enough shifting should be performed such that the edges of major pits are adequately captured. The resulting multivariate image can then be analyzed using MIA techniques (as described in section 2.3.1).

5.4.3.1 Interpretive Texture Analysis of Steel Images Using MIA

Interpretive texture analysis using MIA is now illustrated on two steel surface sample images. The chosen images were previously shown in figure 5.1(a) and (c) representing good and bad steel surfaces, respectively. The trained MIA model developed through texture analysis of these two steel sample images is then used to analyze (and classify) the complete steel surface image dataset.

Both training steel surface images were spatially shifted in 8 adjacent directions by 1 pixel, and the shifted images were stacked above the original images to form two multivariate images, each having 9 variables. Figure 5.10(b) illustrates the 8 directions in which each image was shifted. Such a shifting/stacking strategy ensures a shift by 2 locations in the 4 primary axes (vertical, horizontal, and 2 diagonals). This results in allowing for the capture of both 1st and 2nd derivatives of the pixel intensity variations in the steel image. It should be noted that upon increasing the number of pixel shifts the variable dimension of the resulting multivariate image also increases drastically (8 extra variable images per increase in pixel shift in all adjacent directions). This also affects the computational effort required to process the multivariate image.

After shifting and stacking the steel surface image the three-way array was cropped at the edges to discard all the non-overlapping sections. This resulted in the multivariate images having smaller image plane dimensions than those of the original sample images (original dimensions of each image were 479 × 508 pixels). Resulting dimensions of the shifted and stacked multivariate images were 477 × 506 × 9 pixels. MIA was performed on both the good and bad surface quality multivariate image arrays ($\underline{\mathbf{X}}_{good}$ and $\underline{\mathbf{X}}_{bad}$) using MPCA decomposition. The cumulative percent sum of squares explained by the first 3 PCs in the good and bad surface training sample images were 99.36% and 99.20%, respectively. Only the first 3 PCs have been used in subsequent analyses, with rest of the PCs (4 to 9) being attributed to explaining noise in the multivariate image. Table 5.4 shows the corresponding weights of the first 3 loading vectors ($\mathbf{p}_1$, $\mathbf{p}_2$, $\mathbf{p}_3$) with respect to the nine variable images of the bad ($\underline{\mathbf{X}}_{bad}$) surface quality multivariate image. The variable images have been labeled according to the respective spatial directions in which the original image was shifted. MPCA decomposition of the good ($\underline{\mathbf{X}}_{good}$) surface quality multivariate image resulted in very similar loading vector coefficients. As a result, they have not been shown.

Table 5.4 MPCA loading coefficients for MIA of bad steel surface training image ($\underline{\mathbf{X}}_{bad}$)

	Original	Left	Right	Up	Down	Right & Up	Left & Up	Right & Down	Left & Down
$\mathbf{p}_1^T$	0.3399	0.3349	0.3348	0.3344	0.3348	0.3301	0.3300	0.3305	0.3304
$\mathbf{p}_2^T$	-0.0002	-0.0001	0.0000	**-0.4493**	**0.4489**	**-0.3839**	**-0.3887**	**0.3889**	**0.3832**
$\mathbf{p}_3^T$	-0.0034	**-0.4506**	**0.4538**	-0.0047	-0.0015	**-0.3842**	**0.3844**	**-0.3811**	**0.3879**

Since no mean centering of the image data was performed prior to MPCA decomposition, the first PC explained mainly the average pixel intensity in the image. This is evident by the positive loading vector coefficients of all 9 variable images of $\mathbf{p}_1^T$ in table 5.4. The corresponding $\mathbf{T}_1$ score images of the first PC are illustrated in figure 5.11. Upon comparing $\mathbf{T}_1$ for the good and bad images with their original version in figures 5.1(a) and (c) it can be seen that the score images are blurred versions of the originals. This is due to the fact that PC1 extracts only the pixel contrast information from the multivariate image via averaging over a 3 × 3 pixel neighborhood around each pixel of the steel surface image. This neighborhood has been provided through the 8 adjacent shifts of the steel image.

(a) (b)

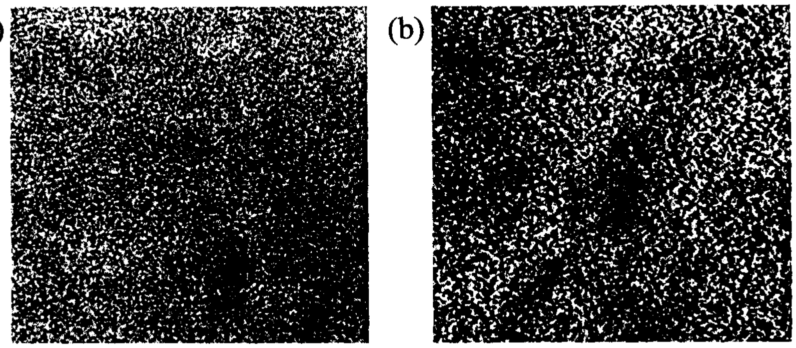

Figure 5.11 (a) $\mathbf{T}_1$ image of good quality steel surface training image; (b) $\mathbf{T}_1$ image of bad quality steel surface training image

Upon extracting the mean pixel intensity variations from the multivariate image, the second and third PCs of MIA extract the remaining feature information. Figure 5.12(a) and (b) illustrates the second PC score images $\mathbf{T}_2$ of the good and bad steel surface training images, respectively. A close observation of both $\mathbf{T}_2$ images reveals that the 2nd PC predominantly extracts horizontal and diagonal edge information in all four directions (i.e. 45°, 135°, 225°, and 315°) with respect to the center of the image.

(a) (b)

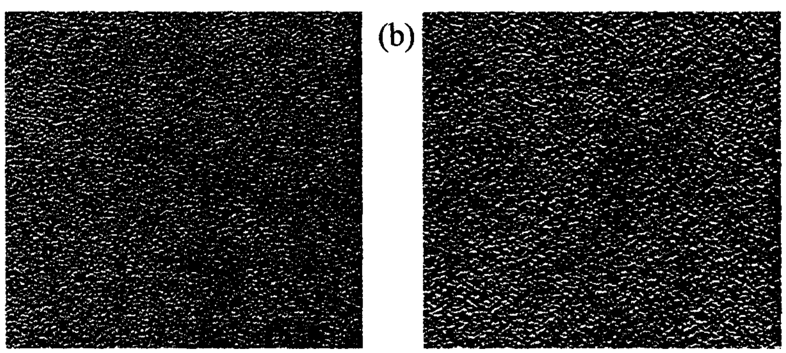

Figure 5.12 (a) $\mathbf{T}_2$ image of good quality steel surface training image; (b) $\mathbf{T}_2$ image of bad quality steel surface training image

The 3rd PC score images $\mathbf{T}_3$ of the good and bad steel surface training samples are illustrated in figure 5.13. It can be seen that the main features extracted by PC3 are the vertical and the diagonal surface pit edge information in all four directions throughout both training images.

(a) (b)

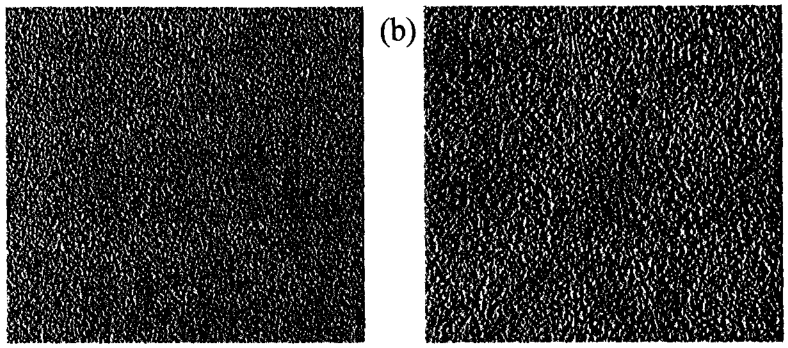

Figure 5.13 (a) T_3 image of good quality steel surface training image; (b) T_3 image of bad quality steel surface training image

A similar conclusion can also be drawn upon observing the $\mathbf{p}_2$ and $\mathbf{p}_3$ loading vector coefficients in table 5.4. It can be seen that the 2nd PC extracts mainly horizontal edge information due to higher coefficient magnitudes for spatial shifts in the vertical and diagonal directions. As a result, the pixel intensity slope information is highlighted through the columns of the $\mathbf{T}_2$ image, thus enhancing horizontal edges of the surface pits. Similarly, the coefficient magnitudes for horizontal and diagonal shifts are higher in the 3rd PC, resulting in better estimation of pixel intensity slopes through the rows of the $\mathbf{T}_3$ image. As a result, the 3rd PC extracts mainly vertical edges of the surface pits. It is also worth noting in table 5.4 that the sum of the loading coefficients for both $\mathbf{p}_2$ and $\mathbf{p}_3$ are approximately zero, which agrees with the convolution kernel of a 1st-derivative edge detection filter in the traditional image processing literature [Baxes, 1994; Pratt, 1978].

Upon closely observing all three PC score images and corresponding loading vector coefficients of the steel surface training images one can gather that for this example MIA serves as a different type of image filter in each PC dimension. PC1 serves as a smoothing filter, whereas PC2 and PC3 server as 1st-derivative horizontal and vertical edge detection filters, respectively.

It can be seen from this example that MIA on spatially shifted and stacked images automatically allows one to develop optimal filters as loading vectors based on pixel intensity variance over a pre-defined neighborhood. In general these filters could be much more complex than the simple smoothing and 1st-derivative edge detection filters obtained above. Depending upon the number of pixel shifts and the chosen spatial direction(s) of shifting (e.g. a shift by every 5th pixel in four adjacent directions) the MPCA loading vectors could define more complex filters, which one could have never decided ahead of time.

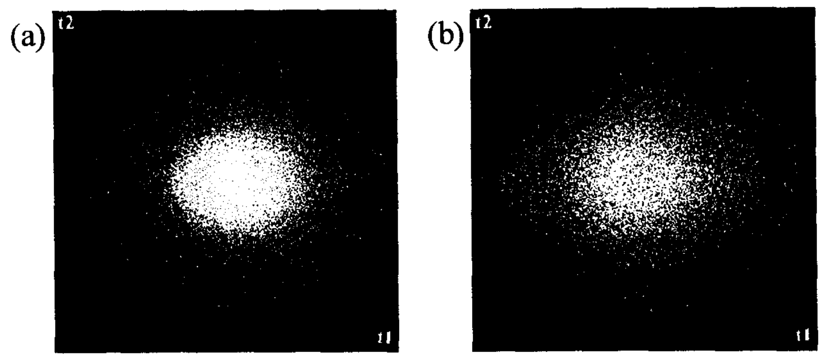

Figure 5.14 (a) Score space of PC12 for good steel surface training image; (b) Score space of PC12 for bad steel surface training image

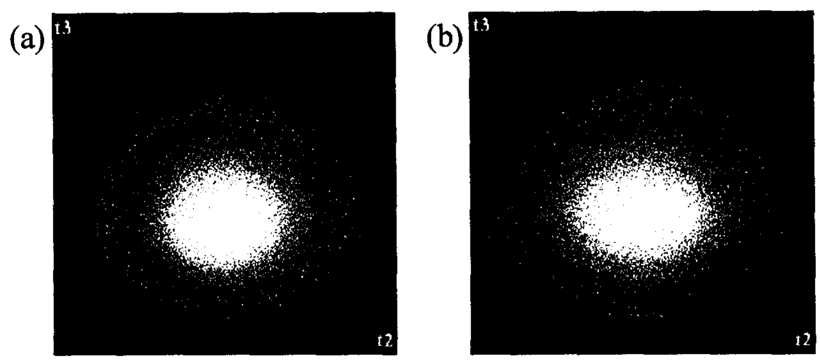

Figure 5.15 (a) Score space of PC23 for good steel surface training image; (b) Score space of PC23 for bad steel surface training image

Besides observing the MIA PCs as intensity images (image space), one could also use scatter plots of score vectors against each other and observe the pixels as point clusters (score space) in a color-coded 2-dimensional histogram. Figure 5.14 illustrates the PC12 ($\mathbf{t}_1$ - $\mathbf{t}_2$) score plot of the good and bad steel surface training images. It can be seen from both score plots in figure 5.14 that majority of the scores form one big point cluster in the middle of the plot. This pattern is due to the fact that the multivariate image was formed using the same image shifted and stacked on top of each other. As a result, it would be expected that majority of the information in the central point cluster represents average pixel contrast through the images. Similar cluster patterns can also be noticed in the PC23 ($\mathbf{t}_2$ - $\mathbf{t}_3$) score plots of the two steel surface training images in figure 5.15.

Further insight of the MIA score space can be gathered upon interrogating score point clusters using the previously described masking strategy to delineate feature pixels upon highlighting the masked score points in the corresponding score images. A close inspection of the PC1 score images in figure 5.11 reveals that pixels belonging to steel surface pit cores are represented by dark shades (i.e. low pixel intensities). Table 5.1 shows image means of the steel surface dataset. Upon comparing the class mean of the bad surface quality images with those of the other two classes it can be confirmed that as the steel surface is compromised, the average pixel intensity reduces across the steel surface image. As a result, one can infer that the corresponding $\mathbf{t}_1$ values of these pixels would be low. This intuition can be confirmed upon masking the low $\mathbf{t}_1$ values (regardless of $\mathbf{t}_2$) in the corresponding $\mathbf{t}_1$ - $\mathbf{t}_2$ score space. Figure 5.16(a) illustrates such a mask (shown as a green rectangle) that interrogates low $\mathbf{t}_1$ values without giving any preference to $\mathbf{t}_2$ in the PC12 score plot of the bad steel surface training image. Such a mask is analogous to thresholding the $\mathbf{T}_1$ image, or a 1-dimensional $\mathbf{t}_1$ histogram. The corresponding masked pixels have been highlighted (as green) and overlaid on the $\mathbf{T}_{1bad}$ image illustrated in figure 5.16(b). Similar masking/highlighting can also be performed on the good surface training image.

Inspecting figures 5.12(b) and 5.13(b), it can be inferred that both low as well as high pixel intensity values of $\mathbf{T}_2$ and $\mathbf{T}_3$ represent those pixels belonging to steel surface pit edges in all eight adjacent directions (horizontal and diagonal in $\mathbf{T}_2$, vertical and diagonal in $\mathbf{T}_3$). As a result, the corresponding mask that highlights pit edges in the training image data ignores the central point cluster in the $\mathbf{t}_2$ - $\mathbf{t}_3$ score plot. Figure 5.17(a) illustrates such a mask (shown in green around the central cluster) which highlights the extreme (t_2, t_3) score combinations in the $\mathbf{t}_2$ -$\mathbf{t}_3$ score plot of the bad surface training sample. The corresponding pixels covered by this mask have been highlighted (as green) and overlaid on the $\mathbf{T}_{1bad}$ image as illustrated in figure 5.17(b). Similar results can also be obtained to highlight surface pit edges in the good steel surface training image.

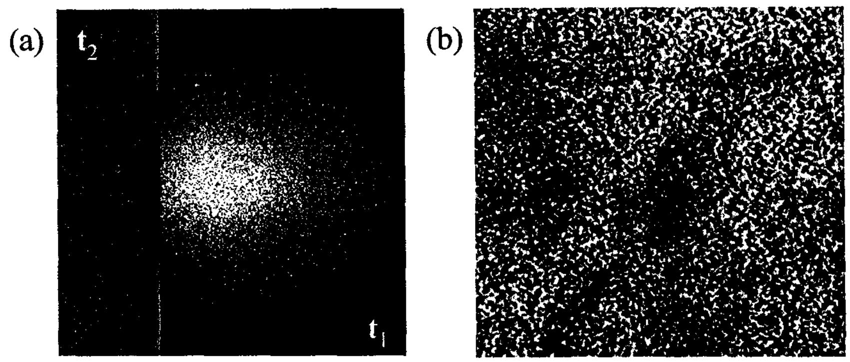

Figure 5.16 (a) Manually applied mask on PC12 score space of bad steel surface training image; (b) Corresponding feature pixels under PC12 mask highlighted (in green) and overlaid on $\mathbf{T}_{1bad}$ score image

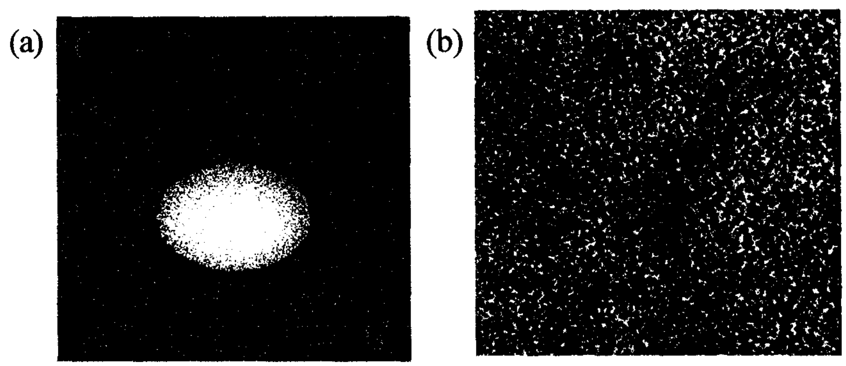

Figure 5.17 (a) Manually applied mask on PC23 score space of bad steel surface training image; (b) Corresponding feature pixels under PC23 mask highlighted (in green) and overlaid on $\mathbf{T}_{1bad}$ score image

5.4.3.2 Classification of Steel Images Using MIA Training Model

Information gathered from the score and image spaces of the training images reveals the ability of MIA techniques to extract relevant texture information from the steel surface images. Once trained, the MIA training model (score space masks and loading vectors) can then be used to extract similar texture properties from each steel surface grayscale image in the dataset. This can be accomplished through the MIA feature-monitoring scheme previously explained in chapter 3 (section 3.4.1). Monitoring charts (similar to figure 3.14) could be plotted upon counting the number of pixels falling under the training model score space masks for each steel surface image. Such a chart provides an objective measure of image texture through a count of pixels belonging to pit cores and edges in each steel surface image. Figure 5.18 illustrates a bar chart representing a total pixel count of pit cores and edges in the 35 steel sample images based on the MIA model developed using the bad steel surface training image.

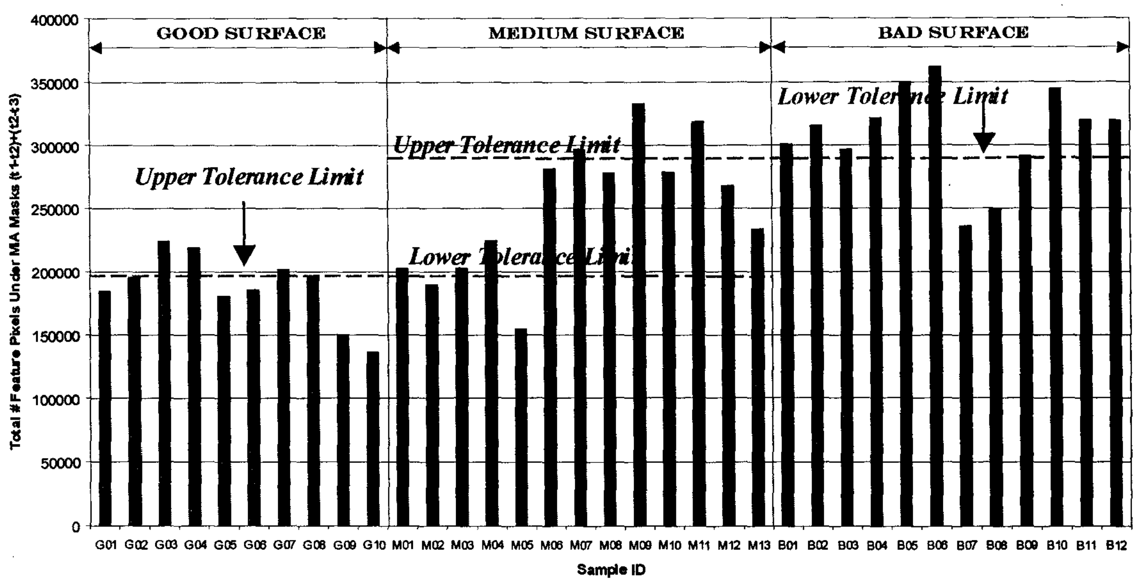

Figure 5.18 Monitoring chart of total pixels from pit cores and edges in 35 steel surface images. Arbitrary tolerance limits have been set to determine class boundaries

From the trends in the bar chart (figure 5.18) it can be seen that good surface quality steel exhibits lower number of pixels falling under the 2 masks, while the number of such pixels increases as the steel surface quality declines. Based on previous industrial experience (or a more rigorous study with a large dataset) appropriate tolerance limits could be set in such a chart to define class boundaries for each of the three steel surface qualities. Class acceptance (or rejection) of a candidate image would then be based on the number of feature pixels between the preset tolerance limits. Since the steel surface dataset used in this study consisted of only 35 samples the tolerance limits in figure 5.18 have been set arbitrarily.

An alternate approach for classifying the steel surface images is to plot the respective feature pixel counts against each other for every image. Such a scatter plot produces an appropriate feature space for image classification, in which each steel surface image is represented by a combination of pixel counts of its pit cores and pit edges, respectively. Steel surfaces depicting similar overall texture characteristics should have (on average) similar feature pixel counts of pit cores and edges. Figure 5.19 illustrates a scatter plot of pixel counts under the PC12 score space mask (pit cores) against counts of pixels under the PC23 score space mask (pit edges). The MIA model developed on the bad steel surface training image was used to mask the score spaces of the 35 steel surface images.

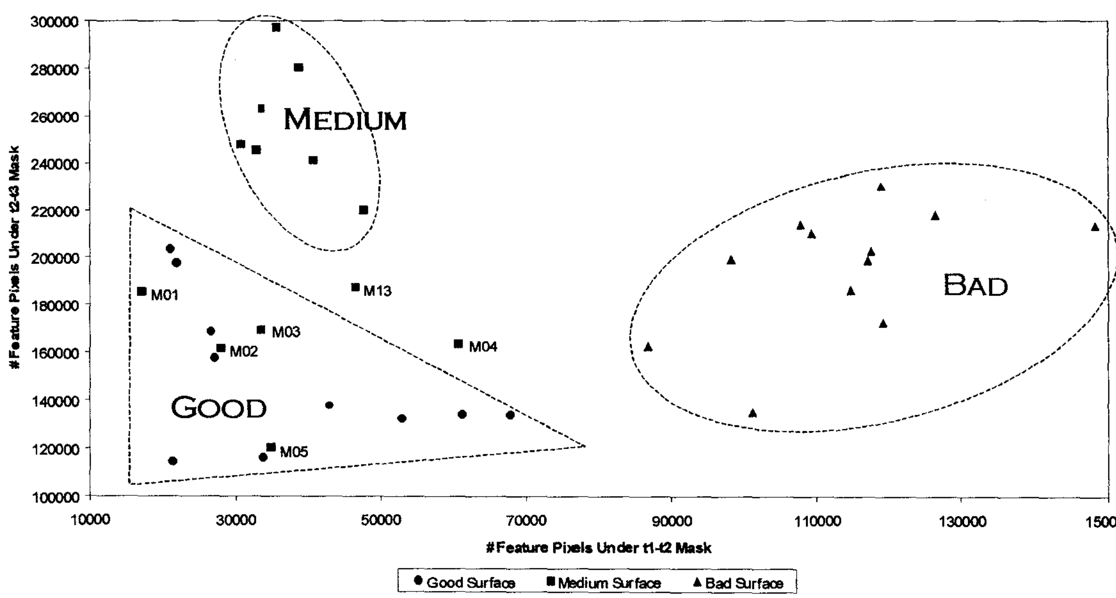

Figure 5.19 Steel sample image classification based on surface pits and edges detected by MIA texture analysis strategy

As seen from figure 5.19 each steel sample image is represented by a single point, which illustrates the surface pit characteristics as a combination of two texture features (# pit core pixels, and # pit edge pixels). The abscissa (x-axis) separates samples representing bad steel surface quality (high pixel counts under $\mathbf{t}_1 - \mathbf{t}_2$ score plot mask) from other samples. This trend is expected since the bad surface quality samples contain mainly deeper pit cores, which occupy a larger surface area as they are joined together in 'snake' like patterns. As a result, it can be said that the x-axis represents image contrast information. On the other hand, the ordinate (y-axis) can be said to represent derivative (edge) information. As seen from figure 5.19 this direction mainly separates samples from good surface quality (low # pixels under $\mathbf{t}_2 - \mathbf{t}_3$ mask) and those belonging to medium surface quality (high # pixels under $\mathbf{t}_2 - \mathbf{t}_3$ mask). Medium surface quality steel contains more pronounced pits than good surface quality samples. However, these pits are not as deep as those found in bad quality steel. Furthermore, medium quality steel does not exhibit the wavy 'snake' like patterns seen in bad surface quality samples. As a result, it is expected that the surface area of pit edges would be higher for medium quality samples as compared to samples from good and bad surface quality.

From the manually highlighted clusters in figure 5.19 (done for visual purposes) it can be seen that adequate classification is achieved between the good and bad surface quality samples. However, some medium surface quality samples (M01 - M05 = 031_aj – 041_aj; M13 = 073_bj) have been misclassified with good quality steel. As explained earlier (section 5.3) the misclassified medium surface quality sample images in figure C.1(b) (Appendix C) cannot be visually differentiated from the good surface quality samples (figure C.1(a)), and probably were improperly classified by the inspector in the first place. Similar misclassification trends were also observed in the previously described (section 5.3) GLCM texture feature based image classification approach. However, the GLCM approach also misclassified good and bad surface quality samples.

As far as the steel surface image dataset is concerned it could be concluded that the proposed MIA based image classification approach produces similar texture analysis results as compared to the 2-D FFT approach, and better results than the GLCM approach. However, being inherently multivariate in nature the MIA texture analysis technique has the added advantage that it can be applied not only to grayscale images, but it can also be used to extract texture from true color (RGB) and other multi-spectral images. The next section discusses some common observations from the results of all texture-based classification approached discussed in this chapter.

Finally, one could also use a MIA score plot matching strategy to classify candidate images from the steel surface dataset. The classification is based on a similarity measure with score plots of training set sample images. Bharati et. al. [2000] used this strategy to propose an automatic classification scheme for the steel surface image dataset. Steel sample images were pre-processed using the shifting/stacking approach followed by MPCA decomposition. The resulting $\mathbf{t}_1 - \mathbf{t}_2$ and $\mathbf{t}_2 - \mathbf{t}_3$ score plots for each candidate image were compared with similar plots obtained from a training set of steel sample images. Classification was performed based on the training sample with which the candidate image showed most similarity. The classification was illustrated with an example study of two classes (good and bad steel surface quality) using a training set of 2 images (1 from each class), and 4 candidate images (2 from each class). The achieved classification accuracy was 100% for the illustrated example. This classification approach has been omitted from the results in this thesis. Interested readers may consult the above reference for further details.

5.5 Discussion of Steel Image Classification Results

Each sample image from the steel surface dataset (used for texture-based classification in this chapter) was pre-assigned by a trained industrial person into one of three separate surface quality classes. As a result, one can objectively determine relative efficiencies of the image classification approaches that have been presented in this chapter.

Four different texture-based image classification schemes were presented; (1) Supervised classification using PLS-DA regression models on raw unfolded texture images, (2) Classification in feature-space of GLCM texture features, (3) Textural feature extraction and classification using MIA score space masks, and (4) MPCA based classification of texture features extracted by 2-D FFT magnitude images. This section discusses relative effectiveness of the four schemes with respect to the achieved image classification results.

The supervised image classification approach using PLS-DA regression modeling will be discussed separately from the other three approaches used in this chapter. This is because the philosophy of the PLS-DA classification approach is to treat the texture image discrimination purely as a data classification problem. The model developed in this approach disregards the spatial integrity of the images since each texture image was unfolded into a row vector prior to modeling. Furthermore, the different images in the dataset are not contiguous, in that pixels in each column of **X** do not really have anything in common. Therefore, column variables are different for each row (unfolded image). An inherent assumption of PCA is that columns and rows of the data matrix have some meaningful interpretation. As this was a pure data analysis problem, PLS-DA model parameters would not change if the image pixels were permuted, or randomly picked form an image to form the row vector. The fitted data based on provided class membership information produced excellent discrimination between the training set images. However, the model performed very poorly when no class membership information was provided in the validation stage (figure 5.9). All validation samples were misclassified, thus indicating the importance of maintaining spatial integrity of the texture images. The classification approach revealed shortcomings of multivariate statistical methods when analyzing image texture. This is due to the strong spatial dependence of texture, which is completely ignored by this approach.

The other three image classification approaches presented in this chapter consider the spatial dependence of texture (directly or indirectly) in the feature extraction stage. However, the way in which steel surface textural features are extracted by the three approaches makes them different. The GLCM and the shifting/stacking MIA based approaches directly incorporate pixel intensity variations around each pixel of the steel image, whereas the feature extraction approach using a 2-D FFT magnitude image relies on the frequency distribution of the pixel intensity variations throughout the steel surface image. The 2-D FFT and shifting/stacking MIA based feature extraction techniques provide the required spatial information to multivariate statistical methods in order to perform texture-based image classification.

The GLCM approach directly incorporated adjacent pixel intensity information in the two texture descriptors of the co-occurrence matrix. The two texture descriptors (contrast and correlation) of the GLCM were used as feature-space for classification. This approach produced several misclassifications between image samples from all three pre-labeled steel surface quality classes (figure 5.4). Perhaps the easiest indicator of the inadequacy of the GLCM based approach is misclassification between good and bad steel surface quality samples. Four good quality samples (G05-G08 = 007_aj-008_bj) were misclassified with three bad quality samples (B08 = 099_aj, B09 = 099_bj, B12 = 108_aj). From a visual inspection of the good and bad steel surface quality samples (figure C.1(a) and (c)) in Appendix C it can be concluded that there should not be any overlap in discriminating samples from these two classes.

On the other hand, classification achieved using the MIA texture analysis technique (figure 5.19) produced better results as compared with the GLCM approach. As mentioned before spatial pixel intensity variations are also considered in the extracted feature-space of the MIA based approach. Upon comparing the feature-spaces of the MIA and GLCM based approaches (figures 5.4 and 5.19) it can be seen that similar sample patterns emerge. However, the MIA based approach can better discriminate between all good and bad surface quality samples. In fact, only six medium surface quality samples (M01-M05 = 031_aj-041_aj, M13 = 073_bj) were not classified according to their pre-labeled classes. Five out of the six misclassified medium surface quality samples using this approach (M02-M05, and M13) are also misclassified using the GLCM based approach. Furthermore, as previously explained (sections 5.3 and 5.4.3.1) four of the six misclassified medium surface quality samples (M01-M03 and M05) cannot be visually discerned from any of the steel samples pre-labeled as good surface quality and may have been initially misclassified by the assessor. Thus, only two medium surface quality samples (M04 and M13) were truly misclassified by the MIA texture analysis based approach.

Steel surface image classification achieved in the multivariate feature-space of 2-D FFT magnitude images also produced better results as compared to the GLCM approach. Classification between the good and bad steel surface quality samples reveals well-separated clusters (figure 5.7). However, there is again some misclassification between good and medium surface quality samples. One pre-labeled good surface quality sample (G09 = 015_aj) is misclassified with the medium surface quality class. However, four pre-labeled medium surface quality samples do not cluster in their pre-labeled class. Three of these samples (M09 = 057_aj, M10 = 061_aj, and M12 = 065_bj) are classified with good surface quality steel, whereas one sample (M13 = 073_bj) classifies with bad surface quality steel. The misclassified medium surface samples using the 2-D FFT approach are not common with those misclassified using the MIA and GLCM based approaches. This is due to the fact that the feature extraction stage in this approach relies on frequency distributions of the spatial pixel intensity variations through the steel surface images. As a result, this classification approach *indirectly* incorporates spatial information in the feature-space.

5.6 Conclusions and Contributions

This chapter looks at the problem of image classification based on overall texture characteristics. To this end a novel multivariate statistical image texture analysis technique has been proposed, which is based on the concepts of Multivariate Image Analysis methods. The proposed technique can interactively extract image texture information, which can then be used for texture-based image classification. Due to the inherent multivariate nature of MIA the proposed scheme can potentially be used to extract textural features from grayscale, true color (RGB), or multi-spectral image data. Performance of the proposed scheme has been tested on a set of steel surface grayscale images, which have been individually pre-labeled into one of three different quality classes based on surface texture characteristics.

The achieved steel image classification results using the proposed scheme have also been compared with those obtained from three other texture-based image classification approaches on the same dataset. The three approaches are: (1) Classification using textural feature descriptors of Gray Level Co-occurrence Matrices (GLCM) of the steel images, (2) Classification in MPCA loading space of 2-D FFT magnitude images of steel images, and (3) Classification using the scores of a PLS-DA model. Fundamental ideas behind these three classification approaches have been previously published in the literature. Besides providing a platform to compare the performance of the proposed texture analysis scheme, these approaches also give insight of various fundamental issues with respect to textural feature extraction from images.

An overview and contrast between multivariate statistical and traditional image texture analysis schemes has also been presented in this chapter. Some fundamental differences between these two types of image analysis approaches have been highlighted. Traditional image texture analysis methods (e.g. approach (1) from above) work in the spatial coordinates of the image in order to extract textural features for classification. Due to the strong spatial dependence of texture, such methods generally produce reasonable classification results. A major shortcoming of straightforward multivariate statistical techniques used for image texture analysis has been illustrated using approach (3) from above. It has been shown through failure of the PLS-DA steel image classification approach that (without any pre-processing) multivariate statistical methods do not perform well in image texture analysis. This is because they don't retain the spatial integrity of pixel intensities when decomposing the image data. Approach (2) also uses multivariate statistical methods (MPCA) to classify the steel image dataset. However, spatial pixel intensity variations are retained through pre-processing each image using a 2-dimensional Fast Fourier Transform during the feature extraction stage of the approach. The 2-D FFT magnitude images carry frequency distributions of pixel intensity variations, which indirectly capture textural features. Classification using multivariate statistical methods of such pre-processed texture images (that capture spatial information) shows good results.

Spatial pixel intensity information has also been captured in the proposed MIA based texture analysis method by pre-processing each image through a spatial shifting and stacking approach. Principal components of pre-processed steel images provide smoothing and edge enhancements, which are interrogated using standard MIA tools. Training models can be developed on representative texture images for monitoring similar information in new images, and using this information in an image classification framework. As a result, the proposed approach incorporates ideas from both traditional as well as multivariate statistical image analysis methods. Besides providing interactive texture analysis of each individual image, the proposed approach incorporates the advantageous aspects of MIA feature monitoring and classification schemes.

Finally, it is evident from the work presented in this chapter that each of the four texture-based image classification methods has its own advantages and shortcomings, and can be more (or less) appropriate in a certain situation. An overall comparison of the proposed MIA texture-based image classification approach with the other three approaches presented in this chapter reveals that it provides better steel image classification accuracy than approaches (1) and (3) from above. Upon comparing its classification accuracy with that of approach (2) it could be argued that both methods perform equally well (based on overall number of misclassified samples). However, the ability of the proposed MIA based approach to provide a more detailed texture analysis of individual images makes it an attractive alternative.

Chapter 6

Summary and Conclusions

The general objective of this thesis was to develop novel multivariate statistical methods that analyze data from digital imaging sensors for monitoring and feedback control of industrial processes equipped with vision systems. In order to achieve this objective several on-line extensions and modifications to Multivariate Image Analysis (MIA) and Multivariate Image Regression (MIR) techniques were proposed throughout this thesis. Industrial applications of the proposed methods were illustrated through preliminary studies in the following three areas: (i) automatic grading of sawn softwood lumber; (ii) predicting pulp end properties through near-infrared (NIR) imaging spectroscopy of finished dry product; and (iii) classification of steel based on surface texture characteristics. In the following sections the work done in each area is summarized, along with an outline of its main contributions, some general conclusions, and a highlight of possible topics to be carried forward as future work.

6.1 Multivariate Image Analysis for Softwood Lumber Grading

The industrial application (addressed in chapter 3) is that of quality grading sawn softwood lumber based on visual inspection of common defects. An on-line MIA feature monitoring technique was proposed. The technique was used to monitor specific defects in RGB color images of lumber boards. The main contribution of this work is in proposing a novel on-line MIA technique, which can be used as part of an overall industrial process monitoring and feedback control scheme. Chapter 3 also provides an exploratory study of chemically complex lumber defects using off-line MIA techniques to analyze multi-spectral lumber images acquired in the NIR wavelength spectrum. A comparison is made of the lumber defect information that can (or cannot) be extracted through NIR multi-spectral imaging sensors versus RGB cameras.

The proposed on-line lumber defect monitoring approach was based on developing a robust (off-line) MIA model on a training lumber sample image consisting of typical defects and inherent lumber variations. Once trained, the MIA model was used to monitor the modeled lumber defects from lumber boards passing under a high-speed line-scan RGB camera. The approach was illustrated on a set of sawn softwood lumber boards from three different species. Typical lumber defects like knots, splits, wane, pitch and bark pockets were extracted using the proposed scheme. Monitoring of the pixels belonging to these defects was performed in the score space of MIA. The monitoring charts involved plotting pixel counts of the various lumber defects for each board as it passed under the imaging scanner. Decision rules (tolerance limits) were used to assign quality grades to the lumber boards. The proposed scheme illustrates a successful application of MIA techniques for industrial process monitoring that could potentially be used on-line at production speeds.

Certain complex lumber defects have been further investigated using their chemical signatures in the NIR wavelength spectrum. Previously no studies had been conducted on lumber in the wavelength range of the NIR imaging spectrometer used in this work. It was shown that multi-spectral NIR reflectance images dissect complex lumber features into various sub-features, which can then be isolated using off-line MIA techniques. The work presented in this chapter used MIA of multi-spectral NIR lumber images to isolate knot sub-features in order to differentiate between two types of knots. A multi-dimensional score space masking and image space highlighting strategy of MIA was developed to accomplish this work. Useful insight was gained upon comparing advantages and shortcomings of using NIR imaging spectroscopy as opposed to RGB imaging for the purpose of lumber grading. Such information is very valuable to the softwood lumber industry for purchase decisions of imaging scanners.

The main objective of this chapter was to prove the feasibility of an on-line MIA scheme for process monitoring in the softwood lumber industry. This work is one of the first attempts to extend the methodology of MIA to treating on-line time varying images. The feasibility study involving classification of lumber defects successfully demonstrated the potential of the approach. The secondary objective of assessing the potential of NIR imaging spectroscopy for extracting finer features on lumber defects was also successful. However, several promising areas for future research arose in these investigations.

One important area for further study would involve developing mathematically sound MIA score space masking strategies to isolate feature pixels in multivariate images. Currently, masking score clusters in the MIA score space is performed using manually created masks based on a trial and error technique. The proposed multi-dimensional MIA score space masking strategy in this chapter is one of several possible ways to isolate sub-features of a complex feature from multiple principal component pairs of a multivariate image. A better approach might be to apply cluster analysis methods from the pattern recognition literature to create masks for delineating pixels belonging to features of interest from background pixels in multivariate images. Other techniques can also be developed to dissect complex features, based on optimizing the multi-dimensional mask boundaries in order to minimize misclassified feature pixels.

A practical problem for further studying involves handling model robustness and equipment calibration issues upon actual on-line implementation of the proposed MIA feature-monitoring scheme in a sawmill. It is well known that there is generally a big difference between the environmental conditions prevailing in a laboratory and a true industrial process. The harsh industrial environment of a typical sawmill would require sturdy vision equipment as well as robust MIA models for proper on-line lumber defect monitoring. Issues like equipment aging could be handled upon regularly updating MIA models, or implementing some image pre-processing scheme to scale the data prior to modeling.

6.2 Multivariate Image Analysis and Regression Modeling of Pulp and Paper Characteristics

Predicting characteristics and end properties of a finished product through an image based empirical model has been addressed in chapter 4. The work introduces NIR imaging spectroscopy to the pulp and paper sectors of the forest products industry. A novel MIR modeling technique has been proposed, which uses multi-spectral NIR reflectance images of finished pulp and paper samples to extract paper ingredient characteristics and predict critical pulp quality indicator variables. The work presented in this chapter contributes to the field by laying the framework for MIR modeling schemes that can be used to relate feature information from process multivariate images (obtained via on-line sensors) with corresponding quality information from (non-image) data obtained from other sources.

The proposed modeling approach is based on extracting a relevant feature space from multi-spectral NIR images of finished pulp and paper samples. Extraction of such a feature space was illustrated through a paper characterization study, which used a MIA based strategy to extract relevant chemical and ingredient information from multi-spectral NIR images of well-characterized paper samples. It was illustrated through PCA based classification of the paper sample feature vectors that NIR imaging spectroscopy can capture vital chemical information from finished pulp and paper. This information could then be used to empirically predict pulp and paper properties.

A novel MIR scheme was developed to relate the feature space extracted from multi-spectral NIR images of finished pulp samples with their end properties. The idea consisted of developing a PLS regression model between spectrally filtered feature vectors of multi-spectral NIR pulp images and corresponding pulp quality data measured through wet chemistry procedures. The proposed scheme was illustrated through a feasibility study on a set of freshly manufactured pulp samples ranging in different quality grades based on their desired end properties. Pulp imaging and chemical analysis were performed in 'at-line' fashion in the quality control laboratory of a pulp mill. Preliminary results of the proposed scheme showed good regression model performance when predicting three out of four pre-selected pulp quality variables from multi-spectral NIR pulp images. Furthermore, the regression models could successfully monitor end property variations through multiple pulp grades with prediction errors being generally comparable to laboratory measurement errors.

The MIR models were further used to investigate spatial variations of pulp end properties across the imaged section of a pulp sample. A sub-windowing technique was proposed to predict pulp quality variables in local regions of the sample. The key result of this approach is that it provides a measure of pulp heterogeneity with respect to its end properties.

The proposed MIR modeling scheme was illustrated through a limited feasibility study in order to prove its ability to empirically model pulp properties through imaging spectroscopy of finished pulp samples. The eventual goal of the project is to continually predict pulp properties from a NIR imaging spectrometer installed on-line. However, prior to achievement of this goal some issues still need to be further investigated. In particular, the following topics provide a basis for future research.

Prior to on-line implementation further at-line studies still need to be conducted with a thorough investigation of a larger pulp sample dataset, which includes a wider selection of pulp grades and quality variables.

Spectral filtering of the pulp sample feature vectors was applied through Orthogonal Signal Correction in order to remove unwanted variations (e.g. pulp surface effects, temperature, humidity and light variations etc.) that were not correlated with pulp quality variations. Several spectral filtering techniques have been proposed in the literature for improving model predictions in presence of such unwanted variations. A thorough study of the effects of spectral filtering techniques on model predictions in the presence of unwanted external variations (induced by experimental and environmental conditions) would provide a better understanding of model robustness (in both off-line and on-line situations).

The nature of the feature extraction step in the proposed MIR scheme enables one to augment external information variables with pulp image feature vectors in order to improve model predictions. A thorough study could be conducted to determine the effects of augmenting the pulp image feature space with external variables that are known to be critical indicators of pulp end properties.

6.3 Texture Based Classification of Steel Surface Images

The problem of image classification based on overall surface texture characteristics has been addressed in chapter 5 of this thesis. The work contributes to the field by proposing a novel MIA based image texture analysis method. The method enables interactive extraction of textural features for image classification and monitoring image texture content. Performance of the proposed approach was tested on a set of pre-labeled steel surface grayscale images with varying degrees of surface roughness characteristics. Image classification achieved by the proposed approach was compared with several conventional and multivariate statistics based texture analysis methods. The contribution of this work is threefold: it provides (i) a new image texture analysis scheme using MIA techniques, (ii) an overview and contrast of several image texture analysis approaches, and (iii) insight of why some multivariate statistics based classification methods perform poorly when segmentation is based on image texture.

Main concepts and steel surface image classification achieved by the proposed MIA based texture analysis approach were compared with those from three other schemes: (1) classification using textural features of gray level co-occurrence matrix (GLCM) of each steel image; (2) unsupervised classification in MPCA loading space of 2-dimensional Fast Fourier Transformed (2-D FFT) magnitude image of each steel image; and (3) PLS-DA regression model based supervised classification of unfolded raw steel images as predictor matrix observations (rows).

Analyzing the poor classification results achieved by approach (3) provided insight of the shortcomings of texture-based classification using multivariate statistical methods. The work provided a better understanding of the importance of conserving spatial pixel information when extracting textural features from images. Such information is completely ignored by multivariate statistical methods, which only concentrate on spectral information in multivariate images. Results obtained by approaches (1) and (2) were better than (3) as these approaches incorporated spatial pixel intensity variations when extracting appropriate textural feature spaces for classification.

Insight gained from approaches (1) to (3) was used to develop the proposed MIA based texture analysis method. Spatial pixel intensity information was incorporated via pre-processing each image through a spatial shifting and stacking approach. The resulting multivariate image, with variable dimension as shifting index, was analyzed using standard MIA tools in order to extract textural features. The approach was applied on the steel image dataset through training a MIA model on a representative image. Pixel counts of textural features were used to classify the images into their respective pre-labeled surface quality classes. Upon comparing the achieved classification results of the proposed approach with those of approaches (1) to (3) it was shown that the MIA based method outperformed these approaches. This is mainly due to the fact that the MIA approach incorporates advantageous features of both conventional and multivariate statistical image analysis methods.

The MIA texture analysis approach presented in this chapter highlighted the possibility of developing a framework to incorporate spatial pixel intensity correlations within current MIA schemes to extract textural information from images. Due to the inherent multivariate nature of MIA such a framework would not only be limited to texture analysis of grayscale images. Color (i.e. multi-spectral) image texture analysis is a rapidly growing field with much research currently underway. It has recently been recognized that multi-resolution analysis (MRA) possesses the ability to incorporate spatial pixel intensity correlations within a multivariate image setup. Future research in developing a unified framework with the aid of MRA and MIA could provide a powerful tool for texture analysis of grayscale, color, and multivariate images.

References

Adel, M., D. Wolf, R. Vogrig, and R. Husson, "Evaluation of Colour Spaces in Computer Vision Application of Wood Defects Detection," IEEE Int. Conf. on Systems, Man and Cybernetics, Le Touquet, France, Oct. 17 – 20, 1993.

Al-Janobi, A., "Performance Evaluation of Cross-Diagonal Texture Matrix Method of Texture Analysis," *Pattern Recognition*, **34**, pp. 171 – 180, 2001.

Andrle, R., "The Angle Measure Technique: A New Method for Characterizing the Complexity of Geomorphic Lines," *Mathematical Geology*, **26**, pp. 83 – 97, 1994.

Antti, H., M. Sjöström, and L. Wallbäcks, "Multivariate Calibration Models using NIR Spectroscopy on Pulp and Paper Industrial Applications," *Journal of Chemometrics*, **10**, pp. 591 – 603, 1996.

Antti, H., "Multivariate Characterization of Wood Related Materials," Ph.D. Thesis, Umeå University, Umeå, Sweden, 1999.

Antti, H., D. Alexandersson, M. Sjöström, and L. Wallbäcks, "Detection of Kappa Distributions in Kraft Pulps using NIR Spectroscopy and Multivariate Calibration Methods," *Tappi Journal*, **83**, pp. 102 – 108, 2000.

Arad, N., and D. Resifeld, "Image Warping Using Few Anchor Points and Radial Functions," *Computer Graphics Forum*, **14**, pp. 35 – 46, 1995.

Arnold, B. R., "ASTM's Paper Aging Research Program," E-MRS Spring Meeting, Strasbourg, France, June 5 – 8, 2001.

Ashjari, B., "Singular Value Decomposition Texture Measurement for Image Classification," Ph.D. Thesis, University of Southern California, Los Angeles, CA, 1982.

Åstrand, E., "Automatic Inspection of Sawn Wood," Ph.D. Thesis, Linköping University, Linköping, Sweden, 1996.

Barnes, R. J., M. S. Dhanoa, and S. J. Lister, "Standard Normal Variate Transformation and De-trending of Near-Infrared Diffuse Reflectance Spectra," *Applied Spectroscopy*, **43**, pp. 772 – 777, 1989.

Baxes, G. A., *Digital Image Processing: Principles and Applications*, John Wiley & Sons, NY, 1994.

Bayer, B. E., "Color Imaging Array," U.S. Patent 3, 971, 065, 1976.

Beebe, K. R., R. J. Pell, and M. B. Seasholtz, *Chemometrics: A Practical Guide*, John Wiley & Sons, NY, 1998.

Bharati, M. H., "Multivariate Image Analysis for Real-Time Process Monitoring," M.Eng. Thesis, McMaster University, Hamilton, 1997.

Bharati, M. H., and J. F. MacGregor, "Multivariate Image Analysis for Real-Time Process Monitoring and Control," *Ind. Eng. Chem. Res.*, **37**, pp. 4715 – 4724, 1998.

Bharati, M. H., and J. F. MacGregor, "Texture Analysis of Images using Principal Component Analysis," Proceedings of SPIE – Process Imaging for Automatic Control, Boston, MA, November 5 – 6, 2000.

Bharati, M. H., J. F. MacGregor, M. Champagne, and M. Barrette, "Using NIR Multivariate Image Regression Techniques to Predict Pulp Properties," Control Systems 2002, Stockholm, Sweden, June 3-5, 2002.

Birkett, M. D., and M. J. Gambino, "Estimation of Pulp Kappa Number With Near-Infrared Spectroscopy," *Tappi Journal*, **72**, pp. 193 – 197, 1989.

Bovik, A., M. Clark, and W. Geisler, "Multichannel Texture Analysis using Localized Spatial Filters," *IEEE Trans. Pattern Anal. Mach. Intell.*, **12**, pp. 55 – 73, 1990.

Brunner, C. C., A. G. Maristany, D. A. Butler, D. VanLeeuwen, and J. W. Funck, "An Evaluation of Color Spaces for Detecting Defects in Douglas-Fir Veneer," *Industrial Metrology*, **2**, pp. 195 – 218, 1992.

Brunner, C. C., A. G. Maristany, D. A. Butler, and J. W. Funck, "Enhancing Color-Image Data for Wood-Surface Feature Identification," Proc. 5th Int. Conf. on Scanning Technology & Process Control For the Wood Products Industry, Atlanta, Oct. 25 – 27, 1993.

Buchanan, B., H. Siesler, and L. Weyer, "Short Course on Near Infrared Spectroscopy: Theory and Application for Pharmaceuticals, Industrial Chemistry and More," Eastern Analytical Symposium, Nov. 2 –3, Atlantic City, NJ, 2000.

Burnham, A. J., R. Viveros, and J. F. MacGregor, "Frameworks for Latent Variable Multivariate Regression," *Journal of Chemometrics*, **10**, pp. 31 – 45, 1996.

Burns, D. A., and E. W. Ciurczak (eds.), *Handbook of Near-Infrared Analysis*, 2nd edition, Marcel Dekker, NY, 1992.

Carlucci, L., "A Formal System for Texture Languages," *Pattern Recognition*, **4**, pp. 53 – 72, 1972.

Champagne, M., B. Meglen, S. wold, and N. Kettaneh-Wold, "The Use of OCS and Wavelets to Improve NIR Readings of Pulp Properties," *Pulp and Paper Canada*, pp. 41 – 43, 2001.

Chang, S. J., J. R. Olson, and P. C. Wang, "NMR Imaging of Internal Features in Wood," *Forest Products Journal*, **39**, pp. 43 – 49, 1989.

Chang, T., and C. C. J. Kuo, "Texture Analysis and Classification with Tree-Structured Wavelet Transform," *IEEE Trans. Image Process.*, **2**, pp. 429 – 441, 1993.

Conners, R. W., C. W. McMillin, K. Lin, and R. E. Vasquez-Espinoza, "Identifying and Locating Surface Defects in Wood: Part of an Automated Lumber Processing System," *IEEE Transactions on Pattern Analysis and Machine Intelligence,* **PAMI-5**, pp. 573 – 583, 1983.

Conners, R. W., C. W. McMillin, and N. Chong, "The Utility of Color Information in the Location and Identification of Defects in Surfaced Hardwood Lumber," Proc. 1st Int. Conf. on Scanning Technology in Sawmilling, San Francisco, 1985.

Cross, G., and A. Jain, "Markov Random Fields Texture Models," *IEEE Trans. Pattern Anal. Mach. Intell.*, **5**, pp. 25 – 39, 1983.

DV srl, "Spectral Scanner User Manual V1.1," Industria 64 35129 Padova, Italy, 2000.

Easty, D. B., S. A. Berben, F. A. DeThomas, and P. J. Brimmer, "Near-Infrared Spectroscopy for the Analysis of Wood Pulp: Quantifying Hardwood-Softwood Mixtures and Estimating Lignin Content," *Tappi Journal*, **73**, pp. 257 – 261, 1990.

Ekstrom, M. P., *Digital Image Processing Techniques*, Academic Press Inc., FL, 1984.

Eriksson, L., E. Johansson, N. Kettaneh-Wold, and S. Wold, *Introduction to Multi- and Megavariate Data Analysis Using Projection Methods (PCA & PLS)*, Umetrics AB, Umeå, Sweden, 1999.

Esbensen, K., and P. Geladi, "Strategy of Multivariate Image Analysis (MIA)," *Chemometrics and Intelligent Laboratory Systems*, **7**, pp. 67 – 86, 1989.

Galloway, M. M., "Texture Analysis using Gray Level Run Lengths," *Comput. Vision Graphics Image Process.*, **4**, pp. 172 – 179, 1975.

Geladi, P., D. MacDougall, and H. Martens, "Linearization and Sctter-correction for Near-Infrared Reflectance Spectra of Meat," *Applied Spectroscopy*, **3**, pp. 491 – 500, 1985.

Geladi, P., and B. R. Kowalski, "Partial Least-Squares Regression: A Tutorial," *Analytica Chimica Acta*, **185**, pp. 1 – 17, 1986.

Geladi, P., "Notes on the History and Nature of Partial Least Squares (PLS) Modelling," *Journal of Chemometrics*, **2**, pp. 231 – 246, 1988.

Geladi, P., H. Isaksson, L. Lindqvist, S. Wold, and K. Esbensen, "Principal Component Analysis of Multivariate Images," *Chemometrics and Intelligent Laboratory Systems*, **5**, pp. 209 – 220, 1989.

Geladi, P., and K. Esbensen, "Regression on Multivariate Images: Principal Component Regression for Modeling, Prediction and Visual Diagnostic Tools," *Journal of Chemometrics*, **5**, pp. 97 – 111, 1991.

Geladi, P., "Some Special Topics in Multivariate Image Analysis," *Chemometrics and Intelligent Laboratory Systems*, **14**, pp. 375 – 390, 1992.

Geladi, P., J. Swerts, and F. Lindgren, "Multiwavelength Microscopic Image Analysis of a Piece of Painted Chinaware: Classification and Regression," *Chemometrics and Intelligent Laboratory Systems*, **24**, pp. 145 – 167, 1994.

Geladi, P., and H. Grahn, *Multivariate Image Analysis*, John Wiley & Sons, Chichester, UK, 1996.

Glasbey, C. A., and G. W. Horgan, *Image Analysis for the Biological Sciences*, John Wiley & Sons, Chichester, UK, 1995.

Glasbey, C. A., and K. V. Mardia, "A Review of Image-Warping Methods," *Journal of Applied Statistics*, **25**, pp. 155 – 171, 1998.

Golub, G. H., and C. F. Van Loan, *Matrix Computations*, The John Hopkins University Press, Baltimore, MD, 1983.

Gonzalez, R. C., and R. E. Woods, *Digital Image Processing*, Addison-Wesley, Singapore, 1992.

Grahn, H., N. M. Szeverenyi, M. W. Roggenbuck, F. Delaglio, and P. Geladi, "Data Analysis of Multivariate Magnetic Resonance Images I. A Principal Component Analysis Approach," *Chemometrics and Intelligent Laboratory Systems*, **5**, pp. 311 – 322, 1989.

Grahn, H., N. M. Szeverenyi, M. W. Roggenbuck, and P. Geladi, "Tissue Discrimination in Magnetic Resonance Imaging: A Predictive Multivariate Approach," *Chemometrics and Intelligent Laboratory Systems*, 7, pp. 87 – 93, 1989b.

Grahn, H., and P. Geladi, "Application of Multivariate Data Analysis Techniques to NMR Imaging," in N. Rutledge (ed.), *Signal Treatment and Signal Analysis in NMR*, Elsevier, Amsterdam, 1995.

Grangier, R. G., D. J. Allison, A. Adam, and A. K. Dixon (eds.), *Grainger & Allison's Diagnostic Radiology: A Textbook of Medical Imaging: Vol. 1*, 4th edition, Churchill Livingstone, NY, 2001.

Hagman, O., "Multivariate Methods to Classify Wooden Surfaces," Proc. Workshop on Scanning Technology and Image Processing on Wood, Skellefteå, Sweden, Aug. 31 – Sep. 1, 1992.

Hagman, O., "On Reflections of Wood," Ph.D. Thesis, Luleå University of Technology, Skellefteå, Sweden, 1996.

Hagman, O., "Multivariate Prediction of Wood Surface Features Using an Imaging Spectrograph," *Holz als Roh- und Werkstoff*, **55**, pp. 377 – 382, 1997.

Haralick, R. M., K. Shanmugam, and I. Dinstein, "Textural Features for Image Classification," *IEEE Trans. Systems Man Cybernet.*, **SMC-3**, pp. 610 – 621, 1973.

Haralick, R. M., "Statistical and Structural Approaches to Texture," *Proc. IEEE*, **67**, pp. 786 – 804, 1979.

Haralick, R. M., "Image Texture Survey," in P. R. Krishnaiah and L. N. Kanal (eds.), *Handbook of Statistics, Vol. 2*, North-Holland Publishing Company, pp. 399 – 415, 1982.

He, D. C., and L. Wang, "Texture Features based on Texture Spectrum," *Pattern Recognition*, **24**, pp. 391 – 399, 1991.

Herrala, E., and J. Okkonen, "Imaging Spectrograph and Camera Solutions for Industrial Applications," *International Journal of Pattern Recognition and Artificial Intelligence*, **10**, pp. 43 – 54, 1996.

Hildrum, K. I., T. Isaksson, T. Næs, and A. Tandberg (eds.), *Near Infra-Red Spectroscopy: Bridging the Gap Between Data Analysis and NIR Applications*, Ellis Horwood, Chichester, UK, 1992.

Höskuldsson, A., "PLS Regression Methods," *Journal of Chemometrics*, **2**, pp. 211 – 228, 1988.

Huang, J., and K. H. Esbensen, "Applications of Angle Measure Technique (AMT) in Image Analysis Part I. A New Methodology for In Situ Powder Characterization," *Chemometrics and Intelligent Laboratory Systems*, **54**, pp. 1 – 19, 2000.

Hyvarinen, T., E. Herrala, and A. Dall'Ava, "Direct Sight Imaging Spectrograph: A Unique Add-on Component Brings Spectral Imaging to Industrial Applications," Proceedings of SPIE – Digital Solid State Cameras: Designs and Applications, San Jose, CA, January 25 – 30, 1998.

Indhal, U., and T. Næs, "Evaluation of Alternative Spectral Feature Extraction Methods of Textural Images for Multivariate Modeling," *Journal of Chemometrics*, **12**, pp. 261 – 278, 1998.

Jackson, J. E., *A User's Guide to Principal Components*, John Wiley & Sons, NY, 1991.

Jenkins, G. M., and D. G. Watts, *Spectral Analysis and its Applications*, Holden-Day Inc., San Francisco, CA, 1969.

Kaneko, T., "Color Composite Pictures from Principal Axis Components of Multispectral Scanner Data," *IBM J. Res. Dev.*, **22**, pp. 386 – 392, 1978.

Kauppinen, H., and O. Silvén, "A Color Vision Approach for Grading Lumber," in G. Borgefors (ed.), *Theory & Applications of Image Processing II – Selected Papers* *from the 9th Scandinavian Conference on Image Analysis*, World Scientific, pp. 367 – 379, 1995.

Keller, J. M., S. Chen, and R. M. Crownover, "Texture Description and Segmentation Through Fractal Geometry," *Comput. Vision Graphics Image Process.*, **45**, pp. 150 – 166, 1989.

Kim, C. W., and A. J. Koivo, "Hierarchical Classification of Surface Defects on Dusty Wood Boards," *Pattern Recognition Letters*, **15**, pp. 713 – 721, 1994.

Klinnkhachorn, P., R. Kothari, and A. Huber, "A Modified Vision System for the Automated Lumber Processing System (ALPS)," Proc. 4th Int. Conference on Scanning Technology in the Wood Industry, San Francisco, Oct. 28 – 29, 1991.

Kvaal, K., J. P. Wold, U. G. Indhal, P. Baardseth, and T. Næs, "Multivariate Feature Extraction from Texture Images of Bread," *Chemometrics and Intelligent Laboratory Systems*, **42**, pp. 141 – 158, 1998.

Lee, S. C., G. S. Qian, J-B Chen, and D. A. Hay, "Scanning Logs for Knots," Proc. 7th Scandinavian Conference on Image Analysis, Aalborg, Denmark, Aug. 13 – 16, 1991.

Lied, T. T., P. Geladi, and K. Esbensen, "Multivariate Image Regression (MIR): Implementation of Image PLSR – First Forays," *Journal of Chemometrics*, **14**, pp. 585 – 598, 2000.

Lied, T. T., "Multivariate Image Regression (MIR) for Quantitative Predictions," Ph.D. Thesis, Telemark University College and the Norwegian University of Science & Technology, Porsgrunn, Norway, 2000.

Lindgren, F., P. Geladi, and S. Wold, "The Kernel Algorithm for PLS," *Journal of Chemometrics*, **7**, pp. 45 – 59, 1993.

Lindgren, F., P. Geladi, and S. Wold, "Kernel-Based PLS Regression; Cross-Validation and Applications to Spectral Data," *Journal of Chemometrics*, **8**, pp. 377 – 389, 1994.

Loum, G., J. Lemoine, E. Petit, and P. Provent, "An Application of Wavelet Transform to Texture Analysis," Proc. 9th Scandinavian Conf. on Image Analysis, Uppsala, Sweden, June, 1995.

Mackay, R. S., *Medical Images and Displays*, John Wiley & Sons, NY, 1984.

Maristany, A. G., D. A. Butler, C. C. Brunner, and J. W. Funck, "Exploiting Local Color Information for Defect Detection on Douglas-Fir Veneer," Proc 4th Int. Conference on Scanning Technology in the Wood Industry, San Francisco, Oct. 28 – 29, 1991.

Martens, H., and T. Næs, *Multivariate Calibration*, John Wiley & Sons, Chichester, UK, 1989.

Matsuyama, T., S. I. Miura, and M. Nagao, "Structural Analysis of Natural Textures by Fourier Transformation," *Comput. Vision Graphics Image Process*, **12**, pp. 286 – 308, 1980.

McClure, W. F., "Near-Infrared Spectroscopy: The Giant is Running Strong," *Analytical Chemistry*, **66**, pp. 43 – 53, 1994.

Næs, T., and H. Martens, " Principal Component Regression: Viewpoints, Background Details and Selection of Components," *Journal of Chemometrics*, **2**, pp. 155 – 167, 1988.

National Lumber Grades Authority, *NLGA Standard Grading Rules for Canadian Lumber*, National Lumber Grades Authority, 260-1055 West Hastings Street, Vancouver, BC, Canada, 1991.

National Lumber Grades Authority, *Canadian Lumber Grading Manual*, National Lumber Grades Authority, 406 – First Capital Place, 960 Quayside Drive, New Westminster, BC, Canada, 1998.

Ohta, Y., T. Kanade, and T. Sakai, "Color Information for Region Segmentation," *Computer Graphics and Image Processing*, **13**, pp. 222 – 241, 1980.

Pölzleitner, W., and G. Schwingshakl, "Real-time Classification of Wooden Boards," SPIE vol. 1384, High Speed Inspection Architectures, Barcoding and Character Recognition, pp. 38 – 49, 1990.

Pratt, W. K., *Digital Image Processing*, John Wiley & Sons, NY, 1978.

Rännar, S., F. Lindgren, P. Geladi, and S. Wold, "A PLS Kernel Algorithm for Data Sets with Many Variables and Fewer Objects. Part 1: Theory and Algorithm," *Journal of Chemometrics*, **8**, pp. 111 – 125, 1994.

Ready, P. J., and P. A. Wintz, "Information Extraction, SNR Improvement, and Data Compression in Multispectral Imagery," *IEEE Transactions on Communication*, **COM-21**, pp. 1123 – 1130, 1973.

Rosenfeld, A., and B. S. Lipkin (eds.), *Picture Processing and Psychopictorics*, Academic Press, NY, 1970.

Russ, J. C., *The Image Processing Handbook*, 3rd edition, CRC Press, FL, 1999.

Sarkar, A., K. M. S. Sharma, and R. V. Sonak, "A New Approach for Subset 2-D AR Model Identification for Describing Textures," *IEEE Trans. Image Process.*, **6**, pp. 407 – 413, 1997.

Savitsky, A., and M. J. Golay, "Smoothing and Differentiation by Simplified Least Squares Procedures," *Analytical Chemistry*, **36**, pp. 1627 – 1632, 1964.

Schultz, T. P., and D. A. Burns, "Rapid Secondary Analysis of Lignocellulose: Comparison of Near Infrared (NIR) and Fourier Transform Infrared (FTIR)," *Tappi Journal*, **73**, pp. 209 – 212, 1990.

Serra, J., *Image Analysis and Mathematical Morphology*, Academic Press Inc. (London) Ltd., UK, 1982.

Shibayama, M., and T. Akiyama, "Estimating Grain Yield of Maturing Rice Canopies Using High Spectral Resolution Reflectance Measurements," *Remote Sensing Environ.*, **36**, pp. 45 – 53, 1991.

Silvén, O., and H. Kauppinen, "Color Vision Based Methodology for Grading Lumber," Proc. 12th Int. Conf. on Pattern Recognition, Jerusalem, Israel, Oct. 9 – 13, 1994.

Singh, A., and A. Harrison, "Standardised Principal Components," *Int. J. Remote Sensing*, **6**, pp. 883 – 896, 1985.

Sjöström, M., S. Wold, and B. Söderström, "PLS Discriminant Plots," in E. S. Gelsema and L. N. Kanal (eds.), *Pattern Recognition in Practice II*, Elsevier, Amsterdam, 1986.

Sobey, P. J., and E. C. Semple, "Detection and Sizing Visual Features in Wood Using Tonal Measures and a Classification Algorithm," *Pattern Recognition*, **22**, pp. 367 – 380, 1989.

Stark, E., and K. Luchter, "Near-Infrared Analysis (NIRA): A Technology for Quantitative and Qualitative Analysis," *Applied Spectroscopy Reviews*, **22**, pp. 335 – 399, 1986.

Svensson, O., "Vibrational Spectroscopy and Multivariate Methods in Chemical Analysis," Ph.D. Thesis, Göteborg University, Göteborg, Sweden, 1999.

Svensson, O., T. Kourti, and J. F. MacGregor, "A Comparison of Orthogonal Signal Correction Algorithms and Characteristics," *Journal of Chemometrics*, **16**, pp. 176 – 188, 2002.

Tang, Y. T., and C. Y. Suen, "Image Transformation Approach to Nonlinear Shape Restoration," *IEEE Transactions on Systems, Man and Cybernetics*, **23**, pp. 155 – 171, 1993.

Thompson, C. M., and L. Shure, "Image Processing Toolbox for use with MATLAB®: User's Guide," The Math Works Inc., 24 Prime Park Way, Natick, MA, 1995.

Tomita, F., and S. Tsuji, *Computer Analysis of Visual Textures*, Kluwer Academic Publishers, MA, 1990.

Trygg, J., and S. Wold, "PLS Regression on Wavelet Compressed NIR Spectra," *Chemometrics and Intelligent Laboratory Systems*, **42**, pp. 209 – 220, 1998.

Trygg, J., and S. Wold, "Orthogonal Projections to Latent Structures (O-PLS)," *Journal of Chemometrics*, **15**, pp. 1 – 18, 2001.

Umetrics, "SIMCA-P 9.0," Umetrics AB, Box 7960, S-907 19 Umeå, Sweden, 2001.

Unser, M., "Texture Classification and Segmentation using Wavelet Frames," *IEEE Trans. Image Process.*, **4**, pp. 1549 – 1560, 1995.

Vaarala, T., I. Moring, and E. Herrala, "Imaging Spectroscopy for On-line Wood Quality Inspection: An Experimental Study," 2nd Int. Seminar on Scanning Technology and Image Processing on Wood, Skellefteå, Sweden, Aug. 14 – 16, 1995.

van den Broek, W. H. A. M., E. P. P. A. Derks, E. W. van de Ven, D. Wienke, P. Geladi, and L. M. C. Buydens, "Plastic Identification by Remote Sensing Spectroscopic NIR Imaging Using Kernel Partial Least Squares (KPLS)," *Chemometrics and Intelligent Laboratory Systems*, **35**, pp. 187 – 197, 1996.

Wallbäcks, L., U. Edlund, and B. Norden, "Multivariate Characterization of Pulp using Solid-state 13C NMR, FTIR, and NIR," *Tappi Journal*, **74**, pp. 201 – 206, 1991.

Wheeler, S. G., and P. N. Misra, "Linear Dimensionality of LANDSAT Agricultural Data with Implications for Classification," Proceedings of 1976 Symposium on Machine Processing of Remote Sensing Data, LARS, Purdue University, IN, pp. 2A-1 – 2A-9, 1976.

Whetsel, K. B., "Near-Infrared Spectrophotometry," *Applied Spectroscopy Reviews*, **2**, pp. 1 – 67, 1968.

Woitkovich, C. P., T. J. McDonough, and E. W. Malcolm, "NIR-Based Yield Estimation in Semichemical Pulping," in *Proc. Tappi Pulping Conference*, Tappi Press, pp. 721 – 733, 1994.

Wold, S., "Cross-Validatory Estimation of the Number of Components in Factor and Principal Components Models," *Technometrics*, **20**, pp. 397 – 405, 1978.

Wold, S., C. Albano, W. J. Dunn III, U. Edlund, K. Esbensen, P. Geladi, S. Hellberg, E. Johansson, W. Lindberg, and M. Sjöström, "Multivariate Data Analysis in Chemistry," in B. R. Kowalski (ed.), *Chemometrics, Mathematics and Statistics in Chemistry*, D. Reidel Publishing Co., pp. 17 – 95, 1984.

Wold, S., H. Antti, F. Lindgren, and J. Öhman, "Orthogonal Signal Correction of Near-Infrared Spectra," *Chemometrics and Intelligent Laboratory Systems*, **44**, pp. 175 – 185, 1998.

Wright, J. A., M. D. Birkett, and M. J. Gambino, "Prediction of Pulp Yield and Cellulose Content from Wood Samples using Near Infrared Spectroscopy," *Tappi Journal*, **73**, pp. 164 – 166, 1990.

Yaglom, A. M., *Theory of Stationary Random Functions*, Prentice-Hall, Englewood Cliffs, NJ, 1962.

Zucker, S. W., "Towards a Model of Texture," *Comput. Vision Graphics Image Process*, **5**, pp. 190 – 202, 1976.

Appendix A

Alignment of Score Plots in a MIA Monitoring Scheme

The basic assumption made when monitoring feature pixels using MIA score space masks developed from score plots of a training image is that the score plots of the corresponding test images would also be aligned with that of the training image. If this assumption were violated, a straightforward application of these masks in the test image score plots would produce erroneous results by misclassifying feature pixels. In this case, the misaligned score plots need to be properly aligned prior to application in the monitoring scheme. As discussed in section 2.3.1 a scatter plot of Principal Component (PC) scores is illustrated as a color-coded 2-dimensional histogram, where the frequency of points in each bin is represented as a brightness value. The histogram is recorded as a false-color image, with a pixel color/intensity representing the brightness value of each bin. Since score plots can be represented in these two ways, there are mainly two types of techniques that can be used to align the misaligned score plot of a new image with that of a training image.

Image-based alignment techniques can be used to align the false color-coded image representations of any two score plots. This type of alignment considers the training image score plot to be a template image with which one would like to align the score plot of another image. Several image-warping methods have been proposed in the literature that can be used to calculate the required transformation in order to align the two images [Tang et. al., 1993; Arad, 1995; Glasbey et. al., 1995]. Matching a new image with a template can involve specifying that certain points be brought into alignment, by the coincidence of object edges, or by local measures of correlation between the two images. Glasbey et. al. [1998] present a review of various linear and non-linear image-warping techniques that can be used to rotate, enlarge or shrink the point clusters in the score plot of a new image in order to match it with the cluster pattern of the training image score plot. However, the complexity of a warping technique versus time constraints for an on-line application warrants a need for good balance. With respect to the on-line lumber defect monitoring study of section 3.4.1 certain types of image-warping techniques would introduce a risk of warping the score point cluster patterns of a lumber sample image without any pitch pockets (i.e. having no cluster at top of its $\mathbf{t}_1 - \mathbf{t}_2$ score plot) into a template score plot that has a pitch pockets point cluster. This would make the problem worse than if no correction were made.

For the on-line lumber defect monitoring study the main problem was the shifting of the point cluster patterns in the new test images due to color contrast variations of clear wood between samples. Since no shape warping was required in this application, some of the simple approaches of aligning the score plots based on their 2-dimensional histogram measures might be good enough.

Histogram-based alignment techniques try to match some characteristics of the 2-dimensional histogram representations of two score plots. One possible approach might include matching statistical measures like mean, median, mode etc. of the two score plot histograms. This type of matching would result in a simple shifting of the point clusters in the score plot of an image to be aligned with that of another.

The lumber defect monitoring study in section 3.4.1 used mean matching of the 2-D histograms to align the score plots of all 38 lumber sample images with that of the training lumber image. This resulted in a shift of the score point clusters of the test images to align their means with the mean score point of the training image score plot. Alternatively, one could use the medians of the two histograms to align the score plots if one wanted to avoid influence of any outlying score points in the manipulation. However, in the case of lumber images mean matching produced sufficient results. The new shifted value of each score point in a test lumber image was calculated using the following equation:

$$(t_{1test\,new}, t_{2test\,new}) = (t_{1test} + [\bar{t}_{1\,tr} - \bar{t}_{1\,test}], t_{2test} + [\bar{t}_{2\,tr} - \bar{t}_{2\,test}]) \tag{A.1}$$

where, $(t_{1test\ new}, t_{2test\ new})$ is the new location of the score point upon shifting the test image score plot; $(\bar{t}_{1\,tr}, \bar{t}_{2\,tr})$ and $(\bar{t}_{1\,test}, \bar{t}_{2\,test})$ are the original locations of the mean score points in the score plots of the training image and the test image, respectively. Figure A.1 illustrates the effect of the histogram mean matching alignment strategy on the score plot of a test lumber image. The original score plot of a test lumber sample image is shown with its adjusted version and a difference image between them to visually determine the amount of shifting achieved. In the difference image black pixels represent areas where the score plot was originally located, whereas white pixels illustrate the new position of the adjusted score plot.

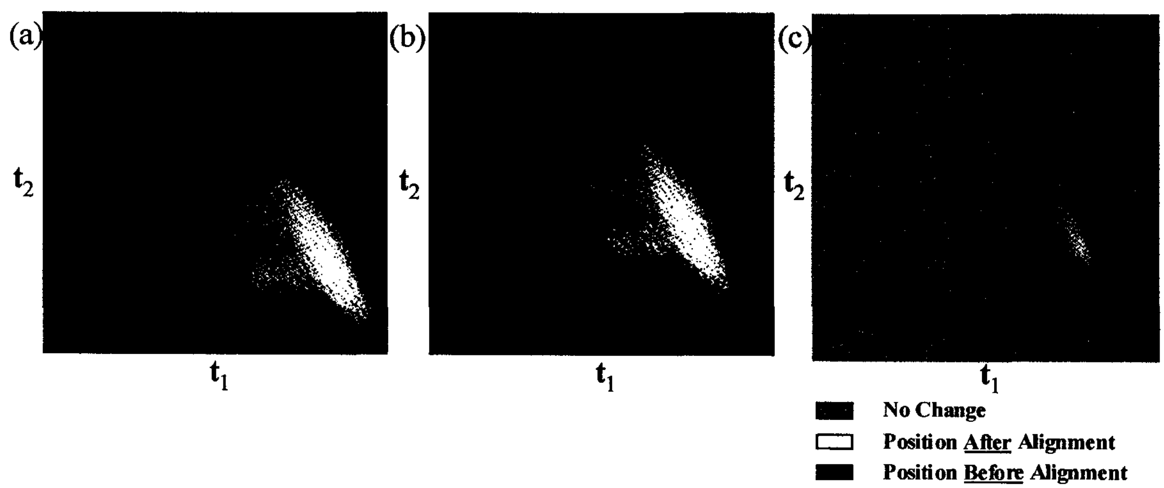

Figure A.1 (a) Unadjusted $t_1 - t_2$ score plot of a test lumber sample image. (b) Adjusted version of score plot in (a) using histogram mean matching alignment with training image. (c) Difference image between the two score plots

Appendix B

Comments on the use of PLS-DA Models in MIR

PLS-DA models have been used for pixel wise classification of interesting features from multivariate images. When using such models in MIR certain basic requirements must be met in order to get good classification. It is important to exercise caution when setting-up the class-membership of the feature pixels in the dummy binary image **Y** used to train the PLS-DA model. In order to achieve good classification using PLS-DA models features must be homogeneous, tightly clustered and separable from background in the variable space of the multivariate image. Section 3.5 discusses these conditions in further detail.

The importance of satisfying the above-mentioned fundamental requirements is illustrated with the following example study from the field of lumber grading. This is followed by a conceptual example, which illustrates a situation where a PLS2-DA model (i.e. with *multiple* **Y** dummy binary images) is needed to achieve good classification even if the above conditions are met.

The first example study includes PLS1-DA modeling (i.e. with a *single* **Y** dummy binary image) and classification of pixels from selected lumber defects in RGB images of two lumber boards. Figure B.1 illustrates two RGB lumber sample images ($\underline{\mathbf{X}}_{\mathrm{I}}$ and $\underline{\mathbf{X}}_{\mathrm{II}}$), which have been segmented using masks in their corresponding ($\mathbf{t}_1 - \mathbf{t}_2$) PC score plots to isolate the spatial locations of pixels from two selected lumber features as binary ($\mathbf{Y}_{\mathrm{I}}$ and

Y_{II}) images. As indicated in figure B.1 the two lumber features of interest to be modeled are pitch pockets in lumber sample I, and rotten wood in sample II.

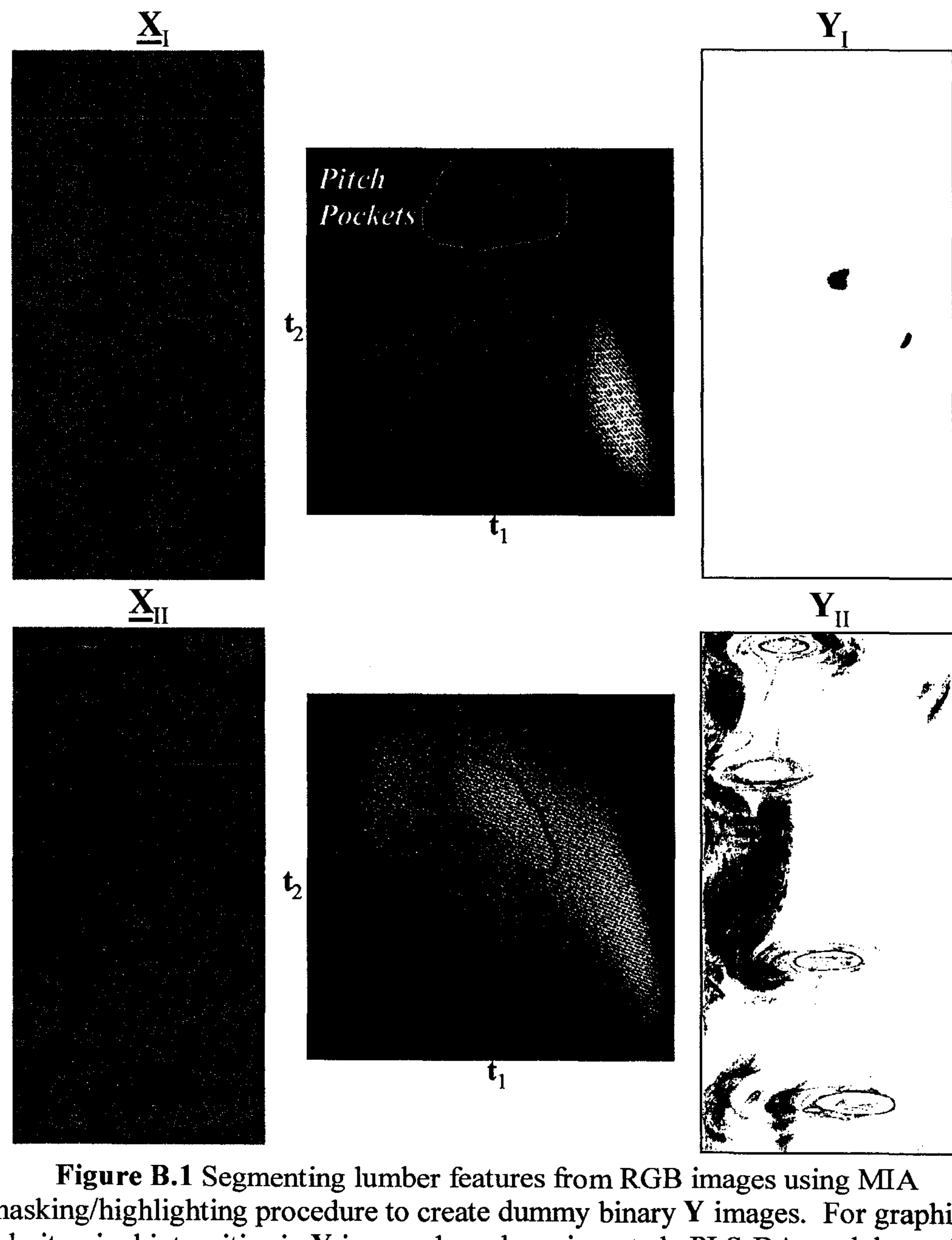

Figure B.1 Segmenting lumber features from RGB images using MIA masking/highlighting procedure to create dummy binary Y images. For graphical clarity pixel intensities in Y images have been inverted. PLS-DA models can be trained between $\underline{\underline{X}}$ and (un-inverted) Y

Two separate PLS-DA models were trained to regress the respective RGB lumber images $\underline{\underline{X}}_I$ and $\underline{\underline{X}}_{II}$ with the corresponding dummy binary images Y_I and Y_{II}, respectively.

Both models used 2 significant PLS components to decompose the data in $\underline{\mathbf{X}}_{\mathrm{I}}$ and $\underline{\mathbf{X}}_{\mathrm{II}}$. The model regression coefficients were re-used on their respective RGB lumber images to obtain model predictions $\hat{\mathbf{Y}}_{\mathrm{I}}$ and $\hat{\mathbf{Y}}_{\mathrm{II}}$, which were scaled into grayscale pixel intensities and visualized as prediction images. Brighter intensities in both prediction images (figure B.2) indicate higher probability of pixels belonging to a feature of interest. Both prediction images were manually thresholded to maximally isolate the feature pixels from background. Error images $\mathbf{E}_{\mathrm{I}}$ and $\mathbf{E}_{\mathrm{II}}$ were then created for both models upon subtracting the original $\mathbf{Y}$ and thresholded $\hat{\mathbf{Y}}$ images. The error image indicates correctly classified pixels in gray, background pixels misclassified as features are indicated in black, whereas feature pixels misclassified as background are indicated in white colors. Figure B.2 illustrates the model predictions and classification errors of the two PLS-DA models.

It can be seen from the prediction images in figure B.2 that the PLS-DA model trained to classify pitch pockets in sample I performs much better than the classification achieved by the model used to isolate rot in sample II. As illustrated in the error image $\mathbf{E}_{\mathrm{II}}$ the PLS-DA model for sample II shows significant misclassifications between feature pixels from rot and knots. This disparity in the classifications achieved by the two models stems from the class-memberships defined in the respective dummy binary images $\mathbf{Y}_{\mathrm{I}}$ and $\mathbf{Y}_{\mathrm{II}}$, which were used to train the respective models.

As seen in the $(\mathbf{t}_1 - \mathbf{t}_2)$ PC score plot of sample I (figure B.1) scores from pixels belonging to pitch pockets are tightly clustered and relatively well separated from the background pixel scores. As a result, the pitch pockets class defined in the corresponding binary image $\mathbf{Y}_{\mathrm{I}}$ is a homogeneous class. Thus it can be seen that the class-membership assignment in sample I meets the basic requirements for using a PLS-DA model to classify the pitch pockets feature from background pixels. On the other hand, the class definition of rot in the binary image $\mathbf{Y}_{\mathrm{II}}$ is inhomogeneous. This is due to the fact that the score points defining rot pixels have been manually segmented from a bigger cluster (representing both rot and clear wood) via MIA masking in the $(\mathbf{t}_1 - \mathbf{t}_2)$ PC score plot of sample II (figure B.1). Furthermore, it can also be seen from this plot that the PC score points representing rot are loosely clustered and inseparable from the bigger score cluster.

As a result, the class definitions assigned in $\mathbf{Y}_{\mathrm{II}}$ do not satisfy the conditions for using PLS-DA to classify rot from background features in sample II.

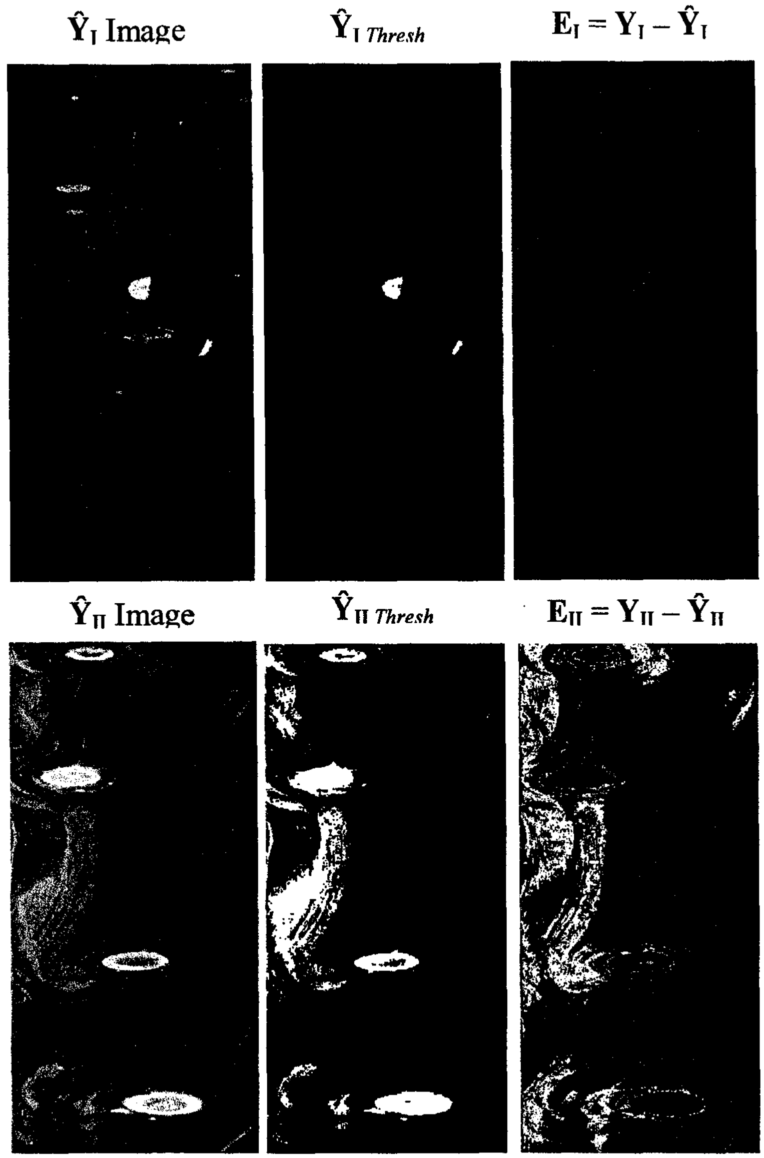

Figure B.2 Model predictions (grayscale and binary) images and classification error images of the two PLS-DA models

The respective discriminant planes of the two PLS-DA models are illustrated in figure B.3. Each plane has been superimposed on the $(\mathbf{t}_1 - \mathbf{t}_2)$ PLS score plot to indicate the boundary of the two classes defined by the class-memberships in the binary images $\mathbf{Y}_{\mathrm{I}}$ and $\mathbf{Y}_{\mathrm{II}}$ during the training stage of the PLS-DA model. Since both models are based on

2 significant PLS components the discriminant plane is in fact a line in the 2-dimensional ($\mathbf{t}_1 - \mathbf{t}_2$) PLS score plots of both lumber samples. As mentioned in section 3.5 the PLS score plots are rotated versions of the PC score plots since PLS-DA tried to rotate the PC scores in order to maximally separate the two classes defined in $\mathbf{Y}_I$ and $\mathbf{Y}_{II}$. Direction of the discriminant line is defined by the PLS inner relation between **X** and **Y** blocks [Hoskuldsson, 1988], whereas its actual location is manually set by the chosen threshold value to discriminate feature pixels in the predicted $\hat{\mathbf{Y}}_I$ and $\hat{\mathbf{Y}}_{II}$ images of the PLS-DA models. Further details on calculating the PLS discriminant plane may be obtained from [Wold et. al., 1984; Sjöström et. al., 1986].

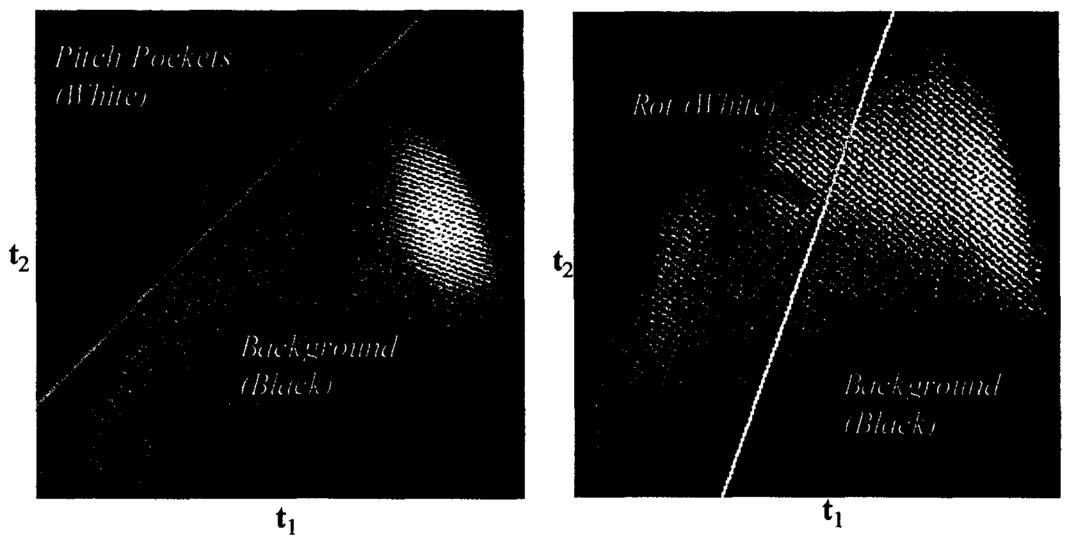

Figure B.3 Class boundaries defined by PLS-DA models to isolate pitch pockets and rot in the ($\mathbf{t}_1 - \mathbf{t}_2$) PLS score plots of respective lumber sample images

Upon observing the class boundaries of the two PLS-DA models in figure B.3 it becomes clear why the disparity exists between their achieved classifications. The PLS-DA model can easily isolate pitch pockets in sample I by placing the discriminant line between its score cluster and the background scores. However, the discrimiant line separating score points of rot from the bigger score cluster of clear wood cannot segment the feature pixels from knots. The obtained results from the above example study indicate the importance of choosing the classes when defining the PLS-DA models. The classes should be tight and well separated from others, thus ensuring that they are homogeneous.

The following conceptual example illustrates a situation where one might not achieve adequate feature pixel classification using a PLS1-DA model even though the above-mentioned conditions have been met. In such cases one might need a PLS2-DA model to segment the feature pixels from background features in a MIR scheme.

The example study aims to segment pixels from one of three distinctly different features in an image. All three features satisfy the conditions of tightly clustered and homogeneous classes in the ($\mathbf{t}_1 - \mathbf{t}_2$) PLS score plot. However, it will be shown that depending upon the separation (and placement) of the three feature pixel score clusters one might (or might not) be able to achieve the desired classification using a PLS1-DA model. Figure B.4 illustrates two different arrangements of the three feature pixel score clusters in the ($\mathbf{t}_1 - \mathbf{t}_2$) PLS score plot. The objective in both arrangements is to segment feature pixels belonging to "class 3" from the other two classes. Segmentation would be illustrated by the placement of the PLS-DA model discriminant line (i.e. class-boundary) between "class 3" and the other two classes. As shown before the location of the discriminant line is dependent on the pre-defined class memberships of each pixel in the **Y** image(s) and thresholds of the corresponding ($\hat{\mathbf{Y}}$) image(s).

Figure B.4(a) illustrates a situation where a PLS1-DA model has been used to segment feature pixels from "class 3" upon defining a single **Y** dummy binary image with class belongings of corresponding member pixels as 1 (white), and non-member pixels as 0 (black). In this case the non-member class ignores differences between pixels belonging to classes 1 and 2, which are themselves tightly clustered and well separated from each other in the ($\mathbf{t}_1 - \mathbf{t}_2$) PLS score plot. The PLS1-DA model simply concentrates on segmentation between this *lumped* "non-member class" and feature pixels from "class 3". As seen in figure B.4(a), due to the arrangement of the score clusters in the ($\mathbf{t}_1 - \mathbf{t}_2$) PLS score plot it is possible to find an adequate PLS1-DA discriminant line to achieve the desired classification. However, if the arrangement of the three score clusters in the ($\mathbf{t}_1 - \mathbf{t}_2$) PLS score plot resembles that of figure B.4(b), then it would be impossible to find a PLS1-DA discriminant line to isolate feature pixels belonging to "class 3" without misclassifications with pixels from the other two features. Figure B.4(b) illustrates two possible PLS1-DA model discriminant lines (dashed blue), which cannot achieve the desired classification.

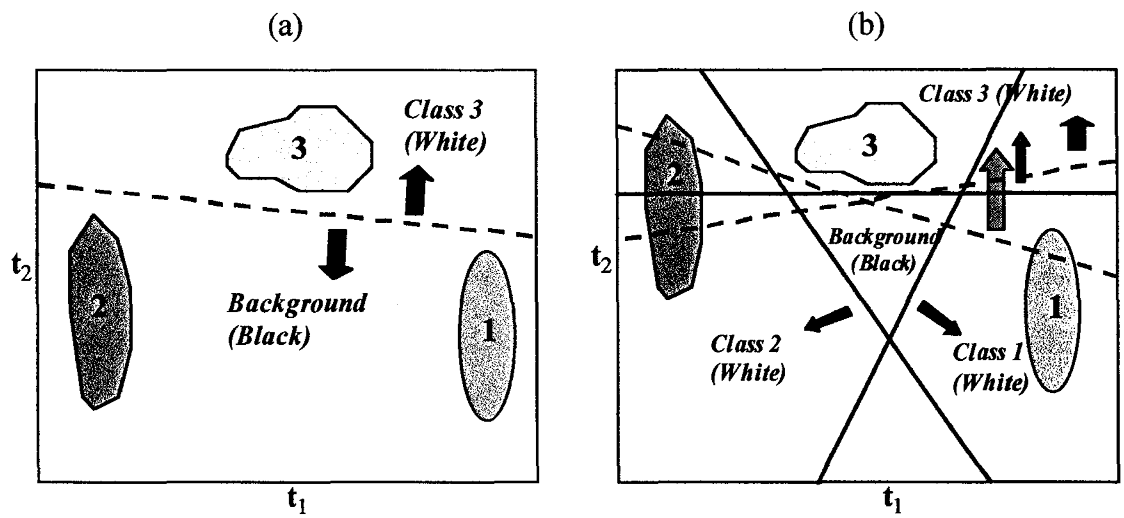

Figure B.4 Segmenting feature pixels in ($\mathbf{t}_1 - \mathbf{t}_2$) PLS score plots based on class-boundaries defined by PLS-DA models. (a) Discrimination using PLS1-DA model is adequate; (b) PLS2-DA model is required to achieve desired discrimination

In such cases it would be better to define a PLS2-DA model with three different **Y** dummy binary images, where each **Y** highlights differences between a unique feature pixel class (as member) and the other two classes (as non-member). In this case the PLS2-DA model does not ignore inherent differences between any of the three feature pixel classes. The resulting PLS2-DA model would produce three different discriminant lines in the ($\mathbf{t}_1 - \mathbf{t}_2$) PLS score plot, where each line aims to isolate a respective feature pixel class from the other two classes. Class-boundaries defined by all three discriminant lines would be considered together by the PLS2-DA model when performing classification. As seen in figure B.4(b) the achieved classification of feature pixels belonging to "class 3" is much better using the discriminant lines defined by the PLS2-DA model (solid red lines) as compared with either of the two possible PLS1-DA discriminant lines.

Appendix C

Steel Surface Image Dataset

The steel surface grayscale image dataset used in chapter 5 for purpose of testing various texture-based image classification techniques consists of 35 sample images. The complete dataset has been divided into three different pre-labeled surface quality classes based on visual grading by steel manufacturing industry personnel. Figure C.1 illustrates the full dataset, which consists of 10 samples pre-labeled as good surface quality [figure C.1(a)], 13 samples pre-labeled as medium surface quality [figure C.1(b)], and 12 samples pre-labeled as bad surface quality [figure C.1(c)]. Each image has dimensions 479×508 pixels (rows $\times$ columns), with 8-bit grayscale resolution.

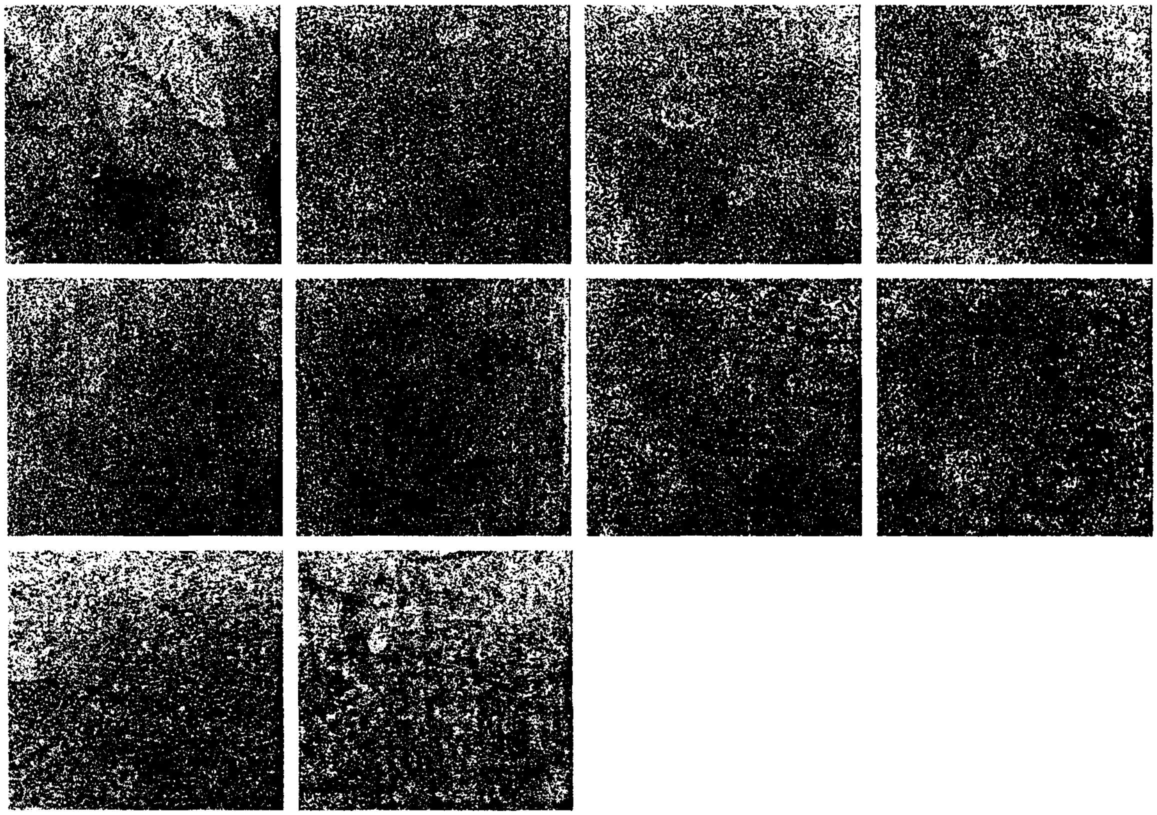

Figure C.1(a) Complete dataset of good steel surface quality images. 1st row (L to R): 001_aj, 003_bj, 004_aj, 004_bj. 2nd row (L to R): 007_aj, 007_bj, 008_aj, 008_bj. 3rd row (L to R): 015_aj, 017_aj

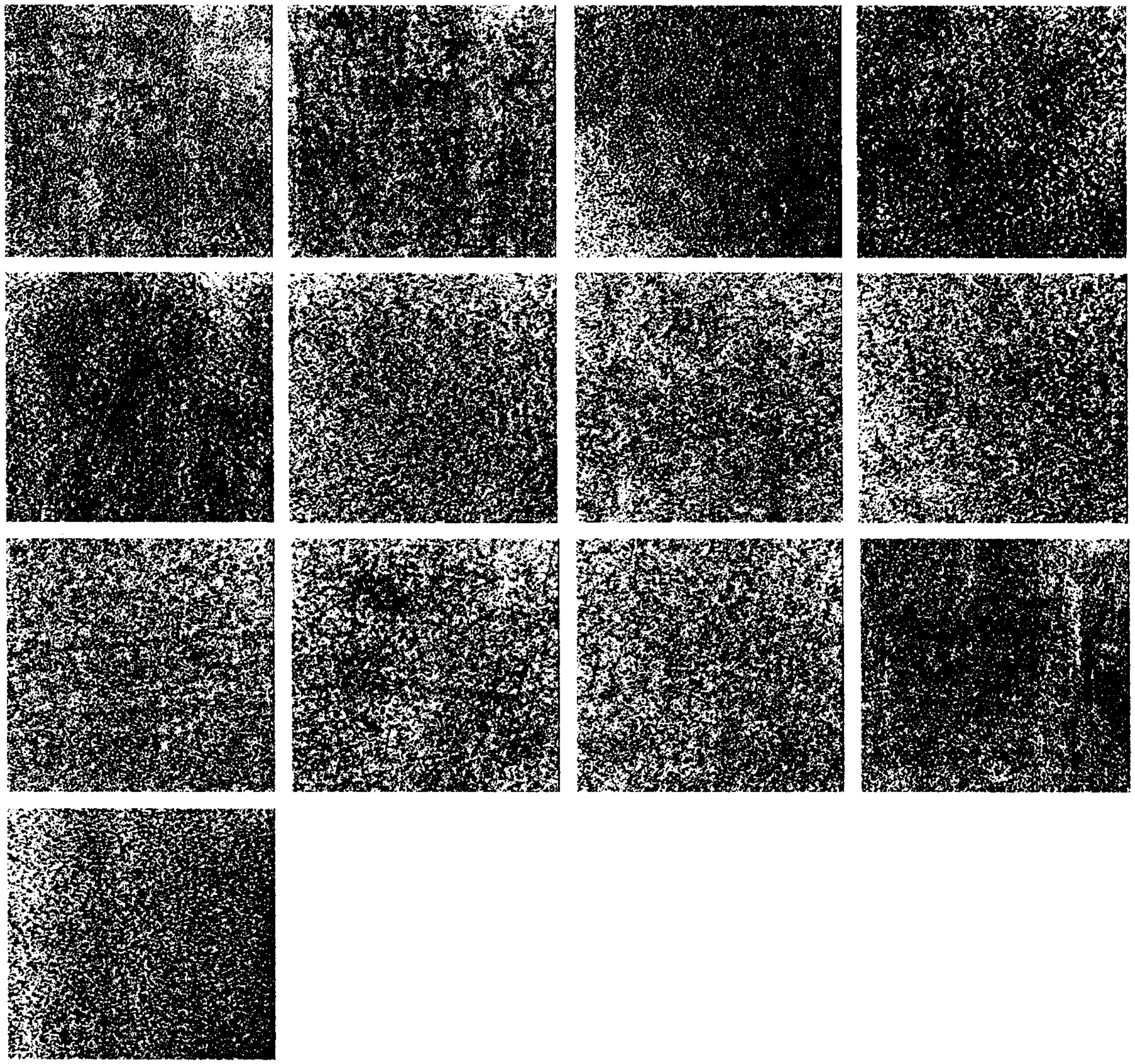

Figure C.1(b) Complete dataset of medium steel surface quality images. 1st row (L to R): 031_aj, 032_bj, 036_bj, 039_aj. 2nd row (L to R): 041_aj, 047_bj, 049_aj, 052_bj. 3rd row (L to R): 057_aj, 061_aj, 063_aj, 065_bj. 4th row: 073_bj

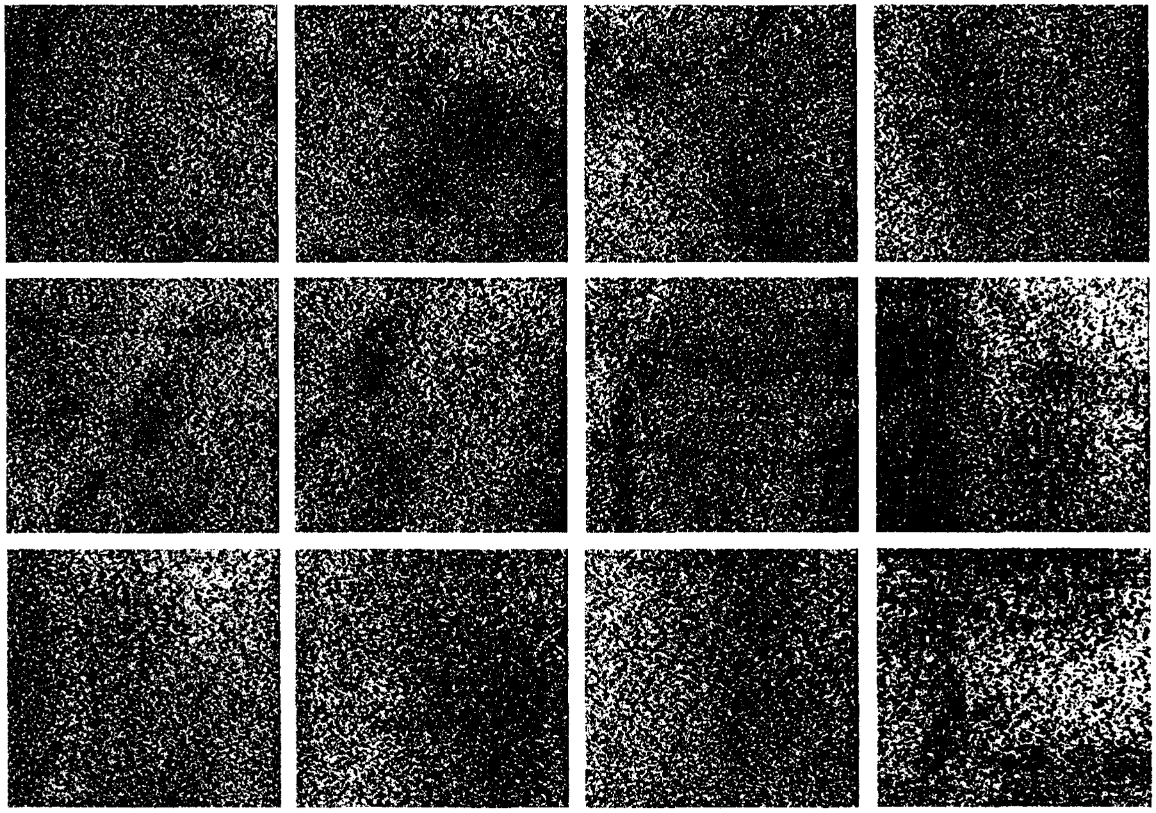

Figure C.1(c) Complete dataset of bad steel surface quality images. 1st row (L to R): 091_aj, 091_bj, 092_aj, 092_bj. 2nd row (L to R): 093_aj, 093_bj, 094_aj, 099_aj. 3rd row (L to R): 099_bj, 100_aj, 100_bj, 108_aj